1-11-2024

Mid-Infrared Dust Reverberation Mapping of Active Galactic Nuclei

Ashley Frank
alf7723@rit.edu

RIT College of Science Astrophysical Sciences and Technology

Mid-Infrared Dust Reverberation Mapping of Active Galactic Nuclei

By

Ashley Frank

A Dissertation Submitted in Partial Fulfillment of the Requirements for the Degree of Doctor of Philosophy. in Astrophysical Sciences & Technology

School of Physics and Astronomy
College of Science
Rochester Institute of Technology
Rochester, NY

January 11, 2024

Approved by:_____

Andrew Robinson, Ph.D Date
Director, Astrophysical Sciences and Technology

RIT | College of Science
Astrophysical Sciences and Technology

ROCHESTER, NEW YORK

CERTIFICATE OF APPROVAL

Ph.D. DEGREE DISSERTATION

The Ph.D. Degree Dissertation of Ashley Frank has been examined and approved by the dissertation committee as satisfactory for the dissertation requirement for the Ph.D. degree in Astrophysical Sciences and Technology.

Dr. Andrew Robinson, Thesis Advisor

Dr. Michael Richmond, Thesis Co-advisor

Dr. David Messinger, Committee Chair

Dr. Misty Bentz, Committee Member

Dr. Jeyhan Kartaltepe, Committee Member

Date _____

ACKNOWLEDGEMENTS

Part of this work was supported by HST proposal 15081.

The biggest thanks go to Dr. Andy Robinson and Dr. Michael Richmond for their guidance and support throughout this project. I would also like to thank the rest of my dissertation committee (Dr. Misty Bentz, Dr. David Messinger, Dr. Jeyhan Kartaltepe) for their helpful comments and advice.

DECLARATION

I, ASHLEY FRANK ("the Author"), declare that no part of this dissertation is substantially the same as any that has been submitted for a degree or diploma at the Rochester Institute of Technology or any other University. I further declare that this work is my own. Those who have contributed scientific or other collaborative insights are fully credited in this dissertation, and all prior work upon which this dissertation builds is cited appropriately throughout the text. This dissertation was successfully defended in Rochester, NY, USA on August 11, 2023.

ABSTRACT

One of the main components of the unified model of AGN (active galactic nuclei) is the circumnuclear dusty torus. The torus often obscures our view of the "central engine" of the AGN, therefore it is important to understand its size and structure. Reverberation mapping can be used to constrain the size of the torus, and relies on the response of the torus dust emission to the variations in the driving optical/UV emission of the accretion disk. The time lag between the optical emission and the infrared response can be used to constrain the distance between the inner region of the AGN, and the IR emission region of the torus.

This project focuses on a sample of 11 AGN, whose mid-IR (3.6 and 4.5 μm) light curves were observed with the Spitzer Space Telescope. The IR light curves were presented in Vazquez (2015). In this work, the optical light curves are constructed with a combination of data from three different ground-based telescopes, in the B, V, and G bands. Cross-correlation analysis has been conducted for four AGN, giving us reverberation lags for these objects. The reliability of the lags have been carefully evaluated by testing their dependence on different analysis procedures. One of these AGN is a changing-look AGN, NGC 6418, whose previous cross-correlation results have been reanalyzed. The optical-IR lag was measured both before and after a large optical flare, and was found to have increased after the flare, likely due to the sublimation of dust in the inner region of the torus.

For eight of the AGN, HST images were used along with the galaxy decomposition program GALFIT to model the distribution of galaxy light and hence to remove the starlight contribution from the optical light curves. This is a necessary step in order to use the torus reverberation mapping code, TORMAC, to model the IR light curves, as the dust emission responds to the optical variations. TORMAC was used to model three of the AGN in our sample, which allows us to constrain other torus structural properties. Some of these properties include the radial cloud distribution, the radial extent of the torus, and the torus inclination angle.

This dissertation produces reverberation mapping results for four AGN (KAZ 163, MRK 507, NGC 6418, and UGC 10697). The optical-IR lags vary from ∼40-140 days, depending on the AGN. Additionally, the 4.5 μm lags the 3.6 μm flux with typical lags between ∼15-30 days. This project increases the number of AGN with mid-IR dust reverberation mapping measurements, for which there have been few previous studies. One of the AGN (NGC 6418) is found to be a rare changing-look AGN. Not only are we able to measure the size of the torus, but through the use of TORMAC we also have a more complete picture of the structure of the torus in our sample of AGN.

CONTENTS

LIST OF TABLES

LIST OF FIGURES

CHAPTER 1

INTRODUCTION

1.1 AGN Overview

Actively accreting supermassive black holes (SMBHs) residing at the centers of galaxies are seen observationally as Active Galactic Nuclei (AGN). AGN radiate large amounts of energy across the entire electromagnetic spectrum. The "central engine" (consisting of the SMBH and the accretion disk) fuels the AGN as the gravitational potential energy from infalling gas is converted into the large bolometric luminosities we observe (Salpeter, 1964; Lynden-Bell, 1969). Quasars are extremely luminous, with visual luminosities of approximately $10^{44} - 10^{47}$ erg/s, while the AGN luminosities of Seyfert galaxies are $10^{41} - 10^{44}$ erg/s.

AGN are broadly separated into the categories of radio-loud or radio-quiet. Approximately 10% of AGN are radio-loud (e.g. quasars, radio galaxies, blazars). Radio emission from the AGN can be seen in jets which extend out on the scale of ∼Mpc and feed radio lobes, or in the form of compact radio cores. In contrast, radio-quiet AGN (e.g. Seyferts, radio-quiet quasars) have less powerful jets on ∼kpc scales and produce significantly less radio emission (Urry & Padovani, 1995).

There are several components found in most radio-loud and radio-quiet AGN, including the SMBH, the accretion disk, the broad and narrow line regions, and the dusty torus (see Fig. 1.1).

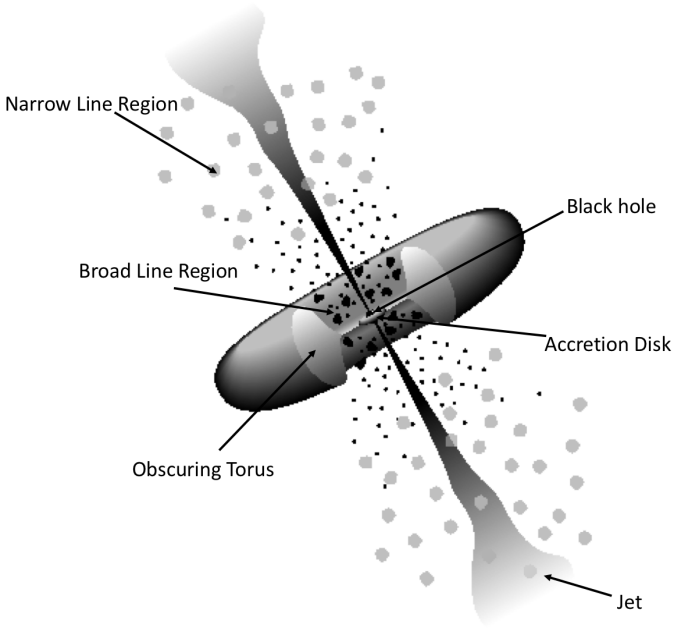

Figure 1.1: The major components of an AGN.

A review of these AGN components and their properties can be found in Heckman & Best (2014) and Netzer (2015). The accretion disk surrounds the SMBH and emits ionizing UV and optical radiation. The broad line region (BLR) is located within the central 1 pc of the AGN and is composed of clouds of dense ($n \sim 10^{9-11}$ cm^{-3}) gas photoionized by the accretion disk continuum. The emission lines from the BLR are Doppler-broadened, with widths of $\sim 10^3 - 10^4$ km/s. Similar to the BLR, the narrow line region (NLR) is also photoionized by the AGN, however it extends over scales $\sim$ 10 pc to kiloparsecs away from the center of the AGN. The line widths are narrower at 300-1000 km/s, and its gas density is lower ($n \sim 10^6$ cm^{-3}) .

1.2 Torus Properties

The focus of my dissertation is on the torus, which plays a major role in the AGN unification scheme. In the current model, the differences in the types of AGN (Type I or Type II) are due to the orientation of the torus toward our line of sight (Antonucci, 1993; Urry & Padovani, 1995).

When observed face-on, we have a direct view of the central engine and the broad line region, and it is observed to be a Type I AGN. We observe Type II AGN edge-on, and the torus blocks our view of the central region, such that the broad line region and central engine are obscured. Intermediate type AGN are also possible, whose spectra exhibit features intermediate between that of Type I and Type II AGN. The relative strength of the broad and narrow components of the Balmer lines determine their classification, with the most common including Seyfert 1.5, 1.8, and 1.9 (Osterbrock, 1977, 1981). Some of the intermediate type AGN occur due to partial obscuration of the broad line region, while others are due to intrinsic differences in the strengths of the broad lines relative to the narrow lines.

The torus therefore obscures the accreting SMBH in a large fraction of AGN, $\sim 70\%$ (Hickox & Alexander, 2018). This hinders our studies of the SMBH growth phase, by blocking our view of the central engine. The torus is also the main source of the observed IR continuum in AGN. Our motivation is that through studying the torus, we can learn more about the central engine that it obscures, as well as learn how the AGN population changes with redshift and luminosity.

The torus is a few parsecs in size and is geometrically and optically thick, generally thought to be composed of clumps of dusty molecular gas (Krolik & Begelman, 1988). The dust composition is thought to follow the standard interstellar grain mixture of 53% silicate and 47% graphite, with the grain sizes following the Mathis-Rumpl-Nordsieck, or MRN, distribution (Mathis et al., 1977). This distribution uses a grain size distribution of $n_{\rm d}(a) \propto a^{3.5}$, with grain sizes ranging from 0.005-0.25 μm.

The sublimation radius is the radius at which dust grains reach the sublimation temperature and defines the inner radius of the torus (Barvainis, 1987). Grains within this radius will sublimate and be destroyed by the UV radiation emitted by the central source. However, this inner edge is not a sharp boundary, as larger grains tend to survive closer to the central source. Also, most of the graphite grains will survive at a distance closer to the central source than will the silicate grains, as the sublimation temperature of graphite is much higher than the sublimation temperature for silicates. Therefore, the sublimation temperature for graphite is used to determine the inner edge of

the torus. This temperature depends on the gas density, although it is typically larger by 300-500K for graphite grains, compared to silicate. The dust sublimation radius from Nenkova et al. (2008b) assumes that the grains follow the standard ISM mixture, and is

$$R_{\rm sub} \approx 0.4\Big(\frac{L}{10^{45}\ {\rm erg\ s^{-1}}}\Big)^{\frac{1}{2}}\Big(\frac{1500{\rm K}}{T_{\rm sub}}\Big)^{2.6}\ {\rm pc}, \tag{1.1}$$

where L is the AGN bolometric luminosity, and $T_{\rm sub}$ is the sublimation temperature for graphite grains. It should be noted that this equation implies that $R_{\rm sub} \propto L^{1/2}$, which is further discussed in Section 1.3 in the context of dust reverberation mapping and IR interferometry.

The infrared (IR) emission of the torus can be observed in the spectral energy distribution (SED) as the mid-IR bump (Barvainis, 1987). This bump in the IR begins at around 1μm, leading to a peak at $\sim 10\mu$m. Early attempts to model the IR SEDs of AGN used a smooth distribution of dust grains, mainly due to the computational difficulties of using clumpy distributions. However, these smooth dust distributions fail to properly reproduce the observed characteristics of the 10 micron silicate feature (Nenkova, 2002). For a smooth and uniform distribution of grains, the temperature of each dust grain of a given composition (and its wavelength of emission) will depend only on its distance from the central engine. Since the dust grains are located over a wide range of radii from the center, the torus dust will emit at a wide range of wavelengths. The grains closest to the center of the AGN will be hottest and emit at near-IR wavelengths (2-3 μm), while the grains farther from the center will be coolest and emit in the far-IR (30-100 μm).

However, infrared interferometric observations show that a large range of temperatures can exist near the central source, which smooth distributions are unable to explain (Jaffe et al., 2004; Tristram et al., 2007). This is easily explained using a clumpy dust distribution (Nenkova et al., 2008a). Due to the optically thick nature of the dust clouds, different temperatures can occur on the different faces of a single cloud, depending on whether the side of the cloud is directly facing the central engine, or is non-illuminated.

Models of a clumpy dust distribution are better able to reproduce many observed features of AGN SEDs, such as the observed depth of the 10 μm silicate feature (Nenkova et al., 2008a,b). The characteristics of this feature depend on the observer's viewing angle: Type 2 AGN show this feature in absorption, while Type 1 AGN show this feature either in emission, or show a slight absorption feature. The silicate feature seen in observations is never very deep, however. Smooth dust distributions fail to reproduce the correct depth of the silicate feature, as a very deep feature is often produced, contradicting observations (Nenkova et al., 2008b, Nikutta et al., 2009).

Clumpy models can also explain the phenomenon that some AGN with Type I optical line spectra also have infrared SEDs characteristic of Type II AGN (Alonso-Herrero et al., 2003). This can be explained as being due to chance, rather than due to the orientation of the AGN: With a clumpy torus model, there is a small probability that no clouds intercept the observer's line of sight in a Type II AGN, which leads to a direct view of the central region.

Many current models assume that the torus contains the obscuring dust, which emits most of the infrared emission seen in AGN SEDs. Some studies using interferometry have revealed a significant portion of mid-IR emission ($\geq 50\%$) originating from the polar region of several AGN on parsec-size scales or larger (Hönig et al., 2013; Asmus et al., 2016; López-Gonzaga et al., 2016), rather than originating from a torus-shaped region. These observations have inspired the development of newer models of the circum-nuclear dust distribution. Rather than viewing the distribution as a single obscuring structure, it has been suggested that there are two regions, a thin disk and a polar region (Hönig, 2019). The disk produces most of the near-IR emission at smaller radii, and emits some mid-IR emission at larger radii. Dusty radiatively-driven winds originating from the inner region produce the polar IR emission (Hönig et al., 2012a; Roth et al., 2012). This polar region includes dust distributed in the shape of a hollow cone surrounding the narrow line region, and produces most of the mid-IR emission. Therefore, the obscuring structure is now considered to be composed of dusty molecular gas that originates from different areas of the AGN, rather than being confined to a single obscuring region. For convenience, I will refer to the obscuring structure as the "torus," however it should be interpreted as the equatorial element of the dust distribution.

The torus dust grains are in radiative equilibrium with the accretion disk's UV emission, causing the dust to emit in the IR. The energy emitted by the dust is given by

$$\Gamma_{\text{emitted}} = 4\pi\sigma_{\text{d}} \int_0^\infty Q_{IR}(\lambda) B(T_d, \lambda) \text{d}\lambda, \tag{1.2}$$

where $\sigma_{\text{d}} = \pi a^2$ is the grain cross section, Q_{IR} is the absorption efficiency of the grains, and $B(T_d, \lambda)$ is the Planck function for the grain temperature. The Planck mean efficiency is defined by the following equation

$$\big\langle Q_P(T_{\text{d}}) \big\rangle = \frac{\pi}{\sigma_{\text{SB}} T_{\text{d}}^4} \int_0^\infty Q(\lambda) B(T_{\text{d}}, \lambda) \text{d}\lambda, \tag{1.3}$$

and can be used to rewrite the equation for the energy emitted by the dust grains

$$\Gamma_{\text{emitted}} = 4\sigma_{\text{d}} \big\langle Q_{\text{IR}}(T_{\text{d}}) \big\rangle \sigma_{SB} T_{\text{d}}^4. \tag{1.4}$$

The energy absorbed by dust at a given wavelength is given by a similar equation

$$\Gamma_{\text{absorbed}} = \sigma_{\text{d}} \int_0^\infty Q_{\text{UV}}(\lambda) \frac{L_\lambda}{4\pi R^2} \text{d}\lambda, \tag{1.5}$$

where Q_{UV} is the UV absorption efficiency of the grains.

By setting the energy emitted equal to the energy absorbed, the grain temperature can be found

$$\sigma_{\text{d}} \int_0^\infty Q_{\text{UV}}(\lambda) \frac{L_\lambda}{4\pi R^2} \text{d}\lambda = 4\sigma_{\text{d}} \big\langle Q_{\text{IR}}(T_{\text{d}}) \big\rangle \sigma_{SB} T_{\text{d}}^4.$$

Setting $Q_{UV} = 1$, the grain temperature can be solved for:

$$\frac{L}{4\pi R^2} = 4 \big\langle Q_{\text{IR}}(T_{\text{d}}) \big\rangle \sigma_{SB} T_{\text{d}}^4$$

$$T_{\rm d} = \Big(\frac{L}{16\pi R^2 \sigma_{SB} \big\langle Q_{\rm IR}(T_{\rm d})\big\rangle}\Big)^{\frac{1}{4}}. \tag{1.6}$$

1.3 Reverberation Mapping

We do not currently have the spatial resolution necessary to image the torus with single-dish telescopes, so we have to rely on other techniques to better understand its structure. Reverberation mapping and IR interferometry are techniques that can be used to constrain the size of the torus. Near-IR (K-band, 2.2 μm) and mid-IR (8-13 μm) interferometry have been used to image the dusty torus on parsec-sized scales in approximately 50 AGN (Swain et al., 2003; Jaffe et al., 2004; Tristram et al., 2007; Kishimoto et al., 2011; Weigelt et al., 2012; Hönig et al., 2012b; Burtscher et al., 2013; Gravity Collaboration et al., 2020; Leftley et al., 2021; Kishimoto et al., 2022). A relation between the interferometric radii and AGN luminosity has been found, which is $r \propto L^{0.5}$, where r is the radius, and L is the AGN luminosity. This relation applies to both measurements of the torus size calculated from near-IR interferometry (Kishimoto et al., 2011; Koshida et al., 2014; Weigelt et al., 2012), and mid-IR interferometry (Tristram et al., 2009; Burtscher et al., 2013). However, Burtscher et al. (2013) found that there is far more scatter in the relation using mid-IR interferometry, than the measurements from the near-IR. This is possibly due to the mid-IR dust originating from different components of the AGN.

While IR interferometry has been used to study the torus, it is limited in that it can only be used on relatively nearby AGN. Reverberation mapping (Blandford & McKee, 1982) can also be used to constrain the size of the torus, and is not limited fundamentally by distance. It has been applied to the BLR (Blandford & McKee, 1982; Clavel et al., 1989; Peterson, 1993; Kaspi et al., 2000; Grier et al., 2019), as well as the torus (Clavel et al., 1989; Suganuma et al., 2006; Koshida et al., 2014; Minezaki et al., 2019). This technique, applied to the BLR, involves analyzing the response of the BLR emission lines to the driving variations in the AGN ionizing continuum. The

emission lines of the BLR will respond to the variations of the optical/UV continuum, with a delay due to light travel times. The process works similarly when applied to the torus: The UV and optical emission from the accretion disk travels to the dust in the torus, where it is absorbed and reprocessed into IR emission. As the UV and optical emission varies, the IR emission will respond, with a delay due to the time it takes for the radiation from the central source to travel to the torus dust. A similar radius-luminosity relation, $r \propto L^{0.5}$, has also been found from both BLR reverberation mapping (Kaspi et al., 2000; Bentz et al., 2009, 2013; Grier et al., 2019) and dust reverberation mapping (Suganuma et al., 2006; Koshida et al., 2014; Minezaki et al., 2019).

Dust grains emitting in the near-IR have a temperature close to the dust sublimation temperature. Therefore, the reverberation lags found from V-band (optical) versus K-band (near-IR) are thought to measure the distance to the inner edge of the torus, as any grains interior to this distance would be sublimated. BLR reverberation radii have been found to be smaller than torus reverberation radii (Suganuma et al., 2006; Koshida et al., 2014), implying that the inner radius of the torus is the outer boundary of the BLR.

When comparing near-IR reverberation mapping results to those measured from near-IR interferometry, the radius measured from interferometry tends to be equal to (or slightly larger than) those measured from reverberation mapping (Kishimoto et al., 2011; Koshida et al., 2014; Weigelt et al., 2012). One possible reason for this discrepancy could be that the radius measured from interferometry is a measurement of the average radius of the K band dust, while K-band reverberation mapping probes the dust at the inner edge of the torus (Kishimoto et al., 2009; Koshida et al., 2014).

A more in-depth description of the physics of reverberation mapping follows here: One can consider the response of the torus dust (or BLR) to a continuum pulse (a δ function). This pulse is confined to the shape of a spherical shell as viewed from the central source, and travels outward. The pulse travels at the speed of light, and will reach the clouds (BLR or dust) after a time $\tau = r/c$, assuming that the clouds are located on the surface of a spherical shell of radius r. The clouds absorb the continuum pulse, and produce emission lines or IR emission, depending on whether they

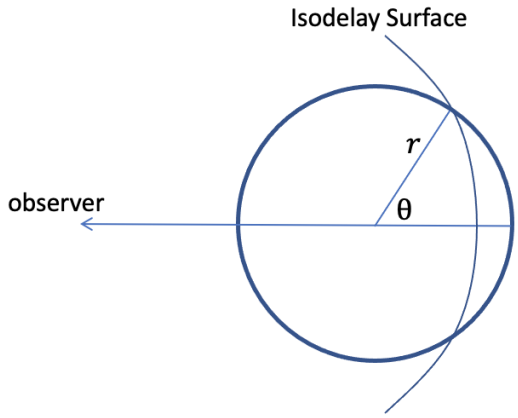

Figure 1.2: The intersection of an isodelay surface and the torus, in the shape of a spherical shell.

are BLR or dust clouds.

If an observer could be located directly in the center of the AGN, then the reverberation response from each cloud would arrive at the same time. However, since the observer is located far from the center of the AGN, then depending on where the cloud is located within the torus, the response of each cloud will take a different amount of time to reach the observer. In the case of a spherical shell, Fig 1.2 shows the annulus within the torus responding to a specific delay time. The surfaces of constant time delay are referred to as "isodelay surfaces." For any time delay τ, the clouds that respond are those located where the torus intersects with the isodelay surface. For clouds at position (r, θ), an observer sees the delay as

$$\tau = (1 + \cos\theta)\frac{r}{c}, \tag{1.7}$$

where θ is the angle between the observer's line of sight and a cloud in the torus. The dust response is the product of the responsivity per unit shell area (ϵ, the number of extra photons produced, given a specific increase in continuum) and the area of the annulus. This can be seen to be

$$\Psi(\theta)d\theta = 2\pi r^2 \epsilon \sin\theta d\theta. \tag{1.8}$$

$\Psi(\theta)$ is called the "transfer function," which describes the response of the torus dust to a delta function pulse of illuminating radiation (Blandford & McKee, 1982). The transfer function contains information on the geometry of the emission region. It can be represented as a function of the time delay:

$$\Psi(\tau)d\tau = 2\pi r c \epsilon d\tau \tag{1.9}$$

The transfer function can be used in the "transfer equation" in order to solve for the response light curve. The transfer equation is the convolution of the driving (optical/UV) light curve with the transfer function, seen as

$$F_r(t) = \int_{-\infty}^{\infty} \Psi(\tau) F_c(t-\tau) d\tau, \tag{1.10}$$

where $F_r(t)$ is the IR response light curve, $F_c(t-\tau)$ is the continuum light curve to which the IR responds to after a delay τ, and $\Psi(\tau)$ is the transfer function. The transfer function can be obtained using Fourier methods (Maoz et al., 1991), however due to the difficulty in obtaining the transfer function accurately and interpreting the results, it is rarely done in practice. For data that is poorly-sampled (or well-sampled), cross correlation analysis can be used to determine the size of the BLR or torus by determining the lag between the continuum light curve and the response light curve.

1.4 Dust Reverberation Models

Several attempts have been made to model the IR response of the torus dust emission (Barvainis, 1992; Kawaguchi & Mori, 2010, 2011). The most comprehensive and general model is TORMAC (Torus Reverberation Mapping Code), developed by Almeyda et al. (2017); Almeyda (2017); Almeyda et al. (2020), which was created in order to explore how various torus parameters affect the torus IR response. TORMAC uses forward modeling by assuming a form for the transfer function (using radiative transfer models) and using an observed optical light curve as input. The model response light curve is given by the convolution of the transfer function with the driving (optical/UV) light curve, as shown in Equation 1.10.

Using an observed optical light curve as input, the code will then produce model IR responses which vary depending on the structural characteristics (e.g. inclination angle, cloud distribution, radial extent) of the torus. The model IR responses can be compared to the observed IR light curves, allowing us to place constraints on other torus properties for our sample of AGN. This is discussed more in Chapter 6.

1.5 Dissertation Synopsis

This project is an optical-mid IR reverberation mapping study of the circum-nuclear torus in a sample of AGN. Our group was awarded time to monitor 12 Type 1 AGN over a period of 2 years using the Spitzer Space Telescope, at the mid-IR wavelengths of 3.6 and 4.5 μm. Mid-IR light curves for this sample were presented by Vazquez (2015). My analysis focuses on 11 of the 12 AGN in our sample (one AGN exhibited no flux variability) spanning a range of redshifts ($0.027 \leq z \leq 0.214$) and luminosities (3.6×10^{43}erg/s $\leq L_{AGN} \leq 1.8 \times 10^{46}$erg/s). Our goal is to constrain the size of the torus in these AGN using the technique of dust reverberation mapping. Most previous dust reverberation mapping studies have focused on the near-IR (K-band) emitting dust (Suganuma et al., 2006; Koshida et al., 2014; Minezaki et al., 2019), however there have been some studies of mid-IR dust emission more recently using WISE data (Lyu et al., 2019; Yang et al., 2020). While

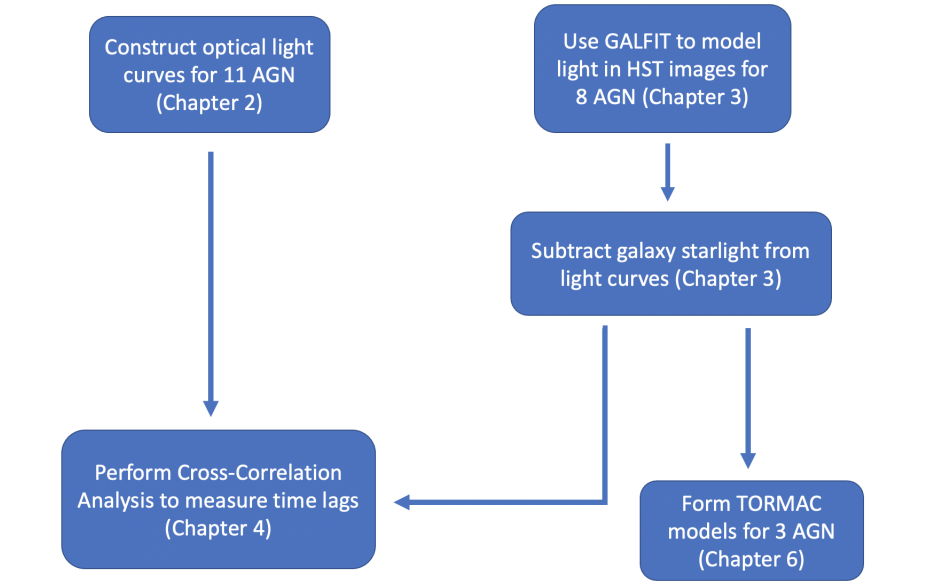

Figure 1.3: A diagram showing the steps of the project. Chapter 5 presents the full analysis of NGC 6418, which is not listed in this diagram.

the studies of Lyu et al. (2019) and Yang et al. (2020) use light curves with a longer time span than in our sample, the WISE IR data is much more sparsely sampled than ours. Our Spitzer IR light curves span a shorter time span, but are very well-sampled.

The main elements of this project include

- Constructing optical light curves
- Performing cross-correlation analysis to measure the time lags
- Reanalyzing data for the changing-look AGN NGC 6418
- Using `GALFIT` to model the light in the *Hubble Space Telescope* (HST) images for our sample of AGN
- Using TORMAC to model selected AGN

Figure 1.3 presents a diagram of the steps of this project. In Chapter 2, the optical light curves

are constructed from new and archival photometry. We have optical HST images for eight of the AGN, and Chapter 3 focuses on using these images to create models with the image decomposition program `GALFIT` (Peng et al., 2002, 2010). `GALFIT` is used to model the host galaxy light that falls within the photometric apertures used to form the optical light curves. Since the optical light curves are a combination of light from the host galaxy and the AGN, the constant contribution of the host galaxy starlight can be subtracted from the optical light curves, leaving the intrinsic AGN variations. The starlight-subtracted light curves are also presented in this chapter.

One of the main goals of this project is to measure the optical-IR lags in order to determine the distance to the 3.6 and 4.5 μm emitting regions. In Chapter 4, cross-correlation analysis is performed. However, it is only able to be used on AGN that show clear optical variations with an IR response, which only applies to five of the eleven objects. We perform cross-correlation analysis both before and after subtracting the starlight contribution.

Chapter 5 focuses on the analysis of one object, NGC 6418, which is a changing-look AGN. Cross-correlation results for the first section of the light curves of NGC 6418 were completed by B. Vazquez and have been published in Vazquez et al. (2015), although I have reanalyzed the data in more detail.

Chapter 6 presents TORMAC models. For three selected AGN (MRK 507, KAZ 163, and MRK 876), the starlight-subtracted light curves (presented in Chapter 3) were used as input into TORMAC. By comparing the TORMAC model IR responses to our observed IR light curves, we were able to constrain other torus parameters for three AGN in our sample.

CHAPTER 2

SPITZER MONITORING CAMPAIGN: INFRARED AND OPTICAL LIGHT CURVES:

The AGN studied in this dissertation were selected based on their proximity ($z < 0.4$), their visual brightness ($m_B < 17$), and their location in or near Spitzer's continuous viewing zones. They are also all Seyfert 1s, which allows the optical continuum of the AGN to be measured, without being obstructed from view by the obscuring torus. Each AGN is listed in Table 2.1, along with several other properties.

Table 2.1: Basic Properties

Name	RA	DEC	redshift	$L_{3.6\mu m}[10^{42}\mathrm{erg/s}]$
2MASSJ19091092+6652212	19h09m10.85s	+66d52m21.20s	0.213617	147
3C390.3	18h42m08.98s	+79d46m17.12s8	0.058208	51.0
IRAS17552+6209	17h55m40.42s	+62d09m40.60s	0.089002	9.68
KAZ102	18h03m28.80s	+67d38m10.00s	0.147160	65.8
KAZ163	17h46m59.84s	+68d36m36.80s	0.065787	19.4
MRK507	17h48m38.37s	+68d42m15.88s	0.058260	9.74
MRK876	16h13m57.18s	+65d43m09.58s	0.139283	169
MRK885	16h29m48.25s	+67d22m41.78s	0.026778	1.50
PGC61965	18h30m23.10s	+73d13m10.00s	0.131948	727
UGC10697	17h02m44.29s	+72d53m29.87s	0.055189	7.18

2.1 Infrared Light Curves

Mid-IR data were obtained with the Infrared Array Camera (IRAC) in channel 1 (3.6 μm) and channel 2 (4.5 μm) during Spitzer's "warm mission". The observations occurred during Spitzer cycles 8 and 9, covering the time frame between August 2011 to January 2013 (MJD 55774-56297) for cycle 8 and February 2013 to January 2014 (MJD 56348-56679) for cycle 9. The observational cadence during cycle 8 was once every 3 days, while cycle 9 had a longer observational cadence of once every 30 days.

The mid-IR light curves for this sample were constructed by B. Vazquez for the purpose of constraining the size of the inner regions of the torus, and were presented in Vazquez (2015).

2.2 Optical Light Curves

I have constructed and analyzed the optical light curves for the sample of AGN. Optical observations were obtained for this set of AGN over the same time period as the Spitzer Campaign using the 2 meter Liverpool Telescope (LT; Steele et al. 2004) at the Roque de los Muchachos Observatory, located in the Canary Islands. The instruments used for these observations were IO:O (a wide field optical camera with a CCD detector spanning 4096 x 4112 pixels) and RATCAM (an optical CCD camera spanning 2048 x 2048 pixels). IO:O has a pixel scale of 0.3 arcsec/pixel and exposure time of 120 seconds, while RATCAM has a pixel scale of approximately 0.135 arcsec/pixel with exposure times ranging from 60-180 seconds. IO:O exposures were obtained in Bessel B and SDSS g' filters, while RATCAM exposures were obtained in the Bessel B and V filters. SDSS i' band and r' band measurements were also obtained with RATCAM for two of the AGN.

The optical data from LT has been supplemented with archival data from the Catalina Sky Survey (CSS; Drake et al. 2009) with a clear filter and Palomar Transient Factory (PTF; Law et al. 2009) with a Mould-r filter. These observations do not cover the entire time frame of the Spitzer Campaign, however some of the observations fall within the campaign, as well as slightly before and after. The CSS images had a 30 second exposure time and pixel size of 2.5″, while the PTF

images have a 60 second exposure time and pixel size of $1''$.

Standard image reduction includes bias subtraction and flat fielding of the images. For LT, an automatic pipeline performed the image processing (Steele et al., 2004). For PTF, standard image reduction was performed with the automated data reduction pipeline at the Infrared Processing and Analysis Center (IPAC; Law et al. 2009). Similarly, the CSS data reduction was done with the Catalina Real-Time Transient Survey (CRTS) pipeline (Drake et al., 2009).

The image analysis software AstroImageJ (AIJ; Collins et al. 2017) was used to perform aperture photometry. AIJ is an image analysis software based on ImageJ, but includes several tools specific to astronomy. For each AGN, I used AIJ to analyze the sets of images from each filter of each telescope. For each image within the image set, the AGN and 5-6 reference stars are identified. As an example, one LT B band (RATCAM) image is shown in Figure 2.1 for the AGN 3C390.3, with 5 reference stars identified. The size of the source aperture is chosen, which is used to measure the flux from each selected object in each image. Too large of a source aperture size will allow too much light from the sky background, which adds background noise. Too small of an aperture will not capture all of the flux from the reference star or AGN. I adopted an aperture radius that is slightly larger than the typical FWHM for the images, usually 1.5-2 times the FWHM. The typical source aperture radii chosen for each AGN is 2.8-3.5$''$ for LT, 5.1$''$ for PTF, and 7.5$''$ for CSS.

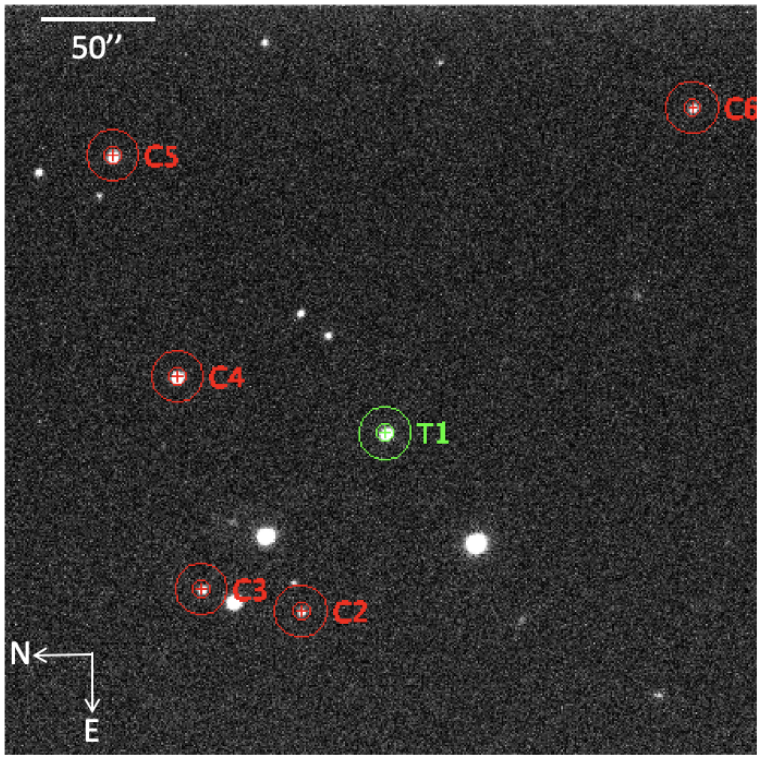

Figure 2.1: 3C390.3 field of view in an LT B band image. The AGN is labeled as 'T1' and each comparison star is labeled C2-C6. The inner aperture surrounding each object defines the source aperture. The sky background annulus is also shown around each object, with the radius defining the source aperture coinciding with the inner radius defining the background region.

An annulus defining the sky background region is also specified. AIJ performs an iterative 2σ cleaning of the specified background region, in order to exclude stars that may fall into the background region. It was necessary to ensure that light from the host galaxy did not fall into the sky background region, therefore the region defining the sky background was sometimes offset from the edge defining the source region. The source aperture and sky annulus are also shown in Figure 2.1. Note that for this image, the radius defining the source aperture coincides with the inner radius defining the background region.

The important measurements from each image include the "source−sky" value and the source error for each object. The source−sky is the sum of the pixel values within the source aperture, with the sky background subtracted. The sky background is the average value of the pixels in the

sky background annulus.

The photometric errors for each object in the images includes error from read-out noise, dark current, and source and sky poisson noise, calculated using the following equation from Collins et al. (2017)

$$N = \frac{\sqrt{GF_* + n_{\rm pix}(1 + \frac{n_{\rm pix}}{n_{\rm b}})(GF_S + F_D + F_R^2 + G^2\sigma_F^2)}}{G}, \tag{2.1}$$

where N is the noise in ADU, G is the gain of the CCD in electrons/ADU, F_* is the net integrated counts within the aperture in ADU, $n_{\rm pix}$ is the number of pixels in the source aperture, n_b is the number of pixels in the sky background region, F_S is the number of sky background counts/pixel in ADU, F_D is the total dark counts per pixel in electrons, F_R is read noise in electrons/pixel/read, and σ_F is the standard deviation of the fractional count lost to digitization in one pixel, which is 0.289 ADU. The photometric error is used as a weight factor in the ensemble photometry code.

A code developed by Dr. Michael Richmond[1] using inhomogeneous ensemble photometry (Honeycutt, 1992) was then used to form the light curves. The technique of inhomogeneous ensemble photometry uses multiple stars in the field of view as reference stars, and therefore more accurate light curves can be created than in standard differential photometry. This technique can also be used even when the number of comparison stars varies from image to image. In strict ensemble photometry, all comparison stars must be used. If one falls out of the field of view, the entire image must be removed, which leads to fewer data points. Inhomogeneous ensemble photometry circumvents this problem, allowing the number of comparison stars to vary from image to image.

The technique of ensemble photometry accounts for changes in sky transparency or seeing, which would cause stars of constant flux to appear to vary over time. This program computes these changes, and corrects the instrumental magnitudes of the comparison stars and the AGN. The AGN light curve will then show the variations of the galaxy nucleus, without being influenced

[1] http://spiff.rit.edu/ensemble/

by external factors such as the sky transparency.

For each chosen object (star or AGN) in every image, the software needs input data that contains each object's X and Y positions, its magnitude, and its estimated uncertainty. The program assumes that each star has a constant intrinsic magnitude, however the measured magnitude $\big(m(i,j)\big)$ will differ from the star's true magnitude $\big(M(i)\big)$ by some image offset value $\big(e(j)\big)$.

The error in each measurement of star i in an image j is then

$$error = m(i,j) - \big(M(i) - e(j)\big). \tag{2.2}$$

The software seeks to minimize this error, and therefore needs to calculate the values of $e(j)$ and $M(i)$. To do this, the program uses a weighted least squares method:

$$\beta = \sum_{j=1}^{M}\sum_{i=1}^{N}\Big(m(i,j) - \big(M(i) - e(j)\big)\Big)^2 w(i,j), \tag{2.3}$$

for N stars and M images, where $w(i,j)$ is the weight of $m(i,j)$. The weight depends on $1/\sigma^2$, where σ is the uncertainty provided by AIJ, shown in Equation 2.1. This weight factor causes the brighter stars (stars that have lower uncertainty) to have more weight.

Once the least squares solution is found, the light curve of each object can be plotted as the equation

$$\text{Corrected Magnitude} = m(i,j) - e(i,j). \tag{2.4}$$

Since the magnitudes entered into the software are instrumental magnitudes, there is not a well-defined zero point. Here, the zero point magnitude is set to be the magnitude of the brightest reference star.

Figure 2.2 shows the light curves produced using ensemble photometry for the AGN 3c390.3

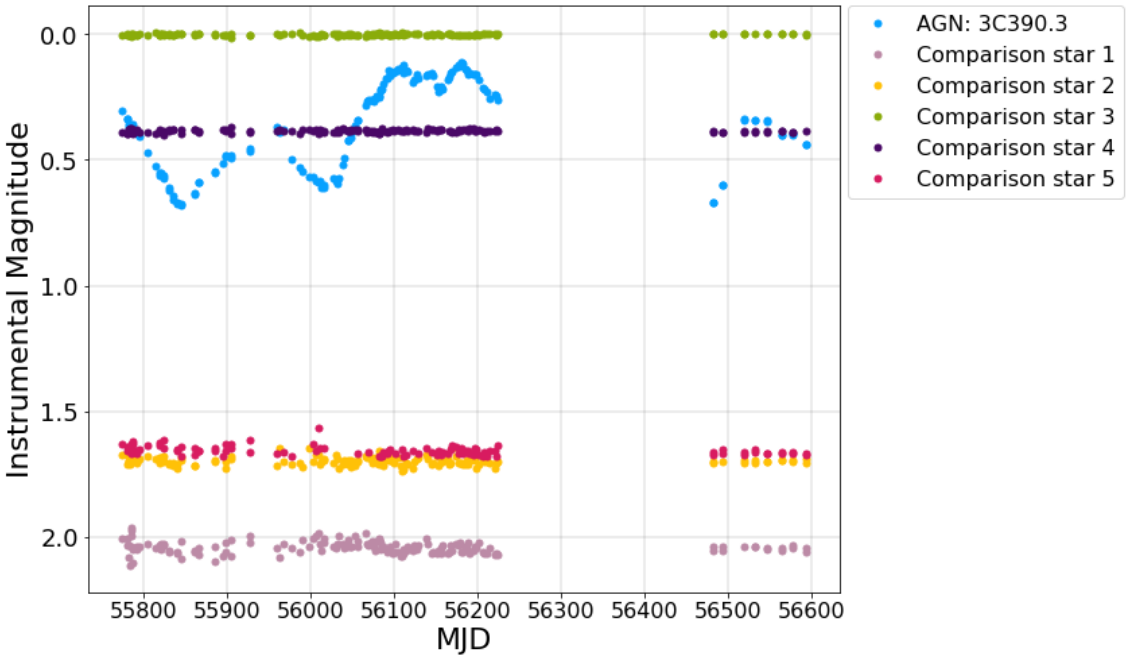

Figure 2.2: 3C390.3 LT B band light curve, along with light curves of the five comparison stars.

and for each comparison star with the LT B band data. The AGN shows significant variability compared to each comparison star. The brightest star is set at an instrumental magnitude of zero. Fainter stars show more scatter around their mean magnitude.

The magnitude values from stars in the field of view were used to convert from instrumental magnitudes. Within the field of view of each AGN, there are a few stars with catalogue magnitude values within the AAVSO Photometric All-Sky Survey (APASS) or the Panoramic Survey Telescope and Rapid Response System (Pan-STARRS) databases. As an example, comparison star 3 has a catalogue B band magnitude of 14.953 with an instrumental magnitude of 0. Taking the difference between the instrumental and apparent magnitudes will tell us the amount to add to each data point of the light curve. This value can be double-checked by performing the same calculations with another comparison star as reference. The AGN light curve is then shifted by this value to convert from instrumental to apparent magnitude. As the comparison stars did not have catalogue magnitude values available with a clear filter, the catalogue V band values were used as reference.

The standard deviation, or the object's scatter from its "true" magnitude is

$$\sigma = \left(\frac{M \sum_{j=1}^{M} [m(i,j) - e(i,j) - M(i)]^2 w(i,j)}{(M-1) \sum_{j=1}^{M} w(i,j)} \right)^{1/2} . \tag{2.5}$$

Since each comparison star's brightness is constant (assuming it is not a variable star), the error for each comparison star is considered to be the scatter around its mean magnitude. Since the AGN is variable, the AGN's uncertainty cannot be calculated in the same way. The AGN's uncertainty was taken to be the same percent uncertainty as whichever star was closest in magnitude to the AGN. In Figure 2.2, this is comparison star 4. There was typically one star in the field of view with the same magnitude value as the AGN, although in some cases there is $\sim$1 magnitude of difference.

2.3 IR and Optical Light Curves for Individual AGN

Table 2.2 summarizes the type of variability of the light curves, and also includes estimates of the bolometric luminosity, dust sublimation radius, and corresponding light crossing time for each AGN. The bolometric luminosity was estimated using the x-ray (2-10 keV) and IR (WISE W3, 12 μm) photometric flux measurements from the NASA/IPAC Extragalactic Database (NED), as well as the luminosity distances from NED. This was converted into a bolometric luminosity using the bolometric correction equations from Runnoe et al. (2012a,b,c). Note that the IR measurements could include a contribution to the IR from the host galaxy.

When using the x-ray data, the bolometric luminosity differs for radio-loud and radio-quiet AGN. Only one AGN in our sample is radio-loud, 3C390.3, for which the following equation is used

$$\log(L_{bol,RL}) = 23.044 + 0.519 \log(L_{x-ray}), \tag{2.6}$$

Table 2.2: This table shows the estimated bolometric luminosity for each AGN, using x-ray or IR bolometric corrections, along with the calculated sublimation radius (R_d) and the corresponding lag (τ). Each AGN is listed in order of increasing sublimation radius, calculated with the bolometric luminosity from the IR bolometric correction. The variability behavior of each AGN, as discussed in the following sections, is also listed.

AGN	X-ray Bolometric Correction			IR Bolometric Correction			Behavior
	L_{AGN} [$\times 10^{45}$erg/s]	R_d [pc]	τ [days]	L_{AGN} [$\times 10^{45}$erg/s]	R_d [pc]	τ [days]	
NGC 6418	-	-	.-	0.0905	0.12	143.4	Strong optical variability with strong IR response
UGC 10697	-	-	-	0.419	0.26	308.6	Comparable optical and IR variability
IRAS 17552+6209	-	-	-	1.21	0.44	524.0	Comparable optical and IR variability
MRK 507	2.63	0.65	772.3	1.26	0.45	534.6	Comparable optical and IR variability
3C390.3	12.5	1.42	1687.7	2.50	0.63	754.1	Strong optical variability with no IR response/slow secular trend
KAZ 102	7.36	1.1	1293.1	3.23	0.72	856.8	Strong optical variability with no IR response/slow secular trend
MRK 885	3.32	0.73	868.9	-	-	-	Little optical variability with strong IR response
KAZ 163	3.78	0.78	926.8	-	-	-	Comparable optical and IR variability
2MASS J19091092+6652212	-	-	-	4.85	0.88	1049.7	Strong optical variability with no IR response/slow secular trend
MRK 876	7.36	1.1	1293.0	7.23	1.1	1281.2	Strong optical variability with no IR response/slow secular trend
PGC 61965	-	-	-	16.4	1.6	1928.6	Strong optical variability with no IR response/slow secular trend

while for radio-quiet AGN, the following equation is used

$$\log(L_{bol,RQ}) = 33.058 + 0.289 \log(L_{x-ray}). \tag{2.7}$$

Using the 12μm IR data, the bolometric correction is

$$\log(L_{bol}) = 8.915 + 0.822 \log(\lambda L_{\lambda}). \tag{2.8}$$

The sublimation radius was calculated from the bolometric luminosity using Equation 1.1. The corresponding light crossing time was evaluated using $\tau = R_d/c$, where τ is the light crossing time, R_d is the estimated sublimation radius, and c is the speed of light. The AGN are listed in the table from smallest to largest sublimation radii, using the bolometric luminosity from the IR bolometric correction, except for MRK 885 and KAZ 163 which only have luminosities from the x-ray bolometric correction.

The optical and IR light curves for each object are presented here. The average magnitude values of the optical light curves produced from the photometry are presented in Table 2.3. The optical light curves are combined from three different telescopes in several different wavebands, and formed using different photometric aperture sizes. In order to combine the optical light curves, the light curve from each waveband was normalized to its own mean value. To get the optical light curves to "match" as well as possible, some of the light curves have been multiplied by a factor, which will shift them to match the LT B band light curve.

This section presents the light curves for 10 of the AGN in our sample, while NGC 6418 is discussed separately in Chapter 5.

2MASS J19091092+6652212 (also known as 1RXS J190910.3+665222)

2MASSJ19091092+6652212 is classified as a NL Sy1 (Narrow Line Seyfert 1) (Véron-Cetty &

Table 2.3: Average Apparent Magnitude Values

Name	LT (B band)	PTF	CSS
2MASSJ19091092+6652212	17.37		16.83
3C390.3	15.29		16.17
IRAS17552+6209	17.91		17.14
KAZ102	16.85	16.81	15.15
KAZ163	16.63	15.48	15.15
MRK507	16.39	14.97	14.98
MRK876	15.04	14.95	14.66
MRK885	16.75		
PGC61965	15.03		
UGC10697	17.42	15.33	

Véron, 2006), and has been little studied. Figure 2.3 shows the LT B band field of view. The light curves for this object are shown in Figure 2.4, and show significant optical variability, with little IR response. The CSS light curve allows us to see the variations before the Spitzer campaign, however the coverage is very sparse. Within the first 884 days of the CSS light curve, the flux rises by ∼42% and reaches a maximum at MJD 55160. Then the CSS light curve seems to follow the same trend as the LT light curves in the regions where they overlap.

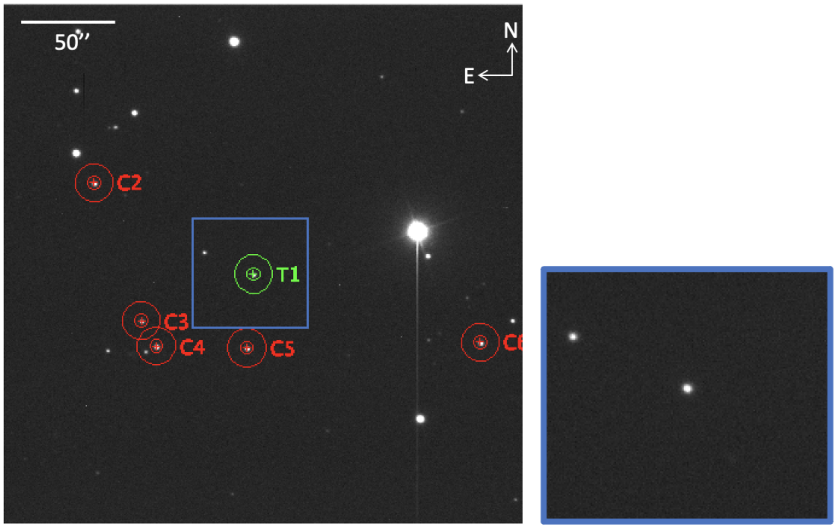

Figure 2.3: Field of view of 2MASSJ19091092+6652212 in an LT B band image, with objects labeled as described in Figure 2.1. The smaller figure on the right shows a closer view of the AGN, within the region enclosed in the blue box.

The first main feature of the B and V band light curves is a sharp decline of ∼ 20% over 55 days

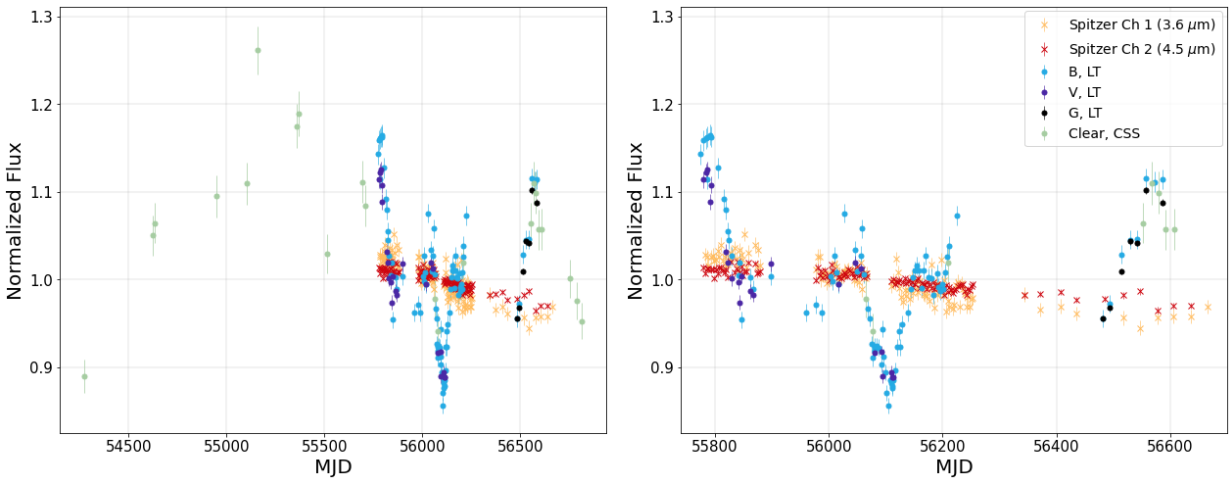

Figure 2.4: 2MASS J19091092+6652212 light curves. The left plot includes the entire time span of the light curves, while the right plot only includes the time period covered by the Spitzer campaign.

(from MJD 55792 to 55847). The next feature is a sharp decline and subsequent rise over ∼90 days (from MJD 56060 to 56150), both on the order of ∼20%. The final feature of the B and g bands begin at MJD 56480 where there is another sharp rise in flux of 15% over 90 days. In contrast, the IR does not track the optical variations, but continuously decreases in flux by less than 10%.

Clearly there are significant optical variations in this AGN, but the IR emission only shows a very slight downward trend. The lack of IR response can be explained by the fairly large bolometric luminosity for this AGN (4.85×10^{45} erg/s) using Equation 1.1. We can infer from this large luminosity that the sublimation radius must be large, and therefore the time lag is large. Using estimates of the dust sublimation radius from Table 2.2, we can estimate the lag as $\tau = r/c$, where r is the sublimation radius, and c is the speed of light. The lag is estimated to be 1050 days, which is ~ 1.2 times longer than the Spitzer campaign. Therefore, the Spitzer monitoring did not span a long enough time baseline to observe the lag. Also it is possible that the IR is responding to the large amplitude increase and decrease in flux seen in the CSS light curves before the Spitzer campaign began.

3C390.3 3C390.3 is classified as a BLRG (Broad Line radio galaxy) (Healey et al., 2007), and is well studied. Figure 2.5 shows the LT B band field of view. The light curves for this object are shown in Figure 2.6, and show significant optical variability, with little IR response. The B band light curve shows the largest amplitude variations. The B band variations begin with a sharp decline and rise in flux of $\sim$ 25% over 170 days. After another decline of $\sim$ 20% over 55 days, a large increase of $\sim$ 50% occurs over 100 days (from MJD 56010 to 56110). Smaller decreases and rises of flux on the order of $\sim$ 10% occur until the end of cycle 8. During the gap between cycle 8 and 9, the optical light curve decreases in flux. When the cycle 9 observations begin at $\sim$MJD 56480, the flux quickly rises by $\sim$ 35% over 40 days, before falling again until the end of the observations. The LT V, R, and I bands all seem to match the B band variations, although the amplitude of variability is smaller. The IR does not respond to these variations, and instead varies by less than 10% throughout the campaign.

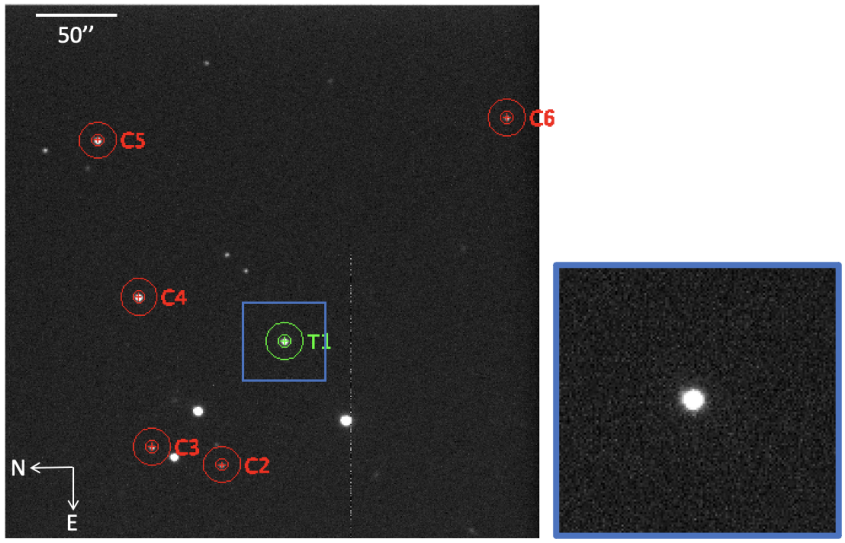

Figure 2.5: Field of view of 3C390.3 in an LT B band image, with objects labeled as described in Figure 2.1. The smaller figure on the right shows a closer view of the AGN, within the region enclosed in the blue box.

The lag corresponding to the sublimation radius estimated using the IR bolometric correction in Table 2.2 is 754 days, which is comparable in length to the Spitzer campaign. However, using

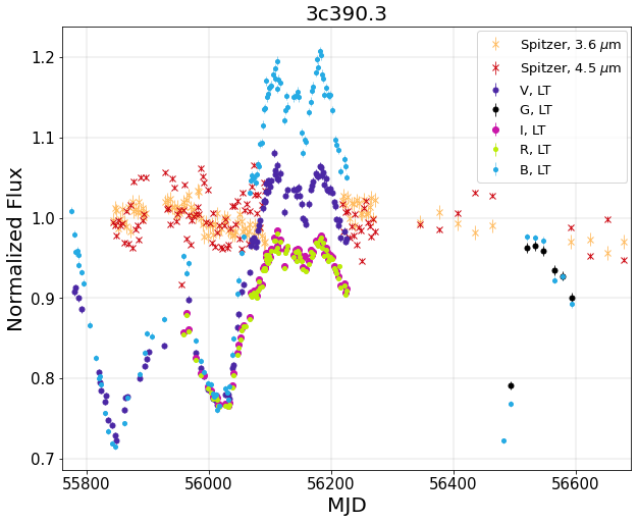

Figure 2.6: 3C390.3 light curves. There are no PTF or CSS observations for this AGN.

the x-ray bolometric correction the lag is calculated to be 1688 days, $\sim$ 2 times longer than the Spitzer campaign.

IRAS 17552+6209 IRAS17552+6209 is a Seyfert 1.9 AGN (Véron-Cetty & Véron, 2006) and has not been well-studied. Figure 2.7 shows the LT B band field of view and Figure 2.8 shows the light curves with significant variations in the IR and optical. The main feature of the IR light curves is a steady decline in brightness of about 12% which occurs over about 400 days, until MJD 56200. The IR flux begins to rise again, reaching a smaller maximum between cycles 8 and 9. The IR reaches its lowest point during cycle 9, with a flux decrease of less than 6%.

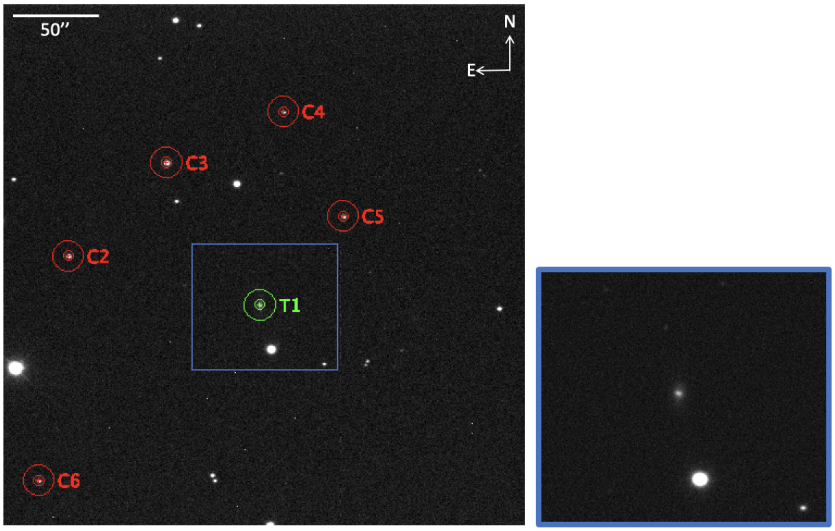

Figure 2.7: Field of view of IRAS 17552 in an LT B band image, with objects labeled as described in Figure 2.1. The smaller figure on the right shows a closer view of the AGN, within the region enclosed in the blue box.

The LT light curves show high frequency fluctuations with amplitudes ranging from 5-10% over timescales of ~ 50 days, although there is significant scatter with large error bars. The CSS light curve covers the time period before the Spitzer campaign, with an amplitude of variability of $\leq 7\%$, with timescales ranging from 60 to 300 days.

The IR and optical light curves are not closely correlated. It is expected that the optical light curve (which drives the IR variations) should decline in flux before the Spitzer campaign, since the IR light curve shows a decline in flux. Although the CSS light curve covers the time before the Spitzer campaign, it does not show a large decline in flux. During the Spitzer campaign, the LT light curves show a few lower amplitude variations. The IR also shows a small rise and then small decrease in flux, which is possibly in response to the small optical variations. The lag corresponding to the sublimation radius estimated from the IR bolometric correction in Table 2.2 is 524 days or ~ 0.58 times as long as the Spitzer campaign, which is comparable to the IR variation timescales.

KAZ 102 KAZ 102 is a Sy 1.2 AGN (Véron-Cetty & Véron, 2006) which is fairly well studied, and quite luminous. Figure 2.9 shows the LT B band field of view. The LT B band light curve is

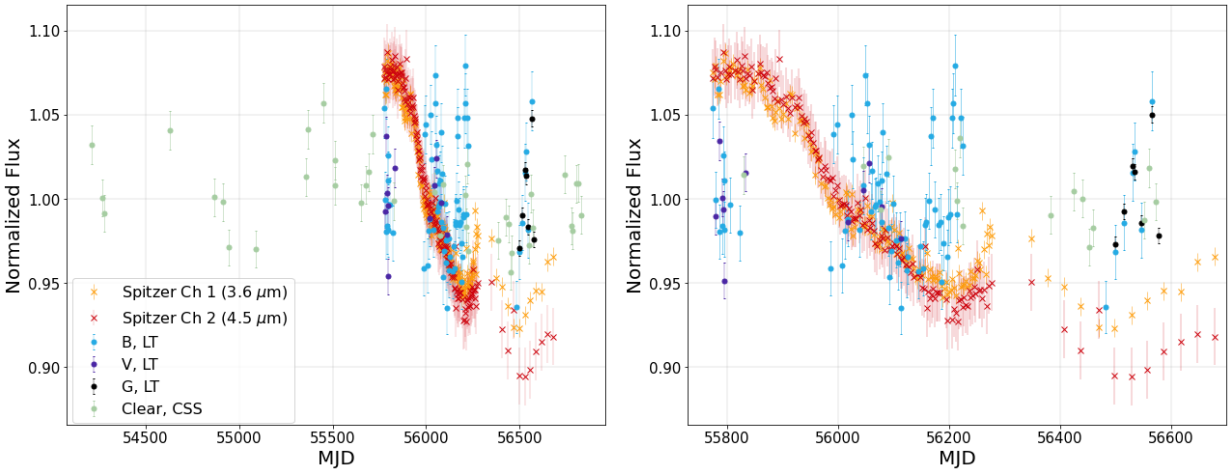

Figure 2.8: IRAS 17552+6209 light curves. The left plot includes the entire time span of the light curves, while the right plot only includes the time period covered by the Spitzer campaign.

shown in Figure 2.10 and exhibits clear variations, with three main peaks with similar amplitudes. The most prominent event is a feature lasting 290 days in which the flux increases by 40%, then decreases by 20%. The LT V and G band light curves have very similar variations to the B band light curve, in the regions where they overlap. The CSS light curve shows an increase in flux over $\sim$ 500 days of greater than a factor of 2, occurring prior to the Spitzer campaign. The IR seems to be responding to the variation seen in the CSS light curve, with a steady increase of $\sim$ 12% throughout cycle 8.

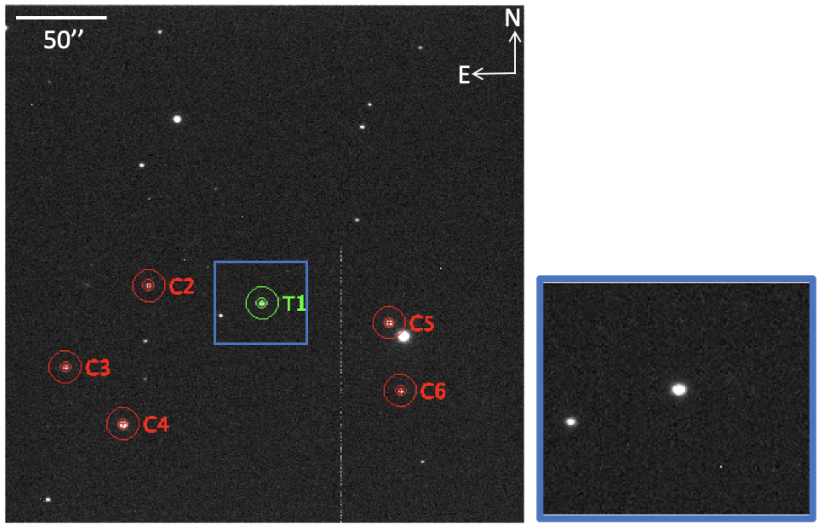

Figure 2.9: Field of view of KAZ 102 in an LT B band image, with objects labeled as described in Figure 2.1. The smaller figure on the right shows a closer view of the AGN, within the region enclosed in the blue box.

The lag corresponding to the sublimation radius for KAZ 102 estimated from the IR bolometric correction in Table 2.2 is 857 days, which is approximately the length of the Spitzer campaign.

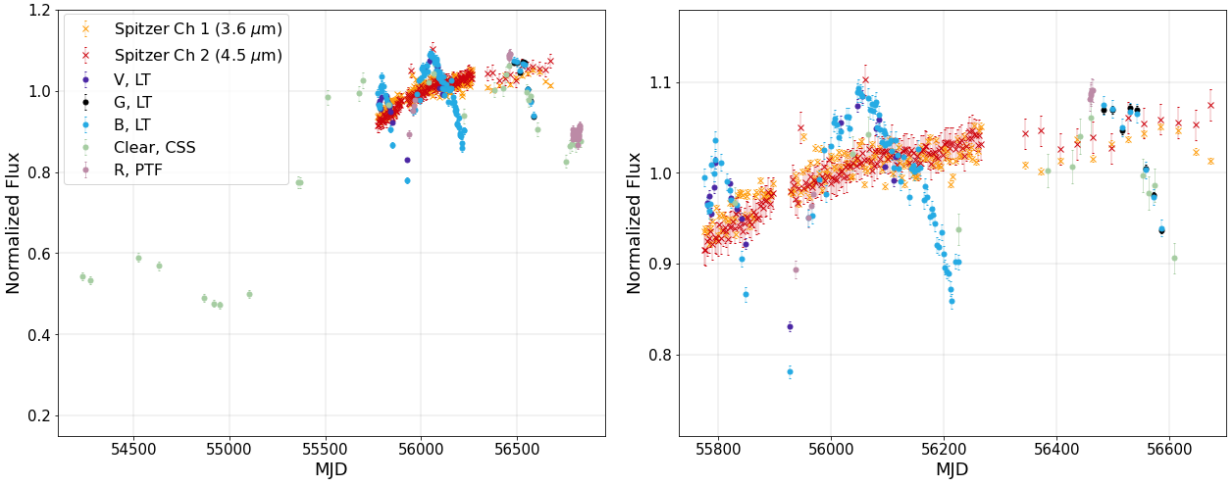

Figure 2.10: KAZ 102 light curves: The left plot includes the entire time span of the light curves, while the right plot only includes the time period covered by the Spitzer campaign.

KAZ 163 KAZ 163 is a NL Sy1 (Boller et al., 1996), which has not been previously well studied. Figure 2.11 shows the LT B band field of view. The main feature in the IR light curves (see Figure 2.12) is a large peak at approximately MJD 55800, followed by a decline of 20% for channel 1, around 250 days later. The flux rises by less around 5% until the end of cycle 8. The 4.5μm light curve has less sharp features, declining by around 10%, before reaching a plateau. Both IR light curves continue to decrease by $\sim 3-4\%$ over the last 300 days.

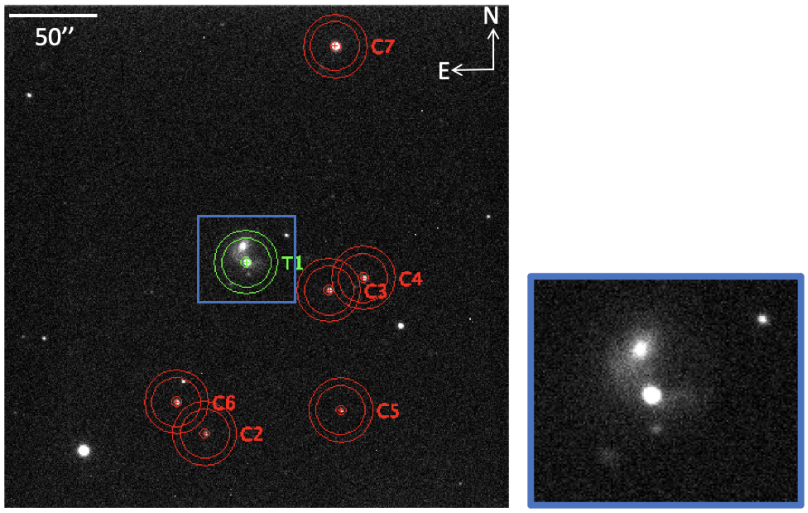

Figure 2.11: Field of view of KAZ 163 in an LT B band image, with objects labeled as described in Figure 2.1. The smaller figure on the right shows a closer view of the AGN, within the region enclosed in the blue box.

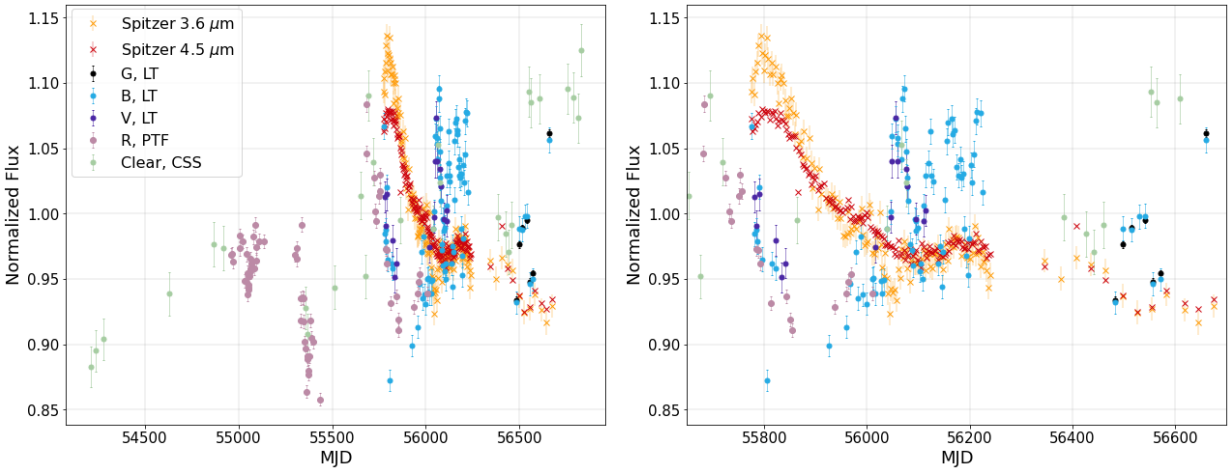

Figure 2.12: KAZ 163 light curves. The left plot includes the entire time span of the light curves, while the right plot only includes the time period covered by the Spitzer campaign.

It is expected that the optical will also have a large peak before MJD 56200, as the optical should drive the IR response. There is a rise in flux of 26% over 250 days (from MJD 55430 to 55680) in the R band PTF light curve before the Spitzer campaign, although there is a gap in the light curve within this region. The flux then falls by 16% over 170 days. The LT B and V bands are consistent with the decline seen in the PTF R band around the start of the Spitzer Campaign. The B band light curve shows rapid variations of $\sim 12\%$ on timescales of $\sim 20-30$ days from MJD 56035 to 56230, which the IR does not respond to. The V and G band light curves seem to match these variations, in the regions that overlap.

While the CSS observations are sparsely sampled, they also show significant variability. Before the Spitzer campaign, there is a rise of $\sim 20\%$ over 330 days. While there are only a few measurements during most of the time span of the Spitzer campaign, the CSS observations show a rise in flux at the end of the campaign ($\sim 13\%$ over 110 days), similar to that of the LT B and G bands.

The lag corresponding to the sublimation radius estimated from the x-ray bolometric correction in Table 2.2 is 927 days, which is approximately the length of the Spitzer campaign.

MRK 507 MRK 507 is a well-studied NL Sy 1 AGN (Khachikian & Weedman, 1974). Figure 2.13 shows the LT B band field of view, and Figure 2.14 shows the light curves. The CSS light curve before the Spitzer campaign is relatively constant, while the R band PTF light curve exhibits a clear rise in flux of $\sim 5\%$ over 160 days, from MJD 55460 to 55300. The main feature of the optical light curves is a rise of $\sim 23\%$ over 250 days seen in the B band between MJD 55960 and 56210, which appears to lead the IR. The IR shows strong variations, beginning with a decline in flux of $\sim 7\%$ over about 220 days. Around MJD 56000, the flux increases by $\sim 20\%$ until MJD 56260. This is the main feature in the IR, with smaller flux variations occurring in cycle 9.

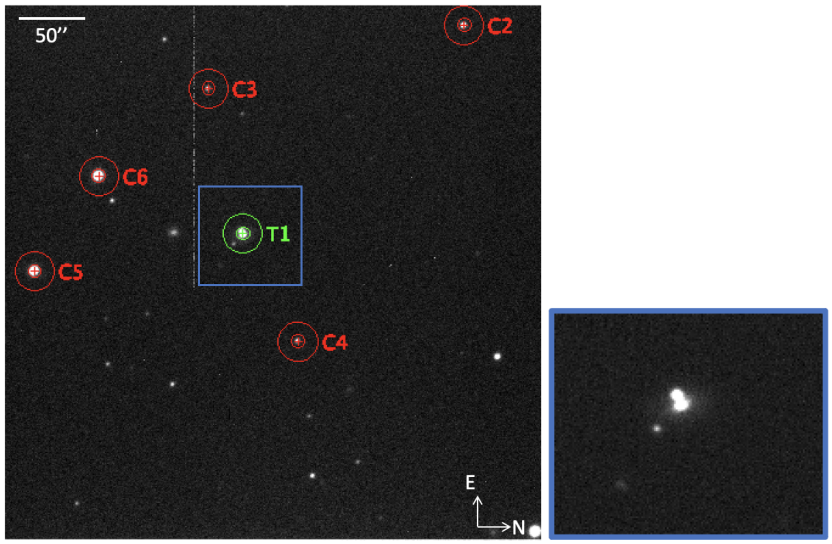

Figure 2.13: Field of view of MRK 507 in an LT B band image, with objects labeled as described in Figure 2.1. The smaller figure on the right shows a closer view of the AGN, within the region enclosed in the blue box.

The lag corresponding to the sublimation radius using the sublimation radius estimated from the IR bolometric correction in Table 2.2 is 535 days, which is ~ 0.6 times the length of the Spitzer light curves.

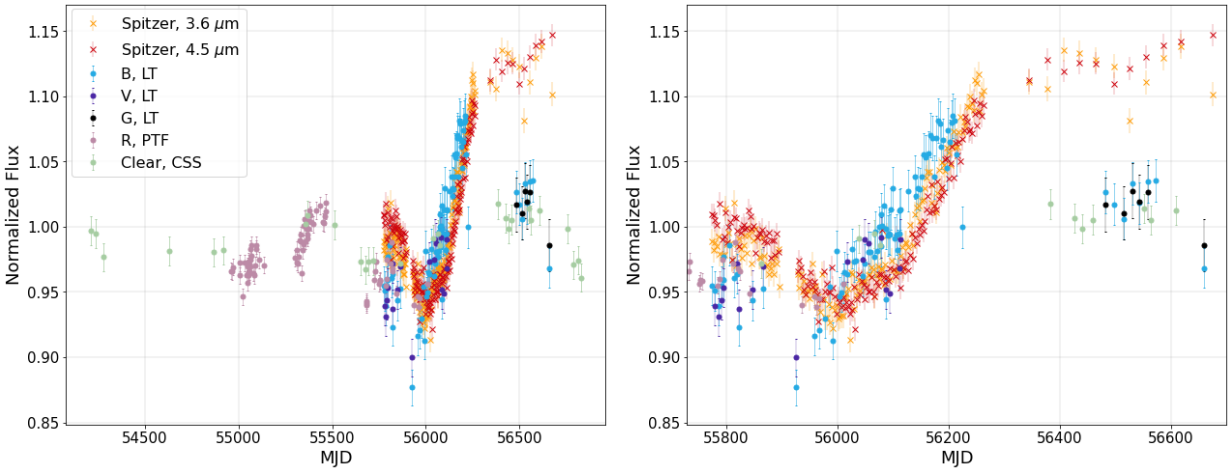

Figure 2.14: MRK 507 light curves. The left plot includes the entire time span of the light curves, while the right plot only includes the time period covered by the Spitzer campaign.

MRK 876 This is a very luminous Sy 1 AGN (Weedman, 1978), which has been previously well studied. Figure 2.15 shows the LT B band field of view. The optical light curves (see Figure 2.16) show significant variability, with the B band maximum at MJD 56030 followed by a large decline of 33% to the lowest point at MJD 56653. During cycle 8, smaller variations can be observed, which the LT V, R, and I bands also follow. The PTF and CSS light curves both rise in flux by $\sim 30\%$ before the Spitzer campaign. In contrast, the Spitzer light curves remain stable and vary by 2-4% during cycle 8, before decreasing in flux by less than 4% before cycle 9.

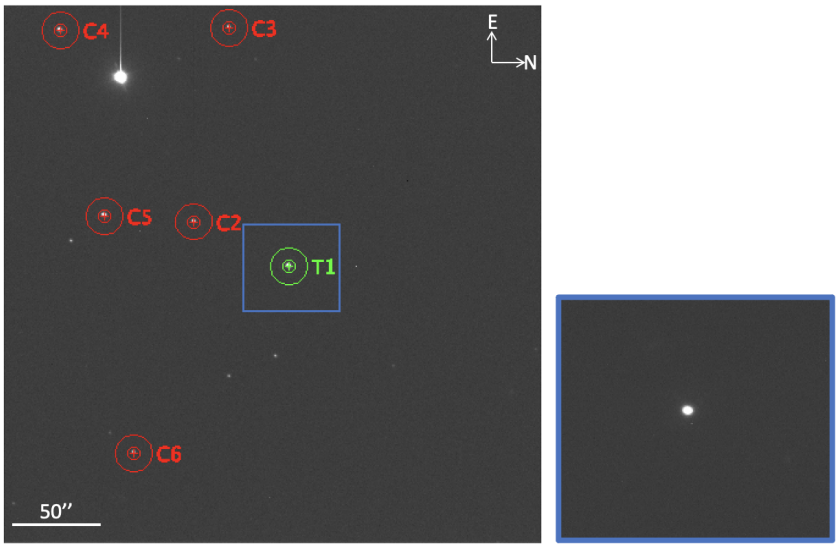

Figure 2.15: Field of view of MRK 876 in an LT B band image, with objects labeled as described in Figure 2.1. The smaller figure on the right shows a closer view of the AGN, within the region enclosed in the blue box.

MRK 876 is one of the brightest objects in our sample. Because of its large bolometric luminosity, it is expected to have a large lag value. The lag corresponding to the sublimation radius estimated from the IR bolometric correction in Table 2.2 is 1281 days, which is ~ 1.4 times the length of the Spitzer light curves.

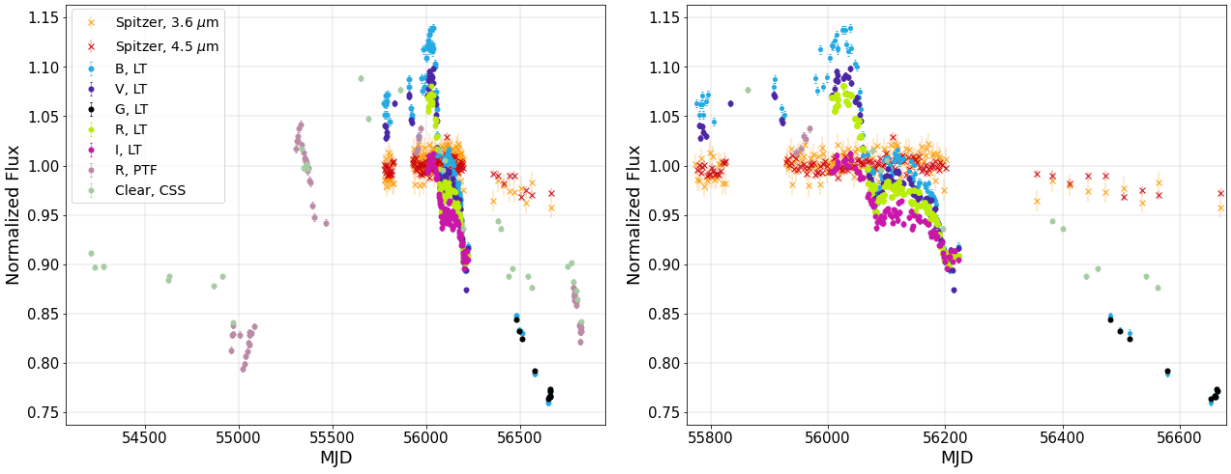

Figure 2.16: MRK 876 light curves. The left plot includes the entire time span of the light curves, while the right plot only includes the time period covered by the Spitzer campaign.

MRK 885 MRK885 is a moderately luminous and well-studied Sy 1 AGN (Véron-Cetty & Véron, 2006). Figure 2.17 shows the LT B band field of view and 2.18 shows the light curves. The IR light curve begins with a large decline in flux of 14% for channel 1 and 18% for channel 2 over ∼60 days from MJD 55775 to MJD 55831. After a small peak, the IR reaches its lowest point around 56100 (a 20% decrease from the beginning peak for channel 1 and 30% for channel 2). Cycle 9 shows a small peak in flux for both channels. In the optical, both the B and V bands show very small variations of only a few percent.

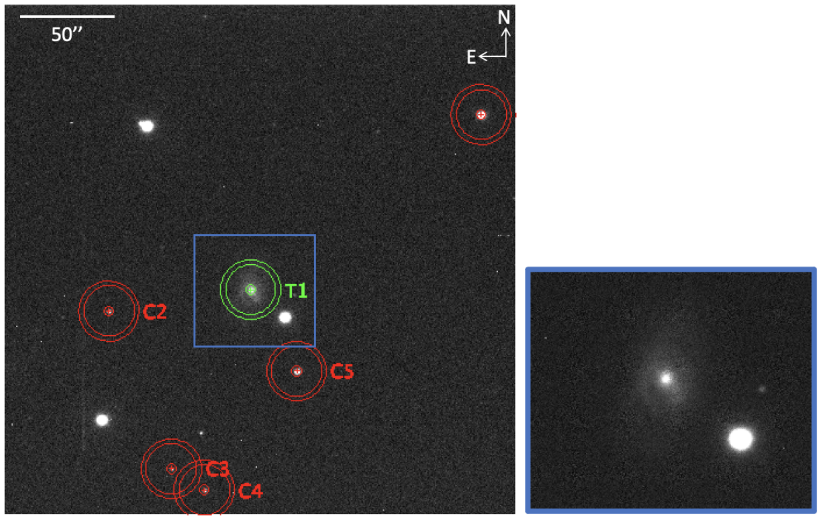

Figure 2.17: Field of view of MRK 885 in an LT B band image, with objects labeled as described in Figure 2.1. The smaller figure on the right shows a closer view of the AGN, within the region enclosed in the blue box.

The lag corresponding to the sublimation radius estimated from the x-ray bolometric correction in Table 2.2 is 869 days, which is approximately equal to the length of the Spitzer campaign.

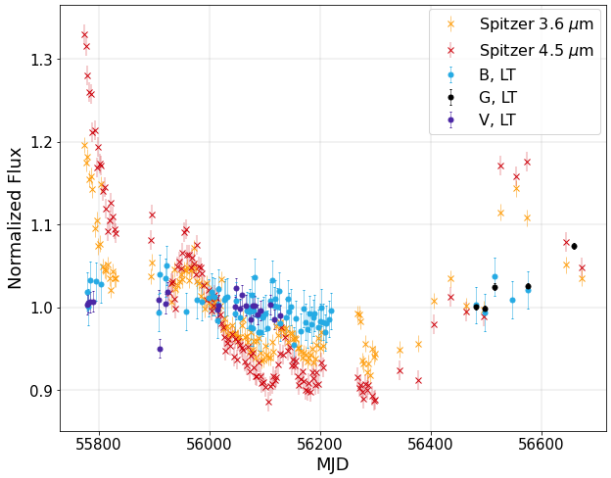

Figure 2.18: MRK 885 light curves, including the time period covered by the Spitzer campaign.

PGC 61965 This object is a Sy 1 AGN (Véron-Cetty & Véron, 2006), with few previous studies. Figure 2.19 shows the LT B band field of view and Figure 2.20 shows the light curves. This AGN has the highest bolometric luminosity in our sample ($L_{AGN} = 16.4 \times 10^{45}$ erg/s). The B band optical light curve peaks at ∼MJD 56000, followed by a steady decline of 30% over ∼ 600 days, however the IR shows a very slow and steady decline of less than 11% throughout the Spitzer campaign. This is another example of a very high luminosity object with large optical variations, but very minimal IR variations. The lag corresponding to the sublimation radius estimated from the IR bolometric correction is 1929 days, which is more than twice the length of the Spitzer campaign.

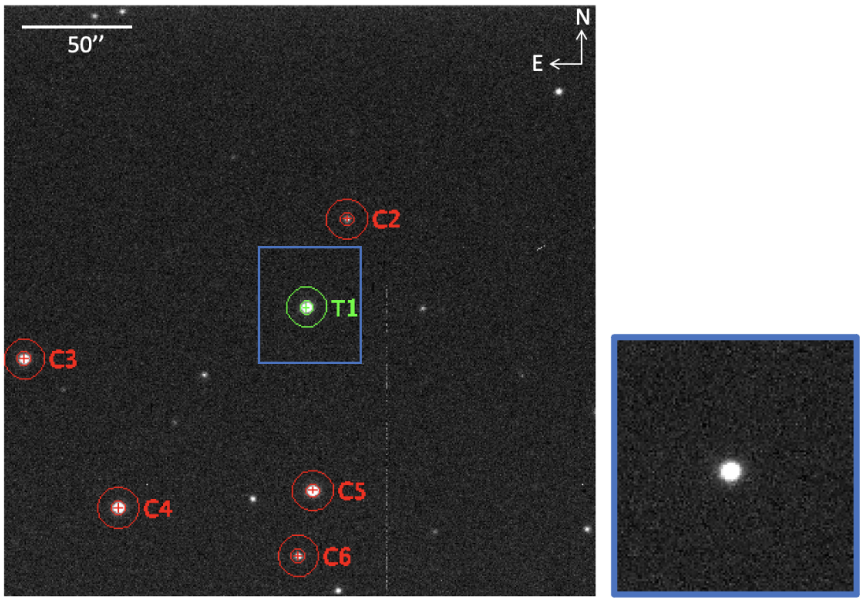

Figure 2.19: Field of view of PGC 61965 in an LT B band image, with objects labeled as described in Figure 2.1. The smaller figure on the right shows a closer view of the AGN, within the region enclosed in the blue box.

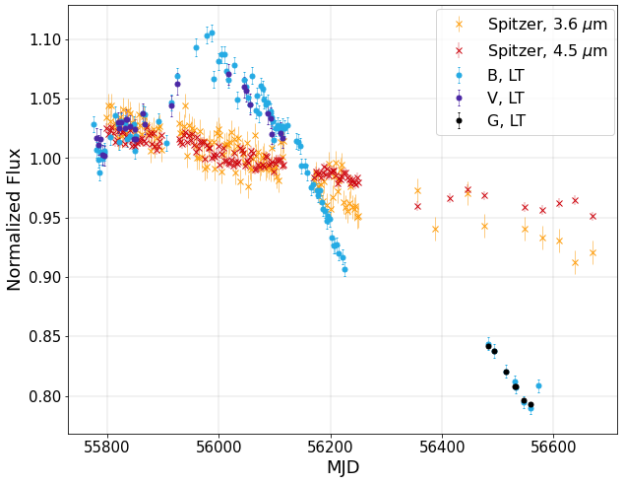

Figure 2.20: PGC 61965 light curves, including the time period covered by the Spitzer campaign.

UGC 10697 This object has been classified as a Sy 1 (Véron-Cetty & Véron, 2006), and has been studied very little. Figure 2.21 shows the LT B band field of view and Figure 2.22 shows the light curves. The IR begins in a high state at MJD 55775, declining until MJD 56160, with $\sim$ 12%

decrease in brightness. After a small gap in coverage, a slow increase in brightness of 20% begins at ∼MJD 56220, and lasts for 372 days to a maximum at ∼MJD 56500. The B band light curve shows similar variations, with a decrease in flux of ∼ 9% over 120 days, from MJD 55978 to 56101. Although there is a lot of scatter, there is clearly an increase in brightness of ∼ 14% over the next ∼ 400 days, with the peak at MJD 56500. The IR seems to follow this variation. The PTF data is sparse and shows little variation.

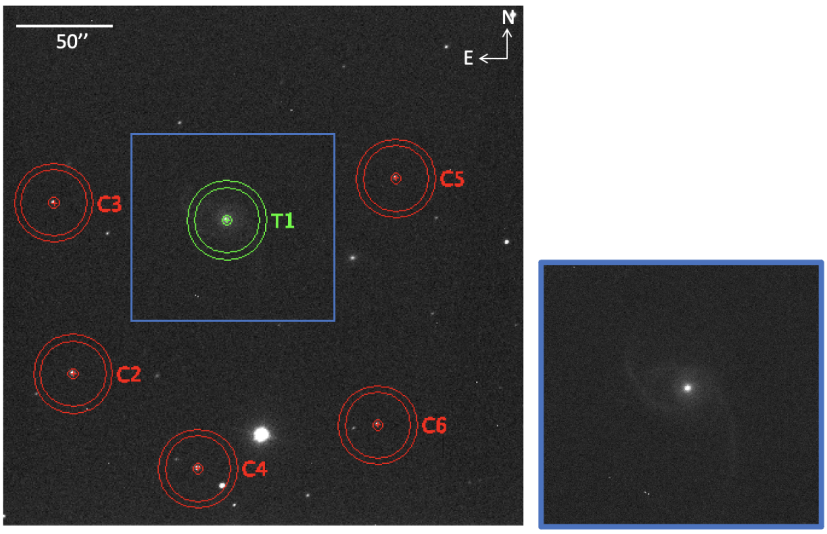

Figure 2.21: Field of view of UGC 10697 in an LT B band image, with objects labeled as described in Figure 2.1. The smaller figure on the right shows a closer view of the AGN, within the region enclosed in the blue box.

The lag corresponding to the sublimation radius estimated from the IR bolometric correction is 309 days, which is ∼ 0.35 times the length of the Spitzer campaign.

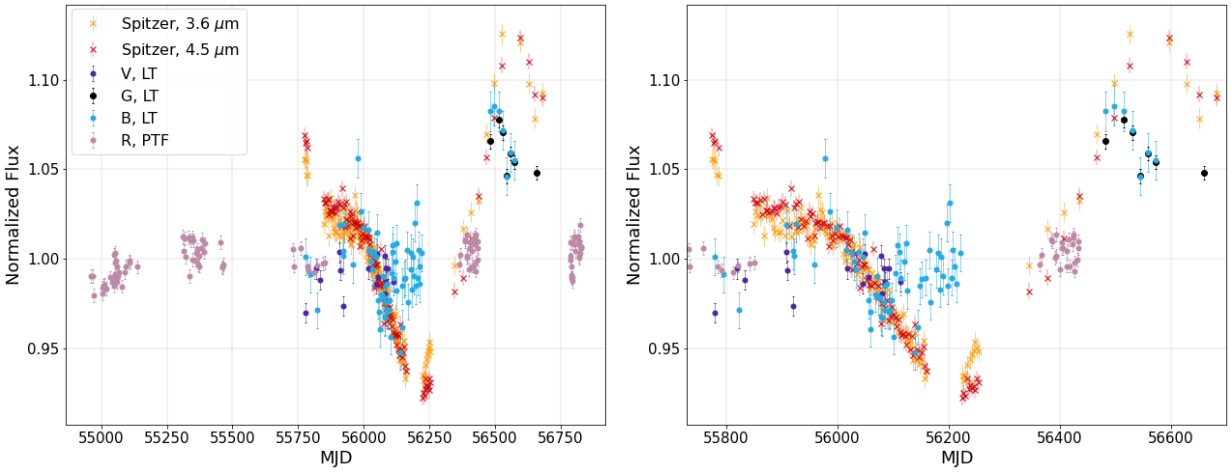

Figure 2.22: UGC 10697 light curves. The left plot includes the entire time span of the light curves, while the right plot only includes the time period covered by the Spitzer campaign.

2.4 Discussion

A comparison of the optical-IR light curve pairs reveals that each AGN exhibits one of the following general types of behavior:

1. **Comparable optical and IR variability:** The AGN exhibiting this type of behavior include IRAS 17552, KAZ 163, MRK 507, NGC 6418, and UGC 10697. This is the expected response for our light curve pairs. The AGN with this light curve trend exhibited optical variations with a similar IR response (this is shown in Tables 2.4 and 2.5, as well as Figure 2.23). NGC 6418 also fits into this category, although its variability amplitude is much higher than that of the other AGN.

2. **Significant optical variability with either no IR response, or a slow secular trend:** The AGN exhibiting this type of behavior include 2MASS J19091092+6652212, 3C390.3, KAZ 102, MRK 876, and PGC 61965. Through estimates of the dust sublimation radius in these objects, it is clear that this could be due to the large bolometric luminosity of the AGN, which leads to a large dust sublimation radius, and thus a very large time lag. The secular

Table 2.4: IR light curve statistics, re-calculated from Vazquez (2015).

AGN	3.6μm		4.5 μm	
	$\frac{f_{max}-f_{min}}{<f>}$	F_{var}	$\frac{f_{max}-f_{min}}{<f>}$	F_{var}
2MASS J19091092+6652212	0.11	0.021	0.056	0.011
3C390.3	0.077	0.015	0.15	0.028
IRAS 17552+6209	0.16	0.046	0.19	0.05
KAZ 102	0.13	0.029	0.19	0.03
KAZ 163	0.22	0.055	0.15	0.040
MRK 507	0.23	0.055	0.23	0.05
MRK 876	0.065	0.0086	0.061	0.0070
MRK 885	0.28	0.059	0.44	0.10
NGC 6418	1.01	0.18	1.3	0.25
PGC 61965	0.13	0.026	0.075	0.016
UGC 10697	0.19	0.039	0.20	0.042

trend of the IR response could also be due to the IR response being "washed out," if the torus light crossing time is much greater than the optical variability timescale.

3. **Strong IR variations with no significant optical variability:** The AGN exhibiting this behavior is MRK 885. This type of variability is the most unexpected, and could be due to a large contribution of starlight to the optical emission, which would dilute the optical light curve. However we also do not have data prior to the IR observations, therefore we may be missing the initial flux decrease in the optical.

By looking at Table 2.2, it is seen that the variability type of "strong optical variability with no IR response/a slow secular trend" tends to occur in the AGN that have a large bolometric luminosity (and large sublimation radius), while the variability type of "strong optical variability with strong IR response" or "comparable optical and IR variability" tends to occur in the AGN with smaller sublimation radii.

Variability statistics were calculated for the optical and IR light curves, shown in Tables 2.4 and 2.5. This includes statistics for the IR (3.6 and 4.5 μm) and optical (original and star light-subtracted) light curves of each AGN. The method for determining the starlight contribution is described in Chapter 3. The B band LT light curve was used as the optical light curve, except for NGC 6418 which used the full combined optical light curve from LT, PTF, and CSS. One column

Table 2.5: Optical light curve statistics

AGN	Original		Star light subtracted	
	$\frac{f_{max}-f_{min}}{<f>}$	F_{var}	$\frac{f_{max}-f_{min}}{<f>}$	F_{var}
2MASS J19091092+6652212	0.31	0.075		
3C390.3	0.49	0.15		
IRAS 17552+6209	0.14	0.030		
KAZ 102	0.31	0.062	0.35	0.070
KAZ 163	0.22	0.048	0.31	0.0677
MRK 507	0.17	0.042	1.61	0.420
MRK 876	0.38	0.088	0.435	0.101
MRK 885	0.096	na		
NGC 6418	1.06	0.24		
PGC 61965	0.32	0.071		
UGC 10697	0.14	0.028		

includes a calculation of the variability amplitude, $\frac{f_{max}-f_{min}}{<f>}$, where f_{max} is the maximum flux value, f_{min} is the minimum flux value, and $< f >$ is the mean flux value. Another column gives the value of F_{var} from Rodríguez-Pascual et al. (1997), which gives a measure of the variability of the light curve. F_{var} is defined as

$$F_{var} = \frac{(\sigma^2 - \Delta^2)^{1/2}}{< f >}, \tag{2.9}$$

where σ^2 is the variance, Δ^2 is the mean square value of the uncertainties, and $< f >$ is the unweighted mean flux.

Figure 2.23 plots the F_{var} and variability amplitudes using the 3.6 μm IR and optical results for each AGN. The AGN are listed in order of increasing sublimation radius, calculated with the IR bolometric correction. The sublimation radii for MRK 885 and KAZ 163 were calculated using the x-ray bolometric correction, since there were no IR measurements for these two AGN. The AGN showing a variability type of strong optical variations with a strong IR response have approximately equal values in the optical and IR for each plot, while the AGN with a variability type of strong optical variations with no IR response/a slow trend tend to have values in the optical that are at least twice as large as that of the IR. MRK 885 shows little optical variability with strong

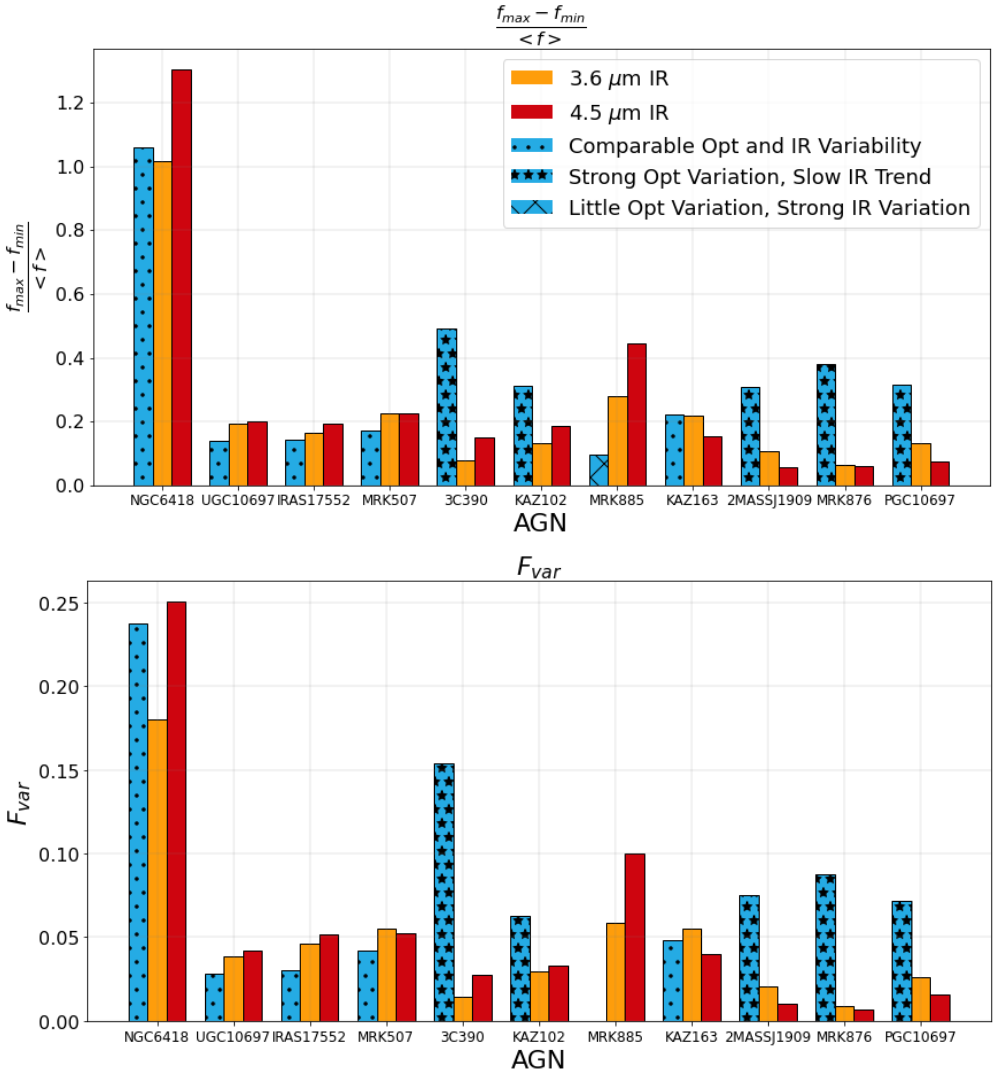

Figure 2.23: Each AGN is listed from left to right in order of increasing sublimation radius, calculated with the IR bolometric correction, except for MRK 885 and KAZ 163 which were calculated using the x-ray bolometric correction. The red bars show the values from the 3.6 μm IR light curve, and the blue bars show the values calculated from the B band LT light curve. The values for NGC 6418 were calculated using the full combined optical light curve. The different shaded patterns within the optical bars represent one of each variability type shown in the light curves for each AGN.

IR variations, and has an IR variability amplitude that is more than twice as large as that of the optical. It was not possible to calculate F_{var} for MRK 885, as the mean square value of the uncertainties was larger than the variance.

CHAPTER 3

GALFIT MODELING OF HST IMAGES

3.1 Introduction

In order to use the reverberation mapping code TORMAC, galaxy-subtracted optical light curves are needed as input. `GALFIT` was used to measure the amount of host galaxy starlight that falls within the photometric aperture sizes that were used to form the optical light curves. The optical light we detect is a combination of light from the AGN (a point source) and starlight from the host galaxy. By subtracting the constant contribution of host galaxy light from the optical light curves, we are left with a light curve showing the intrinsic AGN variability. These starlight-subtracted light curves can then be used as input into the reverberation mapping code, TORMAC.

3.1.1 GALFIT models for 8 AGN

The 2D image decomposition program `GALFIT` (Peng et al., 2002, 2010) can be used to model the distribution of light in galaxy images. `GALFIT` has been used in many AGN studies (Kim et al., 2008; Bentz et al., 2013; Kim et al., 2017; Kokubo & Minezaki, 2020), in order to distinguish between the light from the AGN and the starlight from the galaxy. We have obtained HST images for eight of our AGN, observed using the Wide Field Camera 3 (WFC3) in the F621M filter. This

filter covers a region of the spectrum that is not contaminated by strong emission lines. It was most important to choose a filter that would not include the variable Halpha and Hbeta lines, as our goal is to measure the constant contribution of starlight.

For each AGN, two pairs of images with three different exposure times (approximately 40s, 400s, and 800s) were taken in a 2-point dither pattern. The 40s exposure is below the saturation point for all of the objects in our sample, and could potentially be used to replace saturated pixels around the nucleus of the AGN in the long exposure images. The pipeline-processed and combined images were used for the analysis. They were checked for saturation and found to not be saturated.

`GALFIT` can be used to create simple axisymmetric models, or more complex models that include spiral arms, rings, or other asymmetric features. For our purposes, the simple models are adequate. Each model for our sample of AGN has at least 3 components which include the background sky, a point spread function (representing the AGN point source), and at least one Sérsic profile (representing the galaxy light). The Sérsic profile is defined by the following equation $\Sigma(r) = \Sigma_e \exp\left(-\kappa((r/r_e)^{1/n} - 1)\right)$, where r_e is the effective radius or half-light radius, Σ_e is the pixel surface brightness at r_e, n is a parameter that determines how centrally concentrated the light is, and κ is a parameter tied to n. This equation only depends on one spatial coordinate, r. There are several special cases of the Sérsic profile, including the Gaussian ($n = .5$), exponential ($n = 1$), and de Vaucouleurs ($n = 4$) profiles.

The PSF image can be formed by either using a reference star in the field of view, or a synthetic PSF can be computed using the software Tiny Tim (Krist et al., 2011). For five of the AGN a Tiny Tim model was used. For the other three, a star of comparable brightness to the AGN in the HST image was used as the PSF. When a Tiny Tim PSF was used, I fit the Tiny Tim PSF to the image of a star in the field using `GALFIT`, and then used the resulting model image as the PSF. Using Tiny Tim to model the PSF works well in general, although it does not fit the diffraction spikes well. The model image diffraction spikes tend to be mis-aligned from the diffraction spikes in the science image. This leaves a slightly over-subtracted region in the residual image, with the actual diffraction spikes being under-subtracted.

The parameters that can be specified depend on the component type. For a PSF, the only parameters are the x and y positions, and the magnitude. For Sérsic components, the parameters include the x and y positions, magnitude, effective radius (r_e), Sérsic index (n), axis ratio (q), and position angle (θ).

The input for `GALFIT` includes the science image, as well as an input file specifying the model components and parameters to be optimized. Nonlinear least-squares fitting is used to determine the goodness of fit. `GALFIT` then produces a model image using the optimized parameters, and also forms a residual image. My approach to constructing models involved adding components one-by-one, allowing `GALFIT` to optimize the parameters for each component, before adding the next component. I began by using only a background sky component, and allowing `GALFIT` to fit the sky value. I then add the PSF component, allowing `GALFIT` to optimize both the PSF and sky background values. I then add a Sérsic model component, allowing `GALFIT` to optimize all three components. I continue to add more Sérsic components to model the galaxy light, if there is still a lot of light in the residual images ($> 10\%$ residual fraction within photometric apertures). `GALFIT` also allows the option to set parameters to a fixed value. In most cases, I was able to let `GALFIT` optimize all of the parameters for each component.

When trying to separate the AGN host light from the galaxy starlight, accurate models of the PSF are extremely important. Kim et al (2008) explores the causes of PSF mismatches between the science image and the PSF in HST images, testing the use of PSFs made using Tiny Tim, and PSFs formed from field stars in HST images. There are several factors that can affect the shape of the PSF, which include color differences between the PSF and the AGN, spatial variability between the location of the PSF and the AGN, and a difference in time between when the PSF science images were taken. Another important factor contributing to PSF mismatch is that HST images are undersampled. Smoothing the image to Nyquist sampling can solve this problem. This is done by convolving the science image and PSF image with a Gaussian kernel. I used this approach for several AGN, for which it initially proved difficult to obtain good fits.

In some cases, due to the PSF mismatch, a different procedure was used with the Tiny Tim

PSFs. 2-3 Tiny Tim models were placed less than 1 pixel away from each other, and allowed to optimize. Although several PSFs were placed, they are modeling the light from a single point source. Therefore, the flux from these models was summed. This value is considered to be the flux from the AGN point source.

Here, I discuss my results for the `GALFIT` models for each AGN. The light in the background-subtracted image ($f_{\rm data} - f_{\rm model,background}$) is a combination of light from the PSF and the host galaxy starlight. For each model discussed below, I also calculated both the fraction of light originating from the point source
$F_{\rm PSF} = \left(\frac{f_{\rm model,\ PSF}}{f_{\rm data} - f_{\rm model,\ background}}\right)$, as well as the fraction of light left in the residual
$F_{\rm residual} = \left(\frac{f_{\rm residual}}{f_{\rm data} - f_{\rm model,\ background}}\right)$ within the smallest and largest photometric apertures.

3.1.2 Galaxy-subtracted light curves

After the `GALFIT` model is constructed, I use the model to create an image that only includes the galaxy light. For each object, I measure the flux that falls within the photometric apertures that were used to construct the optical light curves. I also assume that most of the light within the residuals is galaxy light, and therefore I also measure the flux that falls within the photometric apertures of the residual image as well, adding this to my measurement of starlight.

The next step is to convert from the image units of counts into magnitudes. The procedure outlined in the Jupyter Notebook available on the STScI website[1] titled "Calculating WFC3 Zeropoints Using STSynphot" was followed in order to calculate the zeropoints for each observation date. The following equation was used

$$m = -2.5 \log_{10} F(r) + m_{vega,ZP} \tag{3.1}$$

with $F(r) = \frac{N(r)}{EE(r) * t}$, with N representing the measured number of electrons from the image

[1] https://www.stsci.edu/hst/instrumentation/wfc3/data-analysis/photometric-calibration/uvis-photometric-calibration

within the aperture, ee is the encircled energy fraction at radius r, and t is the image exposure time. $m_{vega,ZP} = 24.446$ is the corresponding zero point magnitude given by the Jupyter Notebook.

The HST images use the F621M filter. Therefore, we now have measurements of the amount of galaxy light within one filter for each photometric aperture. However, the optical light curves are in several other wavebands (B, V, G, r', and clear). To determine the amount of starlight in these other wavebands, color corrections need to be used. As suitable spectra were not available for all objects, we estimated color corrections using a 2001 SDSS spectrum of NGC 6418, which is shown in Section 5.5. This spectrum was chosen as the AGN was in a low state at that time.

We want to derive color corrections from the spectrum of the host galaxy, however the spectrum contains light from both the AGN and the host galaxy. Therefore, the AGN portion needs to be removed. The software pPXF (Cappellari, 2017) was used to fit the stellar continuum. The broad and narrow lines were also fitted and subtracted, leaving a line-free continuum spectrum.

Once we have the galaxy spectrum, color corrections can be estimated. To derive the color corrections, the filter response curves were convolved with the line-free spectrum. The following color corrections were used

$$\begin{aligned} m_g &= .905 + m_r \\ m_V &= .336 + m_r \\ m_B &= 1.338 + m_r, \end{aligned} \tag{3.2}$$

with $m_{r'}$, m_g, m_V, and m_B representing the r', g, V, and B band magnitudes, respectively. There was no correction applied to the r' band. The m_V equation was used for the clear filter light curve. Assuming that the population of stars are similar within the galaxy for each of the AGN, we used the same color corrections for each AGN.

Once the color correction is applied, we now have magnitude values of the galaxy starlight within each waveband, for each photometric aperture. This is then converted into a flux value, which can then be subtracted from the original light curves (in flux units). The starlight subtracted light curves are also presented here for each AGN.

Once the starlight-subtracted light curves have been formed, you can see that sometimes the fluxes of the PTF, CSS, and LT light curves are offset from each other. These offsets could be due to several reasons, as discussed in Section 3.1.3. To solve this issue, the light curves were converted to flux values and then multiplied by a small factor, which will shift them to match the LT B band light curve. To plot the final combined optical light curve, the light curve was normalized to its own mean value, and displayed alongside the IR light curve. To construct the combined light curves, typically only the PTF, CSS, and LT B band light curves were used, as the LT g and V bands cover the same time period as the LT B band.

Also note that many of the HST images shown in the following section have been cropped to more clearly show the target galaxy, and larger regions of each image were used as input for `GALFIT`. Tables 3.1-3.7 present the parameters for the best fitting models. For each table, column 1 states the component type (Sky, PSF, or Sérsic). For the sky component, columns 2-4 include the sky gradient in the x and y directions, as well as the sky background at the center of the fitting region. For PSF and Sérsic models, columns 2 and 3 give the angular offset (in arcseconds) from the AGN center, which is modeled as a PSF. The integrated magnitude is given in column 4. Columns 5-8 are included for Sérsic models, and give the effective radius (r_e), Sérsic index (n), axis ratio (b/a) and position angle (P.A; Equals 0° if semi-major axis aligns vertically, and 90° if the component aligns horizontally towards the left).

The analysis for NGC 6418 is presented separately in Chapter 5.

IRAS 17552+6209 The original image, the model image, and the residual image for IRAS 17552+6209 are shown in Figure 3.1. Faint spiral arms can be seen $0.6 - 1.6''$ from the center, with more extended starlight out to $\sim 10''$ radius.

Table 3.1: IRAS 17552 Model Parameters

Sky	$\frac{d(\text{sky})}{dx}$ (10^{-3} counts)	$\frac{d(\text{sky})}{dy}$ (10^{-3} counts)	Sky (Counts)				
PSF	Δx ($''$)	Δy ($''$)	m_{vega}				
Sérsic	Δx ($''$)	Δy ($''$)	m_{vega}	r_e ($''$)	n	b/a	P.A.
Sky	-1.5	4.4	25.0				
PSF	0	0	19.53				
Sérsic	-0.10	-0.04	16.09	3.05	4.7	0.59	46.8
Sérsic	0.14	0.35	17.61	3.06	0.3	0.42	36.8

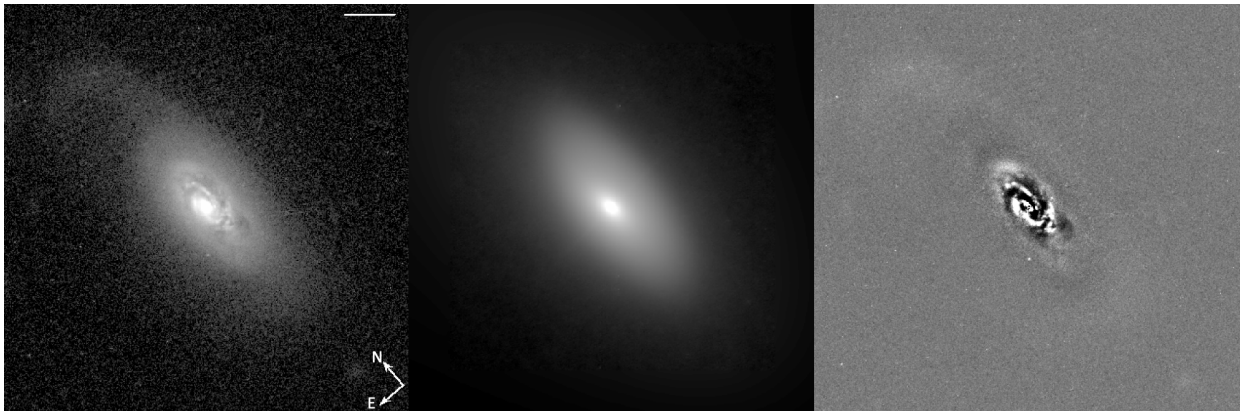

Figure 3.1: Images of IRAS 17552, with each image showing a $20'' \times 20''$ region. The scale bar is $2.5''$ long. The left image shows a portion of the original HST image, the middle image shows the `GALFIT` model, and the right image shows the residual.

This model includes the sky background, a PSF (formed using a field star), and 2 Sérsic components. One Sérsic component fits the more extended galaxy light, while the second component has a higher Sérsic index, with more of the light concentrated at the center. This galaxy was straightforward to model, with no major issues. Although there are slightly positive and negative regions shown in the residual image due to the spiral arms of the galaxy, most of the light in the image seems to be modeled well. The fraction of light originating from the point source within a $2.8''$ aperture is 5.8%, and within $7.5''$ is 4.1%, so the point source is very faint. The fraction of light in the residual image is 1.3% within $2.8''$ and 0.69% within $7.5'$.

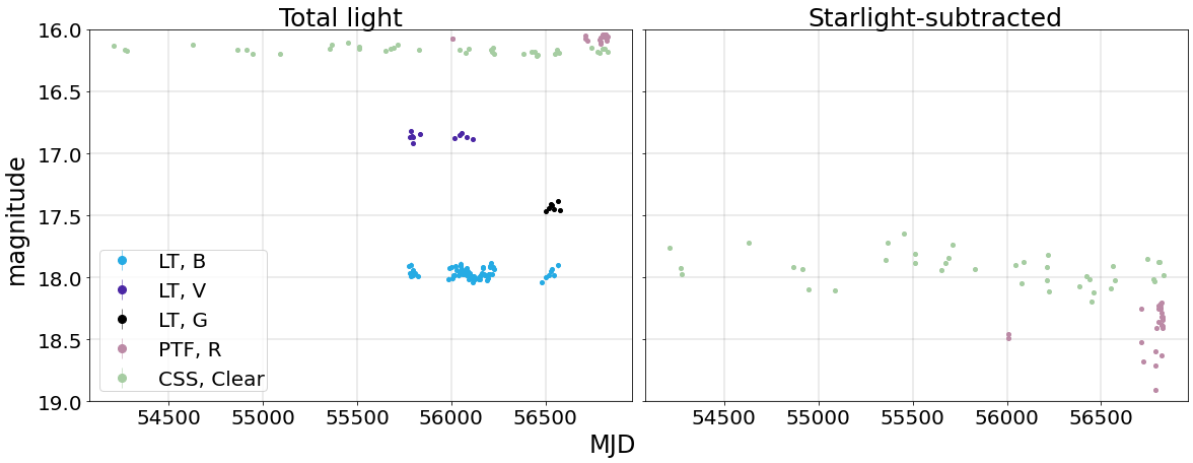

Figure 3.2: IRAS 17552 light curves: The left subplot shows the light curves before subtracting the starlight contribution, while the right subplot has been starlight-subtracted.

In Figure 3.2, the original light curves (containing both light from the point source and light from the host galaxy) are shown on the left, and the starlight-subtracted light curves are shown on the right. The point source was found to be very faint in this object, so a significant amount of starlight has been subtracted. For this AGN, only the CSS and PTF light curves are shown. The three LT light curves are not shown in the starlight-subtracted plots, as negative flux values are obtained when subtracting the starlight contribution. The potential causes of this are discussed at the end of this chapter.

KAZ 102 KAZ 102 has a very bright point source, with little galaxy light (see Figure 3.3). This was a very difficult image to fit with `GALFIT`, and I struggled to get a realistic magnitude value for the PSF component (the optimized magnitude value was much too faint). Reasonable optimized values were finally obtained once a Tiny Tim model was used, and the image was broadened slightly with a gaussian. This model includes the sky background, a PSF (formed using a Tiny Tim model), and two Sérsic components. One Sérsic component is centered on the host galaxy, and another is located at the nearby galaxy to the northeast. The fraction of light originating from the point source within a 2.9″ aperture is 80.2%, and within 7.5″ is 77.8%. The fraction of light in the

Table 3.2: KAZ 102 Model Parameters

Sky PSF Sérsic	$\frac{d(\text{sky})}{dx}$ (10^{-3} counts) Δx ($''$) Δx ($''$)	$\frac{d(\text{sky})}{dy}$ (10^{-3} counts) Δy ($''$) Δy ($''$)	Sky (Counts) m_{vega} m_{vega}	r_e ($''$)	n	b/a	P.A.
Sky	0.76	-.081	28.29				
PSF	0	0	16.43				
Sérsic	0.05	0.01	17.91	0.63	4.0	0.84	-26.5
Sérsic	6.5	9.2	18.63	1.29	3.9	0.41	-81.9

residual image is 4.8% within 2.1$''$ and 2.9% within 7.5$''$.

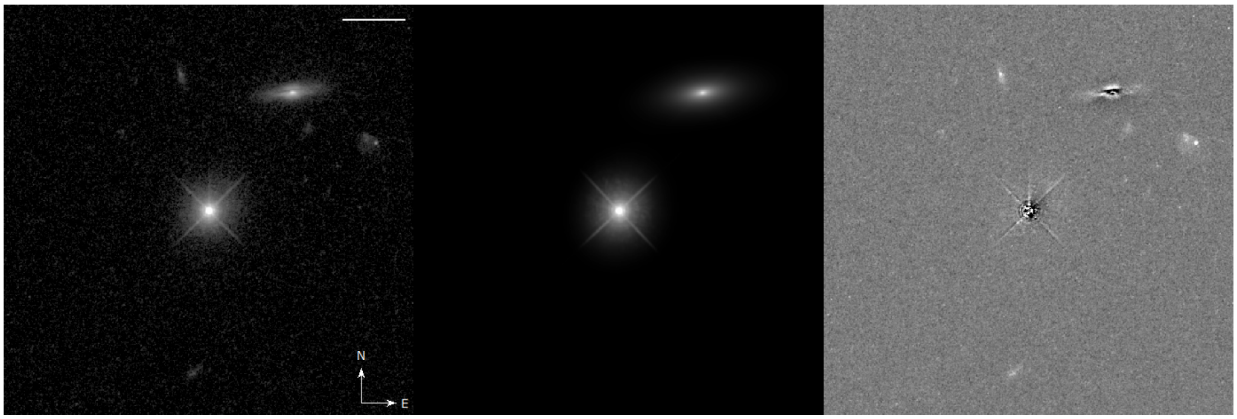

Figure 3.3: Images of KAZ 102, with each image showing a $32'' \times 32''$ region. The scale bar is $5.0''$ long. The left image shows a portion of the original HST image, the middle image shows the `GALFIT` model, and the right image shows the residual.

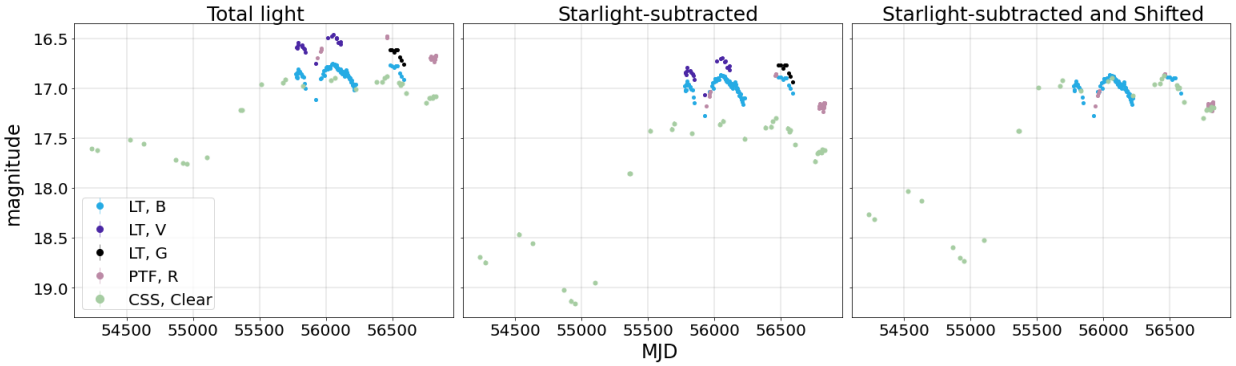

Figure 3.4: KAZ 102 light curves: The left plot shows the light curves before subtracting the starlight contribution, the middle plot has been starlight-subtracted, and the right plot shows the starlight-subtracted and shifted light curves.

Figure 3.4 shows the original light curve (left plot), the starlight-subtracted light curve (middle plot) and the starlight-subtracted and shifted light curves (right plot). Most of the light in this object originates from the point source, so only a small amount of starlight is subtracted. Therefore, the starlight-subtracted light curve does not differ much from the original light curve. Figure 3.5 presents the full light curve alongside the IR, with each light curve normalized to its own mean.

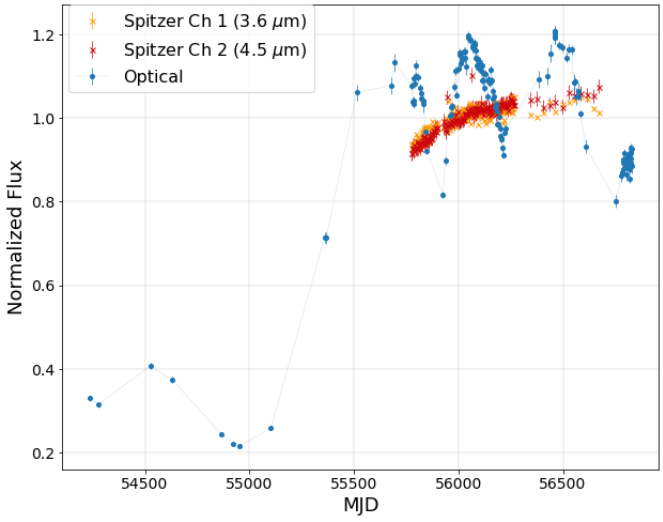

Figure 3.5: KAZ 102 light curves: KAZ 102 IR and starlight-subtracted optical light curve, with each light curve normalized to its own mean.

KAZ 163 KAZ 163 has a very complex distribution of light that includes a few nearby galaxies (see Figure 3.6). This was one of the most difficult images to fit with `GALFIT`, most likely due to how disturbed the extended starlight is. The center of the largest nearby galaxy is $\sim 9.5''$ north of the center of the target AGN, and two more galaxies are located south of the AGN. A few fainter stars and galaxies are located to the west.

A Tiny Tim model was used for the PSF. This model includes the sky background, three PSFs to model the AGN, and one Sérsic component models the host galaxy light. Another Sérsic component was used to fit the light from the northern interacting galaxy, and a small Sérsic model was used to fit the southern galaxy. Another Sérsic component was used to fit the distribution of light west of the AGN. A faint PSF component was used to fit the star at the west side of the image, along with two fainter Sérsic models to fit the small faint galaxies.

Several PSFs are used to model the faint stars located throughout the image. Although these were included in the `GALFIT` models, equivalently they could have simply been masked out of the image.

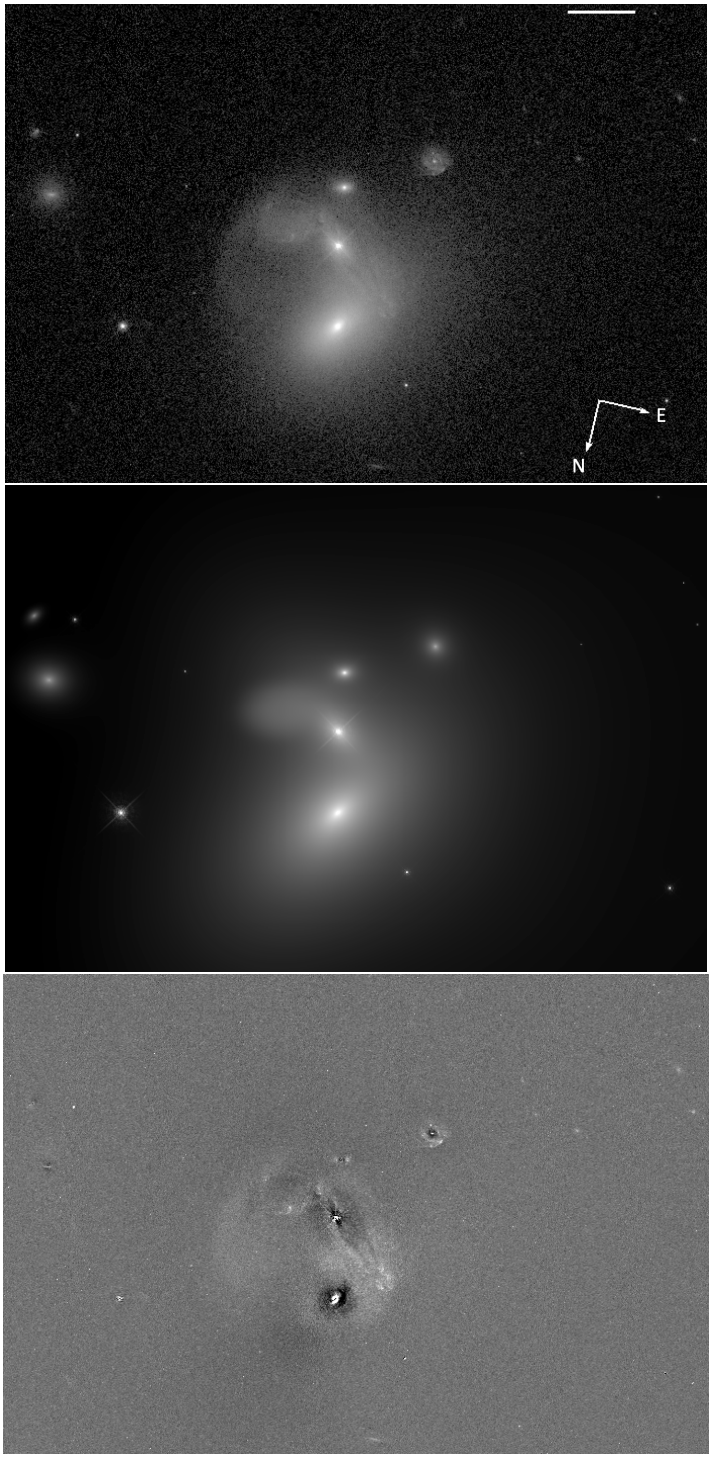

Figure 3.6: Images of KAZ 163, with each image showing a $84'' \times 57''$ region. The scale bar is $8''$ long. The upper image shows a portion of the original HST image, the middle image shows the `GALFIT` model, and the lower image shows the residual.

Table 3.3: KAZ 163 Model Parameters

Sky PSF Sérsic	$\frac{d(\text{sky})}{dx}$ (10^{-3} counts) Δx ($''$) Δx ($''$)	$\frac{d(\text{sky})}{dy}$ (10^{-3} counts) Δy ($''$) Δy ($''$)	Sky (Counts) m_{vega} m_{vega}	r_e ($''$)	n	b/a	P.A.
Sky	1.2	-0.16	31.5				
PSF	0	0	8.90				
PSF	0.04	-0.07	9.27				
PSF	-0.03	-0.08	9.13				
Sérsic	0.04	0.06	6.46	16.45	4.6	0.60	40.1
Sérsic	-0.07	-9.6	5.57	9.44	3.5	0.63	-46.4
Sérsic	0.7	6.8	9.73	0.67	4.8	0.75	-84.0
Sérsic	-6.4	2.5	9.37	3.01	0.4	0.69	-86.4
Sérsic	-35.7	13.5	12.79	0.58	1.7	0.66	-51.0
Sérsic	-34.0	6.0	10.14	1.80	2.0	0.83	83.7
PSF	-30.9	13.1	12.98				
PSF	-25.5	-9.6	9.77				
PSF	-25.4	-9.6	11.88				
PSF	-18.0	7.0					
PSF	38.9	-18.4					
PSF	38.9	-18.4					
PSF	37.5	27.5					
PSF	8.1	-16.5					
PSF	8.0	-16.6					
PSF	40.5	17.4					
PSF	42.2	12.5					
PSF	28.5	10.2					
PSF							
Sérsic	11.4	9.9	10.28	1.77	2.5	0.94	29.8

There are slightly negative regions shown in the residual image surrounding the the center of the AGN and the nearby companion galaxy. The fraction of light originating from the point source within a 2.8″ aperture is 55.9%, and within 7.5″ is 25.4%. The fraction of light in the residual image is 1.9% within 2.8″ and 5.3% within 7.5″.

The original and starlight-subtracted light curves are shown in Figure 3.7, and are shown alongside the IR in Figure 3.8.

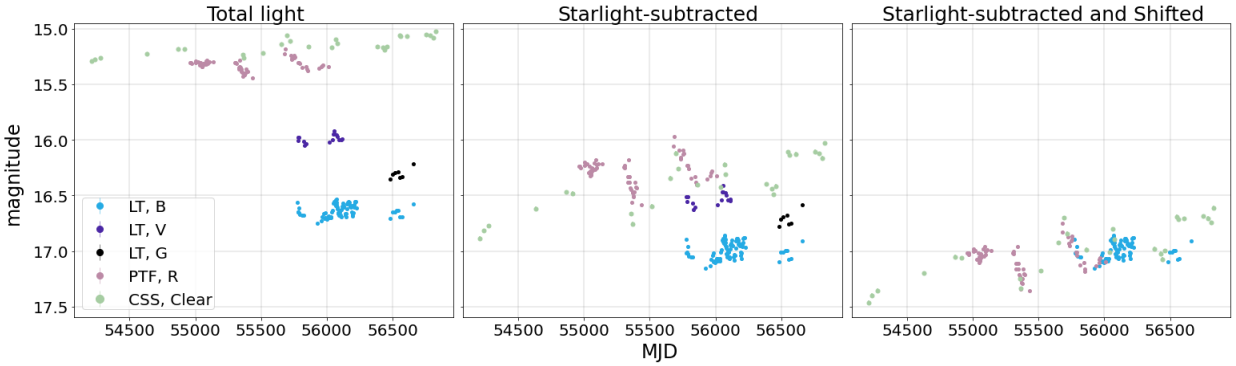

Figure 3.7: KAZ 163 light curves: The left plot shows the light curves before subtracting the starlight contribution, the middle plot has been starlight-subtracted, and the right plot shows the starlight-subtracted and shifted light curves.

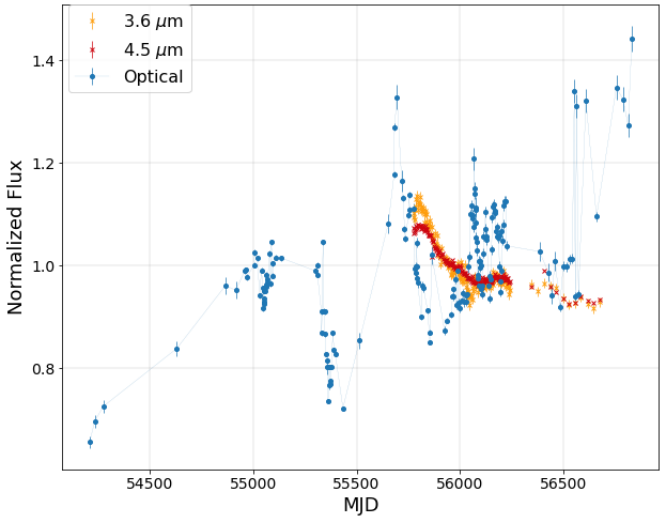

Figure 3.8: KAZ 163 light curves: KAZ 163 IR and starlight-subtracted optical light curve, with each light curve normalized to its own mean.

MRK 507 This galaxy has spiral arms, a bright star located $\sim 2.2''$ from the AGN, and a fainter star located $\sim 6.8''$ from the center of the AGN (see Figure 3.9). Three Tiny Tim models were used to model the AGN. The model includes the sky background, three PSFs to model the AGN, two Sérsic components, and 3 PSFs to model each of the two nearby stars. One Sérsic component has

Table 3.4: MRK 507 Model Parameters

Sky PSF Sérsic	$\frac{d(\text{sky})}{dx}$ (10^{-3} counts) Δx ($''$) Δx ($''$)	$\frac{d(\text{sky})}{dy}$ (10^{-3} counts) Δy ($''$) Δy ($''$)	Sky (Counts) m_{vega} m_{vega}	r_e ($''$)	n	b/a	P.A.
Sky	-.04056	-0.3252	28.9481				
PSF	0	0	10.08				
PSF	-0.05	-0.03	10.06				
PSF	-0.001	0.05	10.18				
Sérsic	-0.88	0.08	8.28	4.15	1.01	0.58	47.1
Sérsic	-0.08	-0.10	7.17	2.57	4.00	0.48	73.90
PSF	-0.93	-2.09	8.06				
PSF	-0.95	-2.15	8.85				
PSF	-0.97	-2.06	10.38				
PSF	6.82	-0.01	10.02				
PSF	6.88	-0.02	11.19				
PSF	6.82	-0.04	10.29				

an index that optimized to a value of $n = 4$, while the other has a lower Sérsic index ($n = 1.01$) and models the more extended galaxy light. There are slightly positive and negative regions shown in the residual image due to the spiral arms of the galaxy.

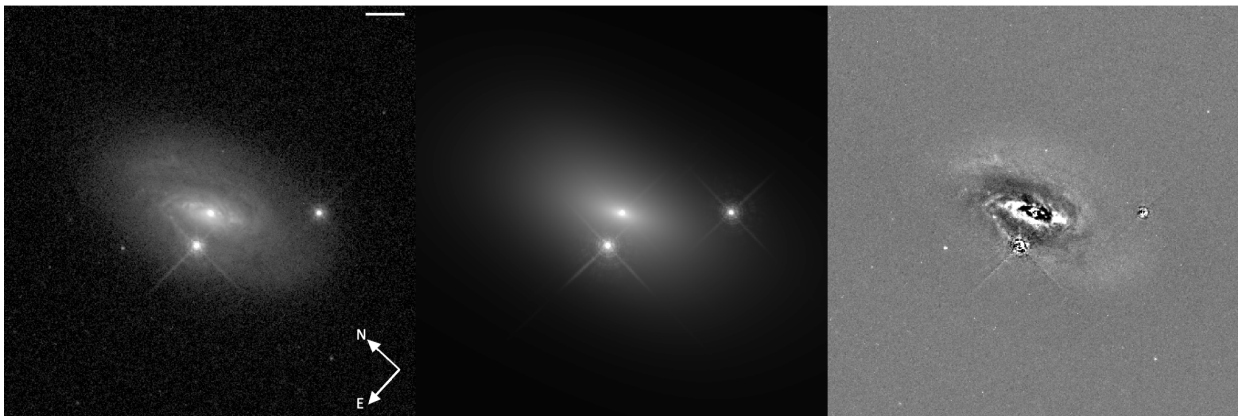

Figure 3.9: Images of MRK 507, with each image showing a $26'' \times 26''$ region. The scale bar is $2.5''$ long. The left image shows a portion of the original HST image, the middle image shows the `GALFIT` model, and the right image shows the residual.

The point source is faint, with most of the light originating from the galaxy. The fraction of light originating from the point source within a $3.5''$ aperture is 11.1%, and within $7.5''$ is 8.7%. The fraction of light in the residual image is 3.4% within $3.5''$ and 3.9% within $7.5''$.

Starlight-subtracted light curves are shown in Figures 3.10 and 3.11. MRK 507 has a very large fraction of starlight ($\sim 90\%$ within the largest and smallest photometric apertures). Subtracting the constant starlight contribution has increased the amplitude of the light curves, which is especially clear in the LT B band.

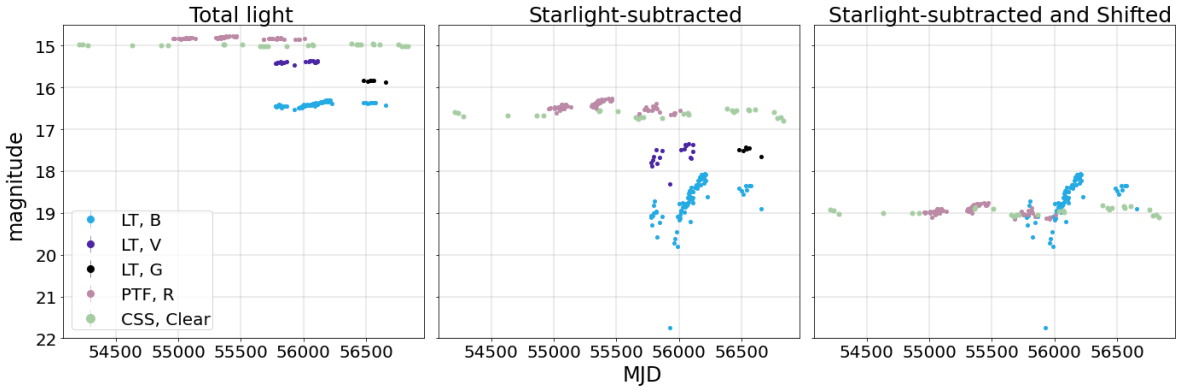

Figure 3.10: MRK 507 light curves: The left plot shows the light curves before subtracting the starlight contribution, the middle plot has been starlight-subtracted, and the right plot shows the starlight-subtracted and shifted light curves.

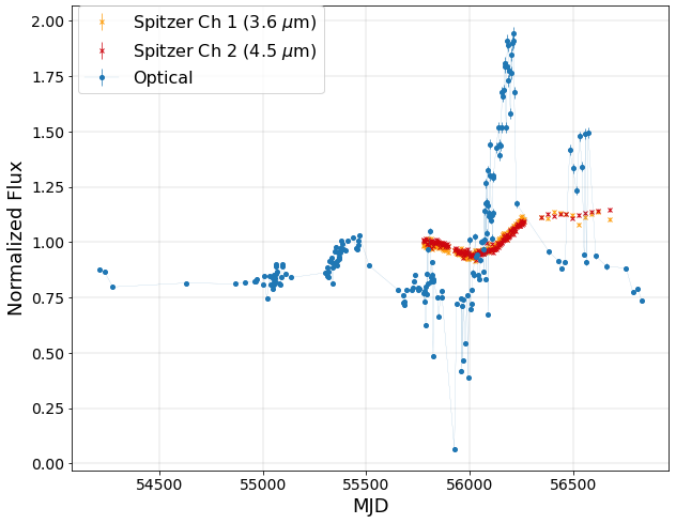

Figure 3.11: MRK 507 light curves: MRK 507 IR and starlight-subtracted optical light curve, with each light curve normalized to its own mean.

MRK 876 This galaxy includes a bright AGN point source and an extended structure of disturbed starlight, which occurs out to a radius of $\sim 11.2''$ (see Figure 3.12). A secondary compact structure (possibly a small interacting galaxy) is located $\sim 2.3''$ from the center of the AGN.

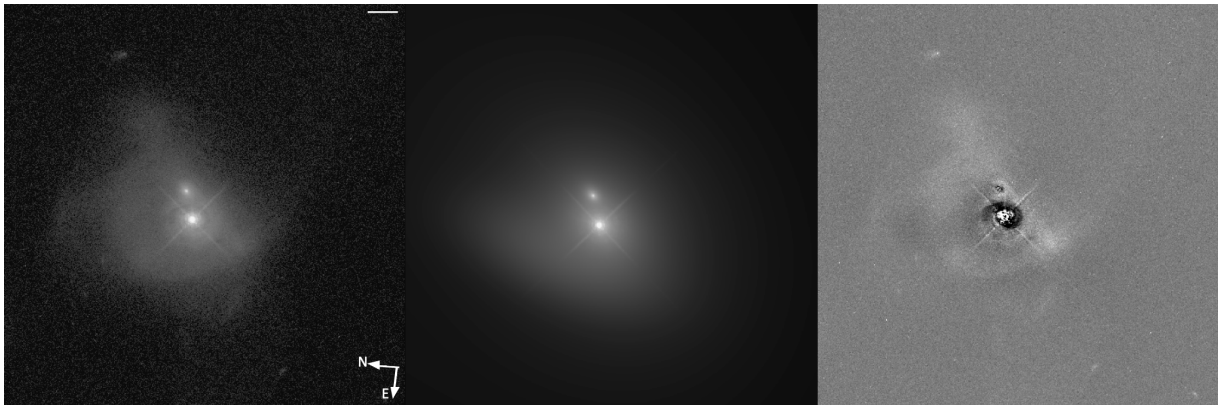

Figure 3.12: Images of MRK 876, with each image showing a $28'' \times 28''$ region. The scale bar is $2.5''$ long. The left image shows a portion of the original HST image, the middle image shows the `GALFIT` model, and the right image shows the residual.

Table 3.5 presents the best-fit model parameters. This model includes the sky background, four PSFs to model the AGN, and two Sérsic components to model the target galaxy. An additional PSF and Sérsic component models the secondary compact galaxy. The two Sérsic components to model the galaxy light seem reasonable, as one models the more extended galaxy light towards the left side of the image, and the other has a higher concentration of light at the center of the host galaxy.

The point source and galaxy light both have a similar contribution to the light in the image. The fraction of light originating from the point source within a $3.2''$ aperture is 56.9%, and within $7.5''$ is 42.5%. The fraction of light in the residual image is 3.6% within $3.2''$ and 6.7% within $7.5''$. Starlight-subtracted light curves are shown in Figures 3.13 and 3.14.

Table 3.5: MRK 876 Model Parameters

Sky PSF Sérsic	$\frac{d(\text{sky})}{dx}$ (10^{-3} counts) Δx ($''$) Δx ($''$)	$\frac{d(\text{sky})}{dy}$ (10^{-3} counts) Δy ($''$) Δy ($''$)	Sky (Counts) m_{vega} m_{vega}	r_e ($''$)	n	b/a	P.A.
Sky	-2.1	0.17	28.8				
PSF	0	0	8.16				
PSF	0.02	0.06	9.07				
PSF	-0.05	0.06	9.08				
PSF	-0.04	-0.05	9.62				
Sérsic	0.08	0.06	6.92	5.30	4.0	0.81	44.8
Sérsic	-3.0	-2.0	8.81	5.03	0.5	0.47	69.3
PSF	-0.46	2.3	14.61				
Sérsic	-0.48	2.3	10.12	0.47	2.1	0.73	42.4

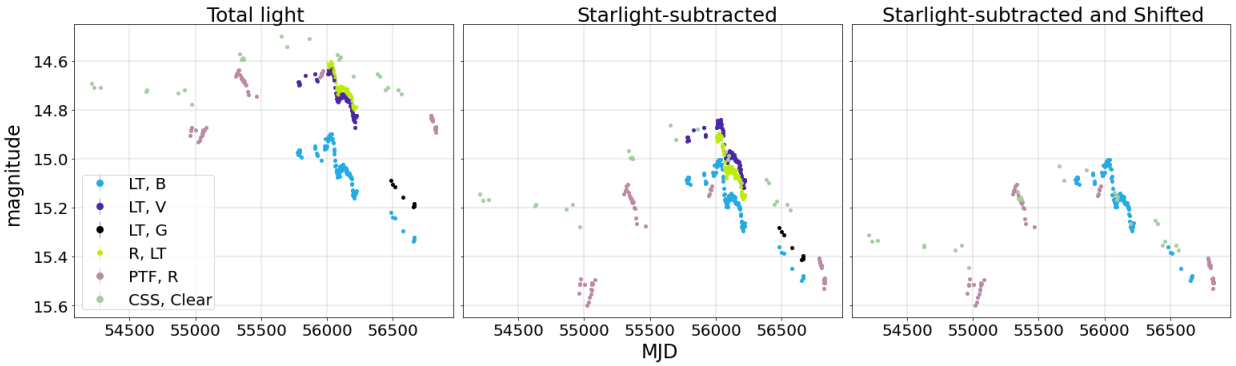

Figure 3.13: MRK 876 light curves: The left plot shows the light curves before subtracting the starlight contribution, the middle plot has been starlight-subtracted, and the right plot shows the starlight-subtracted and shifted light curves.

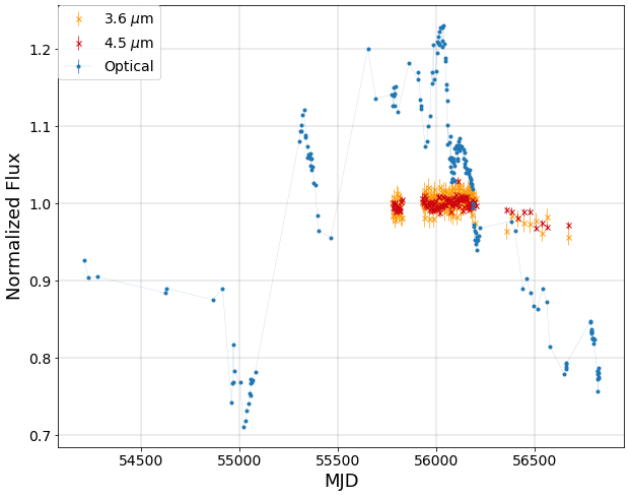

Figure 3.14: MRK 876 light curves: MRK 876 IR and starlight-subtracted optical light curve, with each light curve normalized to its own mean.

MRK 885 MRK 885 has clear spiral arms, and a faint point source (see Figure 3.15). A star in the field was used for the PSF. The saturated star in the lower left corner was specified in the `GALFIT` input file to be masked out of the image. This model includes the sky background, a PSF to model the AGN, and 3 Sérsic components. One of the Sérsic components has a Sérsic index of $n = 4.38$, while another Sérsic component models the more extended light along the length of the galaxy (from the top left to bottom right of Figure 3.15). Another Sérsic component models the bar at the center. The fraction of light originating from the point source within a 2.8″ aperture is 6.10%, and within 7.5″ is 2.6%. The fraction of light in the residual image is 0.58% within 3.2″ and 1.77% within 7.5″.

Table 3.6: MRK 885 Model Parameters

Sky PSF Sérsic	$\frac{d(\text{sky})}{dx}$ (10^{-3} counts) Δx ($''$) Δx ($''$)	$\frac{d(\text{sky})}{dy}$ (10^{-3} counts) Δy ($''$) Δy ($''$)	Sky (Counts) m_{vega} m_{vega}	r_e ($''$)	n	b/a	P.A.
Sky	0.19	-1.0	34.4				
PSF	0	0	18.35				
Sérsic	-0.01	-0.06	13.74	13.02	4.4	0.86	75.9
Sérsic	-0.08	0.11	14.76	14.49	0.3	0.50	55.9
Sérsic	-0.93	-0.44	16.58	4.53	0.3	0.33	-71.9

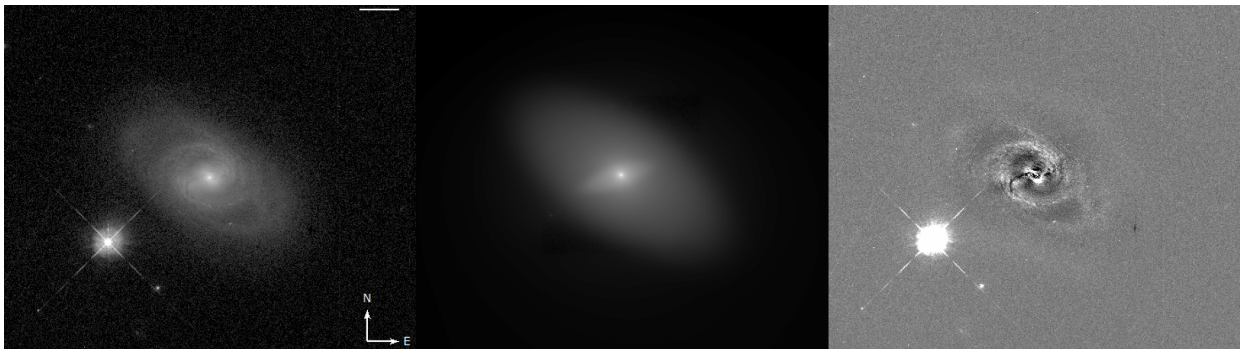

Figure 3.15: Images of MRK 885, with each image showing a $85'' \times 70''$ region. The scale bar is $8''$ long. The left image shows a portion of the original HST image, the middle image shows the `GALFIT` model, and the right image shows the residual.

The original light curves are shown in Figure 3.16. The fraction of starlight is very high for this AGN, therefore a large flux value was subtracted from the light curve. The starlight-subtracted light curves display negative flux values for this AGN.

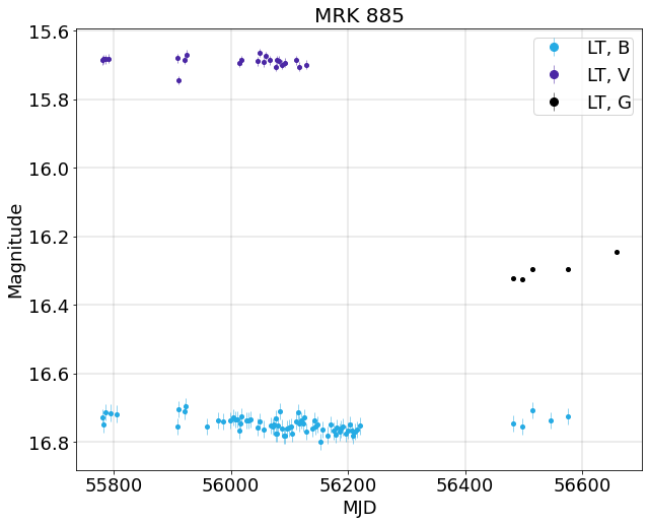

Figure 3.16: MRK 885 light curves: The light curves before subtracting the starlight contribution.

UGC 10697 This object has the faintest point source of the AGN in our sample, compared to the amount of starlight. The bright central bulge is surrounded by asymmetric spiral arm-like features, that are possibly tidal tails. The tidal tails are very extended, and reach out to a radius of $\sim 30''$ (see Figure 3.17). A star in the field was used as the PSF. This model includes the sky background, a PSF, and 3 Sérsic components. One Sérsic component models the more diffuse extended starlight with a Sérsic index of 4.2, while the two other components ($n < .22$) fit the galaxy light at smaller radii.

Table 3.7: MRK 885 Model Parameters

Sky PSF Sérsic	$\frac{d(\text{sky})}{dx}$ (10^{-3} counts) Δx ($''$) Δx ($''$)	$\frac{d(\text{sky})}{dy}$ (10^{-3} counts) Δy ($''$) Δy ($''$)	Sky (Counts) m_{vega} m_{vega}	r_e ($''$)	n	b/a	P.A.
Sky	-0.70	0.51	30.6				
PSF	0	0	19.18				
Sérsic	0.014	0.0	14.75	4.7	4.2	0.97	34.1
Sérsic	3.26	3.05	15.35	16.3	0.2	0.53	-67.2
Sérsic	-0.59	-2.42	16.71	6.1	0.08	0.90	-3.8

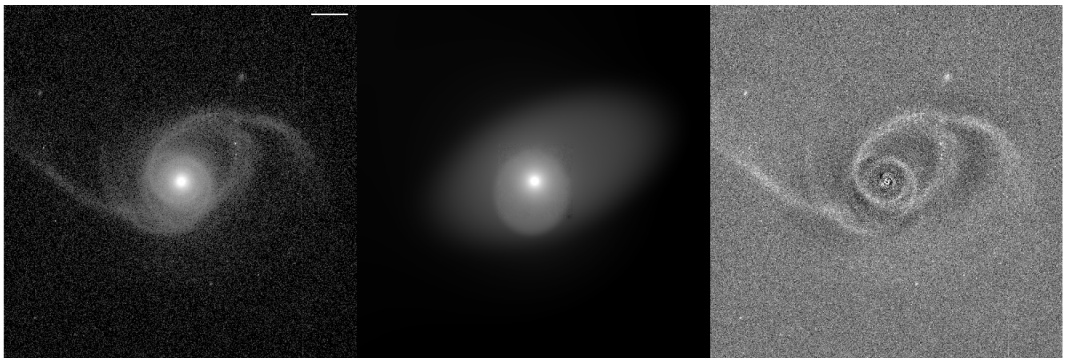

Figure 3.17: Images of UGC 10697, with each image showing a $76'' \times 76''$ region. The scale bar is $8''$ long. The left image shows a portion of the original HST image, the middle image shows the `GALFIT` model, and the right image shows the residual.

The fraction of light originating from the point source within a $2.8''$ aperture is 4.2%, and within $5.1''$ is 2.7%. The fraction of light in the residual image is 0.69% within $2.8''$ and .14% within $5.1''$.

Starlight-subtracted light curves are shown in Figure 3.18. The LT light curves include negative flux values, so only the PTF starlight-subtracted light curve is shown.

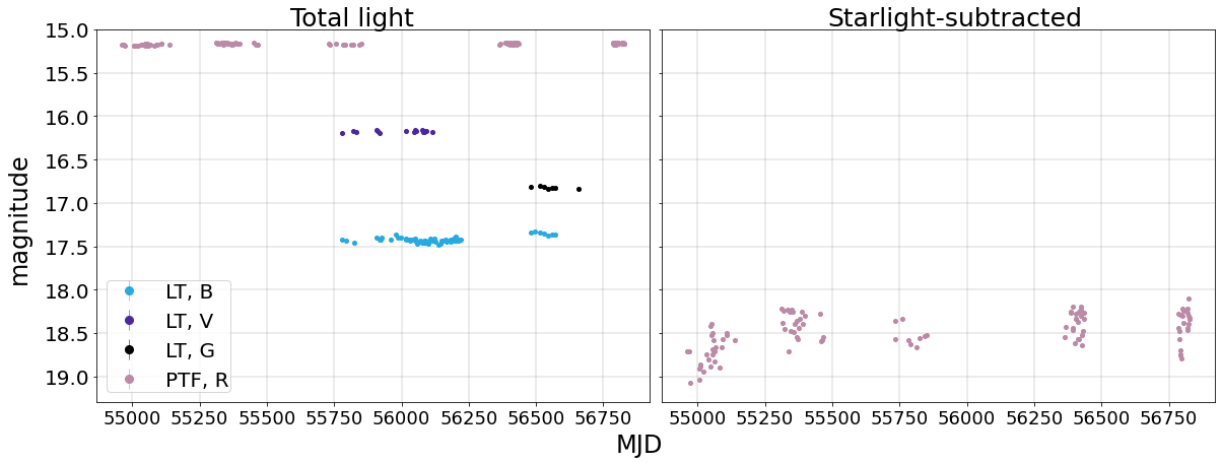

Figure 3.18: UGC 10697 light curves: The left subplot shows the light curves before subtracting the starlight contribution, while the right subplot has been starlight-subtracted.

3.1.3 Negative Fluxes

For four of the AGN (IRAS 17552, MRK 885, NGC 6418, and UGC 10697), negative fluxes are obtained after subtracting the host galaxy contribution, which is not a physically possible result. This issue arises only with the LT light curves, which were formed using the smallest aperture sizes. These four AGN also have point sources that are quite faint compared to the host galaxy, with the PSF fractions ranging from only 4.2-9.7%.

We tried several different techniques to determine where the error could be introduced. For example, we used the HST images to attempt a `GALFIT`-independent way of estimating the fraction of light originating from the point source versus the galaxy light for a few AGN. Beginning with a background-subtracted image, a small aperture radius was chosen (0.25″ or 6.25 pixels) and the average counts/(pixel)^2 was calculated in this region. The counts/(pixel)^2 was also calculated in an annular region just outside of this region (located out to a radius of 9 pixels) . We will assume that this annular region is composed of only galaxy light. The number of counts of galaxy light within the innermost region was then estimated by multiplying the average counts/(pixel)^2 of the annular region by the area of the inner region. Since the total light in this region is composed of

only galaxy light and light from the point source, we can solve for the amount of light from the point source by subtracting the amount of galaxy light from the total light in the inner region.

Since the photometric aperture sizes are larger than $0.25''$, we can crudely estimate the point source fraction by dividing this point source count estimate by the total light within the photometric aperture. This "direct method" of measuring the point source fraction was attempted for NGC 6418, giving a value that only differs by $\sim 7\%$ from the point source fraction calculated with `GALFIT`. This gives us confidence in our `GALFIT` models, as they are giving us similar results to this "direct method" of measuring the point source fraction.

Some potential sources of error include:

1. Color corrections We are using the same color corrections for each AGN. If the stellar population is similar for each galaxy, then this is a valid assumption. However, we do not know what the stellar population is for the other galaxies, as we do not have spectra.

   We have performed a couple tests to check if the color corrections are reasonable. First, for seven of the eight HST images, the light in the science image (background-subtracted) was measured using the same aperture size that was used for the LT photometry. The light within this aperture consists of both starlight and AGN light (within the r band). This was then converted to the B band using the NGC 6418 color corrections, and this value is plotted alongside the pre-starlight subtracted light curves (see Figure 3.19) as a horizontal line.

   If the B-band color corrections are correct, then we would expect this measurement from the HST image to match with the LT B band light curve. For some AGN this does happen (NGC 6418, MRK 507), while for others there is an offset. For MRK 876, the offset is as large as ~ 1.5 magnitudes. This tells us that in some cases, the color correction is accurate (MRK 507), while for others it is not. It should be noted, however, that the HST images were not taken contemporaneously with the light curves. Therefore, it is possible that the large discrepancy could be due to the AGN being in a higher or lower state during the time period of the light curves compared to when the HST images were taken.

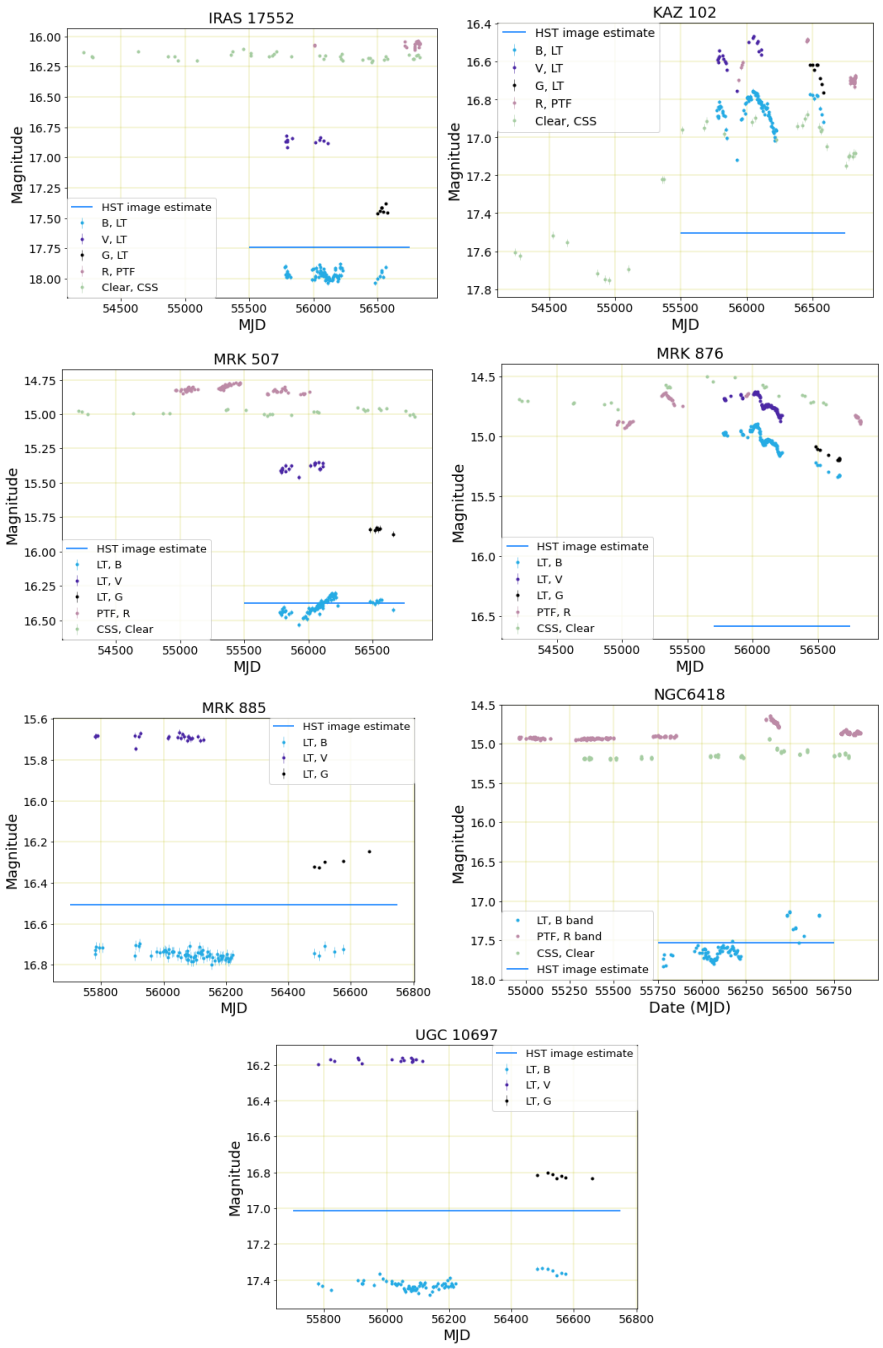

Figure 3.19: Light curves of each AGN, before starlight-subtraction: The horizontal line in each panel shows the measurement of light within the background-subtracted science image (using the same aperture size as the LT photometry), converted to the B band.

2. `GALFIT` uncertainties: This issue of negative fluxes only arises in the AGN that have the smallest point source fractions. The residuals in the `GALFIT` models (a measurement of the uncertainties of the models) are on the same order as the amount of light from the point source in some of these objects, suggesting that the AGN may be too faint to model accurately.

3.1.4 Overall Results

In comparing the starlight-subtracted optical light curves to the original optical light curves for these AGN, larger variability amplitudes are seen in the starlight-subtracted optical light curves, as expected. This is quantified in Table 2.5, where the variability amplitudes for the original optical light curves are compared to the starlight-subtracted optical light curves. It's clear that for the AGN with a smaller fraction of galaxy starlight (KAZ 102, KAZ 163, and MRK 876), the starlight-subtracted light curves look very similar to the original optical light curves.

To summarize, `GALFIT` models were produced for eight of the AGN in our sample, for the purpose of subtracting the starlight contribution from the optical light curves. For four of the AGN (KAZ 102, KAZ 163, MRK 507 and MRK 876) this was completed, with a small "shift" value applied to some of the light curves, in order to match the flux levels of the various data sets. For the other four AGN (IRAS 17552, MRK 885, NGC 6418, and UGC 10697), starlight was only subtracted from the CSS and PTF light curves. The starlight-subtracted LT light curves are negative in their flux values, rendering them unusable.

CHAPTER 4

CROSS-CORRELATION ANALYSIS

4.1 Introduction

Cross-correlation analysis (CCA) can be used to measure the time lag between pairs of light curves, and estimate the uncertainty in the measured lag. The CCA code I used was developed by B. Vazquez (Vazquez, 2015). In this code, 1000 Monte Carlo realizations are computed for each of the input light curves. The method of "Flux Randomization" (FR; Peterson et al. 1998) is used, where every data point in each light curve realization is replaced by a value drawn from a Gaussian distribution. The mean of the distribution is equal to the measured value of that point, and the standard deviation is the uncertainty of the measurement.

For each pair of realized light curves, one of the light curves is shifted in single day time steps within a specified range of potential lags. A linear correlation coefficient is used to evaluate how well correlated the two light curves are for each of the single day increments. This value ranges from -1 (anti-correlated) to 1 (well-correlated) with a value of 0 representing no correlation. The correlation coefficient is shown in the equation below

$$r = \frac{\Sigma_{i=1}^{N}(x_i - \bar{x})(y_i - \bar{y})}{\sqrt{\left(\Sigma_{i=1}^{N}(x_i - \bar{x})^2\right)}\sqrt{\left(\Sigma_{i=1}^{N}(y_i - \bar{y})^2\right)}}, \tag{4.1}$$

where N is the total number of data points in the time series, x_i and y_i are the values of the optical and IR light curves, and $\bar{x}$ and $\bar{y}$ are their respective mean values.

In order to calculate the correlation coefficient, both light curves need to be sampled at the same points along the time axis. For each potential lag value, one of the light curve realizations is linearly interpolated onto the same time stamps as the data points of the other light curve realization. If there is a large gap in one of the light curves, that gap will simply be filled with linearly interpolated points. Since the optical and IR light curves include gaps, the results will generally differ depending on which light curve is interpolated onto the other. Figure 4.1 shows interpolated light curves for KAZ 163, for a few potential lag values within the specified range of lags. In this plot, note that the correlation coeffiecient is only calculated between pairs of points that lie at the same time value. More examples of interpolated light curves are shown when discussing the CCA results of each individual AGN.

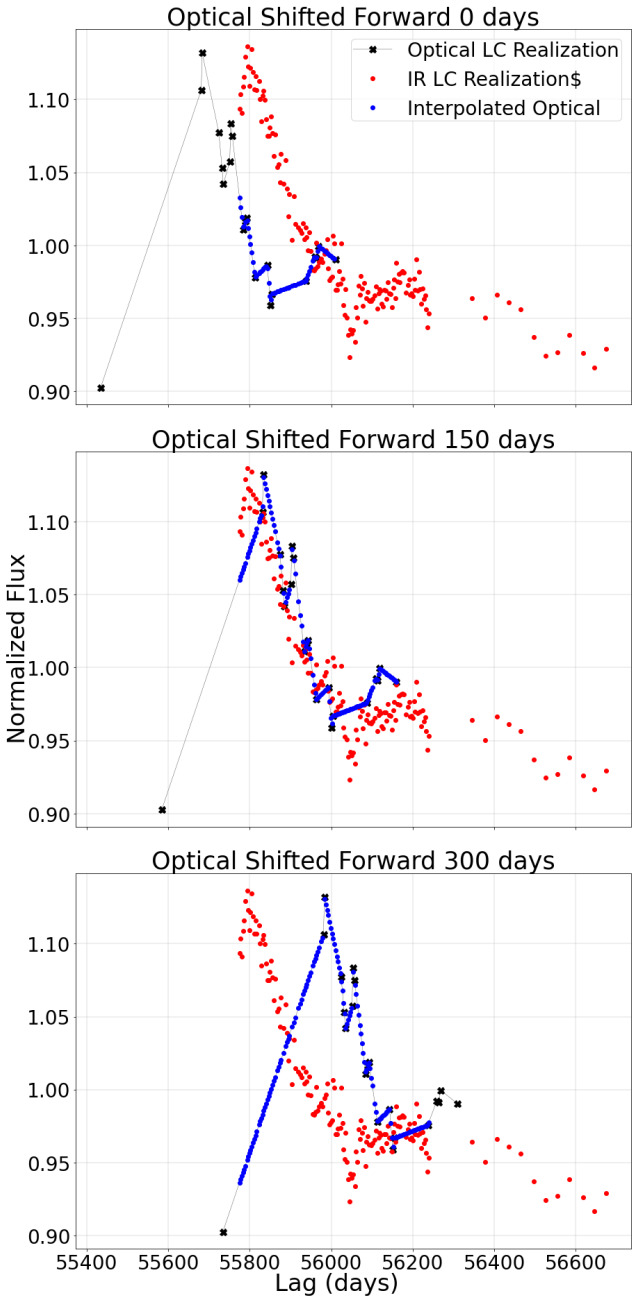

Figure 4.1: Each plot includes one optical light curve realization (the black points), one IR light curve realization (the red points), and the blue points represent the optical data that has been linearly interpolated onto the time stamps of the IR data points. The upper plot includes no shift, the middle plot has the optical light curve shifted forward 150 days, and the lower plot has the optical light curve shifted forward 300 days.

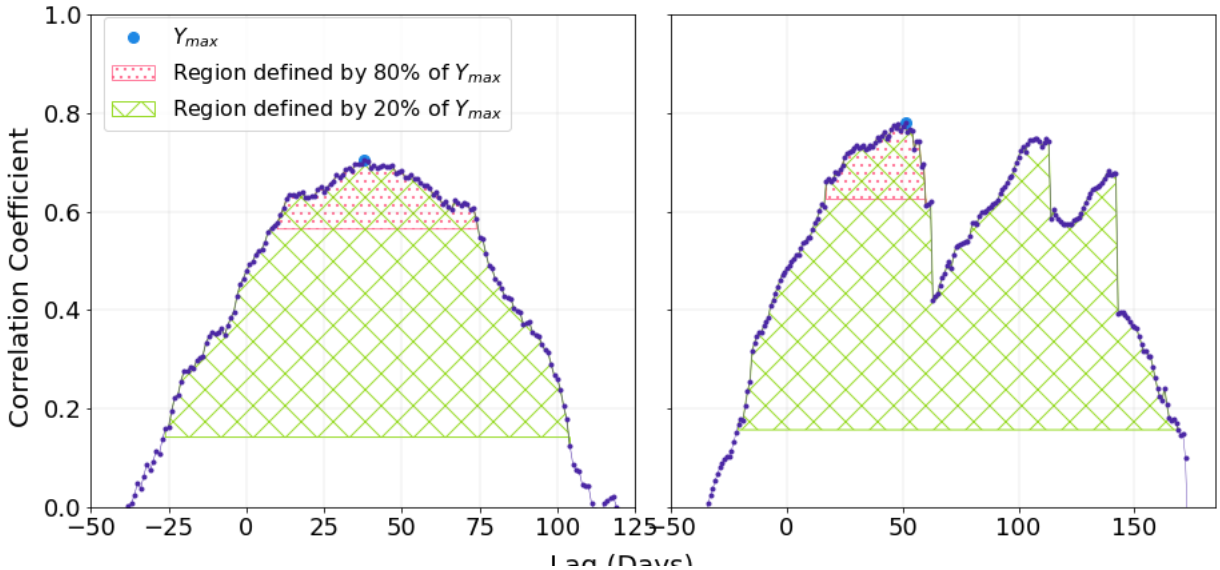

Figure 4.2: Two examples of CCFs: The maximum value of the correlation coefficient is labeled as Y_{max}. Two regions are defined, one of which is the area defined by 80% of Y_{max}, and the other is defined by 20% of Y_{max}.

The Cross-Correlation Function (CCF) is defined as the convolution of the driving and response light curves, and is shown below

$$F_{CCF}(\tau) = \int_{-\infty}^{\infty} F_r(t) F_d(t-\tau) dt,$$

where F_r is the response light curve (IR) and F_d is the driving light curve (optical). The CCF is built up from each calculated value of the correlation coefficient, evaluated at each lag in the given range of lag values. The centroid of the CCF is used to estimate the time delay for each pair of optical and IR light curves, where the calculation of the centroid only considers values that are within 80% of the peak CCF value, as suggested by Peterson (2001). This process is repeated for each Monte Carlo realization and a distribution of the lag values is formed. This is called the "cross-correlation centroid distribution" (CCCD) where the median value of the distribution represents the lag. The interquartile range (IQR) of the CCCD is used as a measure of the uncertainty. The

same percent threshold values were used for both PYCCF and the Vazquez (2015) code.

Although it is recommended to use values that are within 80% of the peak CCF value for the calculation of the centroid, we have also tested the use of other percentages. Figure 4.2 illustrates this for one iteration. The left panel shows a typical CCF, with a regular shape. The maximum correlation coefficient is labeled (Y_{max}) as well as two regions defined by using either 80% of Y_{max}, or 20% of Y_{max}. With a CCF with a symmetric shape like this, either percentage will produce a similar lag. In the right panel, the CCF has an irregular shape. For this CCF, choosing to use 80% of Y_{max} will produce a very different lag value than 20%. The use of different percent threshold values is discussed more when presenting the CCA results of each individual AGN.

We also used two other codes to determine the lag, PYCCF (Sun et al., 2018) and JAVELIN (Zu et al., 2016). PYCCF works very similarly to the Vazquez (2015) code, however PYCCF can also include random subset selection (RSS) (Peterson et al., 1998). When using RSS, for each pair of light curve realizations only a subset of the original data points are used. Approximately 37% of the original number of points are randomly removed. Using RSS allows us to test whether the lag result strongly depends on only a small number of the data points, and gives a more conservative estimate of the uncertainty.

While the Vazquez (2015) code will linearly interpolate one of the individual light curve realizations onto the same time stamps as the other light curve realization, PYCCF includes the option of interpolating both light curves. To do this, one CCF is formed by interpolating the optical light curve onto the IR timestamps, and then another CCF is formed by interpolating the IR light curve onto the optical timestamps. The final CCF is formed by calculating the average correlation coefficient values from each of the two CCFs, for each lag value.

JAVELIN works very differently from PYCCF and the Vazquez (2015) code. Here, the input optical light curve is modeled as a damped random walk. The parameters used to describe the damped random walk are the amplitude (σ) and the damping timescale (τ), which are determined using MCMC chains. Likelihood distributions of these parameters are formed.

To determine the lag, different optical light curves are formed from the likelihood distributions

of these parameters. It is assumed that the IR light curve is simply a scaled, smoothed, and shifted version of the optical light curve. Therefore, each version of the optical light curve is smoothed, scaled, and shifted to match the response light curve.

JAVELIN assumes a top hat transfer function, which may or may not provide a good match to the actual transfer function. The response light curve is described by the lag (t), the width of the top hat smoothing function (w), and the scaling factor (s). Likelihood distributions are produced for each of these parameters. To determine the lag, the distribution of lag values is used, where the median value is considered to be the lag and the IQR is the uncertainty.

4.2 Individual AGN

CCA can be applied to the AGN in our sample that show clear features in the optical light curve, with a corresponding IR response, that is, those objects whose variability is classified as "Comparable optical and IR variability" or "Strong optical variability with a strong IR response" in Table 2.2. Here, I show CCA results between the optical-3.6 μm, optical-4.5 μm, and 3.6 μm-4.5 μm light curves for KAZ 163, MRK 507 and UGC 10697, with NGC 6418 discussed separately in Chapter 5.

4.2.1 KAZ 163

KAZ 163 is a NL Sy1 with an estimated bolometric luminosity of 3.78×10^{45}erg/s, as discussed in Section 2. Before subtracting the starlight contribution, CCA was performed with the LT B band, PTF, and CSS light curves individually, cross-correlated with the IR. Then, the combined starlight subtracted optical light curve (consisting of the LT B band, PTF, and CSS light curves) was cross-correlated with the IR. Finally, the two IR channels were cross-correlated with each other.

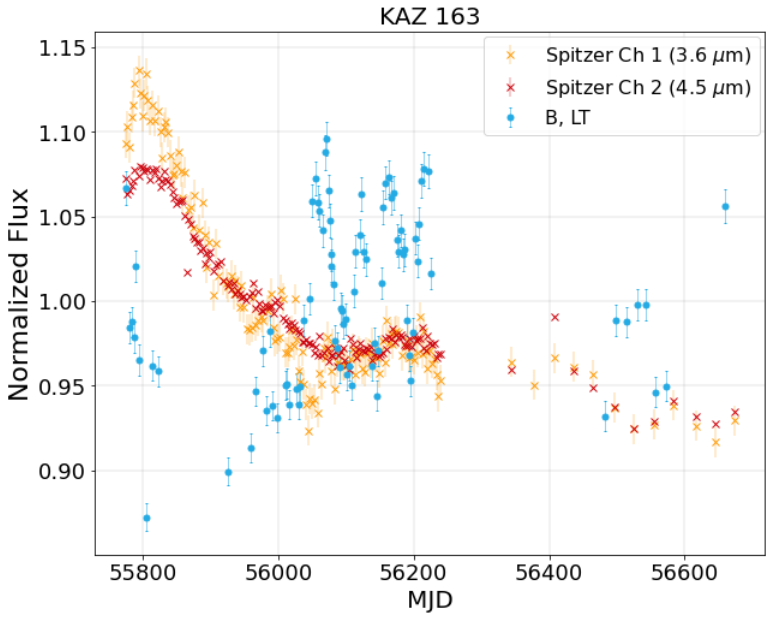

Figure 4.3: KAZ 163 Light Curves: The orange and red points represent the IR Spitzer data, while the blue points represent the B band optical data from LT.

KAZ 163: Before Host Galaxy-Subtraction: LT B band-IR Analysis Figure 4.3 shows the B band and IR light curves for KAZ 163. The LT B band light curve covers the same time period as the Spitzer campaign. Although the B band light curve does not capture the rise in flux that the IR light curves are evidently responding to at the beginning of the campaign, CCA was still attempted for these pairs of light curves.

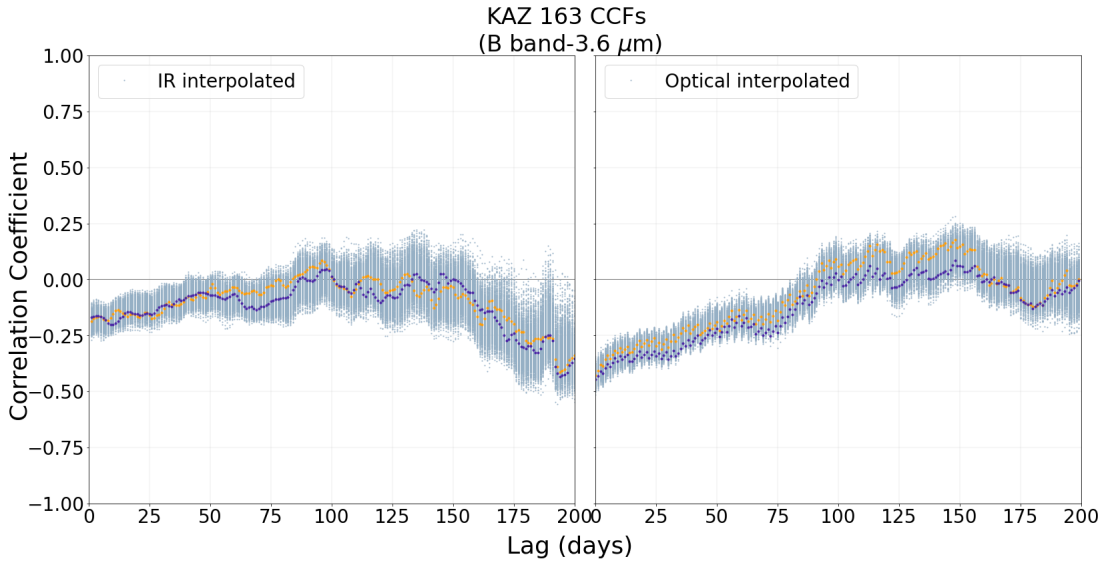

Figure 4.4: KAZ 163 CCFs for the LT B band-3.6μm analysis: Each plot includes 1000 CCFs formed from the Monte Carlo iterations, shown in light blue. The left plot shows the CCFs for IR interpolation, while the plot on the right shows the CCFs for optical interpolation. As examples, the purple and orange points highlight two individual CCFs.

A few example CCFs are shown in Figures 4.4 and 4.5, for the B band-3.6 μm and B band-4.5 μm analysis, respectively. The figures show the results from interpolating the IR light curve onto the time stamps of the optical light curve (this will be referred to as "IR interpolation"), as well as interpolating the optical onto the IR time stamps (this will be referred to as "optical interpolation"). It's clear that little correlation is found within these pairs of light curves, regardless of the interpolation type. For each CCF, most of the maximum correlation coefficient values fall below a value of 0.25. In fact, many of the CCFs have negative correlation coefficient values. This is evident for both the B band-3.6 μm and B band-4.5 μm analysis.

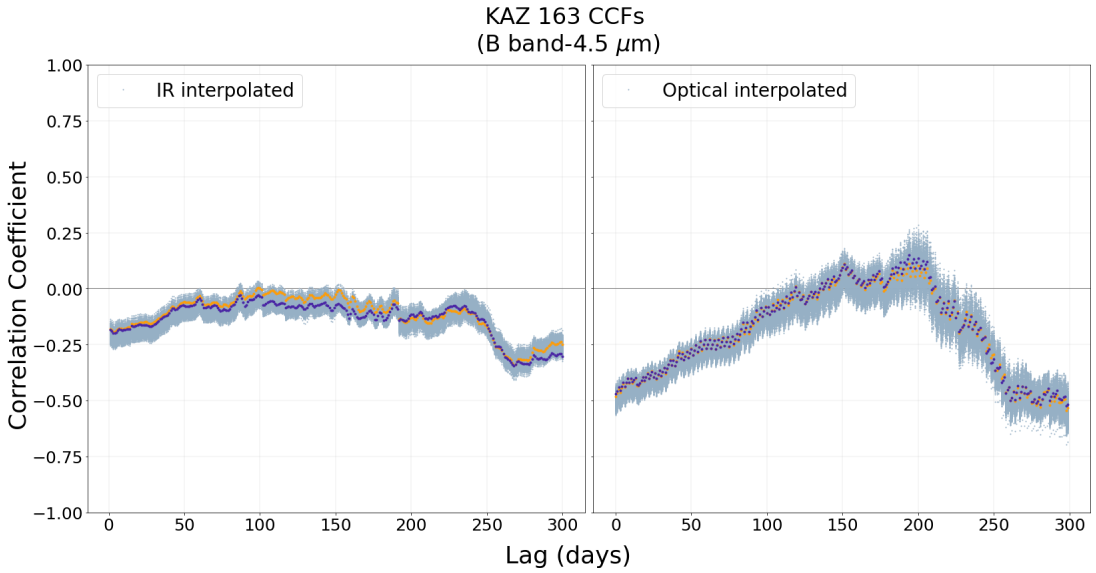

Figure 4.5: KAZ 163 CCFs for the LT B band-4.5μm analysis: Each plot includes 1000 CCFs formed from the Monte Carlo iterations, shown in light blue. The left plot shows the CCFs for IR interpolation, while the plot on the right shows the CCFs for optical interpolation. As examples, the purple and orange points highlight two individual CCFs.

The poor correlation between the B band-IR light curves is likely due to the B band light curve not including the main feature that the IR is responding to, which is a large increase of flux in the optical, which occurred just prior to the beginning of the Spitzer campaign and is seen in the PTF and CSS light curves. The B band light curve includes high frequency fluctuations between MJD 56035 to 56230, but corresponding features are not observed in the IR. The CCA for these two light curve pairs will not be explored further, as there is clearly little correlation between them.

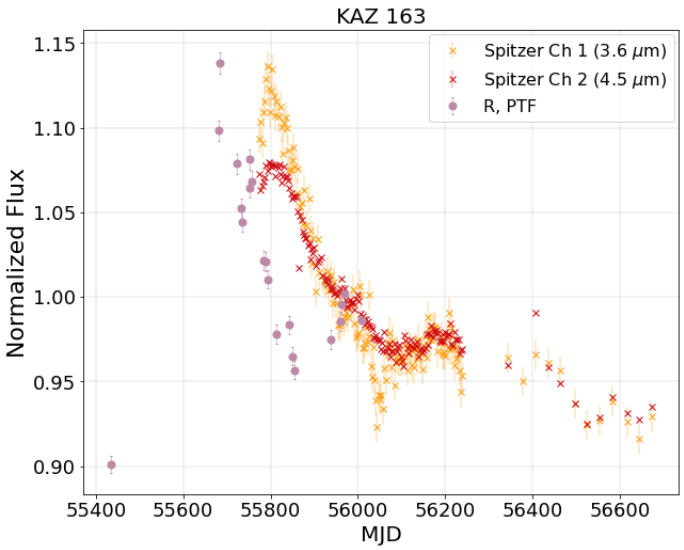

Figure 4.6: KAZ 163 light curves: The orange and red points represent the IR Spitzer data, while the pink points represent the R band optical data from PTF.

KAZ 163: Before Host Galaxy-Subtraction: PTF R band-IR Analysis Figure 4.6 shows the PTF and IR light curves used in the cross-correlation analysis. While there are fewer data points in the PTF data compared to the LT B band data, this light curve does contain the main features that the IR is responding to, which is the rise in flux during the gap from MJD 55430 to 55680, the decline in flux from MJD 55680 to 55854, and the small rise in flux from MJD 55854 to 55969. Unfortunately, there are only two PTF data points before the large peak in flux, one of which occurs only 2 days before the peak flux value, and the other occurs 250 days before the peak. Therefore, it is not clear at what point the optical begins to rise.

Figure 4.7 shows examples of the different interpolation types. I tried three different types of interpolation for the pairs of light curves:

- **IR interpolation:**

  Since there are no large gaps in the IR data, one would expect this to provide the most accurate interpolation. However, since there are fewer optical data points, there are fewer data points being used in the CCA (See the left subplot of Figure 4.7).

- **Optical interpolation:**

  There are a few large gaps in the optical data. The code will linearly interpolate within these regions. (See the middle subplot of Figure 4.7).

- **Optical interpolation, with the first optical point removed:** There is a large gap in the optical data between the first and second points. To test how sensitive the result is to this gap, I tried removing the first point in the PTF light curve (See the right subplot of Figure 4.7).

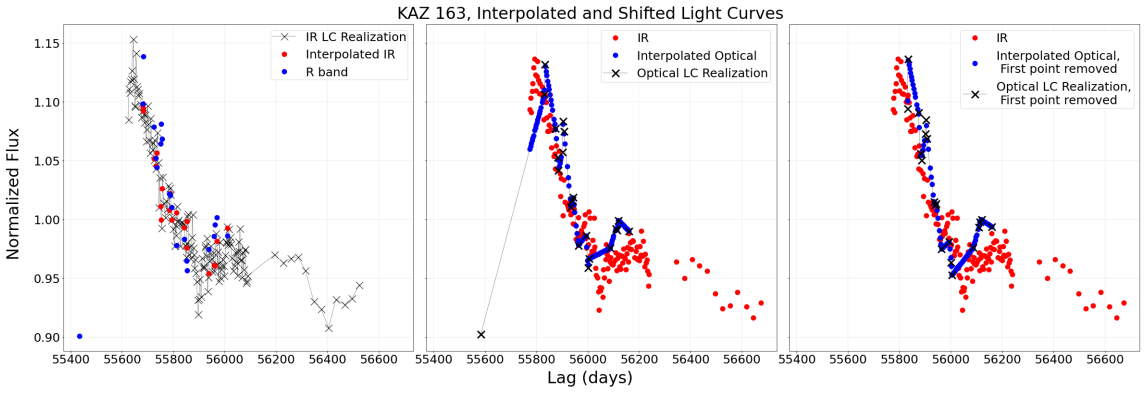

Figure 4.7: Examples of interpolated R band and 3.6 μm light curves for KAZ 163 :
IR interpolation: The plot on the left shows one IR light curve realization (the black points), the blue points represent the optical light curve, and the red points represent the IR points linearly interpolated onto the time stamps of the optical data points. Here, the IR light curve has been shifted back by 150 days.
Optical interpolation: The plot in the middle is similar, showing one of the optical light curve realizations in black, the red points represent the IR light curve, and the blue points represent the optical points linearly interpolated onto the time stamps of the IR data points. Here, the optical light curve has been shifted forward by 150 days.
Optical interpolation: The plot on the right shows the same light curves as the middle plot, however the first PTF data point was removed for this analysis.

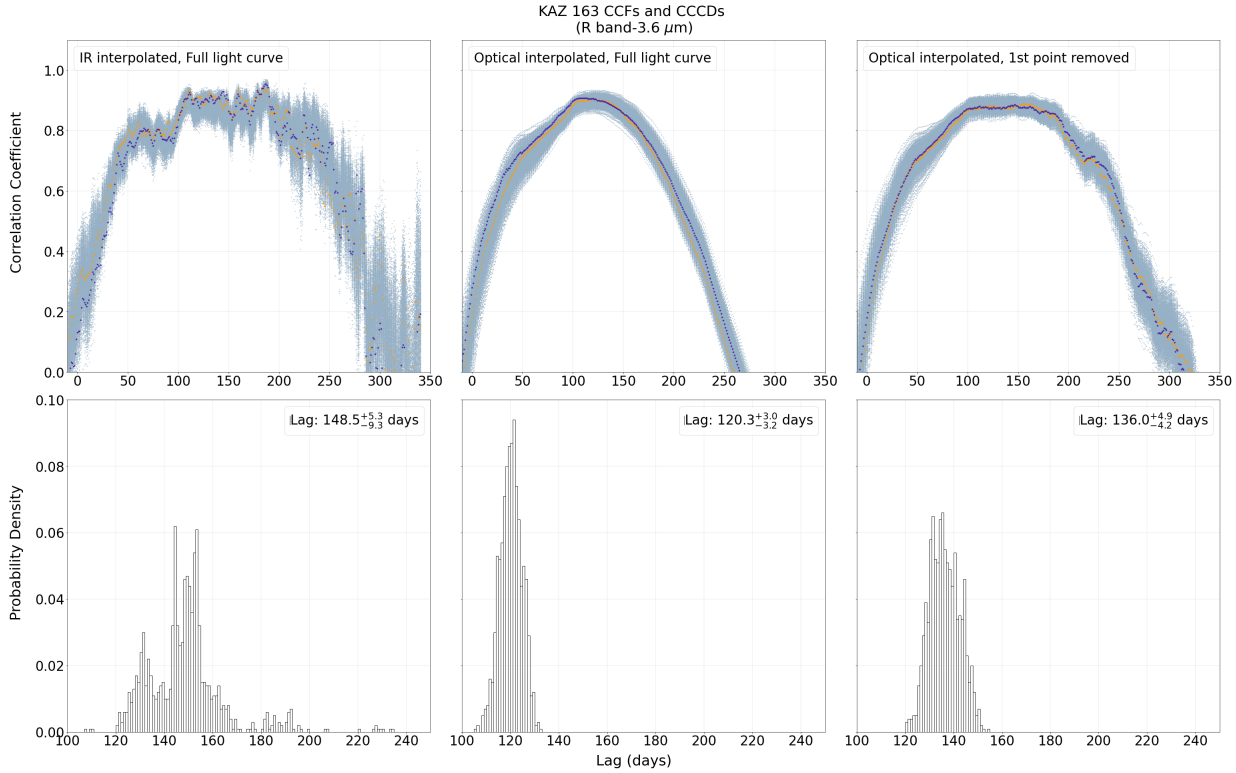

Figure 4.8: KAZ 163 CCFs and CCCDs for the PTF R band-3.6μm analysis:
The subplots on the left show the CCFs for IR interpolation. The subplots in the middle show the CCFs for optical interpolation. The subplots on the right show the CCFs for optical interpolation, with the first optical point removed. Each CCF plot includes 1000 CCFs formed from the Monte Carlo iterations, shown in light blue. As examples, the purple and orange points highlight two individual CCFs.

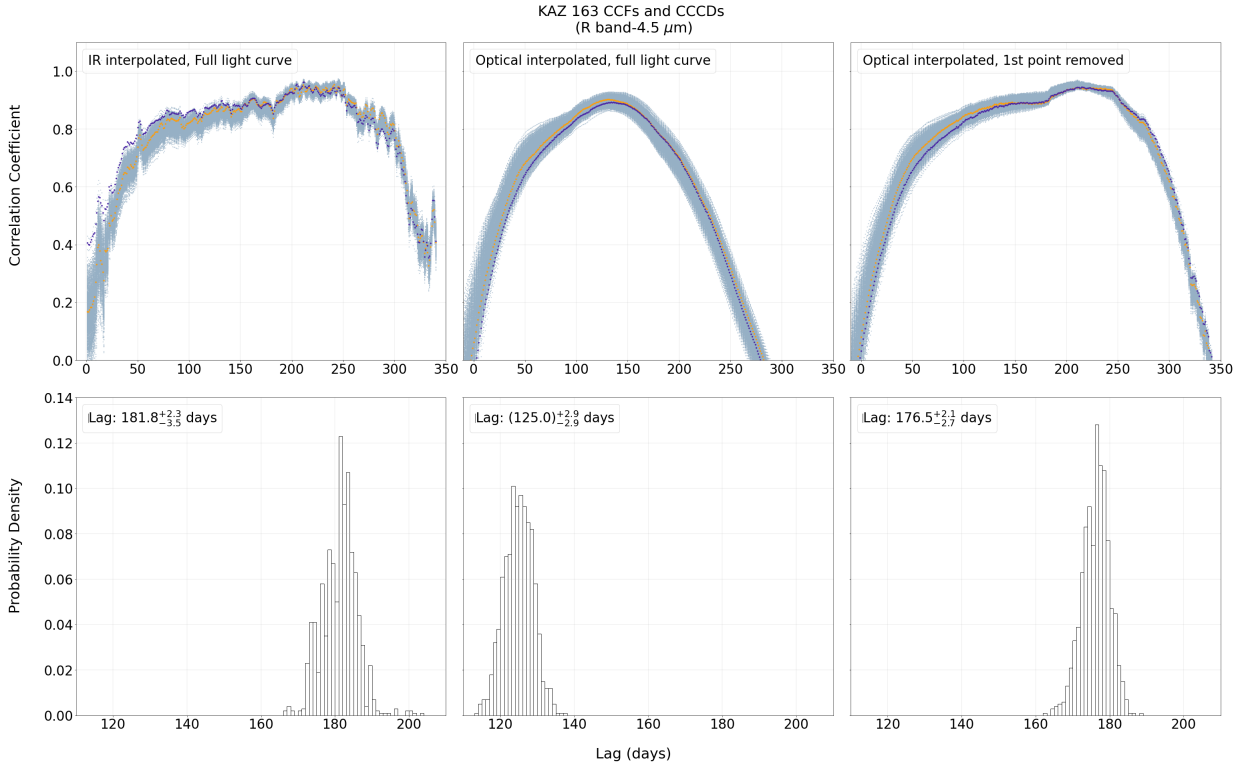

Figure 4.9: KAZ 163 CCFs and CCCDs for the PTF R band-4.5μm analysis:
The subplots on the left show the results using IR interpolation. The subplots in the middle show the CCFs for optical interpolation. The subplots on the right show the CCFs for optical interpolation, with the first optical point removed. Each CCF plot includes 1000 CCFs formed from the Monte Carlo iterations, shown in light blue. As examples, the purple and orange points highlight two individual CCFs.

The CCF and CCCD results formed using different interpolation types are shown in Figures 4.8 and 4.9. The lag calculated using IR interpolation is $148.5^{+5.3}_{-9.3}$ days for the 3.6μm-optical analysis and $181.8^{+2.3}_{-3.5}$ days for the 4.5μm-optical analysis. This interpolation produces CCFs that are very broad and noisy. It is clear why this occurs when looking at Figure 4.7. There are fewer data points in the optical light curve, so fewer points are being used for the CCA. Also, for most of the lag values being tested, the first PTF data point is not used (except when shifted to larger lag values), therefore the peak in flux, which is the main feature of both light curves, is not included in the analysis.

Optical interpolation with the first PTF point removed gives a lag value of $136.0^{+4.9}_{-4.2}$ days for the 3.6μm-optical analysis, and $176.5^{+2.1}_{-2.7}$ days for 4.5μm-optical analysis. The CCFs and CCCDs are shown in the far right subplots. These CCFs have a similar shape as the IR interpolated CCFs (subplots on the left), as they have a broad and flat shape. The CCFs formed using optical interpolation are less noisy, and the lag result is 12.5 days shorter for the optical-3.6μm analysis, and 5.3 days shorter for the optical-4.5μm analysis. The two sets of results are consistent, within the errors.

It is clear why the IR interpolated CCFs have a similar shape to those formed using optical interpolation with the first PTF point removed. Figure 4.7 (see the far-left and far-right subplots) shows that the main feature in the light curves for these two interpolation directions is the dip in flux in the IR at ∼MJD 56050. Therefore, the overall shapes of the CCFs are similar. However, the interpolated optical light curve does include one data point just 2 days before the peak flux value, which helps define this feature. Therefore, the CCFs are less broad when using optical interpolation with the first point removed.

The CCFs shown in the middle subplots (optical interpolation) have the most well defined peaks, and also have the shortest calculated lag. The 3.6μm-optical lag is $120.3^{+3.0}_{-3.2}$ days, and the 4.5μm-optical lag is $125.0^{+2.9}_{-2.9}$ days. Looking at Figure 4.7, it seems that this is due to both light curves including the main light curve features, the peak (seen in the IR at ∼MJD 55800) and the dip (seen in the IR at ∼MJD 56050) in flux. Since the main increase in optical flux is defined mainly by linearly interpolated optical points, it is possible that the lag is not quite as well-defined as this result suggests, and instead the estimated errors should be larger. To get a more conservative estimate of the lag errors, we can compare the results obtained using the full light curve and optical interpolation with the results from removing the first point. In this case, the calculated lag ranges from 120.3 to 136.0 days for the 3.6μm-optical CCA, and 125.0 to 176.5 days for the 4.5μm-optical CCA.

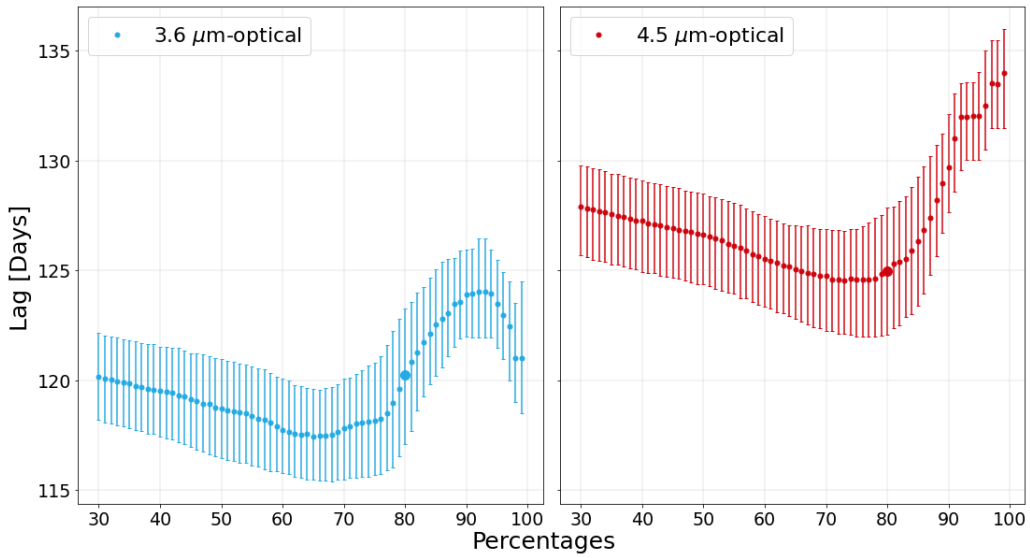

Figure 4.10: KAZ 163: Dependence of measured lags on CCF percentage threshold value. The left plot shows results for 3.6μm-optical, and the right plot is 4.5μm-optical. The two larger points indicate the 80% threshold values.

The lags reported above were calculated from the CCF centroids, evaluated using the standard threshold value of 80% of the CCF peak. However, to investigate how sensitive the lags are to the threshold value, the CCA was repeated while varying the percent threshold value. Figure 4.10 shows the lag results calculated using different percentage threshold values for each IR channel cross-correlated with the optical. These lags were calculated using the full optical light curve with optical interpolation. The most stable region for the 3.6 μm-optical analysis falls between the ∼50-77% threshold values, where the mean lag is 118.0 days. Since our measured lag value is only 2.3 days larger, using an 80% threshold value seems reasonable. The most stable region for the 4.5 μm-optical analysis falls between the ∼70-80% threshold values, where the average lag value is 124.6 days, only half a day shorter than our measured lag. Using 80% is an appropriate threshold value.

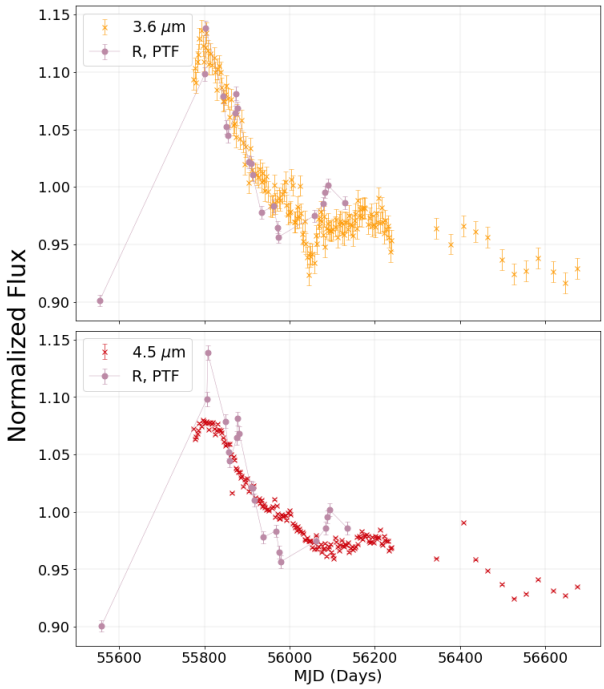

Figure 4.11: KAZ 163 PTF and IR light curves: The optical light curves are shifted forward by 120.3 days for the optical-3.6 μm analysis (top panel) and 125.0 days for the optical-4.5 μm analysis (bottom panel).

Figure 4.11 shows the optical LCs shifted forward by the measured lag values obtained from the full optical and IR light curves with optical interpolation. Although the optical light curve has sharper features than the IR light curves, the main IR and optical features appear to match well generally for both IR channels. The 3.6μm light curve matches the optical light curve quite well, while the 4.5μm light curve is much more smoothed out.

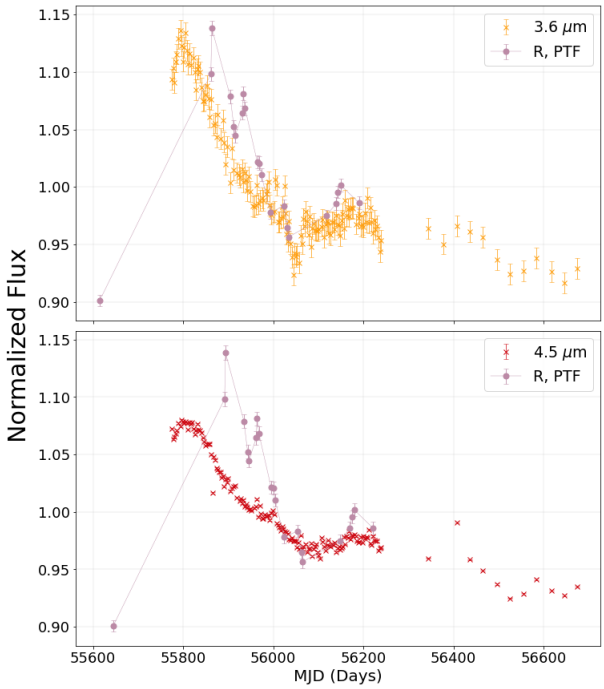

Figure 4.12: KAZ 163 PTF and IR light curves, shifted by JAVELIN lag values: The optical light curves are shifted forward by 180.5 days for the optical-3.6 μm analysis (top panel) and 211.1 days for the optical-4.5 μm analysis (bottom panel).

For the 3.6μm-optical analysis, the lags obtained with JAVELIN range from 125-180 days, depending on the input lag range. Using a maximum lag range of 200 days results in a measured lag of $180.5^{+4.6}_{-5.8}$ days which is 60 days larger than the lag measured using the Vazquez (2015) code. Although, there are several smaller peaks in the CCCD, one of which is at $\sim$ 125 days, consistent with the results obtained from the Vazquez (2015) code. For the 4.5μm-optical analysis, JAVELIN finds a lag of $211.1^{+0.2}_{-0.2}$ days, 86 days larger than the lag measured using the Vazquez (2015) code. Figure 4.12 shows the optical light curves shifted forward by the lag values calculated using JAVELIN. These lag values are clearly much larger than those measured using the Vazquez (2015) code. JAVELIN appears to be measuring the lag corresponding to the dip in flux, located at $\sim$MJD 56050 in the IR.

To compare the lag values calculated from using the different versions of the light curves,

different types of interpolation and different codes, see Figures 4.13 and 4.14. As expected, the Vazquez (2015) code and PYCCF (FR only) give very similar lags. Including both FR and RSS with PYCCF gives a similar result as using FR only, however the error bars are larger, as expected. Excluding the first PTF point clearly leads to larger lag values, likely due to the peak of the optical light curve being less well-defined.

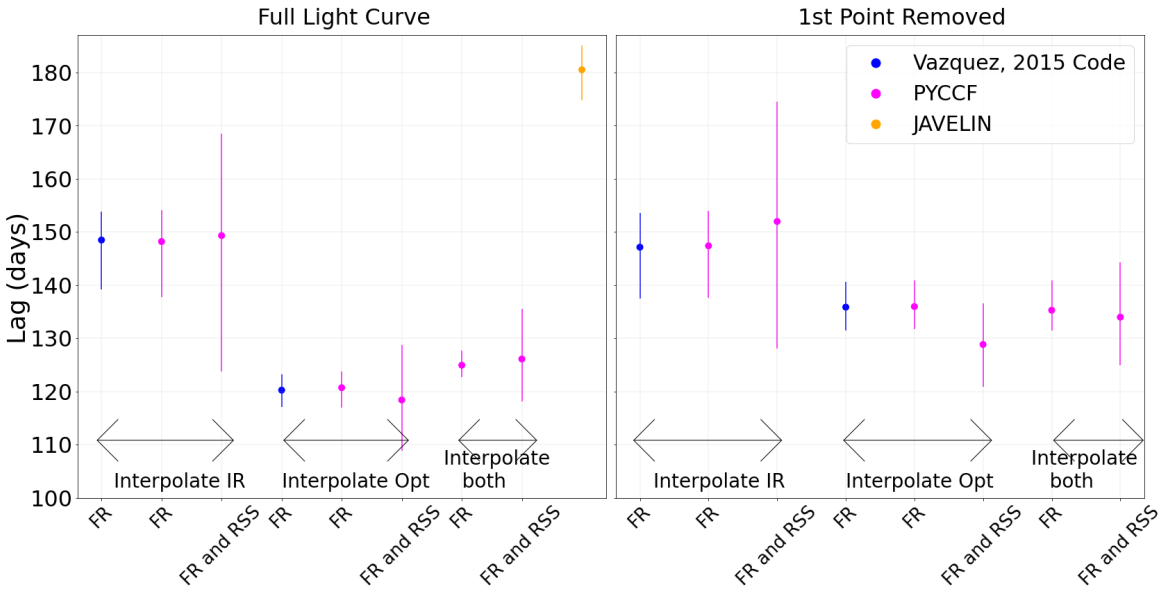

Figure 4.13: KAZ 163 lag comparisons for the 3.6μm-optical analysis: The plot on the left shows the lags obtained using the full PTF light curve, while the right plot shows the lags for the PTF light curve with the first optical data point removed. The blue data points represent lag values calculated using the Vazquez (2015) code, the orange point represents the lag calculated using JAVELIN, while the PYCCF results are shown in pink. The labels on the x-axis indicate whether flux randomization (FR) or both flux randomization and random subset selection (FR and RSS) was used. The labels above the x-axis specify whether the corresponding lags were calculated using IR interpolation, optical interpolation, or interpolating both.

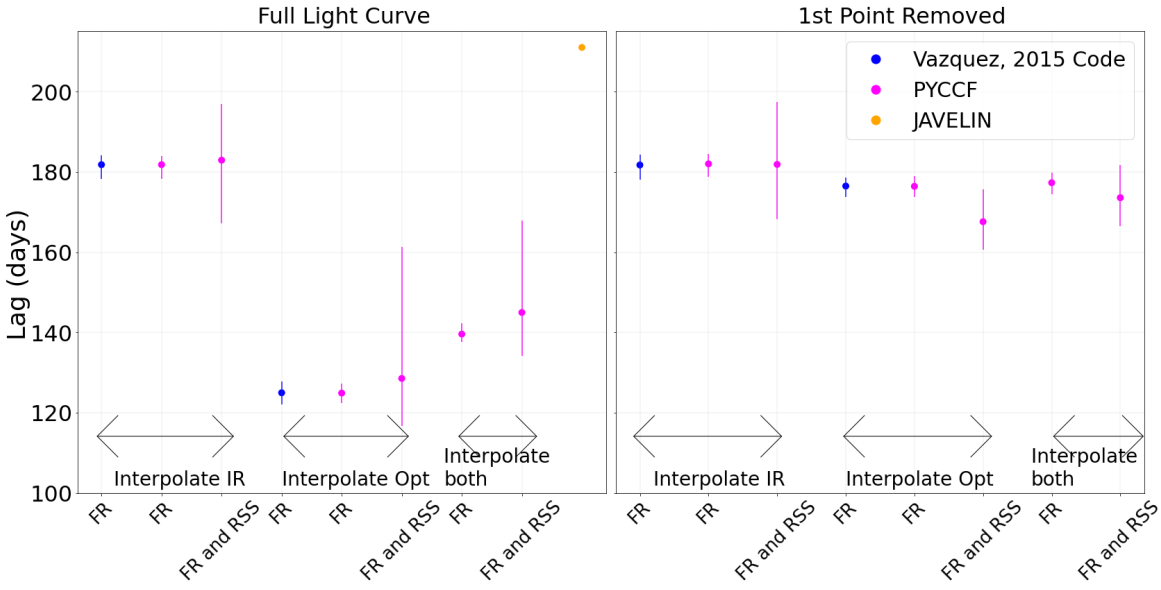

Figure 4.14: KAZ 163 lag comparisons for the 4.5μm-optical analysis: The plot on the left shows the lags obtained using the full PTF light curve, while the right plot shows the lags for the PTF light curve with the first optical data point removed. The blue data points represent lag values calculated using the Vazquez (2015) code, the orange point represents the lag calculated using JAVELIN, while the PYCCF results are shown in pink. The labels on the x-axis indicate whether flux randomization (FR) or both flux randomization and random subset selection (FR and RSS) was used. The labels above the x-axis specify whether the corresponding lags were calculated using IR interpolation, optical interpolation, or interpolating both.

KAZ 163 Before Host Galaxy-Subtraction: CSS-IR Analysis Figure 4.15 shows the optical CSS light curve (clear filter). Figures 4.16 and 4.17 show the CCFs for the optical-3.6μm and the optical-4.5μm analysis. The optical data is sparsely sampled, so the CCFs formed using IR interpolation are very noisy with little correlation for both IR light curves. Using optical interpolation gives much smoother CCFs, although the CCFs do not have well-defined peaks which leads to uncertain lag values. Therefore, the CSS-IR analysis will not be explored further.

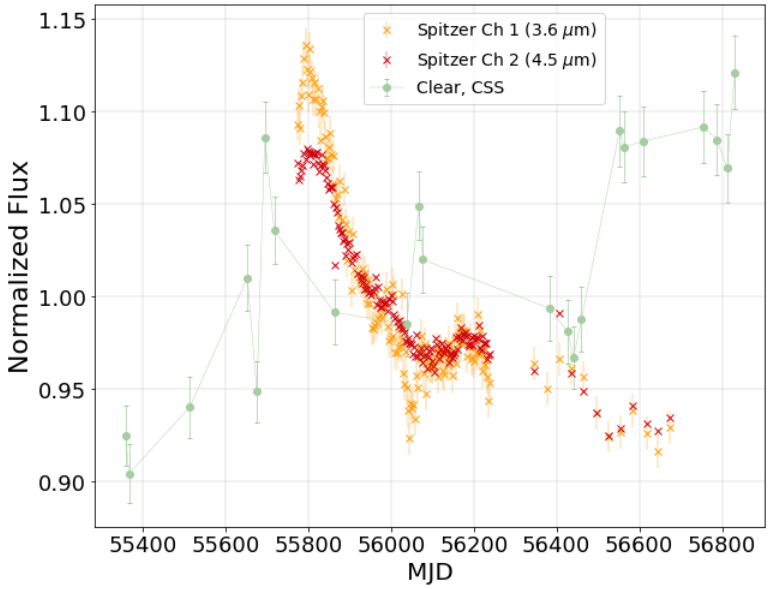

Figure 4.15: KAZ 163 CSS and IR light curves: The orange and red points represent the IR Spitzer data, while the green points represent the CSS clear filter data points.

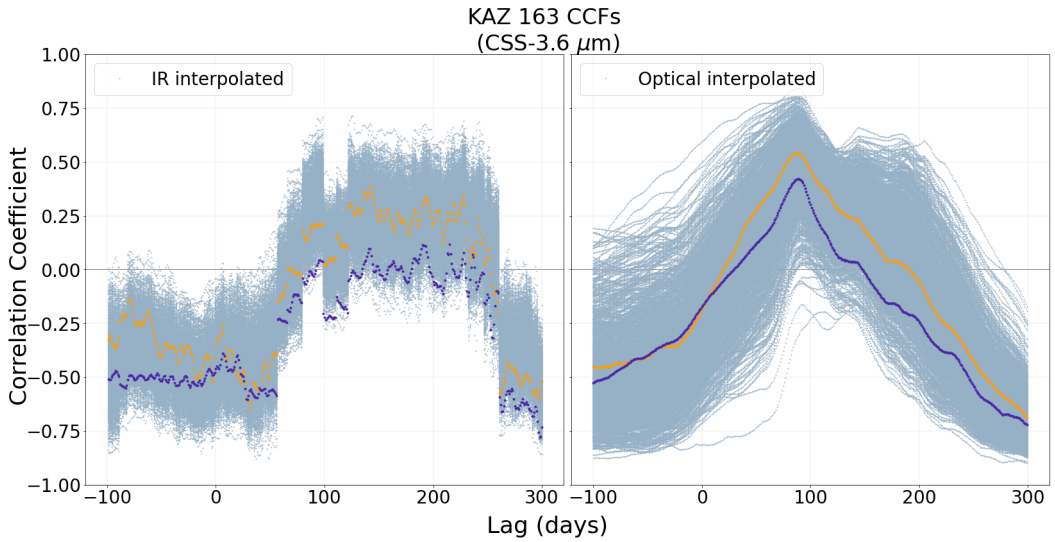

Figure 4.16: KAZ 163 CCFs for the CSS-3.6μm analysis: The subplot on the left shows the CCFs for IR interpolation. The subplot on the right shows the CCFs for optical interpolation. Each plot includes 1000 CCFs formed from the Monte Carlo iterations, shown in light blue. As examples, the purple and orange points highlight two individual CCFs.

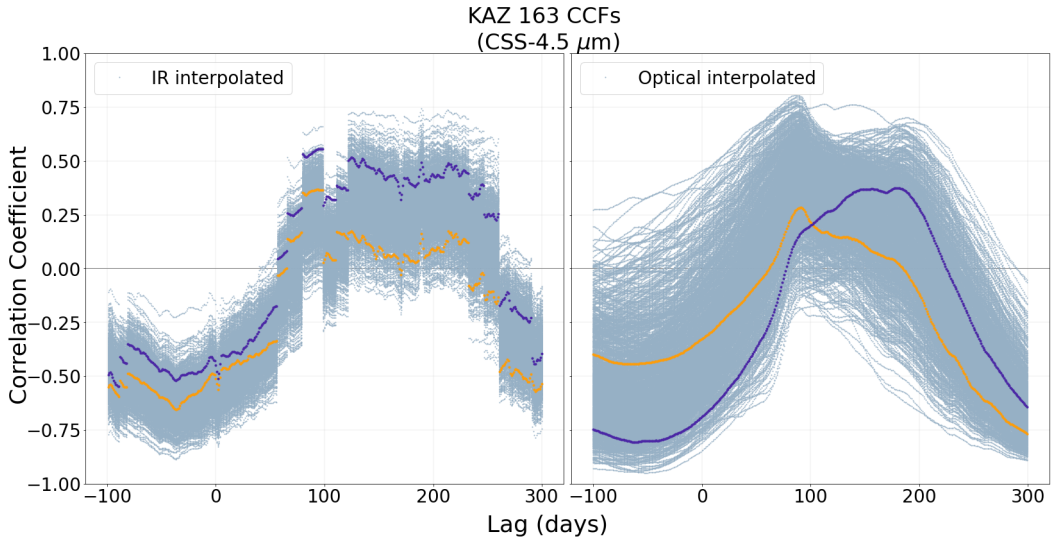

Figure 4.17: KAZ 163 CCFs for the CSS-4.5μm analysis: The subplot on the left shows the CCFs for IR interpolation. The subplot on the right shows the CCFs for optical interpolation. Each plot includes 1000 CCFs formed from the Monte Carlo iterations, shown in light blue. As examples, the purple and orange points highlight two individual CCFs.

After Host Galaxy-Subtraction: After subtracting the starlight contribution from each optical light curve, they can be combined and cross-correlated with the IR light curves. The combined optical light curve consisting of the data from LT (B band), PTF (R band), and CSS (clear filter) is shown in Figure 4.18. Examples of the interpolated light curves are shown in Figure 4.19.

Figures 4.20 and 4.21 show the CCFs and CCCDs for the combined optical light curve cross-correlated with each IR light curve. Using IR interpolation leads to CCFs that are very broad and flat. The correlation coefficient values are also low, with typical maximum correlation coefficients with values less than 0.5. This is likely due to the same reasons discussed in the PTF-IR section: there are fewer data points overall with this interpolation type, and only a few data points defining the optical rise in flux.

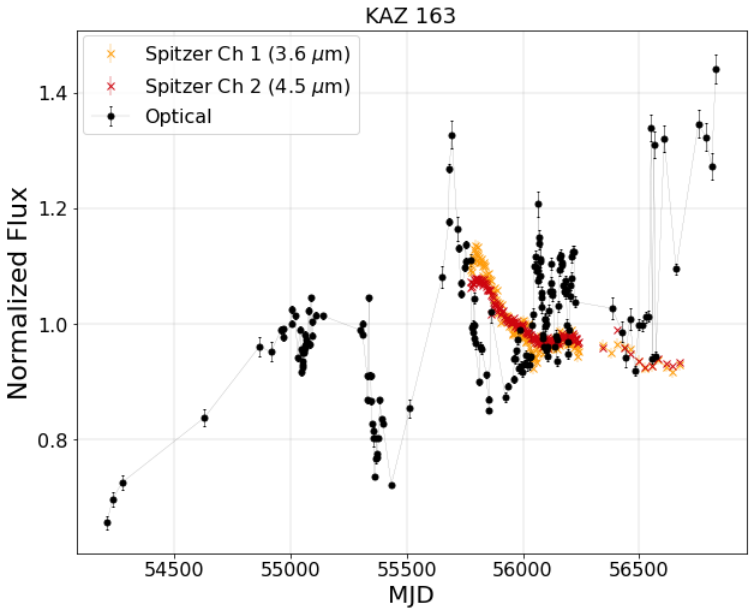

Figure 4.18: KAZ 163 IR and starlight-subtracted optical light curves: The starlight-subtracted optical light curve, which is a combination of LT, PTF, and CSS data is shown in black. The orange and red points represent the IR Spitzer data.

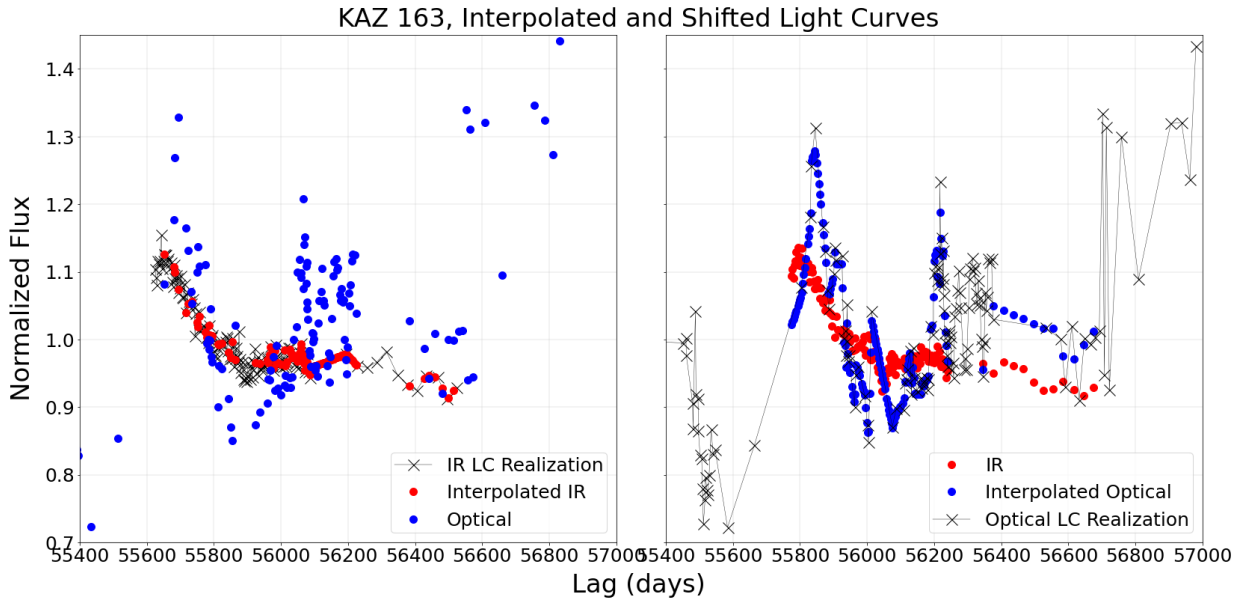

Figure 4.19: Examples of the interpolated combined optical and and 3.6 μm light curves for KAZ 163: The plot on the left includes one IR light curve realization (the black points), the optical light curve is shown as blue points, and the red points represent the IR points linearly interpolated onto the time stamps of the optical data points. Here, the IR light curves have been shifted back by 150 days.
The plot on the right is similar, including one of the optical light curve realizations in black, the IR light curve is shown in red, and the blue points represent the optical points linearly interpolated onto the timestamps of the IR data points. Here, the optical light curve has been shifted forward by 150 days

Optical interpolation leads to smoother CCFs with a higher and clear peak. The interpolated light curves shown in the right subplot of Figure 4.19 show that there is a more defined optical peak, although there are several large regions of linearly interpolated optical points. Using optical interpolation appears to be the best method of determining the lag for these light curves.

Using optical interpolation, the measured lag is $121.3^{+1.7}_{-1.8}$ days for the 3.6μm-optical analysis, and $133.3^{+2.9}_{-2.0}$ days for the 4.5μm-optical analysis. These lag values are similar to those measured from the PTF-IR CCA, before subtracting the starlight contribution. The lag measured for the 3.6μm IR channel is 1.0 day longer, and for the 4.5μm IR channel is 8.3 days longer than the results obtained before subtracting the starlight. It is not surprising that the results should be

similar, since the PTF light curve contains the main features that are present in the combined starlight-subtracted light curve.

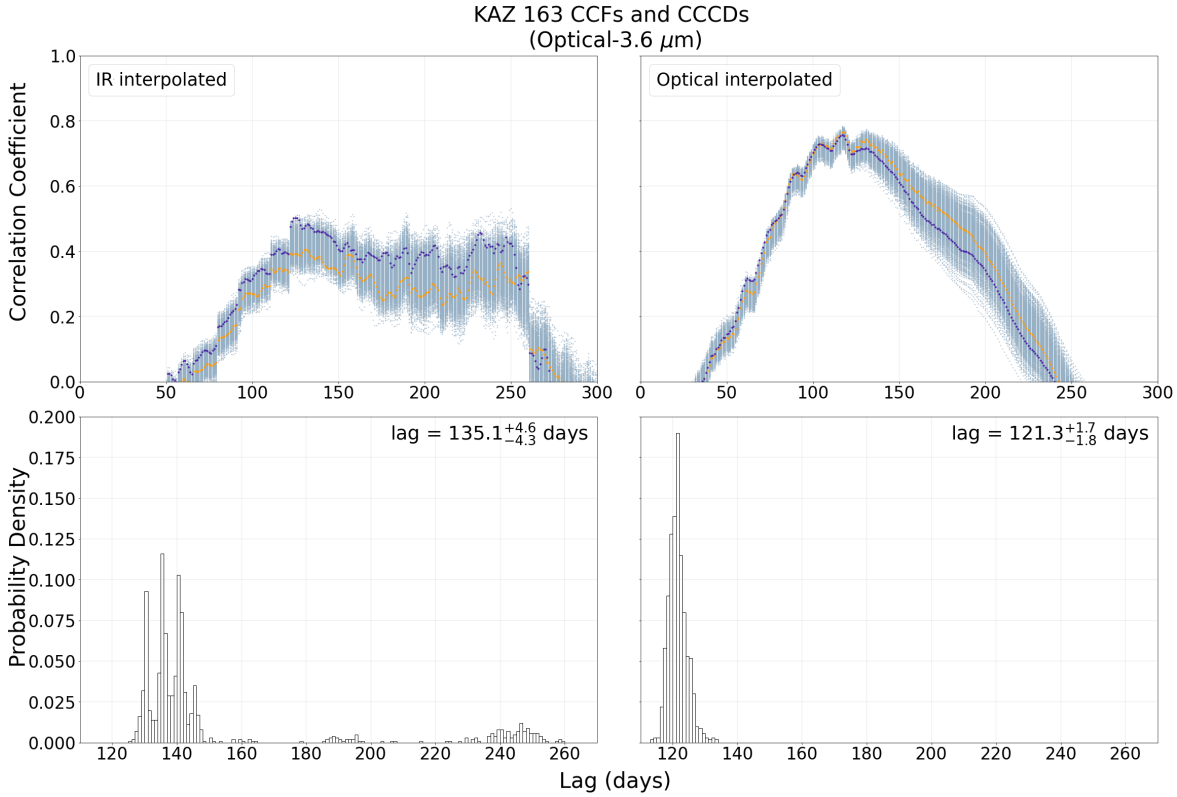

Figure 4.20: KAZ 163 CCFs (top subplots) and CCCDs (bottom subplots) for the combined optical-3.6μm analysis. The subplots on the left show the results of using IR interpolation, while the subplots on the right show the results of using optical interpolation. In the top plots, 1000 CCFs formed from the Monte Carlo iterations are shown in light blue. As examples, the purple and orange points highlight two individual CCFs.

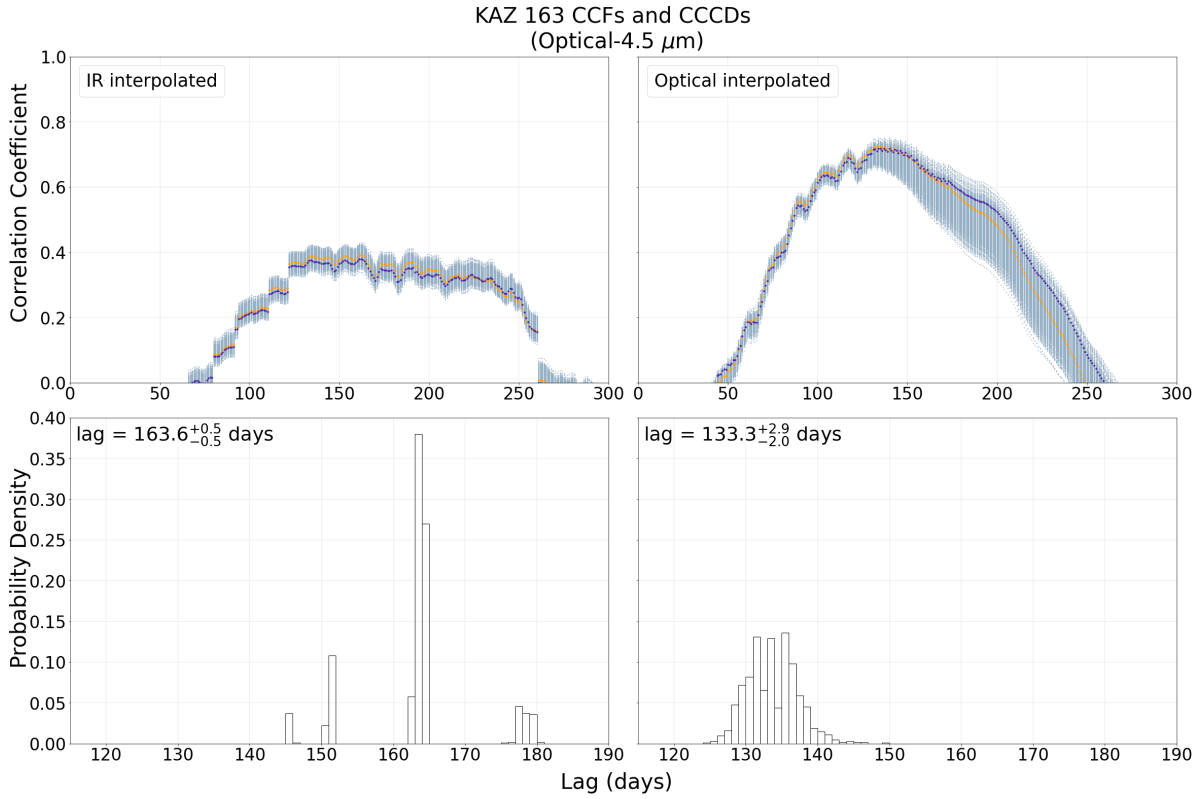

Figure 4.21: KAZ 163 CCFs (top subplots) and CCCDs (bottom subplots) for the combined optical-4.5μm analysis. The subplots on the left show the results of using IR interpolation, while the subplots on the right show the results of using optical interpolation. In the top plots, 1000 CCFs formed from the Monte Carlo iterations are shown in light blue. As examples, the purple and orange points highlight two individual CCFs.

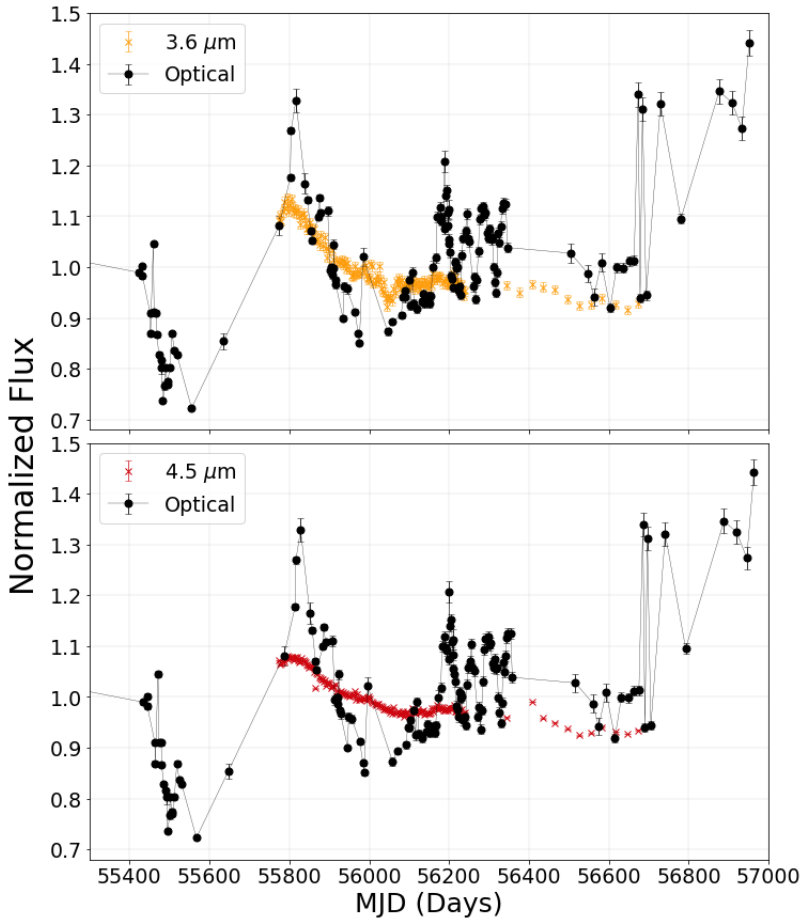

Figure 4.22: KAZ 163 shifted optical light curves: The optical light curves are shifted forward by 121.3 days for the optical-3.6 μm analysis (top panel) and 133.3 days for the optical-4.5 μm analysis (bottom panel).

Figure 4.22 shows the optical light curve shifted forward by the measured lag values. Although the IR light curves are heavily smoothed compared to the optical, as would be expected, the main features match well.

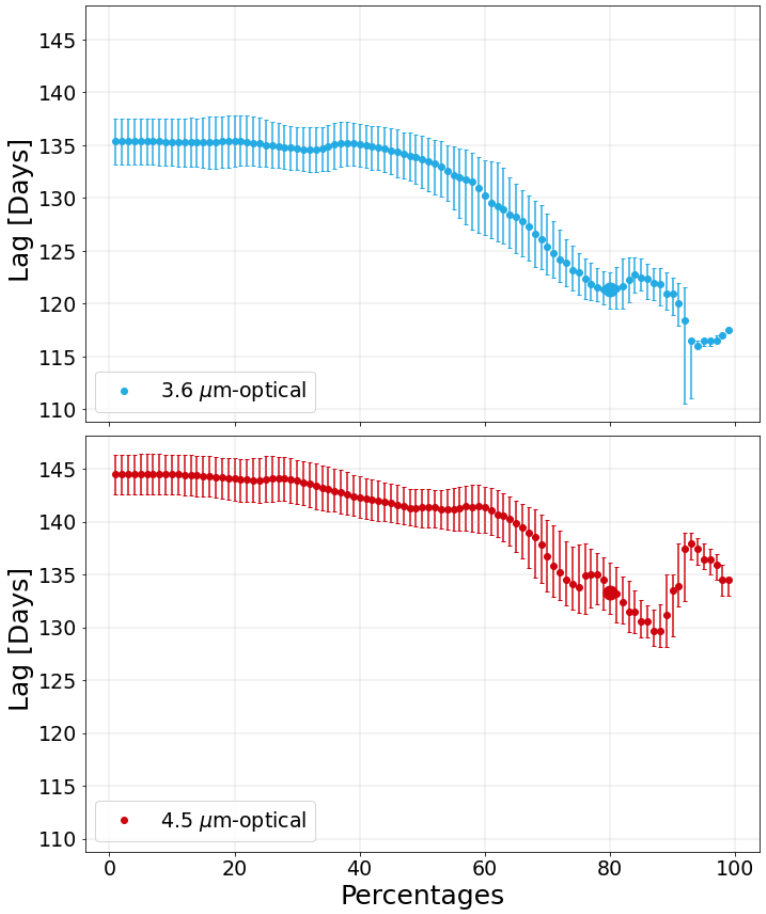

Figure 4.23: KAZ 163 dependence of measured lags on CCF percentage threshold value: The upper plot shows results for 3.6μm-optical, and the lower plot is 4.5μm-optical. The two larger points indicate the 80% threshold values.

As discussed in the PTF-IR analysis section, typically a value of 80% of the peak CCF value is used as the cutoff for calculating the centroid, and hence the lag, for each iteration. Different percentage threshold values were tested, and the resulting lag values are shown in Figure 4.23. For both plots, the most stable region appears to be at a threshold less than $\sim 50\%$, although for the lags reported here, 80% was used. Depending on which threshold value is chosen below 80%, the lags vary by $\sim 10 - 15$ days.

For the 3.6μm-optical and 4.5μm-optical analysis, JAVELIN produces lags of $177.1^{+48.6}_{-2.2}$ days

and $207.6^{+4.0}_{-0.1}$ days, respectively. Neither of the JAVELIN lags are consistent with those of the Vazquez (2015) code, as the 3.6μm-optical lag from JAVELIN is 55.8 days larger and the 4.5μm-optical lag from JAVELIN is 74.3 days larger. Figure 4.24 shows the optical light curves shifted forward by the lag values calculated from JAVELIN. The JAVELIN lags are clearly too large in that they violate causality (the optical peak flux now occurs much later than the IR peak).

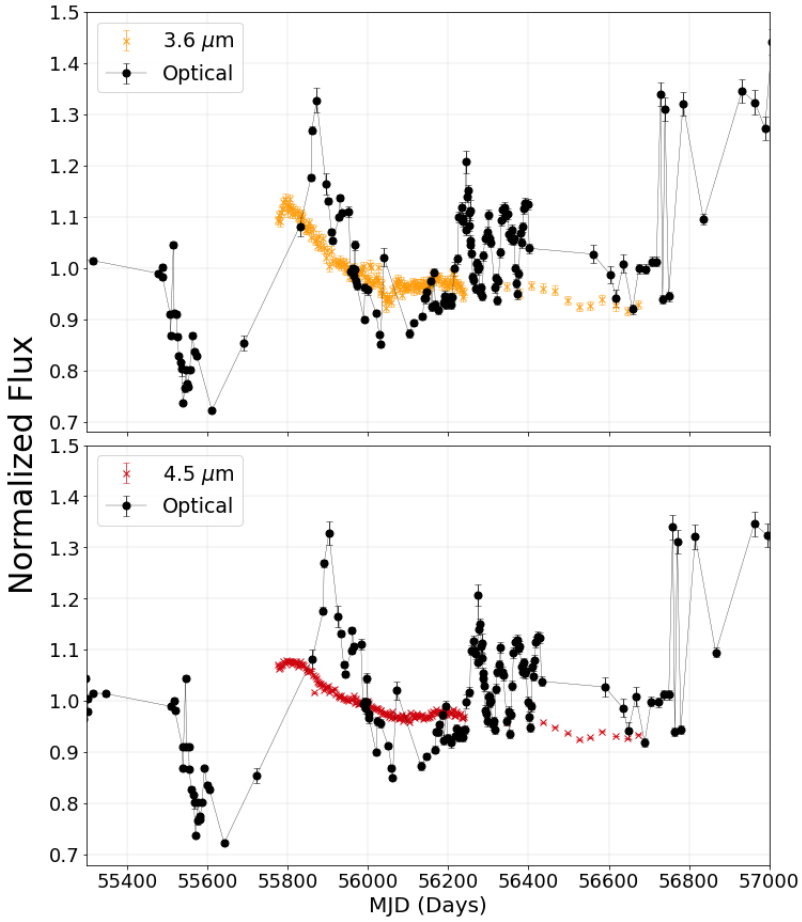

Figure 4.24: KAZ 163 optical light curves and IR light curves, shifted by JAVELIN lag values: The optical light curves are shifted forward by 177.1 days for the optical-3.6 μm analysis (top panel) and 207.6 days for the optical-4.5 μm analysis (bottom panel).

Figures 4.25 and 4.26 compare the lag results obtained by cross-correlating the starlight-subtracted light curves with the IR, using different codes. Using both FR and RSS with PYCCF

leads to a similar result as using FR only, although the uncertainties are larger. Interpolating both light curves with PYCCF leads to lag values that are slightly larger than those calculated with optical interpolation alone, but slightly smaller than the lags obtained with IR interpolation. The lags calculated using JAVELIN are significantly larger than those from PYCCF or the Vazquez (2015) code.

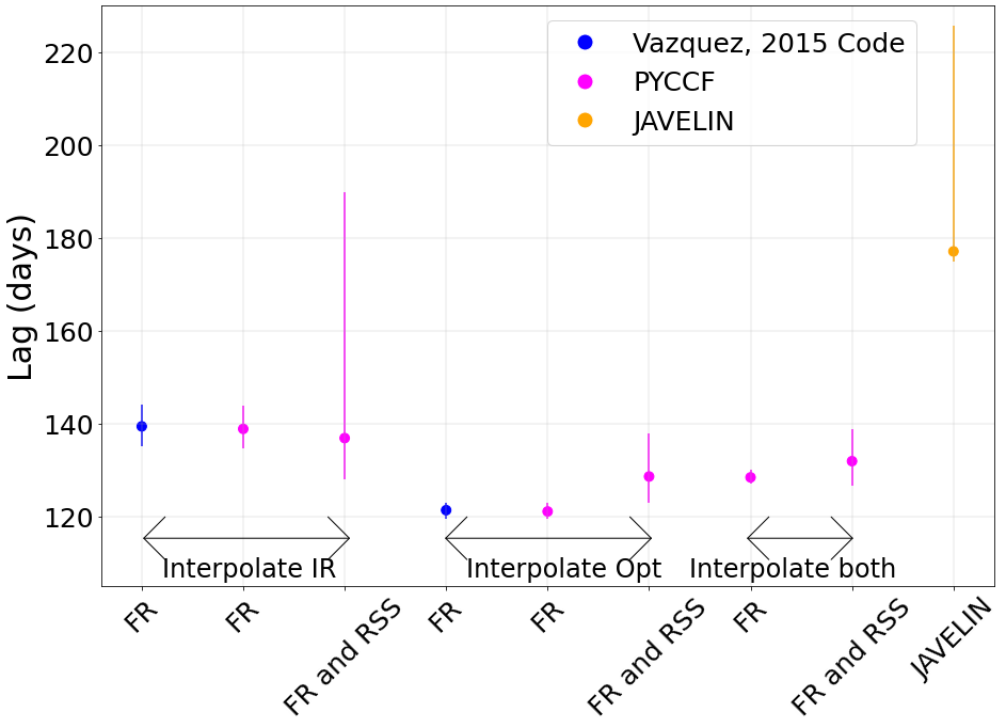

Figure 4.25: KAZ 163 lag comparisons for the 3.6μm-optical analysis. The blue data points represent lag values calculated using the Vazquez (2015) code, the orange point represents the lag calculated using JAVELIN, while the PYCCF results are shown in pink. The labels on the x-axis indicate whether flux randomization (FR) or both flux randomization and random subset selection (FR and RSS) was used. The labels above the x-axis specify whether the corresponding lags were calculated using IR interpolation, optical interpolation, or interpolating both.

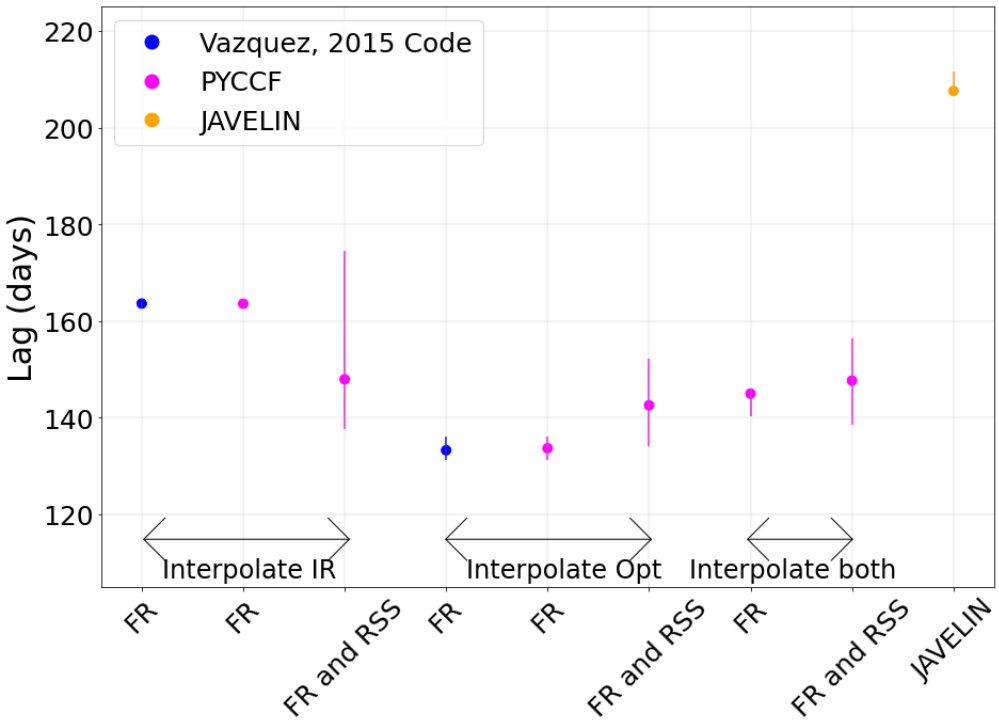

Figure 4.26: KAZ 163 lag comparisons for the 4.5μm-optical analysis. The blue data points represent lag values calculated using the Vazquez (2015) code, the orange point represents the lag calculated using JAVELIN, while the PYCCF results are shown in pink. The labels on the x-axis indicate whether flux randomization (FR) or both flux randomization and random subset selection (FR and RSS) was used. The labels above the x-axis specify whether the corresponding lags were calculated using IR interpolation, optical interpolation, or interpolating both.

KAZ 163 3.6-4.5μm Analysis The two IR channels were also cross-correlated with each other to determine the lag between them. The different interpolation types for this analysis include interpolating the 3.6 μm light curve onto the timestamps of the 4.5 μm light curve (this will be referred to as "3.6 μm interpolation"), and similarly interpolating the 4.5 μm light curve onto the timestamps of the 3.6 μm light curve (referred to as "4.5 μm interpolation"). Since both light curves are sampled at the same rate, we should not encounter the same issues mentioned previously, where one order of interpolation leads to noisy CCFs. Figure 4.27 shows this, as both interpolation types produce similar CCFs. The calculated lag values still differ, though.

Figure 4.28 shows the CCCDs for the Vazquez (2015) code (using FR only) and PYCCF (using

both FR and RSS). The Vazquez (2015) code produces a lag result of $32.8^{+1.2}_{-1.8}$ days when interpolating the 4.5 μm light curve onto the 3.6 μm timestamps, while interpolating in the opposite order gives a shorter lag result of $18.3^{+2.9}_{-3.0}$ days. As expected, using both FR and RSS leads to a similar calculated lag value as FR only, however the CCCD is broader when including RSS, leading to a larger uncertainty.

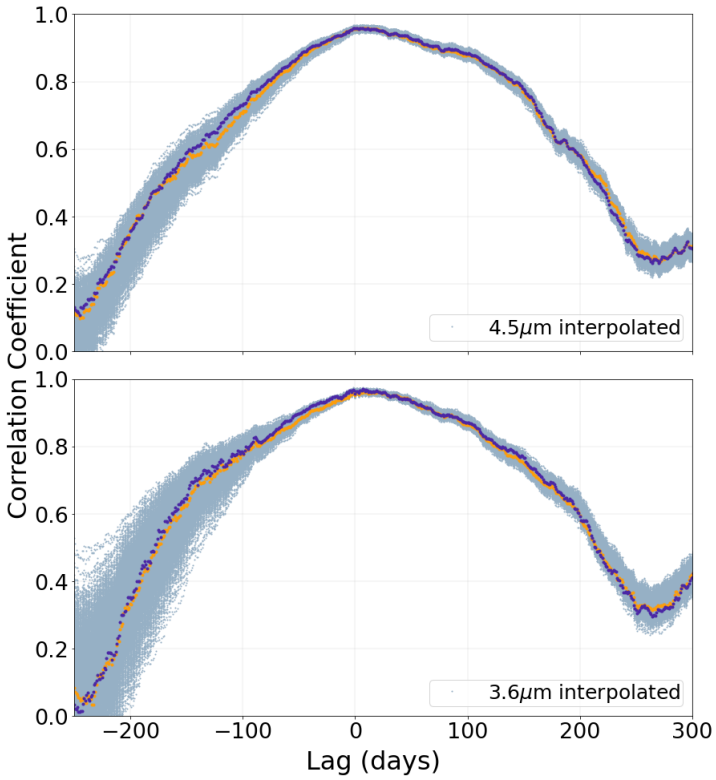

Figure 4.27: KAZ 163 CCFs for the 3.6-4.5μm analysis: The top subplot shows the CCFs for 4.5 μm interpolation, and the bottom subplot shows the CCFs for 3.6 μm interpolation. Each plot includes 1000 CCFs formed from the Monte Carlo iterations, shown in light blue. As examples, the purple and orange points highlight two individual CCFs.

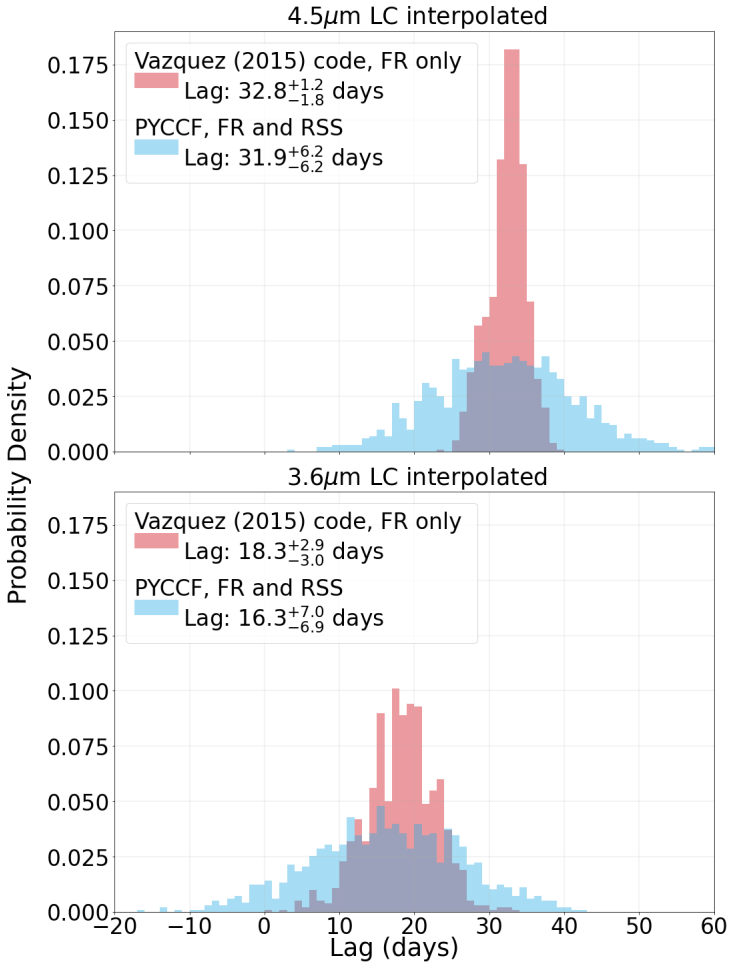

Figure 4.28: KAZ 163 CCCDs from both the Vazquez (2015) code and PYCCF for the 3.6-4.5 μm analysis. The top plot shows the results of using 4.5 μm interpolation, while the bottom plot shows the results of using 3.6 μm interpolation. For both subplots, the CCCDs formed from the Vazquez (2015) code include FR, while PYCCF includes both FR and RSS.

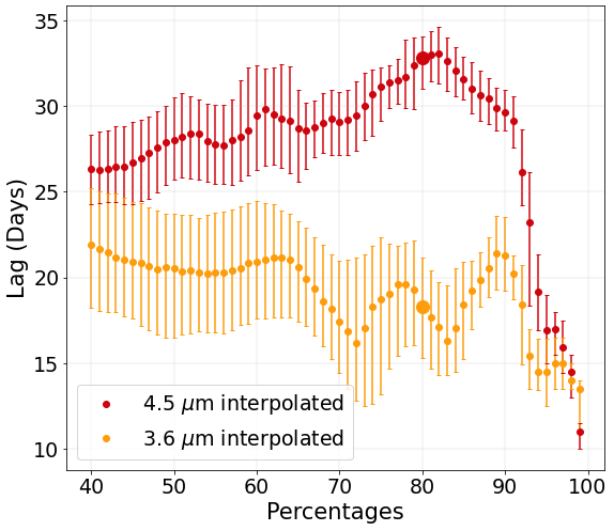

Figure 4.29: KAZ 163 dependence of measured lags on CCF percentage threshold value: The red points show results for 4.5 μm interpolation, and the orange points show results for 3.6 μm interpolation. The two larger points are indicating the 80% threshold values.

Figure 4.29 shows the dependence of the lag on the percentage threshold value for the IR channels cross-correlated with each other. As the peaks of the CCFs approximately coincide, using a large percentage threshold value leads to a similar lag for both interpolation types. However, the threshold range where the lag values are most stable when interpolating the 4.5 μm light curve (from ∼40%-73%) has a mean lag of 28.2 days, while interpolating the 3.6 μm light curve gives a lag of 20.8 days in the 50%-66% percent threshold range.

Figure 4.30 shows the IR light curves, with the 3.6μm light curve shifted forward by the measured lag values. It is difficult to determine which lag value is more reasonable. The smaller lag value seems to provide a better match between the main peak of the light curves. It is also interesting to note that the 4.5μm light curve is smoother and less sharply peaked than the 3.6 μm light curve.

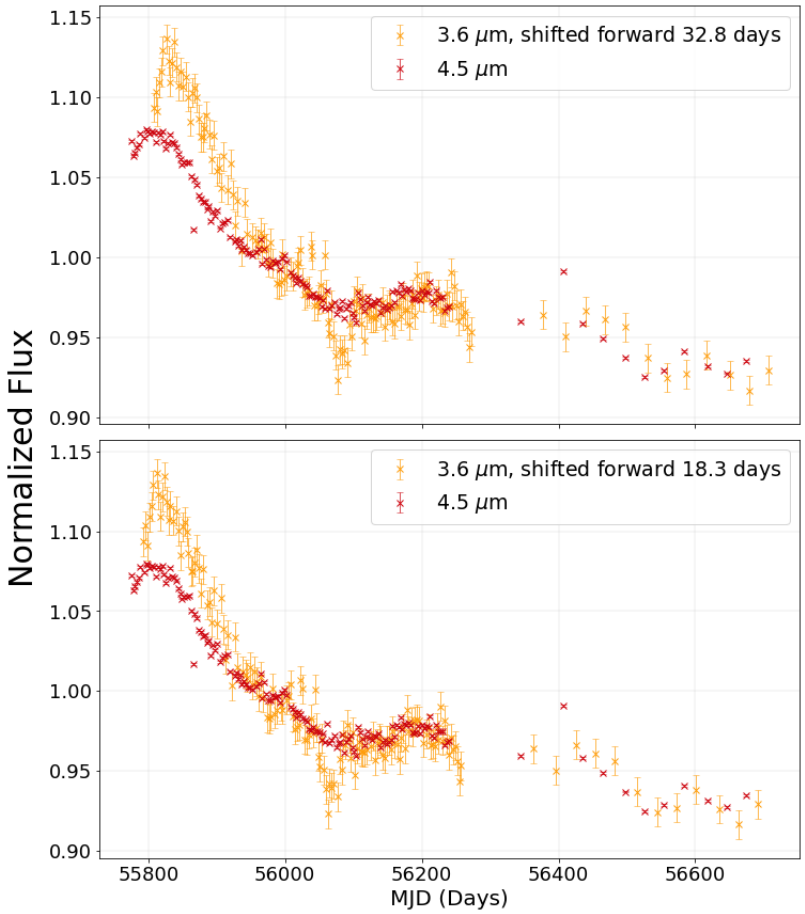

Figure 4.30: KAZ 163 shifted IR light curves: The top subplot shows the 3.6 μm light curve shifted forward by the lag value of 32.8 days, calculated from using 4.5 μm interpolation. The bottom subplot shows the 3.6 μm light curve shifted forward by the lag value of 18.3 days, calculated from using 3.6 μm interpolation.

Summary of KAZ 163 Lags Table 4.1 gives a summary of the lag results. Without subtracting the starlight contribution, the PTF-IR analysis can be used to constrain the lag. Using the full PTF light curve with optical interpolation produces more sharply peaked CCFs, as it includes the main features in the light curve (see Figure 4.7). Shifting the optical light curve forward by the measured lag values shows that these lags appear to be reasonable(see Figure 4.11).

While the PYCCF lag results are similar to those of the Vazquez (2015) code, the JAVELIN results are not consistent. Comparing Figures 4.11 and 4.12, it seems that JAVELIN is measuring

Table 4.1: KAZ 163 Summary of Lag Results: The '3.6μm-PTF' and '4.5μm-PTF' columns show the lag results of each IR light curve cross-correlated with the PTF light curve (using optical interpolation, with full light curve). The '3.6μm-Combined optical' and '4.5μm-Combined optical' columns show the lag results of each IR channel cross-correlated with the combined starlight-subtracted light curve (a combination of LT, PTF, and CSS data). The '3.6-4.5μm' column gives the lag results from interpolating the two IR channels with each other, with 3.6 μm interpolation. Each row gives the lag results using the Vazquez (2015) code using FR only, PYCCF using both FR and RSS, and JAVELIN.

	3.6μm-PTF	4.5μm-PTF	3.6μm-Combined optical	4.5μm-Combined optical	$3.6 - 4.5\mu$m
Vazquez (2015)	$120.3^{+3.0}_{-3.2}$	$125.0^{+2.9}_{-2.9}$	$121.3^{+1.7}_{-1.8}$	$133.3^{+2.9}_{-2.0}$	$18.3^{+2.9}_{-3.0}$
PYCCF (FR and RSS)	$118.4^{+10.3}_{-9.5}$	$128.5^{+32.8}_{-11.8}$	$128.6^{+9.3}_{-5.7}$	$142.6^{+9.7}_{-8.5}$	$16.3^{+7.0}_{-6.9}$
JAVELIN	$180.5^{+4.6}_{-5.8}$	$211.0^{+0.2}_{-0.2}$	$177.1^{+48.6}_{-2.2}$	$207.6^{+4.0}_{-0.1}$	-

the lag between the optical and IR light curve that corresponds to the dip in flux at ∼MJD 56050 in the IR, while PYCCF and the Vazquez (2015) code lags seem to correspond to the peak in flux, seen in the IR at ∼MJD 55800.

After subtracting the starlight contribution, the optical light curves of the LT B band, PTF R band, and CSS clear filter were combined and cross-correlated with each IR channel. Similar to the pre-starlight-subtracted results, the most clearly peaked CCFs are produced when interpolating the optical onto the IR timestamps. The lags for the starlight-subtracted light curves and the non starlight-subtracted PTF light curves are fairly consistent.

The PYCCF lag results are similar to those of the Vazquez (2015) code, while the JAVELIN results are not consistent. Comparing Figures 4.11 and 4.12, it seems that JAVELIN is measuring the lag between the optical and IR light curve that corresponds to the dip in flux at ∼ 56050 in the IR, while PYCCF and the Vazquez (2015) code lags seem to correspond to the main peak in flux.

Cross-correlating the two IR channels with each other leads to a lag between 16.3-32.8 days, depending on which light curve is interpolated onto the other. Using 3.6μm interpolation appears to give a more reliable lag, as indicated by shifting the light curves by the measured lag values (see Figure 4.30). Comparing the 3.6μm-PTF analysis and the 4.5μm-PTF analysis, the lags differ by 4.7 days when using the Vazquez (2015) code. However, the difference in lag values between the

3.6μm-combined optical and the 4.5μm-combined optical is 12 days. This only differs by a few days from the 3.6-4.5μm lag when using 3.6μm interpolation, and is within the errors.

4.2.2 MRK 507

MRK 507 is a NL Sy 1 AGN, with an estimated bolometric luminosity of $1.26-2.63\times10^{45}$erg/s, as discussed in Section 2. For this AGN, the PTF and CSS light curves do not show similar variations to the IR light curves, therefore CCA will not be performed for these individually. Before subtracting the starlight contribution, CCA was performed with the LT B band cross-correlated with the IR. Then, the combined starlight subtracted optical light curve (consisting of the LT B band, PTF R band, and CSS light curves) was cross-correlated with the IR. Finally, the two IR channels are cross-correlated with each other.

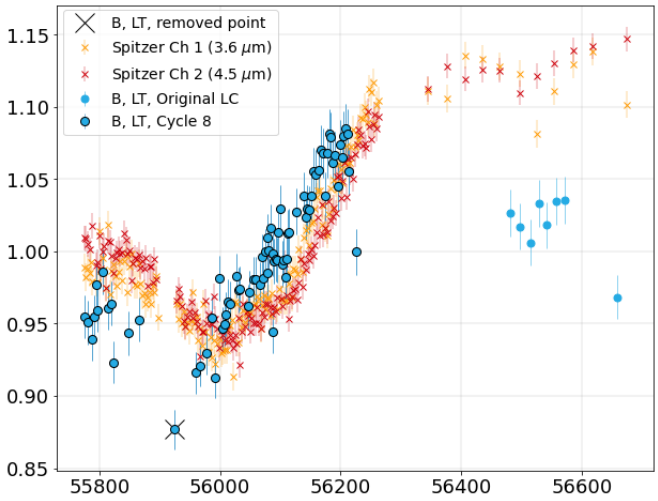

Figure 4.31: The different versions of the MRK 507 IR and optical light curves that were used for CCA. The orange and red points represent the IR Spitzer data, while the blue points represent the optical data from LT (B band). The points circled in black show the cycle 8 section of the optical light curve, and the point with an 'X' is the possible outlying datum that was removed to test its influence on the CCA.

MRK 507 Before Host Galaxy-Subtraction: LT B band-IR Analysis CCA was performed for several different variations of the LT B band and IR light curves. These different versions of

the light curves are shown in Figure 4.31. CCA was first performed using the entire B band and IR light curves. Then, in an effort to determine the lag for the main feature of the light curves, which is the decrease in flux from the beginning of the Spitzer campaign until ∼MJD 56000, and the subsequent increase in flux from ∼MJD 56000 until the end of cycle 8, CCA was also performed using only the cycle 8 data. CCA was also conducted for the complete light curves excluding the possible outlying data point shown in Figure 4.31. However, removing this datum had no effect on the CCA results, and will therefore not be discussed further.

The lag results also differ depending on which light curve is interpolated onto the timestamps of the other. Figure 4.32 shows examples of each of these interpolated light curves, while the CCFs and CCCDs are shown in Figures 4.33 and 4.34 for each IR channel cross-correlated with the optical.

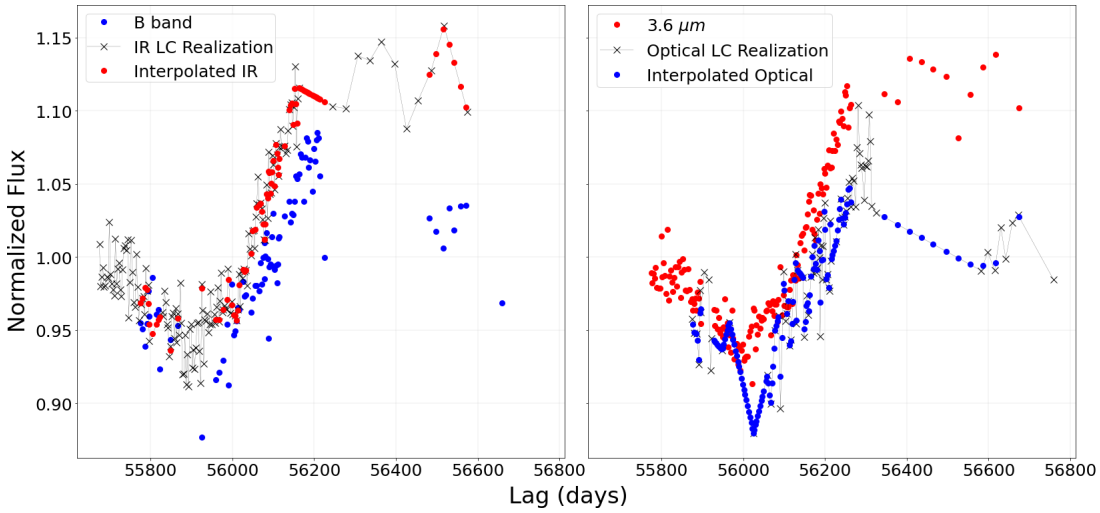

Figure 4.32: Examples of interpolated LT B band and 3.6 μm light curves for MRK 507: The plot on the left shows one IR light curve realization (the black points), the blue points represent the optical light curve, and the red points represent the IR data linearly interpolated onto the time stamps of the optical data points. Here, the IR light curve has been shifted back by 100 days. The plot on the right is similar, showing one of the optical light curve realizations in black, the red points represent the IR light curve, and the blue points represent the optical data linearly interpolated onto the time stamps of the IR data points. Here, the optical light curve has been shifted forward by 100 days.

First we will compare the lags measured when using the full span of the light curves (see the top two plots of Figures 4.33 and 4.34). With IR interpolation, the lag is $92.7^{+5.2}_{-4.5}$ days for the 3.6μm-optical analysis and $123.2^{+5.3}_{-5.8}$ days for the 4.5μm-optical analysis. Using optical interpolation, the lag is $89.0^{+4.5}_{-4.3}$ days for the 3.6μm-optical analysis, and $106.1^{+5.1}_{-6.2}$ days for the 4.5μm-optical analysis. The CCFs look slightly less noisy and less broad with optical interpolation, however the CCCDs all have clear peaks and a similar width for each case. The lag values are consistent for the 3.6μm-optical lag, but not for the 4.5μm-optical lag.

Next, we will look at the lag results for the cycle 8 portion of the light curves (see the bottom two plots of Figures 4.33 and 4.34). With IR interpolation, the lag is $58.6^{+5.2}_{-4.5}$ days for the 3.6μm-optical analysis and $72.6^{+7.5}_{-4.6}$ days for the 4.5μm-optical analysis. With optical interpolation, the corresponding lags are $71.4^{+4.3}_{-3.8}$ days and $83.9^{+3.3}_{-3.5}$ days. As was true when using the full span of the light curves, the CCFs look slightly less noisy and less broad when interpolating the optical onto the time stamps of the IR, although the CCCDs have clear peaks and similar widths for each case. For the cycle 8 analysis, the 4.5 μm-optical analysis gives consistent lag results for both interpolation types, in contrast to the lag results of the full light curve. For both IR channels cross-correlated with the optical, the lag values are larger when using the full optical light curve, compared to using only cycle 8.

Figures 4.35 and 4.36 show the IR and optical light curves, with the optical light curves shifted forward by their measured lag values for each interpolation type when using the full light curves or cycle 8 only. The lags are reasonable, although the shifted light curve shown in the top subplot of Figure 4.36 suggests that the measured lag is slightly too large for the optical-4.5μm, full light curve analysis. The cycle 8 shifted light curves also appear to be reasonable, with each IR and optical light curve overlapping for the rise in flux. However, for the full light curves, the measured lags also produce a reasonable overall match between the IR and optical light curve features.

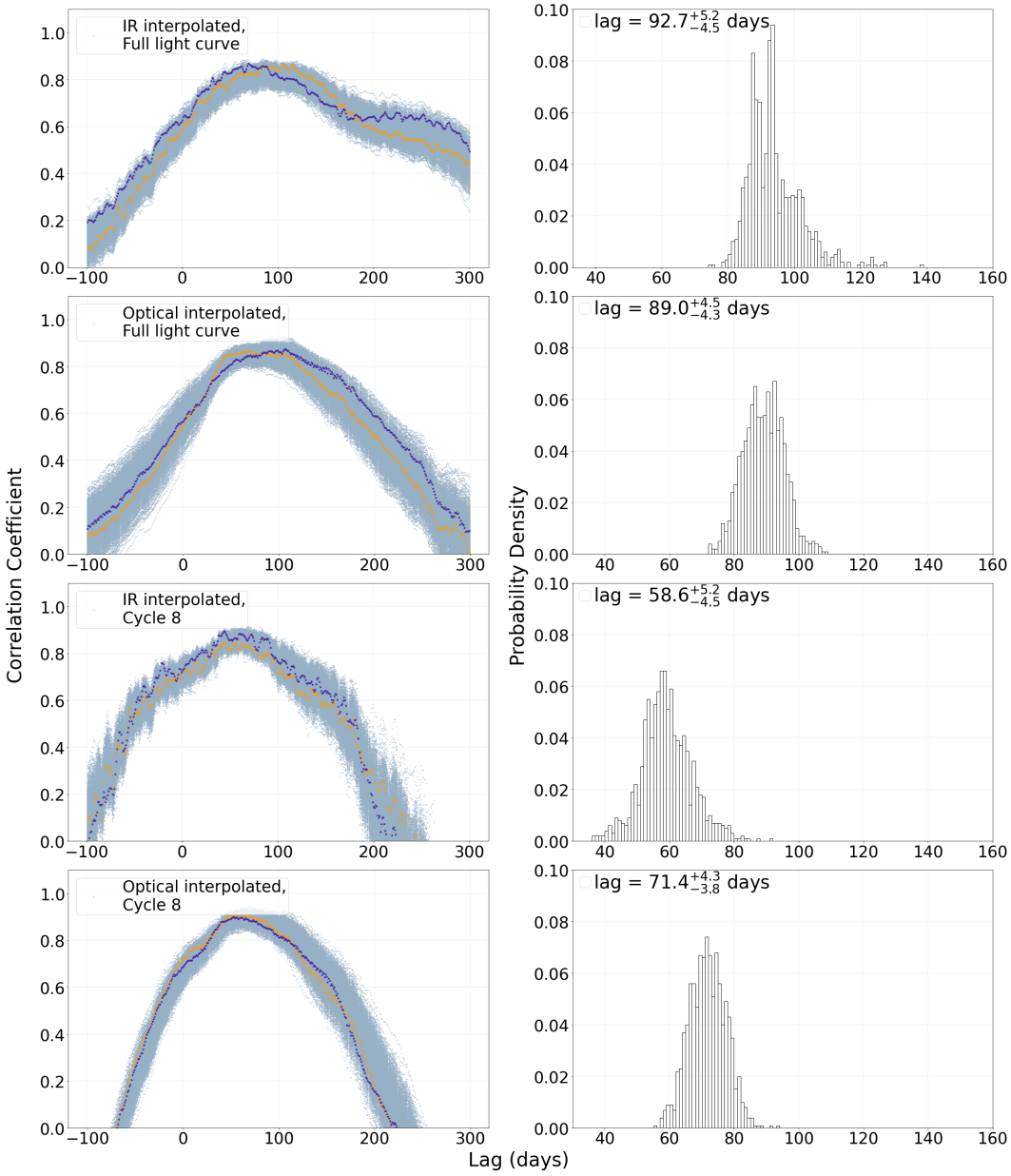

Figure 4.33: MRK 507 CCFs and CCCDs for the LT B band-3.6μm analysis: The top two plots show the results of using the full optical light curve and either IR interpolation (top row), or optical interpolation (second row). The bottom two plots show the results of using only the cycle 8 data and either IR interpolation (third row), or optical interpolation (fourth row). Each CCF plot includes 1000 CCFs formed from the Monte Carlo iterations, shown in light blue. As examples, the purple and orange points highlight two individual CCFs.

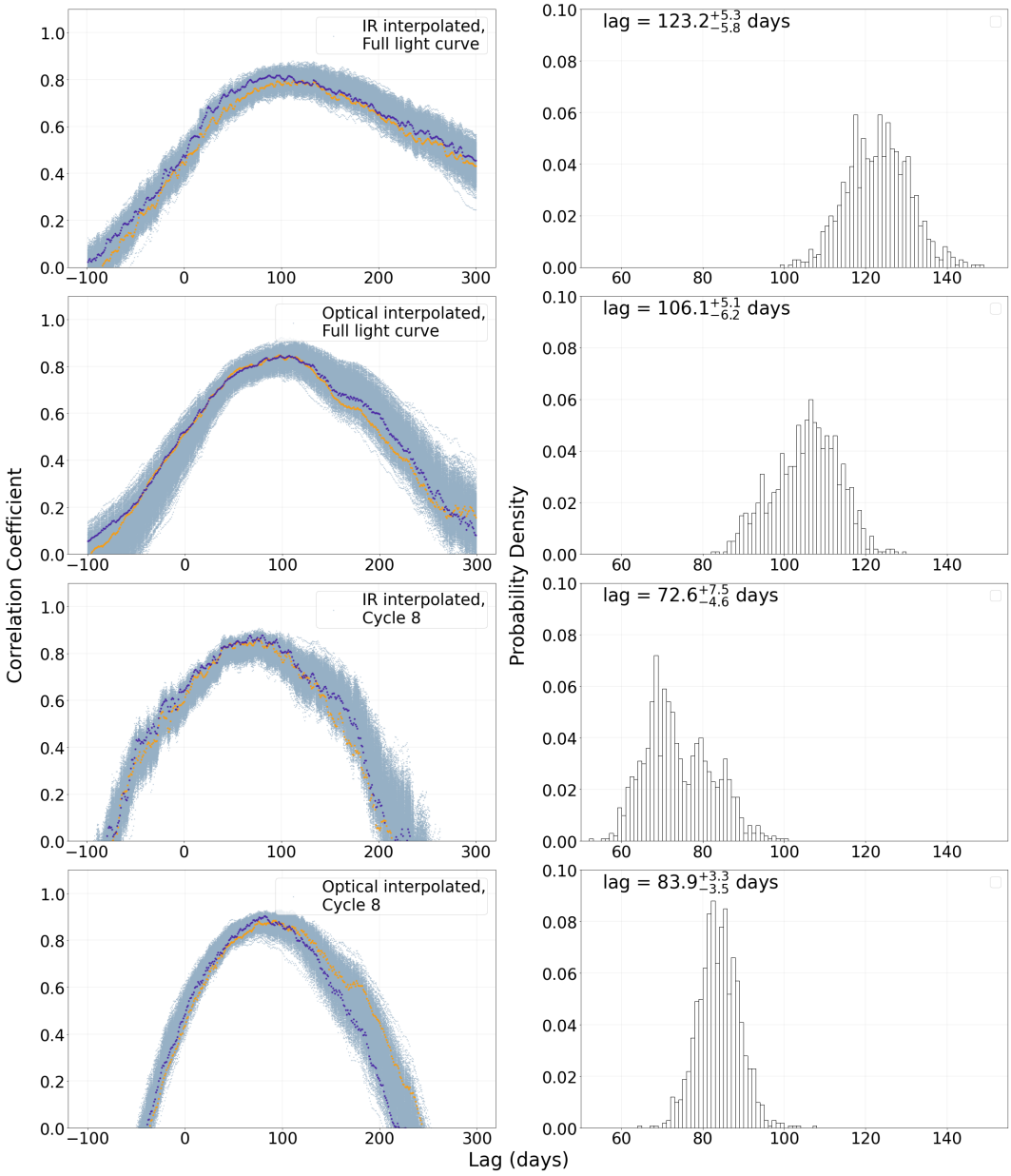

Figure 4.34: CCCDs for the LT B band-4.5μm analysis: The top two plots show the results of using the full optical light curve and either IR interpolation (top row), or optical interpolation (second row). The bottom two plots show the results of using only the cycle 8 data and either IR interpolation (third row), or optical interpolation (fourth row). Each CCF plot includes 1000 CCFs formed from the Monte Carlo iterations, shown in light blue. As examples, the purple and orange points highlight two individual CCFs.

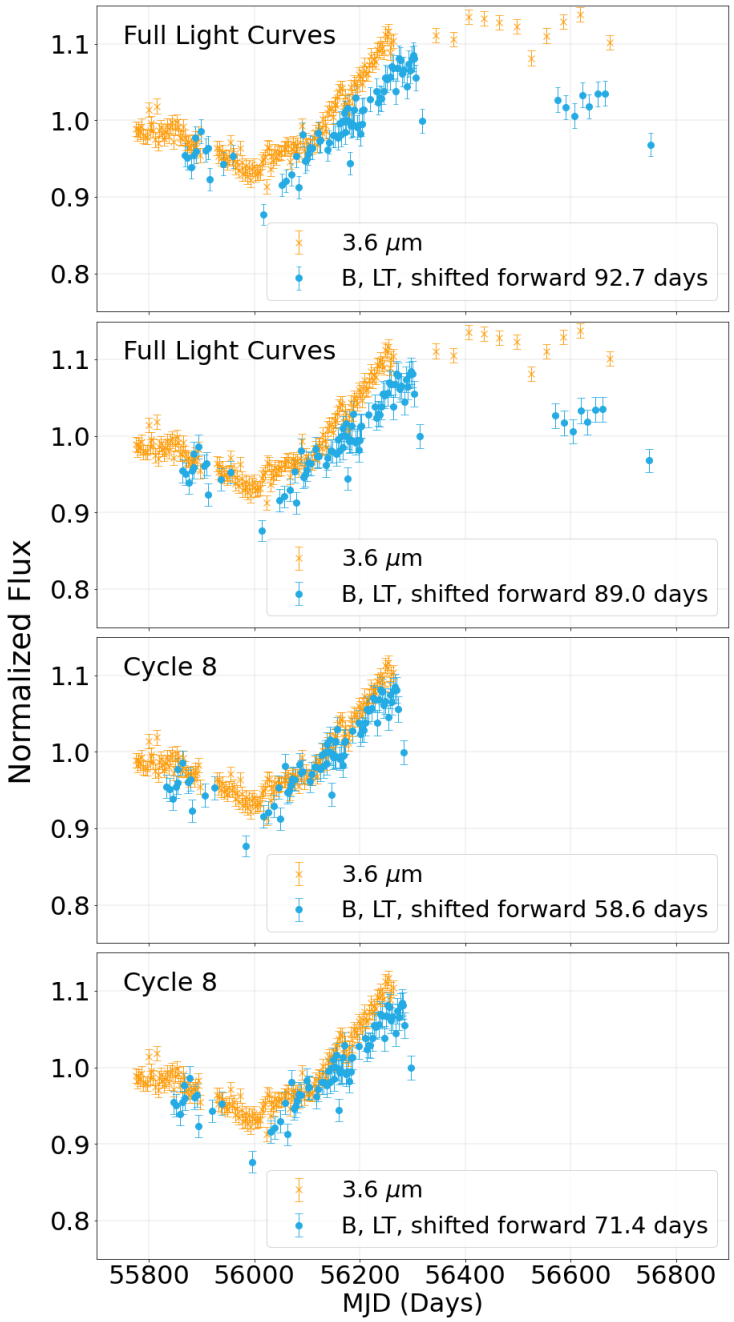

Figure 4.35: MRK 507 3.6μm and shifted optical light curves: The optical light curves are shifted forward by the measured lag values obtained from the optical-3.6 μm analysis when using either the full light curves (top two plots) or only cycle 8 (bottom two plots). The lags were calculated using IR interpolation (first and third plots) or optical interpolation (second and fourth plots).

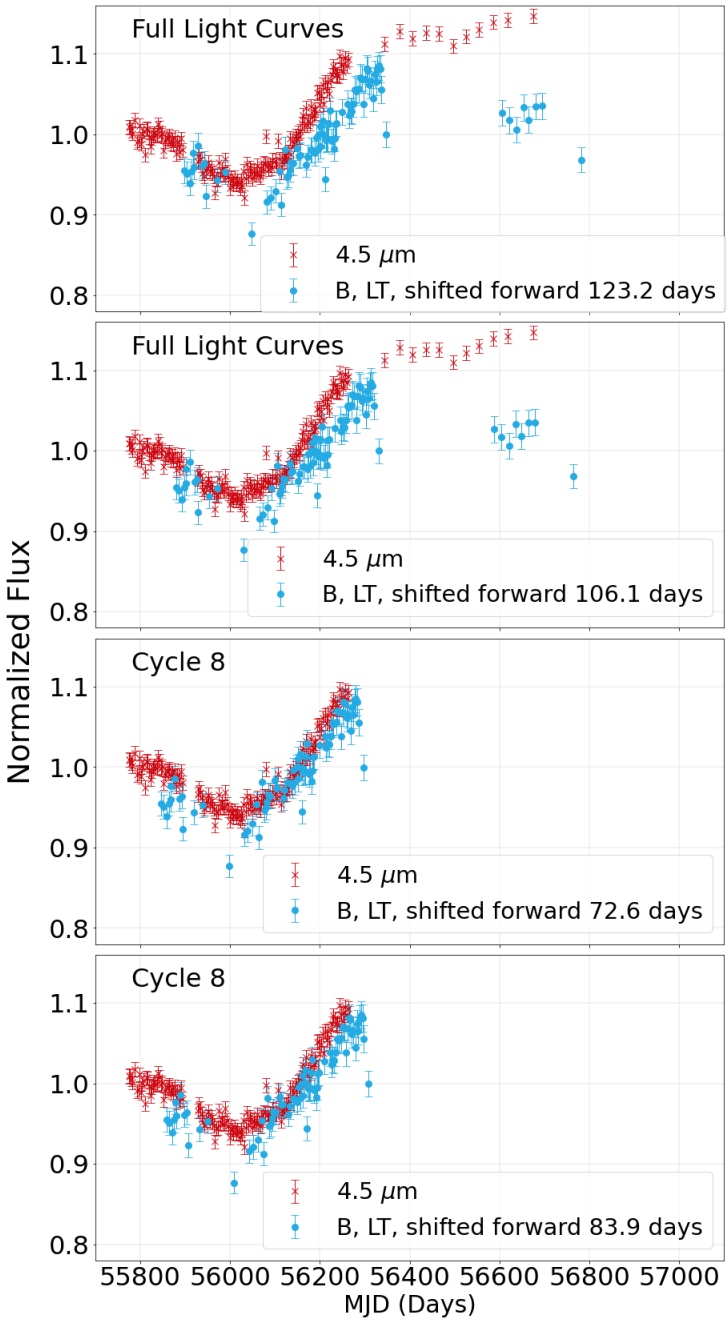

Figure 4.36: MRK 507 4.5 μm and shifted optical light curves: The optical light curves are shifted forward by the measured lag values obtained from the optical-4.5 μm analysis when using either the full light curves (top two plots) or only cycle 8 (bottom two plots). The lags were calculated using IR interpolation (first and third plots) or optical interpolation (second and fourth plots).

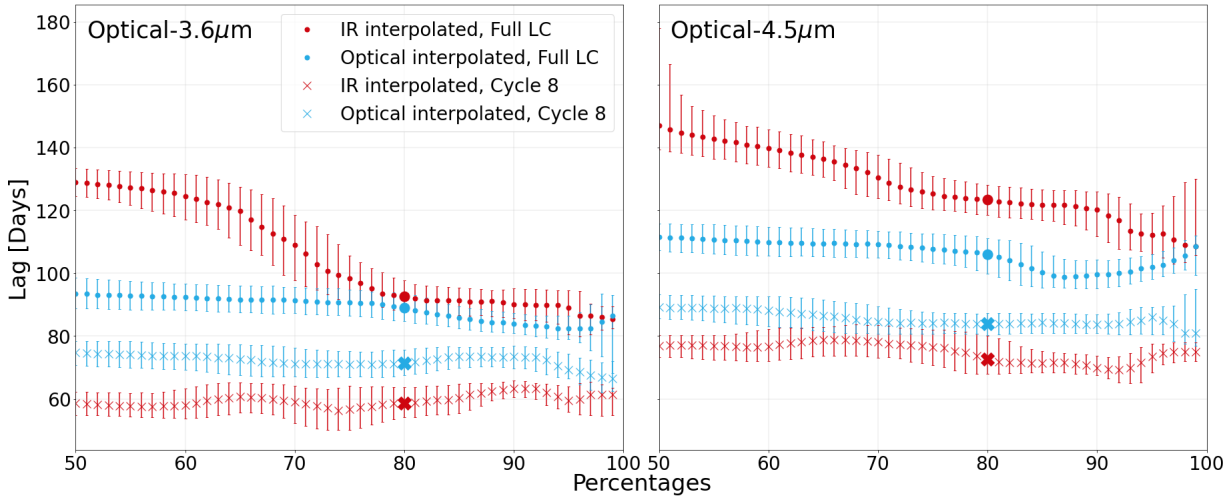

Figure 4.37:

MRK 507 dependence of measured lags on CCF percentage threshold value for the 3.6 μm-optical analysis (left plot) and the 4.5 μm-optical analysis (right plot): The red points represent IR interpolation, while blue represents optical interpolation. The dots indicate lags calculated for the full light curve, and 'x's represent the lags calculated using cycle 8. The larger points indicate the 80% threshold percentage values.

Different CCF threshold percentage values were tested, and the lag values calculated for each interpolation type for either the full light curves or cycle 8 only. Figure 4.37 shows the results for the 3.6 μm-optical and 4.5 μm-optical analysis. The least stable lag is that of the IR interpolation with the full light curve, for both IR channels. The CCFs for this analysis were the least symmetrical, so it is clear why this occurs. For each interpolation type and length of the light curves, the 80% value falls in a stable region.

The JAVELIN results differ from those of the Vazquez (2015) code. Lags were measured for the optical-IR analysis using both the full light curves, and also only the cycle 8 portion of the light curves. For the 3.6μm-optical analysis of the full light curve, the lags are almost twice as large as those of cycle 8; a lag of $133.3^{+6.0}_{-7.7}$ days was calculated, while for the cycle 8 data the lag was $78.12^{+46.9}_{-8.0}$. For the 4.5μm-optical analysis, a lag of $137.2^{+5.1}_{-5.0}$ days was calculated for the full light

curve, similar to that of cycle 8, where the lag was $133.1^{+61.2}_{-13.2}$ days. Figures 4.38 and 4.39 show the IR and optical light curves, with the optical shifted forward by the measured lag values from JAVELIN. For the 3.6μm light curve analysis, the shift for the full light curves appears to be too large, while the cycle 8 shift seems more reasonable. For the 4.5μm light curve analysis, both lag values are clearly too large.

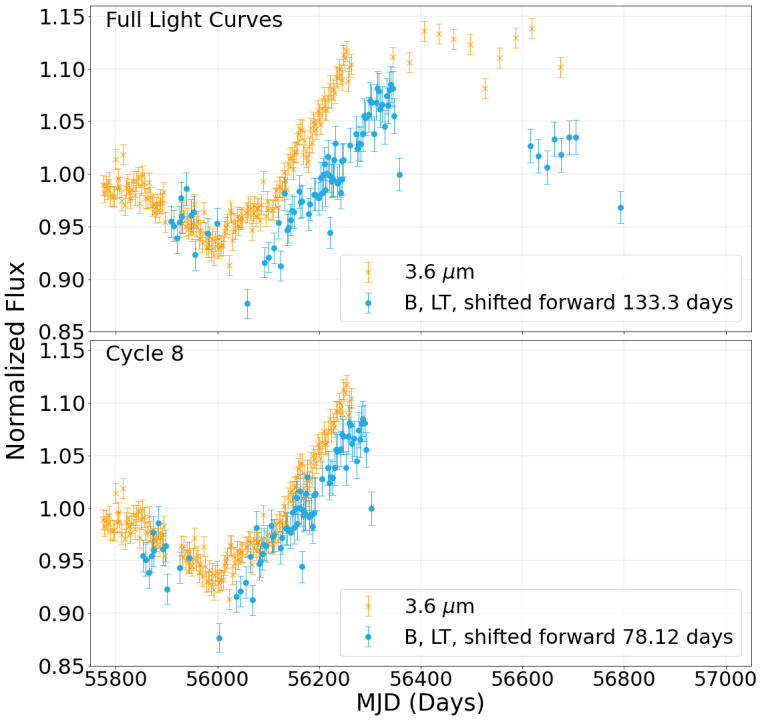

Figure 4.38: MRK 507 3.6 μm and shifted optical light curves: The optical light curves are shifted forward by the lag values calculated using JAVELIN for the full light curve analysis (133.3 days) in the top plot and the cycle 8 light curve analysis (78.1 days) in the bottom plot.

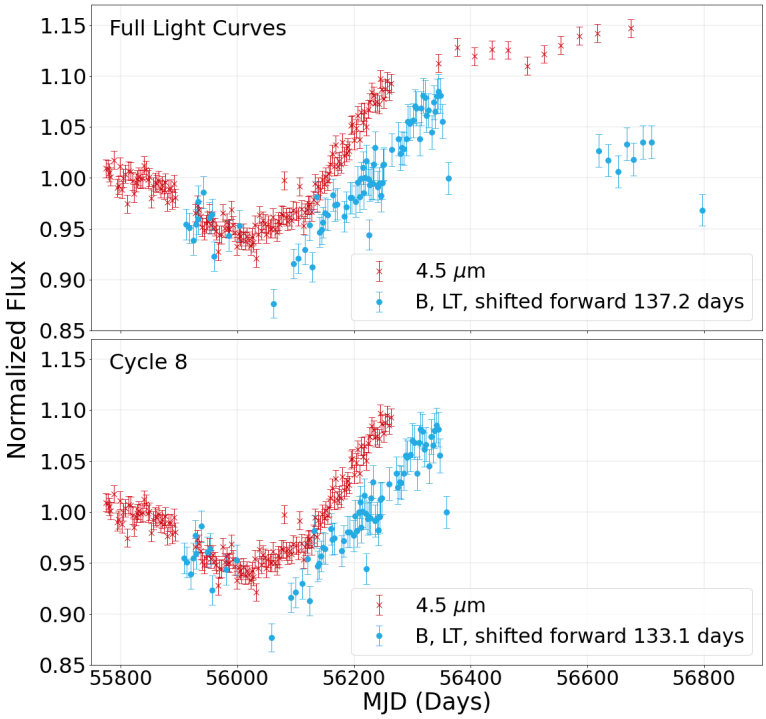

Figure 4.39: MRK 507 4.5 μm and shifted optical light curves: The optical light curve is shifted forward by the lag values calculated using JAVELIN for the full light curve analysis (137.2 days) in the top plot and the cycle 8 light curve analysis (133.1 days) in the bottom plot.

CCA was also performed with PYCCF. A comparison of the lags calculated using each code is shown in Figures 4.40 and 4.41. With PYCCF, when using only FR, the lag results are the same as using the Vazquez (2015) code. When using both FR and RSS with PYCCF, the CCCDs are more broad, however the overall lag results are very similar to those measured using FR only, falling within the errors. As expected, using the PYCCF option of interpolating both light curves returns lag values that are between those measured using optical or IR interpolation.

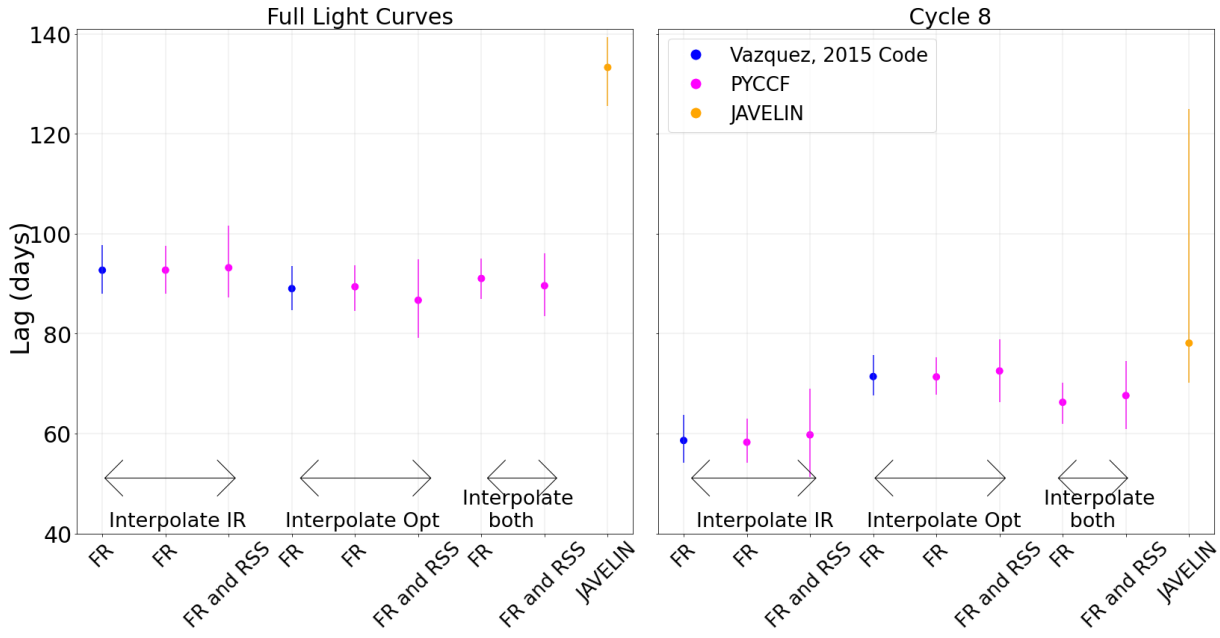

Figure 4.40: MRK 507 lag comparisons for the 3.6μm-optical analysis: The blue data points represent lag values calculated from the Vazquez (2015) code, the PYCCF results are shown in pink, and the JAVELIN results are shown in orange. The labels on the x-axis indicate whether flux randomization (FR) or both flux randomization and random subset selection (FR and RSS) was used. The labels above the x-axis specify whether the corresponding lags were calculated using IR interpolation, optical interpolation, or interpolating both. The left plot includes the results from the analysis of the full span of the light curves, and the plot on the right shows the results from the CCA using only the cycle 8 data.

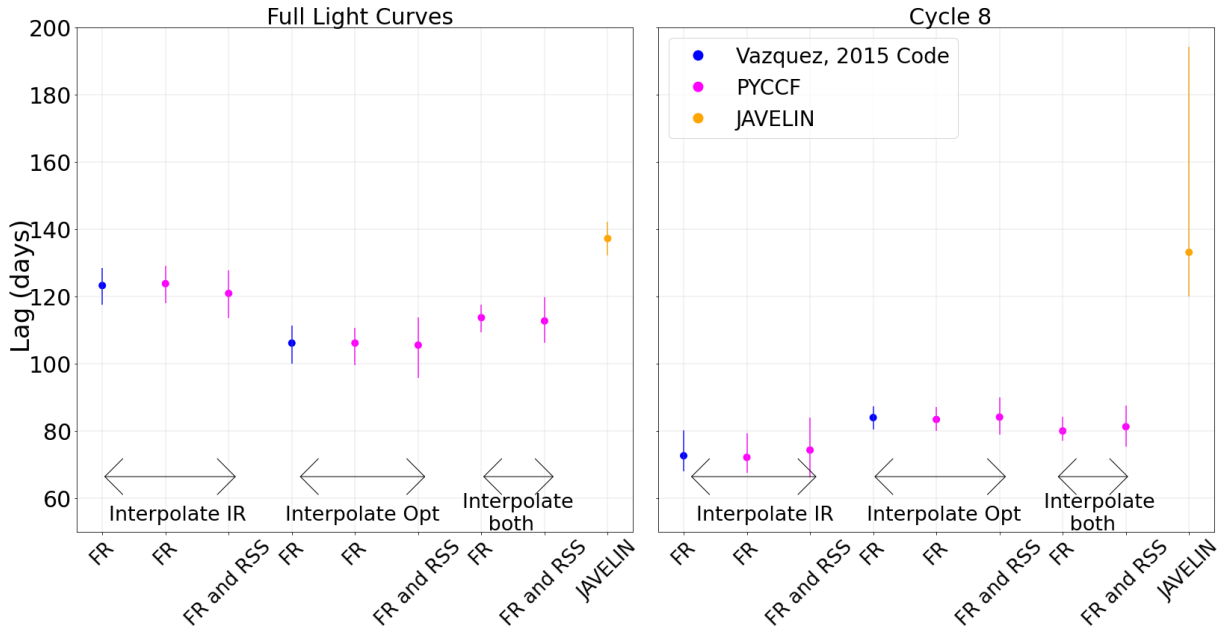

Figure 4.41: MRK 507 lag comparisons for the 4.5μm-optical analysis: The blue data points represent lag values calculated from the Vazquez (2015) code, the PYCCF results are pink, and the JAVELIN results are orange. The labels on the x-axis indicate whether flux randomization (FR) or both flux randomization and random subset selection (FR and RSS) was used. The labels above the x-axis specify whether the corresponding lags were calculated using IR interpolation, optical interpolation, or interpolating both. The left plot includes the results from the analysis of the full span of the light curves, and the plot on the right shows the results from the CCA using only the cycle 8 data.

The PYCCF and Vazquez (2015) codes appear to give more reliable lag values than JAVELIN. Using the full light curves and the results of PYCCF and the Vazquez (2015) code, the lag was measured to be between 86.7-93.2 days for the optical-3.6μm analysis, and 105.5-123.2 days for the optical-4.5μm analysis, depending on the direction of interpolation. Using only the cycle 8 data with PYCCF and the Vazquez (2015) code produces a lag between 58.6-72.5 days for the optical-3.6μm analysis, and 72.6-84.1 days for the optical-4.5μm analysis, depending on the order of interpolation.

After Host Galaxy Subtraction: The starlight contribution was subtracted, and CCA was performed for the combined optical and IR light curves. The combined optical light curve consists of data from LT (B band), PTF (R band), and CSS (clear filter). The light curves are shown in Figure 4.42.

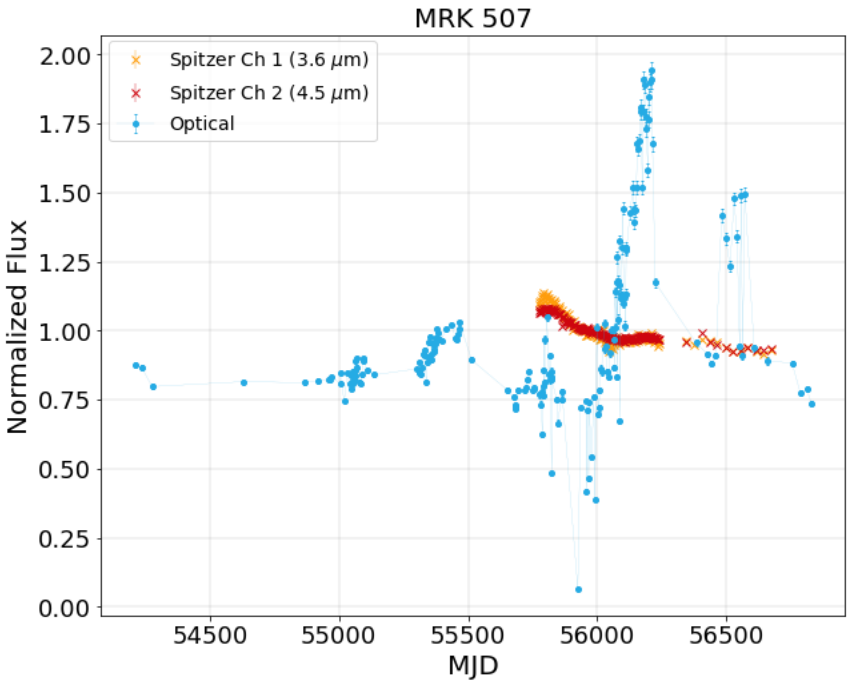

Figure 4.42: MRK 507 IR and starlight-subtracted optical light curves: The starlight-subtracted optical light curve, which is a combination of LT, PTF, and CSS data is shown in blue. The orange and red points represent the IR Spitzer data.

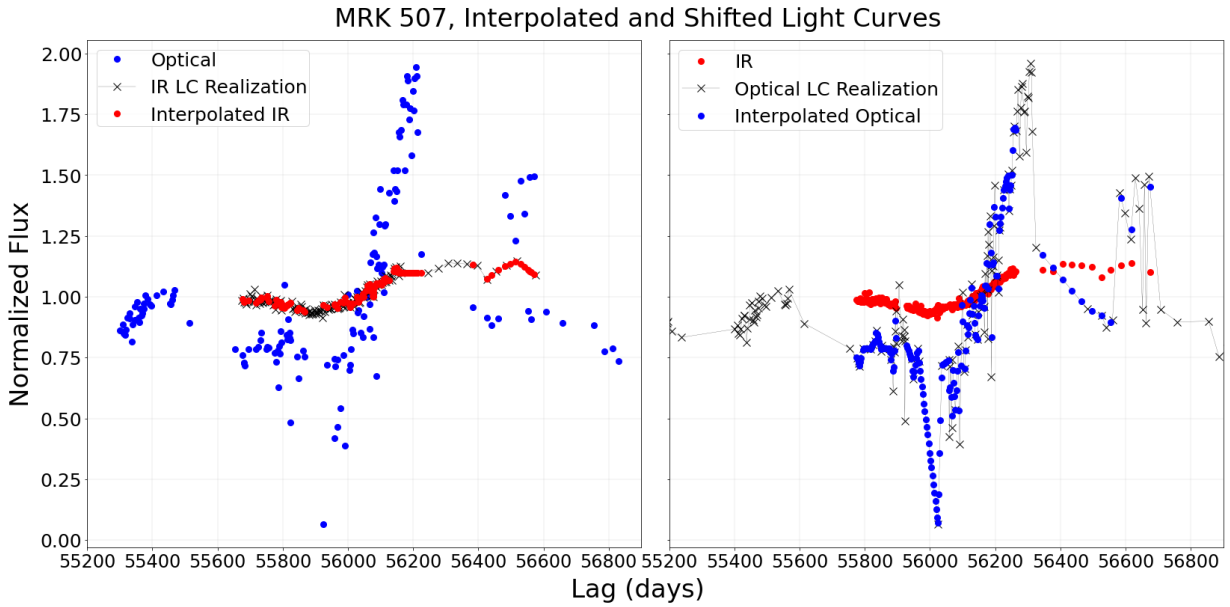

Figure 4.43: Examples of the interpolated combined optical and and 3.6 μm light curves of MRK 507: The plot on the left includes one IR light curve realization (the black points), the optical light curve is shown as blue points, and the red points represent the IR points linearly interpolated onto the time stamps of the optical data points. Here, the IR light curves have been shifted back by 150 days.
The plot on the right is similar, including one of the optical light curve realizations in black, the IR light curve is shown in red, and the blue points represent the optical points linearly interpolated onto the timestamps of the IR data points. Here, the optical light curve has been shifted forward by 150 days

Examples of the interpolated light curves are shown in Figure 4.43, and the CCFs and CCCDs are shown in Figures 4.44 and 4.45. The results obtained using the full span of the light curves will be discussed first (see the top two plots of Figures 4.44 and 4.45). Using IR interpolation, the lag is $112.9^{+5.4}_{-5.1}$ days for the 3.6μm-optical analysis and $143.3^{+5.6}_{-4.4}$ days for the 4.5μm-optical analysis. This is much larger than the lag calculated using optical interpolation, which is $85.7^{+1.3}_{-0.6}$ days for the 3.6μm-optical analysis and $99.1^{+2.2}_{-2.0}$ days for the 4.5μm-optical analysis. It is clear why the IR interpolated lags are larger, as the CCFs are much more broad and flatten off for larger lag values, although it is unclear what light curve features cause this to occur. Using optical interpolation appears to be the best method of determining the lag when using the full span of the light curves.

These lags only differ by a few days from those measured from the PTF-IR CCA, before subtracting the starlight, with optical interpolation.

Now the analysis for the cycle 8 portion of the light curves will be discussed (see the bottom two plots of Figures 4.44 and 4.45). With IR interpolation, the lag is $60.7^{+1.9}_{-1.6}$ days for the 3.6μm-optical analysis and $80.0^{+1.9}_{-1.9}$ days for the 4.5μm-optical analysis. With optical interpolation, the corresponding lags are $67.1^{+1.1}_{-1.4}$ days and $82.7^{+1.4}_{-1.1}$ days. The CCCDs have clear peaks and similar widths. The lag values for the 3.6μm-optical analysis for the two interpolation types do not fall within the errors, although the lags only differ by 6.4 days. The 4.5μm-optical lags are consistent for each interpolation type. As in the case of KAZ 163, each lag value only differs by a few days from the lags calculated prior to the starlight subtraction, for each corresponding interpolation type.

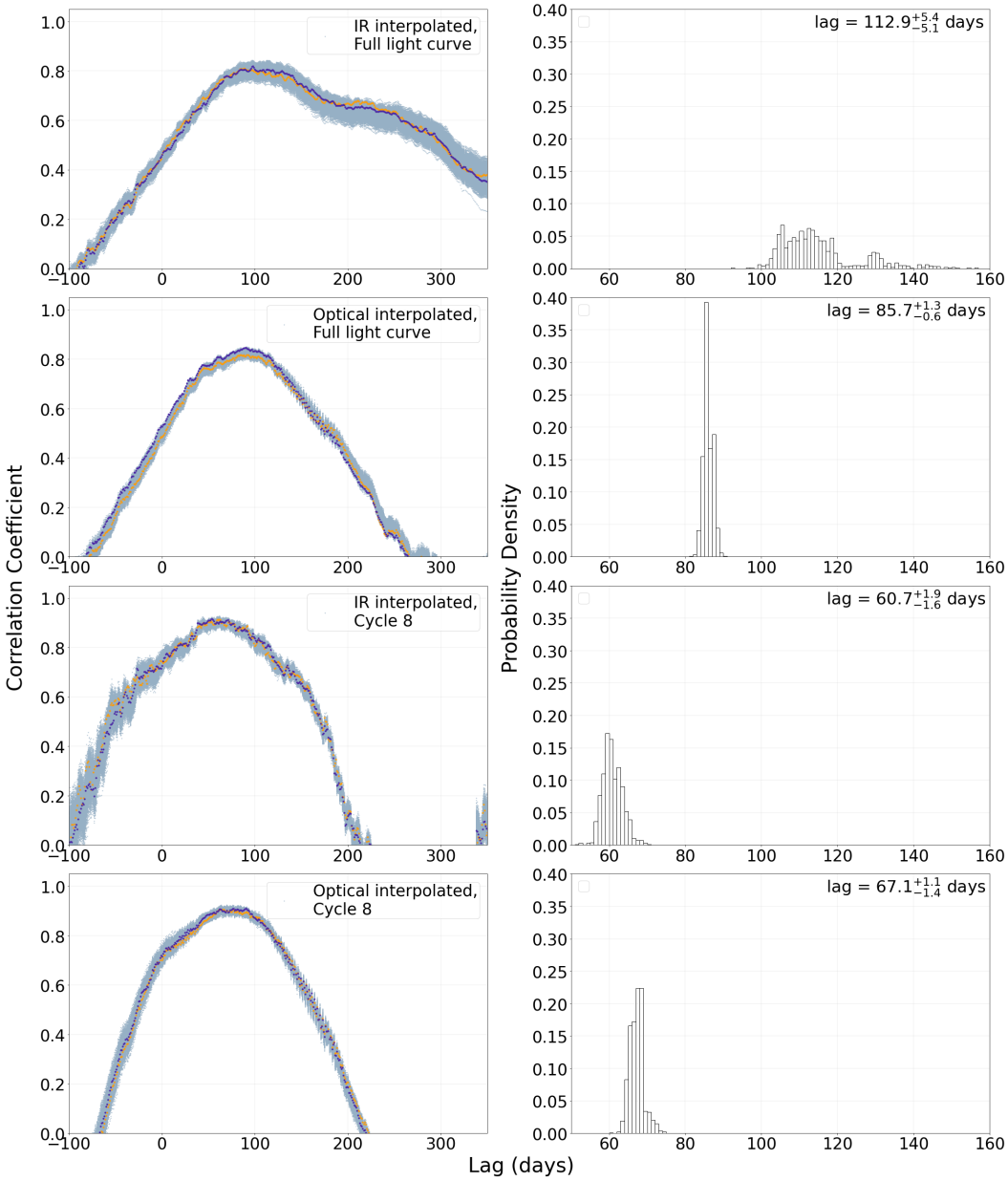

Figure 4.44: ‘

MRK 507 CCFs and CCCDs for the combined optical-3.6μm analysis: The top two plots show the results of using the full optical light curve and either IR interpolation (top row), or optical interpolation (second row). The bottom two plots show the results of using only the cycle 8 data and either IR interpolation (third row), or optical interpolation (fourth row). Each CCF plot includes 1000 CCFs formed from the Monte Carlo iterations, shown in light blue. As examples, the purple and orange points highlight two individual CCFs.

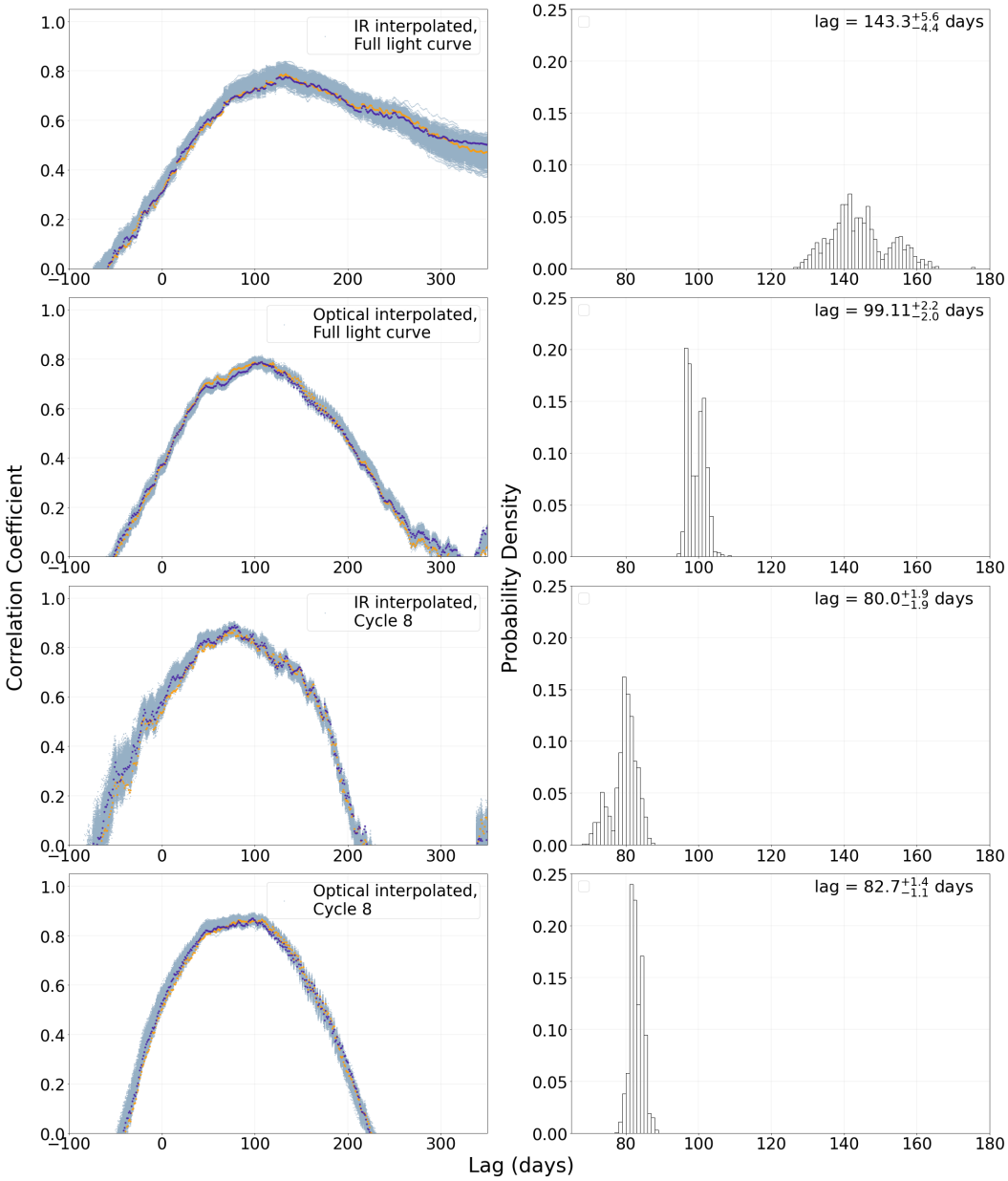

Figure 4.45: ‘

MRK 507 CCFs and CCCDs for the for the combined optical-4.5μm analysis: The top two plots show the results of using the full optical light curve and either IR interpolation (top row), or optical interpolation (second row). The bottom two plots show the results of using only the cycle 8 data and either IR interpolation (third row), or optical interpolation (fourth row). Each CCF plot includes 1000 CCFs formed from the Monte Carlo iterations, shown in light blue. As examples, the purple and orange points highlight two individual CCFs.

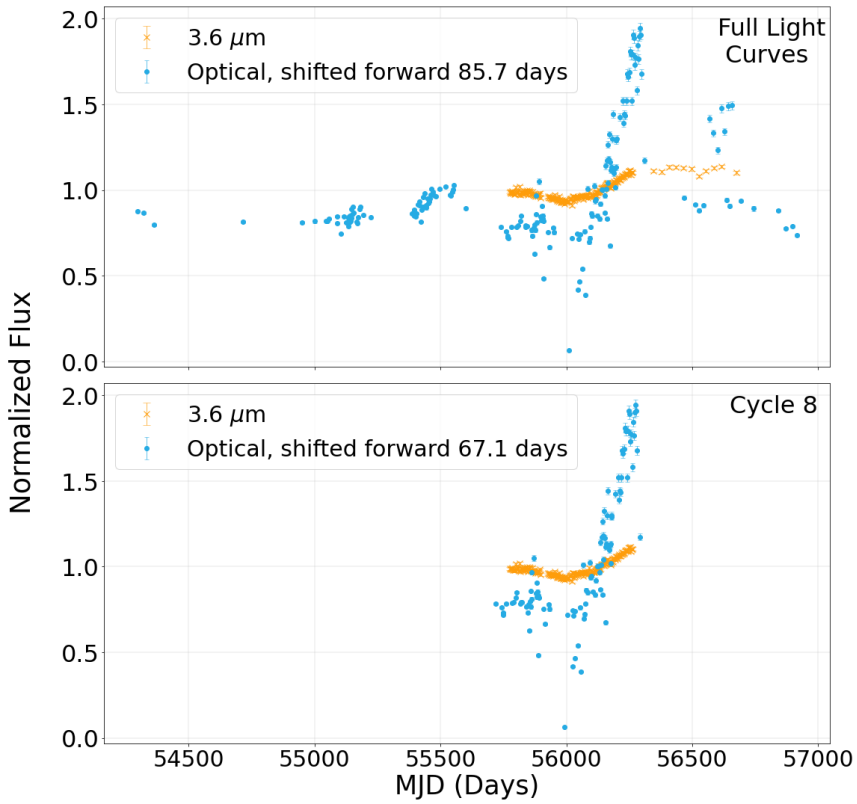

Figure 4.46: MRK 507 3.6 μm and shifted optical light curves: The optical light curves are shifted forward by the measured lag value using optical interpolation for the full light curves shown in the top plot, and for the cycle 8 analysis shown in the bottom plot.

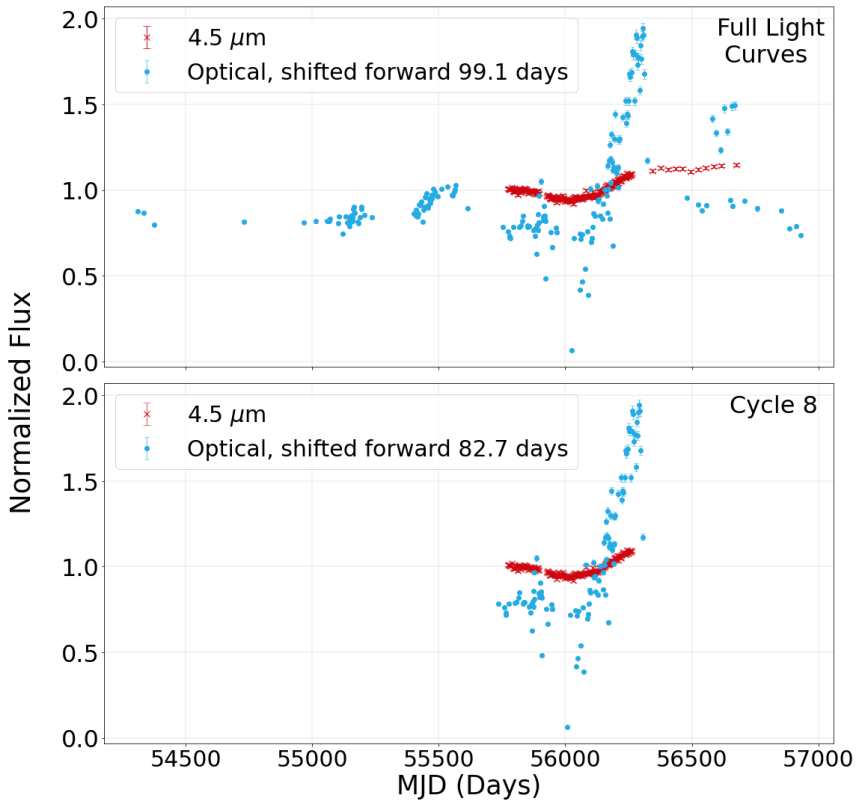

Figure 4.47: MRK 507 4.5 μm and shifted optical light curves: The optical light curves are shifted forward by the measured lag values using optical interpolation for the full light curves shown in the top plot, and for the cycle 8 analysis shown in the bottom plot.

Figures 4.46 and 4.47 shows the optical light curve shifted forward by the measured lag values, with the results from using optical interpolation for each IR channel cross-correlated with the optical light curve. In each case, the lag value appears to produce a reasonable match between the main features in the optical and IR light curves.

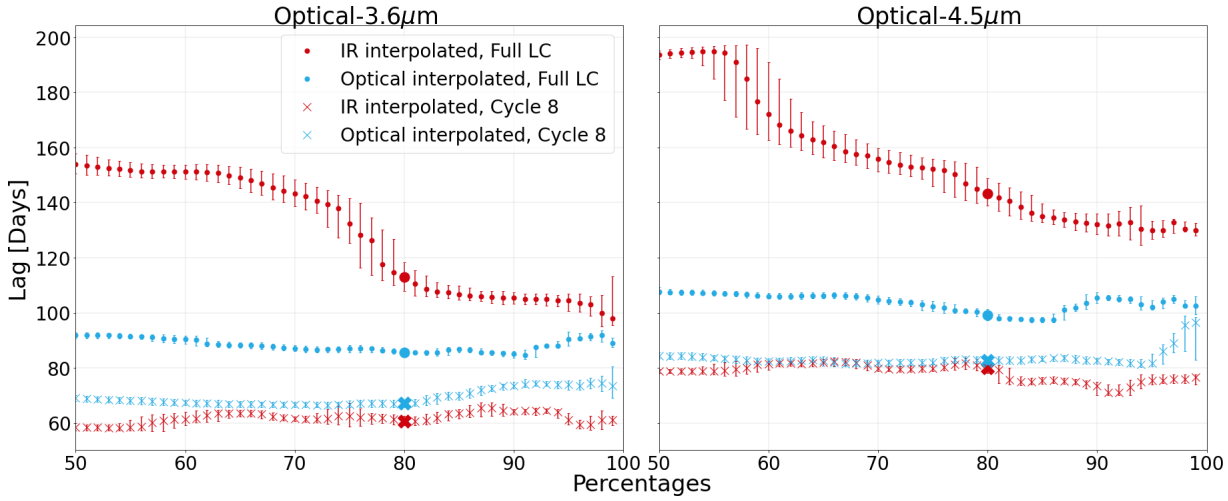

Figure 4.48: MRK 507 dependence of measured lags on CCF percentage threshold value for the 3.6 μm-optical analysis (left plot) and the 4.5 μm-optical analysis (right plot): The red points represent IR interpolation, while blue represents optical interpolation. The dots indicate lags calculated for the full light curve, and 'x's represent the lags calculated using cycle 8. The larger points indicate the 80% threshold percentage values.

Different CCF threshold percentage values were tested for both the full light curves and cycle 8 only. Figure 4.37 shows the results for the 3.6 μm-optical and 4.5 μm-optical analysis. As was true before subtracting the starlight, the least stable lag is that of the IR interpolation with the full light curve, for both IR channels. The CCFs for this interpolation type were the least symmetrical. For each interpolation type and length of the light curves, the 80% value falls in a stable region.

The lag results of the starlight-subtracted optical light curves cross-correlated with the IR light curves using different codes are shown in Figures 4.49 and 4.50. For the full light curves, the lag values measured with JAVELIN are much larger than those of the Vazquez (2015) code. For the 3.6μm-optical and 4.5μm-optical analysis of the full light curves, the JAVELIN results are $114.3^{+2.9}_{-6.5}$ days and $152.9^{+5.7}_{-5.0}$ days, respectively. For cycle 8, the lags are $73.2^{+11.8}_{-5.2}$ days and $92.5^{+3.1}_{-3.3}$ days. While the JAVELIN lags do not quite lie within the uncertainties of the results using other codes, the JAVELIN lags only differ by a few days.

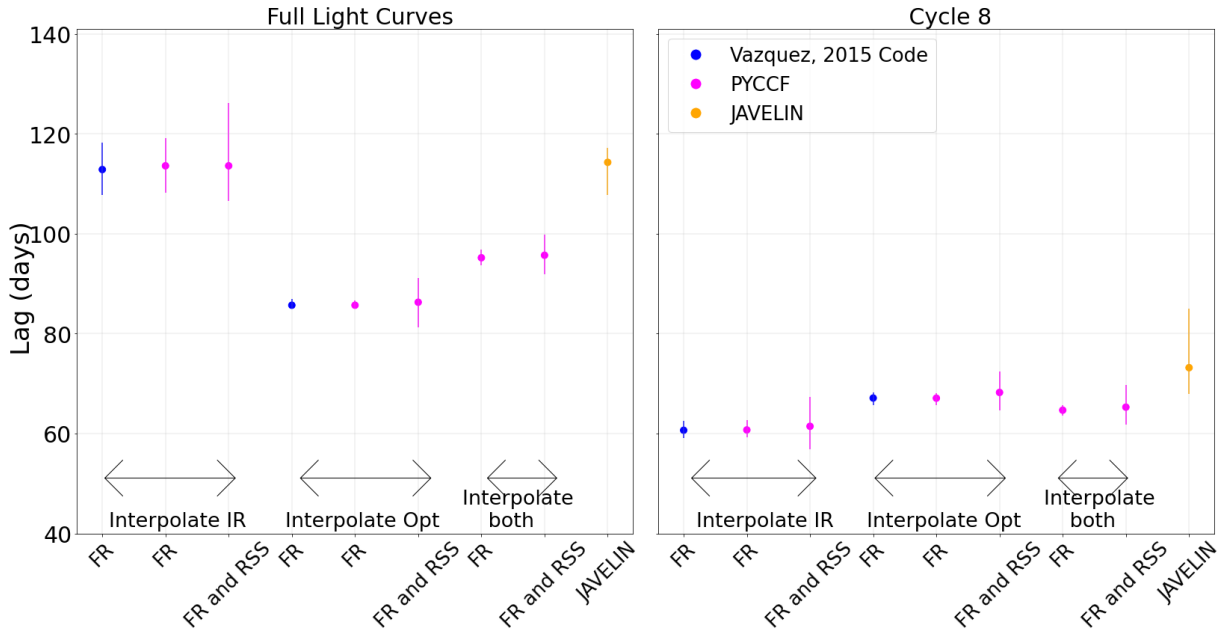

Figure 4.49: MRK 507 lag comparisons for the 3.6μm-optical analysis: The blue data points represent lag values calculated from the Vazquez (2015) code, the PYCCF results are shown in pink, and the JAVELIN results are shown in orange. The labels on the x-axis indicate whether flux randomization (FR) or both flux randomization and random subset selection (FR and RSS) was used. The labels above the x-axis specify whether the corresponding lags were calculated using IR interpolation, optical interpolation, or interpolating both. The left plot includes the results from the analysis of the full span of the light curves, and the plot on the right shows the results from the CCA using only the cycle 8 data.

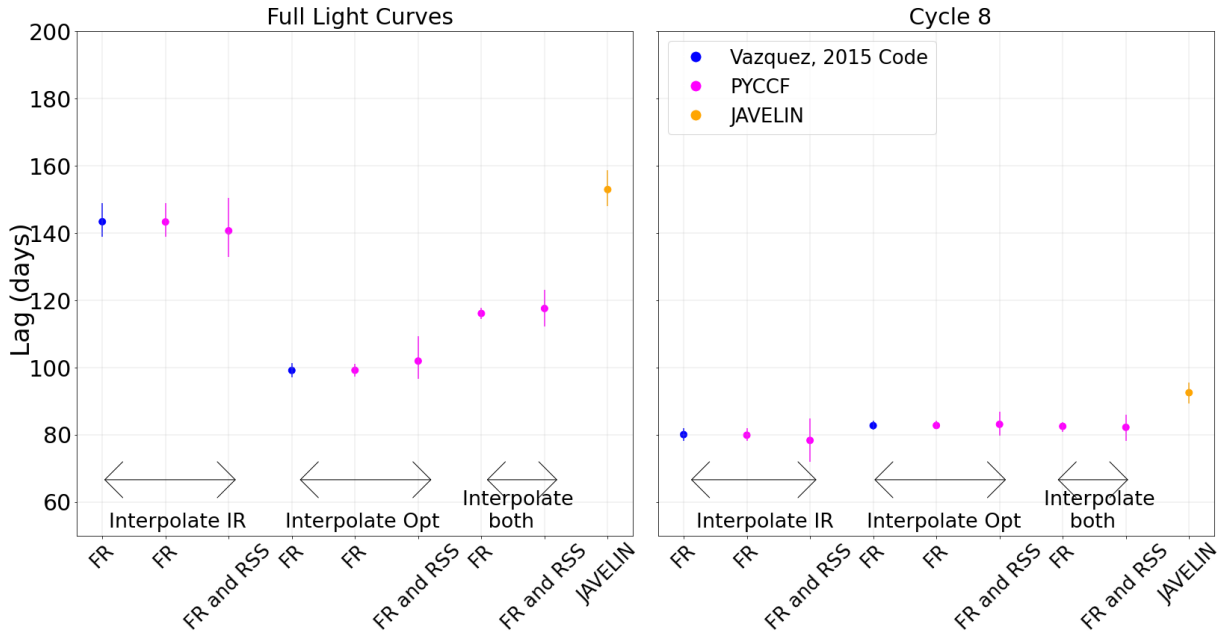

Figure 4.50: MRK 507 lag comparisons for the 4.5μm-optical analysis: The blue data points represent lag values calculated from the Vazquez (2015) code, the PYCCF results are shown in pink, and the JAVELIN results are shown in orange. The labels on the x-axis indicate whether flux randomization (FR) or both flux randomization and random subset selection (FR and RSS) was used. The labels above the x-axis specify whether the corresponding lags were calculated using IR interpolation, optical interpolation, or interpolating both. The left plot includes the results from the analysis of the full span of the light curves, and the plot on the right shows the results from the CCA using only the cycle 8 data.

MRK 507 3.6-4.5μm Analysis: There is also a lag between the two IR channels, therefore CCA was completed for the IR light curves cross-correlated with each other. The CCFs and CCCDs are shown in Figures 4.51 and 4.52 respectively, for both types of interpolation (3.6μm or 4.5μm interpolation). The shapes of the CCFs are slightly different. Using 4.5μm interpolation produces a CCF with a more gradual slope as the lag values increase, while the opposite is true for 3.6μm light curve interpolation. When looking at the CCCDs, it is clear that the lag results are different, depending on which light curve is interpolated. This is unexpected, since both IR light curves appear to have very similar features. The CCCDs formed from PYCCF are also shown in Figure 4.52. Including both flux randomization and random subset selection gives similar results to those

from the Vazquez (2015) code, although the distribution is more broad.

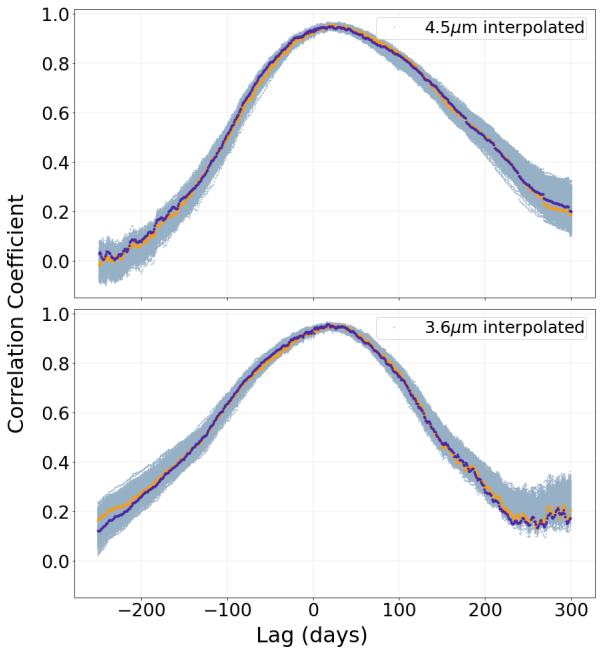

Figure 4.51: MRK 507 CCFs for the 3.6-4.5μm analysis: The top subplot shows the CCFs for 4.5 μm interpolation, and the bottom subplot shows the CCFs for 3.6 μm interpolation. Each plot includes 1000 CCFs formed from the Monte Carlo iterations, shown in light blue. As examples, the purple and orange points highlight two individual CCFs..

Different threshold percentages were also tested, and the lag results are shown in Figure 4.53. There is not a stable region for either interpolation type, although as the threshold percentage value increases, the measured lag values converge. Also, the range of measured lags is much smaller for the 3.6μm interpolation (12 days), compared to that for 4.5μm interpolation (25 days).

Visually inspecting the light curves, it is difficult to determine which lag seems more reasonable, as both shifted light curves look very similar (see Figure 4.54). The 14 day lag appears to be a better match for the main increase in flux of the two light curves that occurs from MJD 56022-56262. For the 31 day shift, the 3.6 μm light curve appears to be slightly lagging the 4.5 μm light curve in this region, although maybe the light curves overlap more for the initial flux decrease.

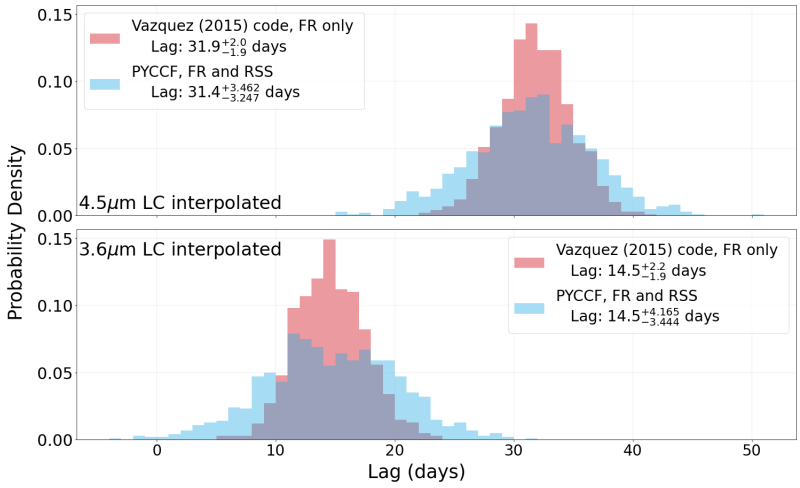

Figure 4.52: MRK 507 CCCDs from both the Vazquez (2015) code and PYCCF for the $3.6-4.5\mu$m analysis. The top plot shows the results of using 4.5μm interpolation, while the bottom plot shows the results of 3.6μm interpolation. For both subplots, the CCCDs using the Vazquez (2015) code used flux randomization (FR), while PYCCF used both flux randomization and random subset selection (FR and RSS).

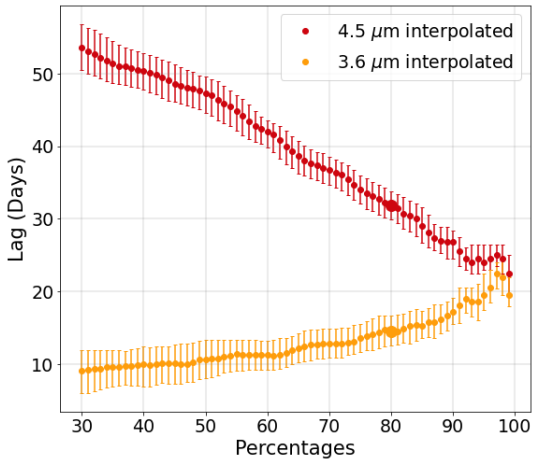

Figure 4.53: MRK 507 3.6-4.5 μm dependence of measured lags on CCF percentage threshold value: The red points show the results for 4.5 μm interpolation and the orange points show the results of 3.6 μm interpolation.

Summary of MRK 507 Lags Before subtracting the starlight contribution, the PTF and IR light curves can be used to constrain the lag for both the full span of the light curves, and cycle

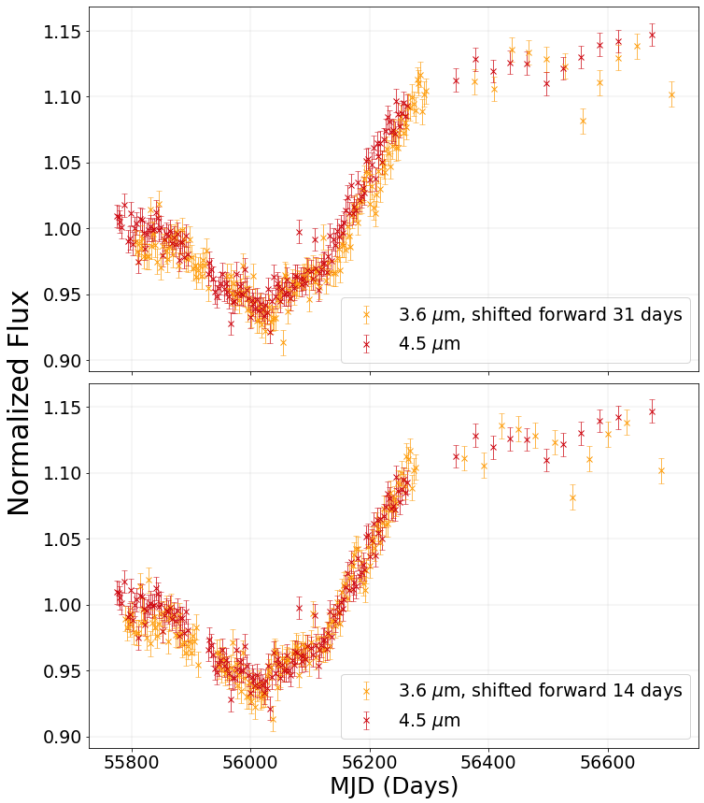

Figure 4.54: MRK 507 shifted IR light curves: The top plot shows the 3.6 μm light curve shifted forward by the measured lag value of 31.9 days, from the 4.5 μm interpolation. The bottom plot shows the 3.6 μm light curve shifted forward by the measured lag value of 14.5 days, from 3.6 μm interpolation.

8 only. Tables 4.2 and 4.3 present the lag results for each IR light curve cross-correlated with the optical for each interpolation direction, using the full light curves or only cycle 8.

With the exception of the 3.6μm-optical analysis for cycle 8, the JAVELIN lags appear to be too large when comparing Figures 4.35 and 4.36 to Figures 4.38 and 4.39. The PYCCF and Vazquez (2015) codes give more reliable lag values based on the shifted light curves. For both the full light curve analysis and cycle 8 analysis, interpolating the optical onto IR timestamps gives less noisy and narrower CCFs, although the width of the CCCDs are all similar (see Figures 4.33 and 4.34). Using IR interpolation for the full light curves produces CCFs with a strange shape (CCFs flatten for large lags), although all of the CCCDs are well-behaved. There are no clear benefits to either

of the interpolation types.

Given that PYCCF and the Vazquez (2015) codes calculate more reasonable lag values, the best estimates of the lag are the following: For the full light curves, the measured lags are between 86.7-93.2 days for the optical-3.6μm analysis, and 105.5-123.2 days for the optical-4.5μm analysis. The cycle 8 lags are between 58.3-72.5 days for the optical-3.6μm analysis, and 72.1-84.1 days for the optical-4.5μm analysis.

Using only the Cycle 8 data always produces shorter lags than using the full light curves. While the shifted light curves using the lags from only cycle 8 show the light curves overlapping for the rise in flux, the lags for the full light curves produce a reasonable overall match between the IR and optical light curve features.

The starlight contribution was then subtracted, and CCA was performed on the combined optical-IR light curves. With the full span of the light curves, using IR interpolation produces CCFs that are very flat for large lag values (see Figures 4.44 and 4.45). Using optical interpolation produces CCFs with a clearer peak. For the cycle 8 analysis, both interpolation types produce well-shaped CCFs and CCCDs, with no clear benefit to either interpolation type. When shifting the light curves by the calculated lag values, the lags appear to be reasonable (see Figures 4.46 and 4.47). The lags produced by JAVELIN using the full span of the light curves appear to be too large, although the results are more reasonable when using only the cycle 8 section.

Considering the PYCCF and the Vazquez (2015) codes, the best estimate of the lags are as follows: For the full span of the light curves and considering only optical interpolation or interpolating both light curves, the lag is measured to be between 85.7-95.7 days for the optical-3.6μm analysis, and 99.1-117.5 days for the optical-4.5μm analysis. Considering any of the interpolation types with PYCCF or the Vazquez (2015) codes, the cycle 8 lag was measured to be between 60.7-68.2 days for the optical-3.6μm analysis, and 78.3-83.1 days for the optical-4.5μm analysis.

The lag was also measured between the two IR channels. Depending on the order of interpolation, it is between 14.5 and 31.9 days, with the 14.5 day lag producing a better match between the shifted light curves (See Figure 4.54). For the Vazquez (2015) code, the differences between the

measured IR-optical lags for each IR channel is 13.4-30.5 days when using the full light curves, and 12.5-19.3 days when using only cycle 8, depending on which interpolation type is used and whether the lags are taken from the starlight-subtracted or not-starlight-subtracted light curves. These are consistent with the lags measured between the two IR channels.

	Before Starlight-Subtraction				After Starlight-Subtraction	
	3.6μm-optical		4.5μm-optical		3.6μm-optical	4.5μm-optical
	Interp IR	Interp Opt	Interp IR	Interp Opt	Interp Opt	Interp Opt
Vazquez (2015)	$92.7^{+5.2}_{-4.5}$	$89.0^{+4.5}_{-4.3}$	$123.2^{+5.3}_{-5.8}$	$106.1^{+5.1}_{-6.2}$	$85.7^{+1.3}_{-0.6}$	$99.1^{+2.2}_{-2.0}$
PYCCF (FR and RSS)	$93.2^{+8.4}_{-6.0}$	$86.7^{+8.3}_{-7.6}$	$120.9^{+6.8}_{-7.4}$	$105.5^{+8.2}_{-9.9}$	$86.3^{+4.8}_{-5.0}$	$101.9^{+7.4}_{-5.4}$
JAVELIN	$133.3^{+6.0}_{-7.7}$		$137.2^{+5.0}_{-5.1}$		$114.3^{+2.9}_{-6.5}$	$152.9^{+5.7}_{-5.0}$

Table 4.2: Summary of MRK 507 Lag Results, Full Light Curves: The '3.6μm-B band' and '4.5μm-B band' columns show the results for each IR light curve cross-correlated with the LT B band light curve, for each order of interpolation. Each row gives the lag results using the Vazquez (2015) code using FR only, PYCCF using both FR and RSS, and JAVELIN.

	Before Starlight-Subtraction				After Starlight-Subtraction			
	3.6μm-optical		4.5μm-optical		3.6μm-optical		4.5μm-optical	
	Interp IR	Interp Opt	Interp IR	Interp Opt	Interp IR	Interp Opt	Interp IR	Interp Opt
Vazquez (2015)	$58.6^{+5.2}_{-4.5}$	$71.4^{+4.3}_{-3.8}$	$72.6^{+7.5}_{-4.6}$	$83.9^{+3.3}_{-3.5}$	$60.7^{+1.9}_{-1.6}$	$67.1^{+1.1}_{-1.4}$	$80.0^{+1.9}_{-1.9}$	$82.7^{+1.4}_{-1.1}$
PYCCF (FR and RSS)	$59.8^{+9.2}_{-8.4}$	$72.5^{+6.3}_{-6.3}$	$74.3^{+9.8}_{-8.1}$	$84.1^{+5.8}_{-5.2}$	$61.5^{+5.9}_{-4.6}$	$68.2^{+4.1}_{-3.6}$	$78.3^{+6.6}_{-6.5}$	$83.1^{+3.7}_{-3.4}$
JAVELIN	$78.12^{+46.9}_{-8.0}$		$133.1^{+61.2}_{-13.2}$		$73.2^{+11.8}_{-5.2}$		$92.5^{+3.1}_{-3.3}$	

Table 4.3: Summary of MRK 507 Lag Results, Cycle 8: The '3.6μm-B band' and '4.5μm-B band' columns show the results for each IR light curve cross-correlated with the LT B band light curve, for each order of interpolation. Each row gives the lag results using the Vazquez (2015) code using FR only, PYCCF using both FR and RSS, and JAVELIN.

4.2.3 UGC 10697

UGC 10697 has been classified as a Sy 1 and has an estimated bolometric luminosity of 0.42×10^{45}erg/s. As discussed in Chapter 3, negative fluxes were obtained for UGC 10697 after subtracting the starlight contribution, therefore the starlight-subtracted CCA results will not be presented.

Before Host Galaxy-Subtraction: LT B band-IR Analysis Figure 4.55 shows the optical and IR light curves used for the CCA. The analysis was performed with either optical or IR

interpolation. Examples of these two interpolation types are shown in Figure 4.56.

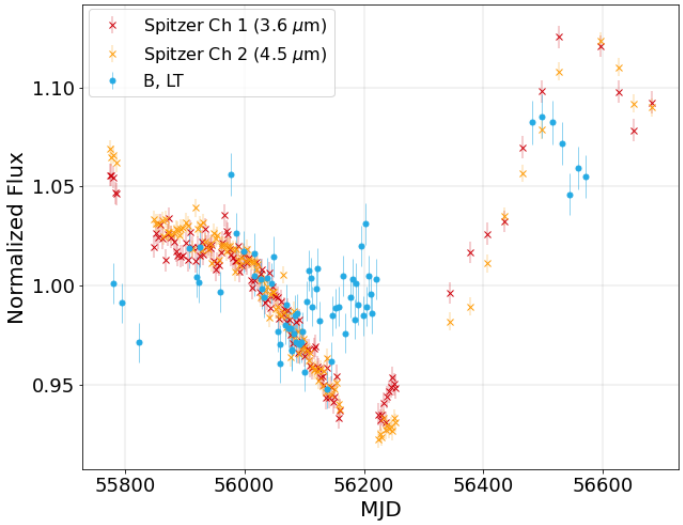

Figure 4.55: UGC 10697 LT B band and IR light curves: The orange and red points represent the IR Spitzer data, while the blue points represent the LT B band data.

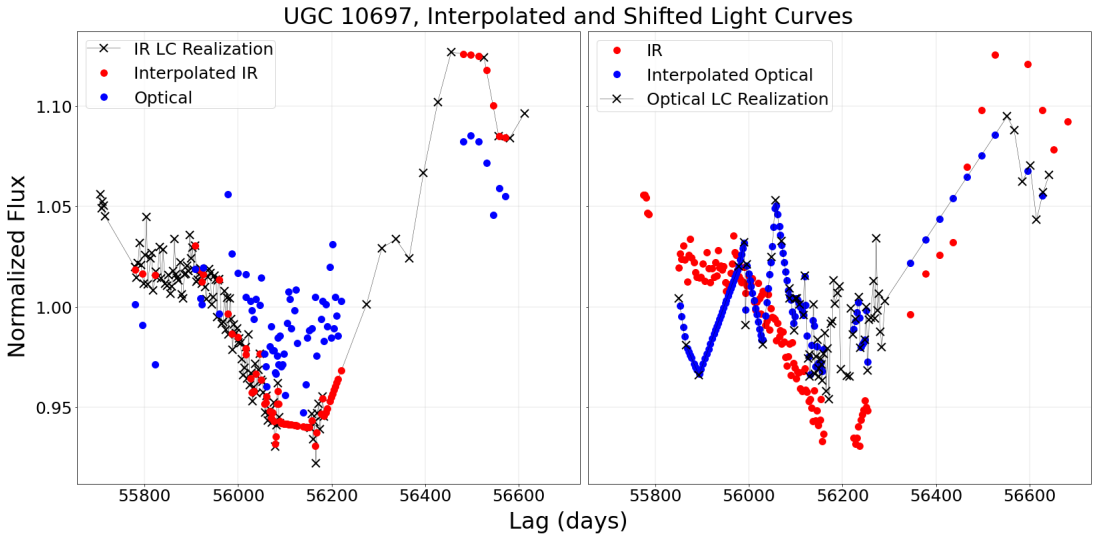

Figure 4.56: Examples of interpolated optical and and 3.6 μm light curves for UGC 10697: The plot on the left shows one IR light curve realization (the black points), the blue points represent the optical light curve, and the red points represent the IR points linearly interpolated onto the time stamps of the optical data points. Here, the IR light curves have been shifted back by 70 days. The plot on the right is similar, showing one of the optical light curve realizations in black, the IR light curve is shown in red, and the blue points represent the optical points linearly interpolated onto the time stamps of the IR data points. Here, the optical light curve has been shifted forward by 70 days.

The lags calculated using IR interpolation are $67.5^{+4.1}_{-4.2}$ days and $81.7^{+3.7}_{-2.3}$ days for the 3.6μm-optical and 4.5μm-optical analysis, respectively. With optical interpolation, the lags are shorter; $15.8^{+28.5}_{-6.4}$ days and $16.2^{+41.4}_{-6.6}$ days respectively for each IR channel cross-correlated with the optical. CCFs and CCCDs are shown in Figures 4.57 and 4.58. In contrast to the two AGN described above, the CCFs formed using IR interpolation appear to have clearer peaks and higher peak values of the correlation coefficients than those formed using optical interpolation. The CCCDs generated using IR interpolation also have a single peak, compared to the multiple peaks of the CCCDs obtained with optical interpolation. Looking at Figure 4.56, this could be caused by the large gaps between the points during the first section of the optical light curve (from ∼MJD 59000 to 56000, ∼MJD 56000 to 56020, and ∼MJD 56020 to 56080), which are filled with linearly interpolated points. These regions may cause multiple peaks to appear in the CCCDs, as the code finds correlations

between the linear features of the IR light curve, and the interpolated linear regions of the optical light curve. Interpolating the IR light curve onto the timestamps of the optical leads to a clearer result, with a well defined peak in the CCF and a single peak in the CCCD.

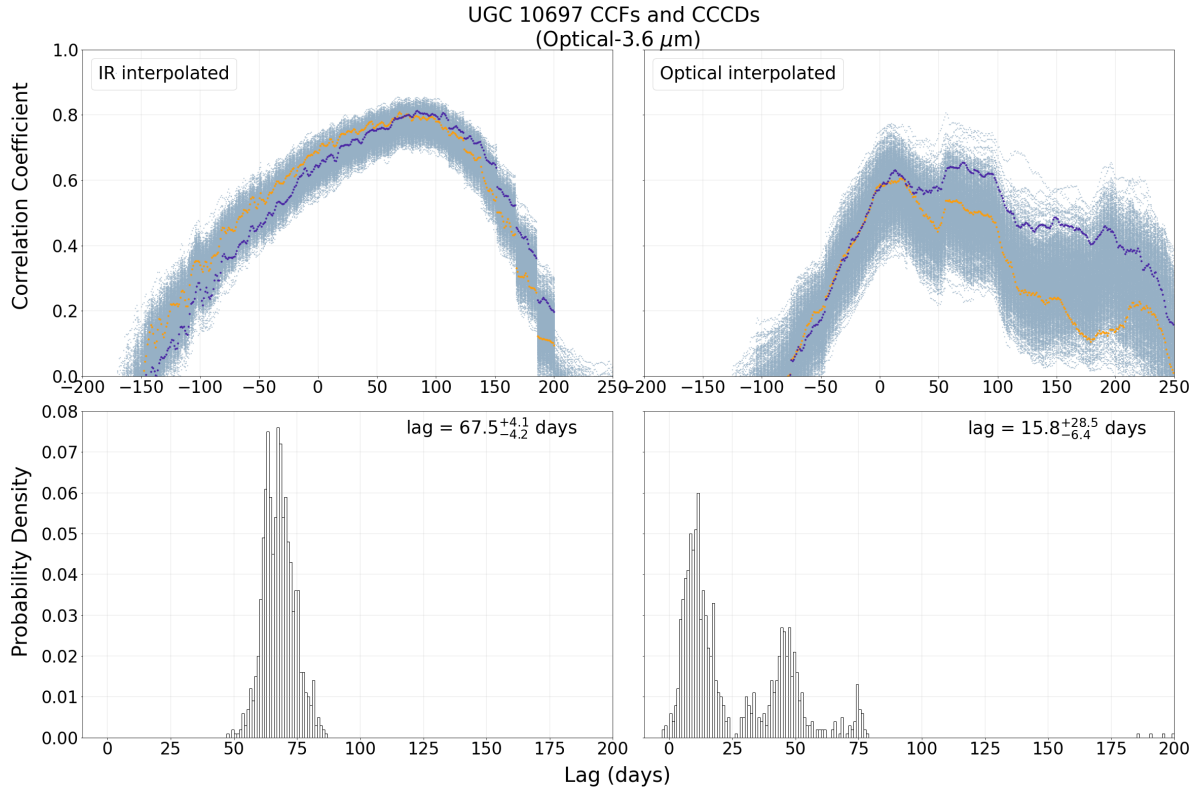

Figure 4.57: UGC 10697 CCFs (top subplots) and CCCDs (bottom subplots) for the B band-3.6μm analysis. The subplots on the left show the results from using IR interpolation, and the subplots on the right show the results from using optical interpolation. The upper plots include 1000 CCFs formed from the Monte Carlo iterations, shown in light blue. As examples, the purple and orange points highlight two individual CCFs.

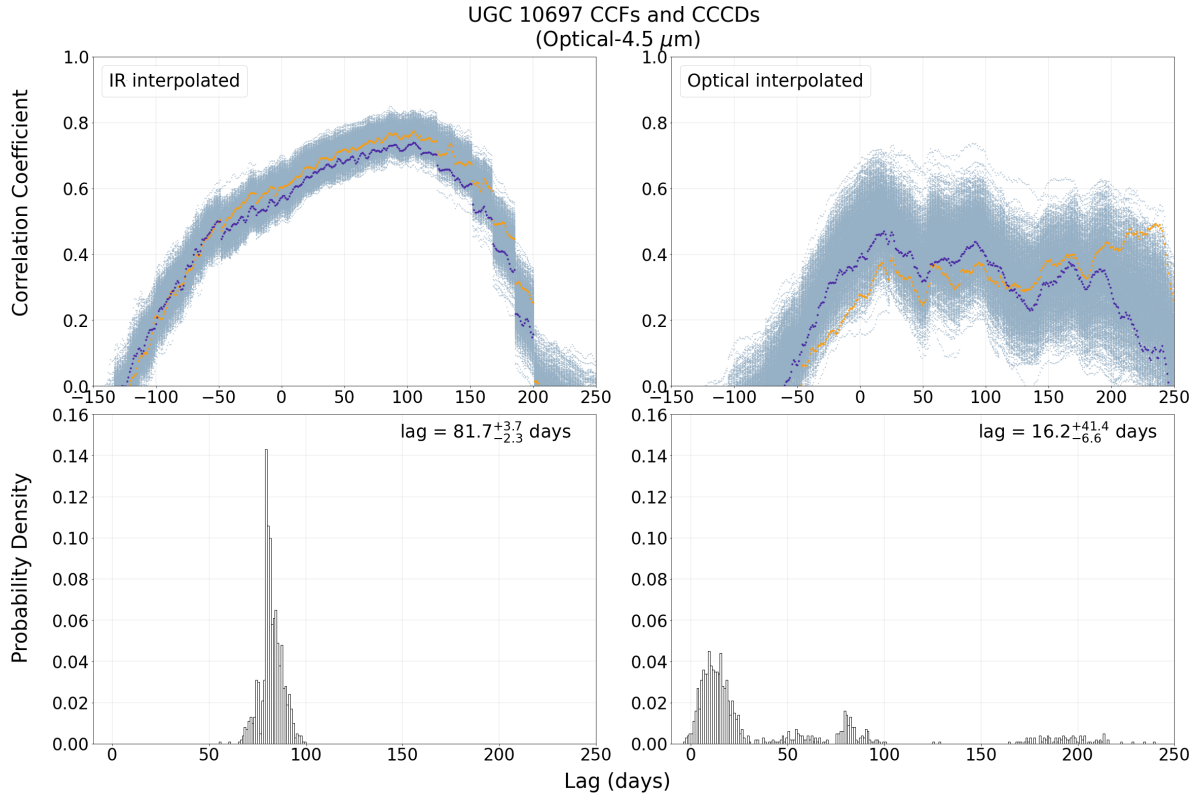

Figure 4.58: UGC 10697 CCFs (top subplots) and CCCDs (bottom subplots) for the B band-4.5μm analysis. The subplots on the left show the CCFs that result from using IR interpolation, and the subplots on the right show the CCFs that result from using optical interpolation. The upper plots include 1000 CCFs formed from the Monte Carlo iterations, shown in light blue. As examples, the purple and orange points highlight two individual CCFs.

Plots of the measured lag values vs the CCF threshold percentage values are shown in Figure 4.59. The most stable region for both plots is between threshold values of approximately 1-50%. It is clear why this occurs when looking at the CCFs in Figures 4.57 and 4.58. The peaks of the CCFs are skewed towards larger lag values, so lowering the percent threshold value leads to shorter measured lags. Although choosing a different percentage value would lead to a different measured lag, the lag-threshold trends for the two IR channels have similar slopes, so the difference between the lag values of each channel cross-correlated with the optical tends to be $\sim$ 10 days.

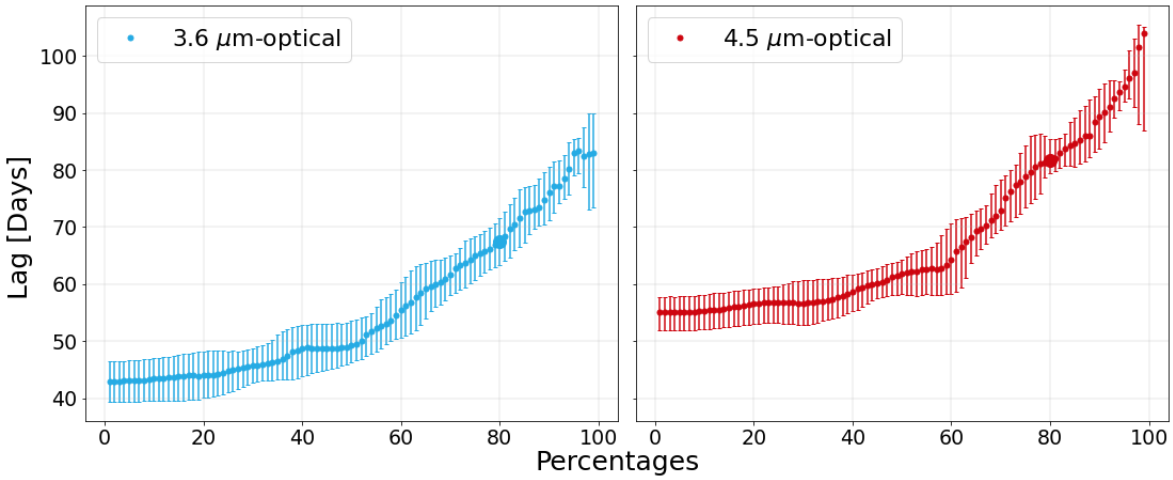

Figure 4.59: UGC 10697 dependence of measured lags on CCF percentage threshold value: The upper plot shows results for 3.6μm-optical, and the lower plot for 4.5μm-optical. The two larger points indicate the 80% threshold values.

Figure 4.60 shows the optical light curve shifted forward by the measured lag values. For both IR channels cross-correlated with the optical, the measured lags appear to be reasonable. The main feature of the IR light curves is a minimum at ∼MJD 56200 and a sharp increase in flux leading to a peak in the IR at ∼MJD 56600. The shifted light curves show that the lag is being measured between these main features.

The lag measured with JAVELIN is $71.4^{+5.4}_{-5.5}$ days for 3.6μm-optical analysis, which is within the errors of the Vazquez (2015) and PYCCF results. The 4.5μm-optical lag is $93.8^{+3.5}_{-4.4}$ days measured by JAVELIN, which is not quite within the errors of the Vazquez (2015) and PYCCF results. A comparison of the lags measured with each code is shown in Figures 4.62 and 4.63.

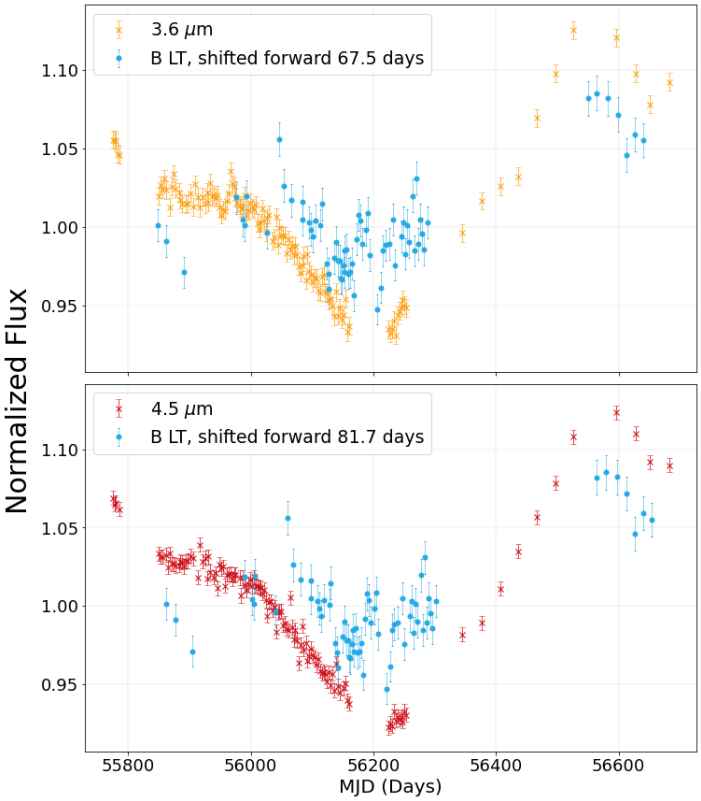

Figure 4.60: UGC 10697 shifted optical light curves: The optical light curves are shifted forward by 67.5 days for the optical-3.6 μm analysis (top panel) and 81.7 days for the optical-4.5 μm analysis (bottom panel).

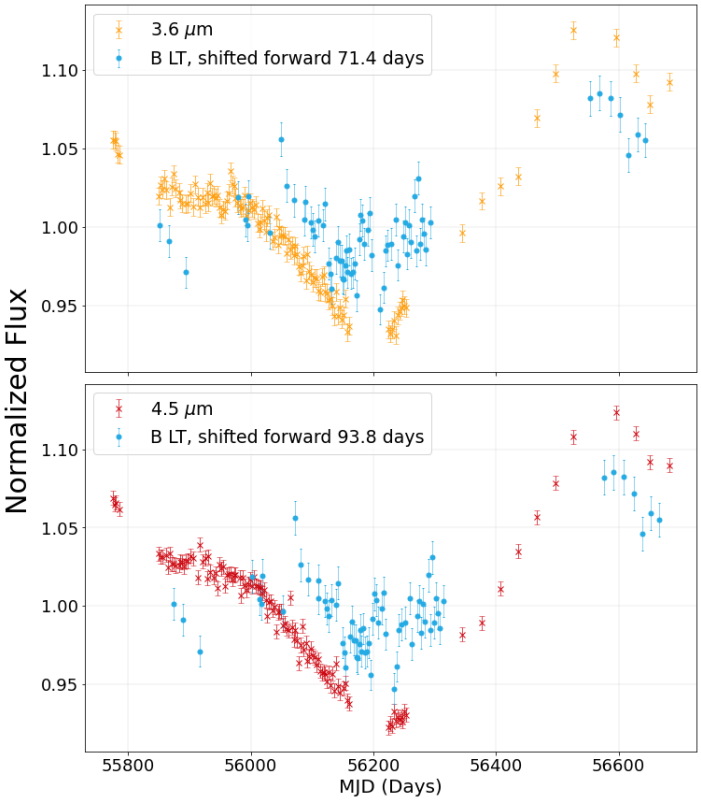

Figure 4.61: UGC 10697 PTF and IR light curves, shifted by JAVELIN lag values: The optical light curves are shifted forward by 71.4 days for the optical-3.6 μm analysis (top panel) and 93.8 days for the optical-4.5 μm analysis (bottom panel).

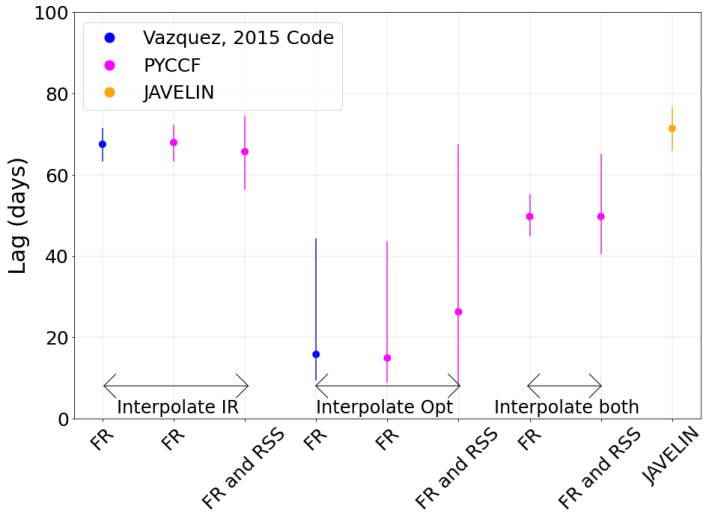

Figure 4.62: UGC 10697 lag comparisons for the 3.6μm-optical analysis: The blue data points represent lag values calculated from the Vazquez (2015) code, the PYCCF results are shown in pink, and the JAVELIN results are shown in orange. The labels on the x-axis indicate whether flux randomization (FR) or both flux randomization and random subset selection (FR and RSS) was used. The labels above the x-axis specify whether the corresponding lags were calculated using IR interpolation, optical interpolation, or interpolating both. The left plot includes the results from the analysis of the full span of the light curves, and the plot on the right shows the results from the CCA using only the cycle 8 data.

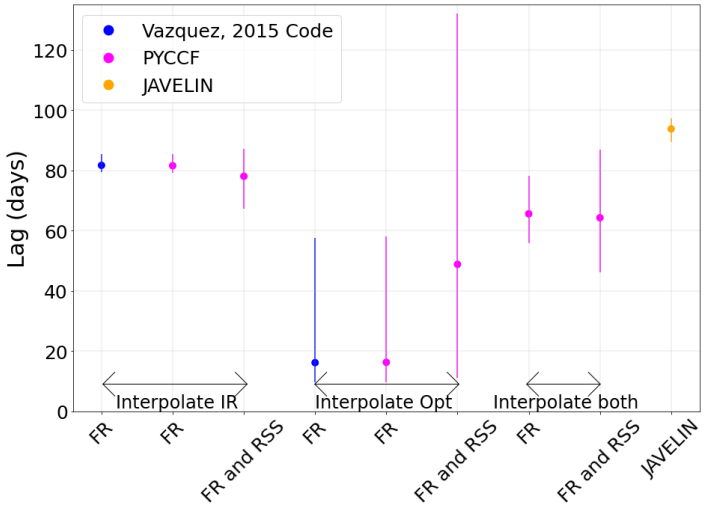

Figure 4.63: UGC 10697 lag comparisons for the 4.5μm-optical analysis: The blue data points represent lag values calculated from the Vazquez (2015) code, the PYCCF results are shown in pink, and the JAVELIN results are shown in orange. The labels on the x-axis indicate whether flux randomization (FR) or both flux randomization and random subset selection (FR and RSS) was used. The labels above the x-axis specify whether the corresponding lags were calculated using IR interpolation, optical interpolation, or interpolating both. The left plot includes the results from the analysis of the full span of the light curves, and the plot on the right shows the results from the CCA using only the cycle 8 data.

3.6-4.5 Analysis The lag was then measured between the two IR channels. Figures 4.64 and 4.65 show the CCFs and CCCDs for both interpolation types. The lag values calculated using the Vazquez (2015) code is $8.4^{+1.9}_{-1.9}$ days with 4.5μm interpolation, or $21.8^{+1.9}_{-1.8}$ days with 3.6μm interpolation. The CCCDs calculated with PYCCF are also included in Figures 4.64 and 4.65. Since the PYCCF results included both FR and RSS, the measured lag values only differ by a day from the Vazquez (2015) lag values, although the uncertainties are larger.

Figure 4.67 shows the IR light curves shifted by the measured lag values. With 4.5μm interpolation, the lag seems to be measured between the feature of the decrease in flux of the first half of the campaign, while the lag measured using 3.6μm interpolation appears to correspond to the increase in flux during the last half of the campaign.

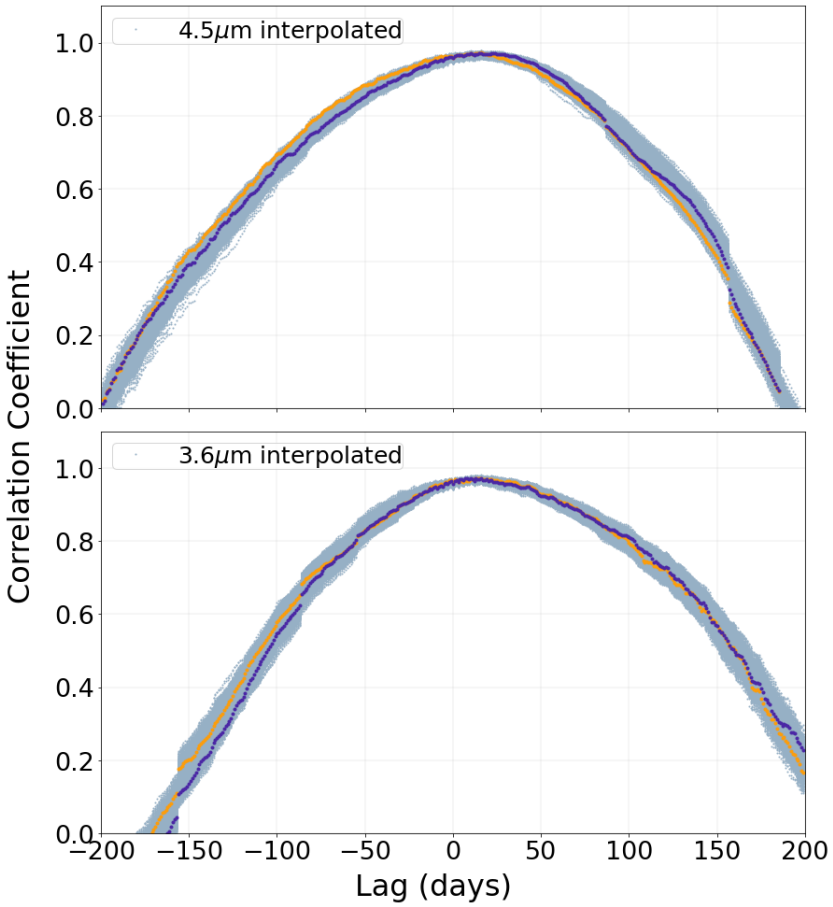

Figure 4.64: UGC 10697 CCFs for the 3.6-4.5μm analysis: The top subplot shows the CCFs for 4.5 μm interpolation, and the bottom subplot shows the CCFs for 3.6 μm interpolation. Each plot includes 1000 CCFs formed fromo the Monte Carlo iterations, shown in light blue As examples, the purple and orange points highlight two individual CCFs.

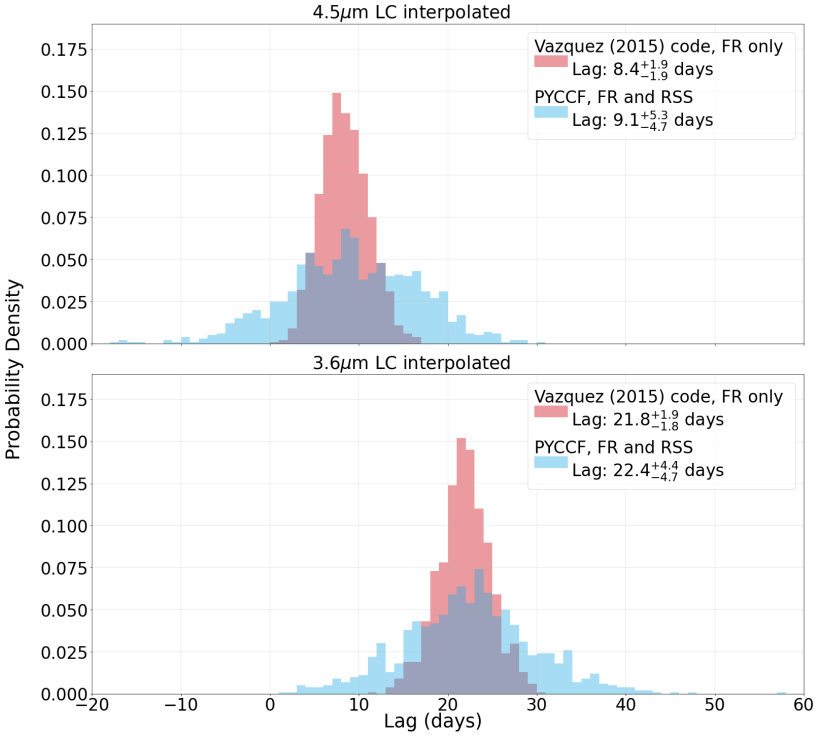

Figure 4.65: UGC 10697 CCCDs from both the Vazquez (2015) code and PYCCF for the 3.6-4.5 μm analysis. The top plot shows the results of using 4.5 μm interpolation, while the bottom plot shows the results of using 3.6μm interpolation. For both subplots, the CCCDs formed from the Vazquez (2015) code include FR, while PYCCF includes both FR and RSS.

Figure 4.66 shows different percentage threshold values for the IR channels cross-correlated with each other. As the peaks of the CCFs coincide, using a large percentage threshold value leads to a similar lag for both interpolation types.

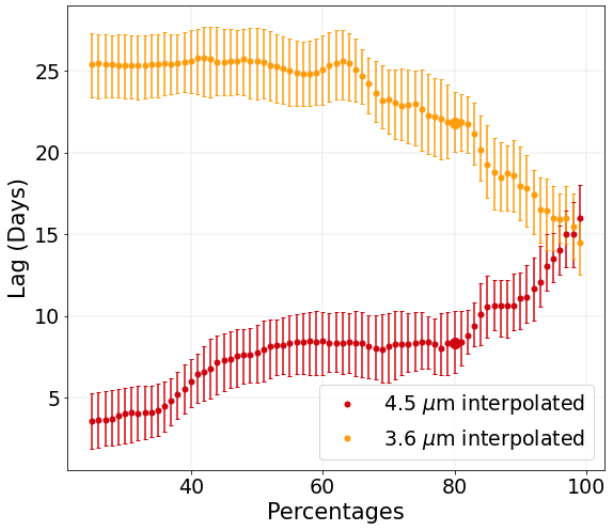

Figure 4.66: UGC 10697 dependence of measured lags on CCF percentage threshold value: The red points show results for 4.5 μm interpolation, and the orange points show results for 3.6 μm interpolation. The two larger points are indicating the 80% threshold values.

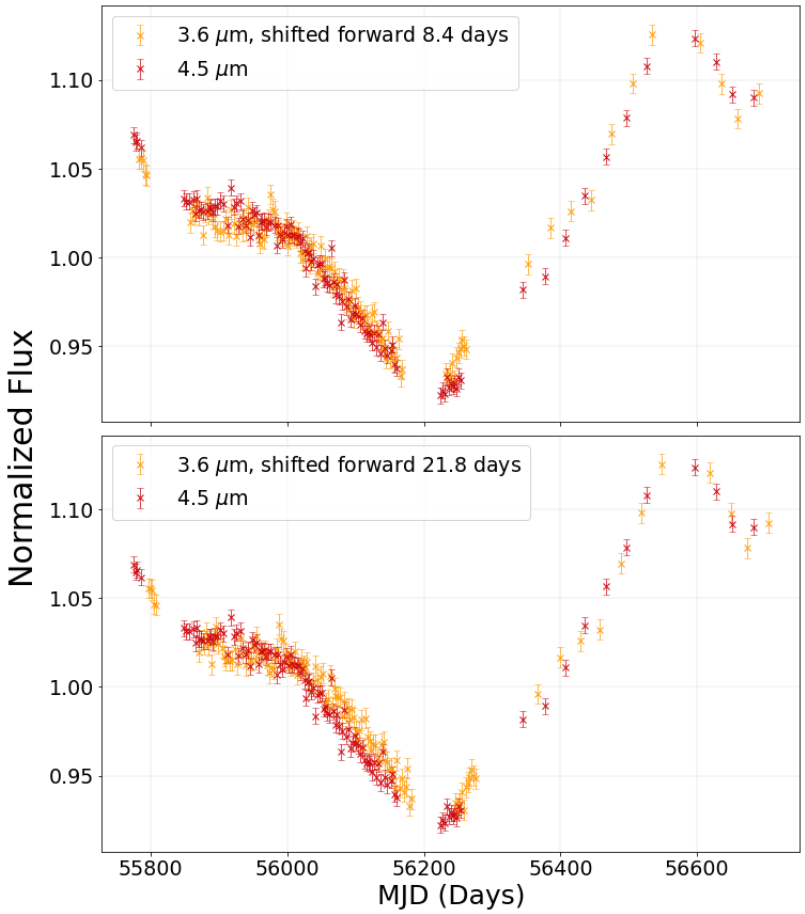

Figure 4.67: UGC 10697 shifted light curves: The top subplot shows the 3.6 μm light curve light curve shifted forward by the measured lag value from using 4.5 μm interpolation, with a lag of 8.4 days. The bottom subplot shows the 3.6 μm light curve light curve shifted forward by the measured lag from using 3.6 μm interpolation, with a lag of 21.8 days.

Summary of UGC 10697 Lags The lag results are summarized in Table 4.4. The lags reported with the Vazquez (2015) code and PYCCF were calculated using IR interpolation, as this produced CCFs with clearer peaks and higher peak values of the correlation coefficient. The CCCDs also have a single clear peak (see Figures 4.57 and 4.58). The lag measured with JAVELIN is within the errors of the Vazquez (2015) and PYCCF results for the 3.6μm-optical analysis, but not for the 4.5μm-optical results, although the lag is only a few days off from the errors.

Cross-correlating the two IR channels with each other leads to a lag result between 8.4 and 22.4

days, depending on which IR light curve is interpolated onto the other. The difference between the 3.6μm-optical and 4.5μm-optical lags is 14.2 days, which differs by $\sim$6 days from the 3.6-4.5μm result with the Vazquez (2015) code. The difference between the 3.6μm-optical and 4.5μm-optical lags calculated with JAVELIN is 22.4 days, which only differs by one day from the lag calculated using 4.5μm interpolation. The lag between the two IR channels is clearly between 8.4 and 22.4 days.

Table 4.4: UGC 10697 Summary of Lag Results: The '3.6μm-LT' and '4.5μm-LT' columns show the lag results of each IR light curve cross-correlated with the LT B band light curve using IR interpolation. The '3.6-4.5μm' column gives the lag results from cross-correlating the two IR channels with each other, with 4.5 μm interpolation. Each row gives the lag results using the Vazquez (2015) code using FR only, PYCCF using both FR and RSS, and JAVELIN.

	3.6μm-LT	4.5μm-LT	$3.6 - 4.5\mu$m
Vazquez (2015)	$67.5^{+4.1}_{-4.2}$	$81.7^{+3.7}_{-2.3}$	$8.4^{+1.9}_{-1.9}$
PYCCF (FR and RSS)	$65.7^{+8.8}_{-9.4}$	$78.1^{+9.0}_{-10.9}$	$9.1^{+5.3}_{-4.7}$
JAVELIN	$71.4^{+5.4}_{-5.5}$	$93.8^{+3.5}_{-4.4}$	-

4.3 Comparison to Sublimation Radii

In Chapter 2, the sublimation radii (and corresponding lags) were calculated using Equation 1.1 and the bolometric luminosities were estimated using the bolometric correction equations. These values are shown in Table 2.2. A comparison of the measured lags of the AGN and their calculated sublimation radii is discussed here.

KAZ 163 The lag associated with the sublimation radius is $\tau_{\rm sub} = 926.8$ days, while the reverberation lags are $\sim 120 - 130$ days. $\tau_{\rm sub}$ is larger than the reverberation lag by $\sim$a factor of 7.

MRK 507 The lag associated with the sublimation radius is $\tau_{\rm sub} = 772.3$ or $\tau_{\rm sub} = 534.6$ days, depending on whether the IR or x-ray bolometric corrections are used to calculate the luminosity.

The reverberation lags are approximately $90 - 100$ days. $\tau_{\rm sub}$ is larger than the reverberation lag by $\sim$a factor of 5.5 to 8

UGC 10697 The lag associated with the sublimation radius is $\tau_{\rm sub} = 308.6$ days, while the reverberation lags are $\sim 70 - 80$ days. $\tau_{\rm sub}$ is larger than the reverberation lag by approximately a factor of ~ 4.0

For each AGN, the predicted sublimation radius is much larger than our reverberation lags. There are several possibile explanations as to why this could occur. There is a large uncertainty associated with our calculated bolometric luminosities. For the AGN in which we were able to calculate the luminosity using both the x-ray and IR bolometric corrections, the sublimation radius estimates sometimes differed by more than a factor of 2.

There is also a known discrepancy between the theoretical calculation of the sublimation radius, and the results of dust reverberation mapping (Kishimoto et al., 2007). K-band (2.2μm) dust reverberation mapping results tend to be smaller than the theoretical value predicted by Equation 1.1 (which corresponds to the standard ISM grain composition and size distribution) by approximately a factor of 3. The sublimation temperature therefore depends on both grain size and composition, with a higher temperature associated with large graphite grains (Baskin & Laor, 2018). The discrepancy could be due to the typical grain size being larger than assumed (and thus grains are able to survive closer to the center), or typical sublimation temperatures being higher than expected.

CHAPTER 5

NGC 6418

5.1 Introduction

In this chapter, results are presented for one of our target objects, NGC 6418. This AGN is highlighted as it exhibited the largest variability of the 12 objects in our sample (see Tables 2.4 and 2.5). In this chapter, the IR and optical light curves, CCA results, and spectra will be presented. Through these results, we will show that NGC 6418 is a changing-look AGN.

Changing-look AGN are relatively rare, although several have been discovered in the past few years (Denney et al., 2014; Shappee et al., 2014; LaMassa et al., 2015; Runnoe et al., 2016; MacLeod et al., 2019; Green et al., 2022). An AGN is considered to be "changing-look" when it changes from Type I to Type II (or Type II to Type I). There are several possibilities as to the cause of this phenomenon, including either a change in obscuration or a change in the accretion rate. This will be discussed more in Section 5.7.

NGC 6418 has been spectroscopically classified as a Seyfert 1 AGN (Véron-Cetty & Véron, 2006) and has been identified to be an x-ray source (Remillard et al., 1993; Wang et al., 2016). In previous observations, its spectrum was largely dominated by the stellar continuum, being described as an "embedded AGN" by Remillard et al. (1993). Remillard et al. (1993) also detected strong

broad Halpha, but not strong Hbeta, implying that there is significant extinction.

Initial CCA results for the first half of the observations (cycle 8) were presented in Vazquez et al. (2015) and Vazquez (2015). Here, we present a new analysis of the complete data set from Cycles 8 and 9, based on a new version of the optical light curve and a more thorough evaluation of the CCA results. Also, in Vazquez et al. (2015), a different method was used to calculate the centroid of each CCF, by fitting a cubic spline to the CCF and using it to set a threshold for the minimum value of the correlation coefficient. Here, we are using the 80% threshold value instead, as suggested by Peterson (2001), however other threshold values were also explored.

5.2 GALFIT

This galaxy has a bright central bulge with a bar enclosed within a tightly-wound two arm spiral observed out to a radius of $\sim 10''$, with more extended star light out to a radius of $\sim 18''$ (see Figure 5.1). The GALFIT model used to fit the image includes the sky background, a point source (formed using a TinyTim PSF) to model the AGN and two stars in the field of view, and three Sersic components. Two Sersic components are used to fit the more extended galaxy light. One component has a smaller half light radius, and fits the light more concentrated at the center, and another component is placed diagonally from the upper left to lower right region of the galaxy. Another component fits the more extended starlight. The fraction of light originating from the PSF within a $1.2''$ aperture is 8.3%, and within $6.3''$ is 2.5%, so the point source is faint. The fraction of light in the residual image is 1.1% within $1.2''$ and 1.1% within $6.3''$.

Table 5.1: NGC 6418 Model Parameters

Sky PSF Sérsic	$\frac{d(\text{sky})}{dx}$ (10^{-3} counts) Δx ($''$) Δx ($''$)	$\frac{d(\text{sky})}{dy}$ (10^{-3} counts) Δy ($''$) Δy ($''$)	Sky (Counts) m_{vega} m_{vega}	r_e ($''$)	n	b/a	P.A.
Sky	-0.32	-0.45	25.11				
PSF	0	0	10.44				
PSF	-8.2	-7.0	11.67				
PSF	-12.9	-10.9	6.57				
Sérsic	-0.04	0.03	6.67	7.2	1.2	0.48	30.1
Sérsic	0.04	0.02	7.73	0.9	1.7	0.78	-47.9
Sérsic	0.34	-0.42	6.42	11.5	0.6	0.90	-62.9

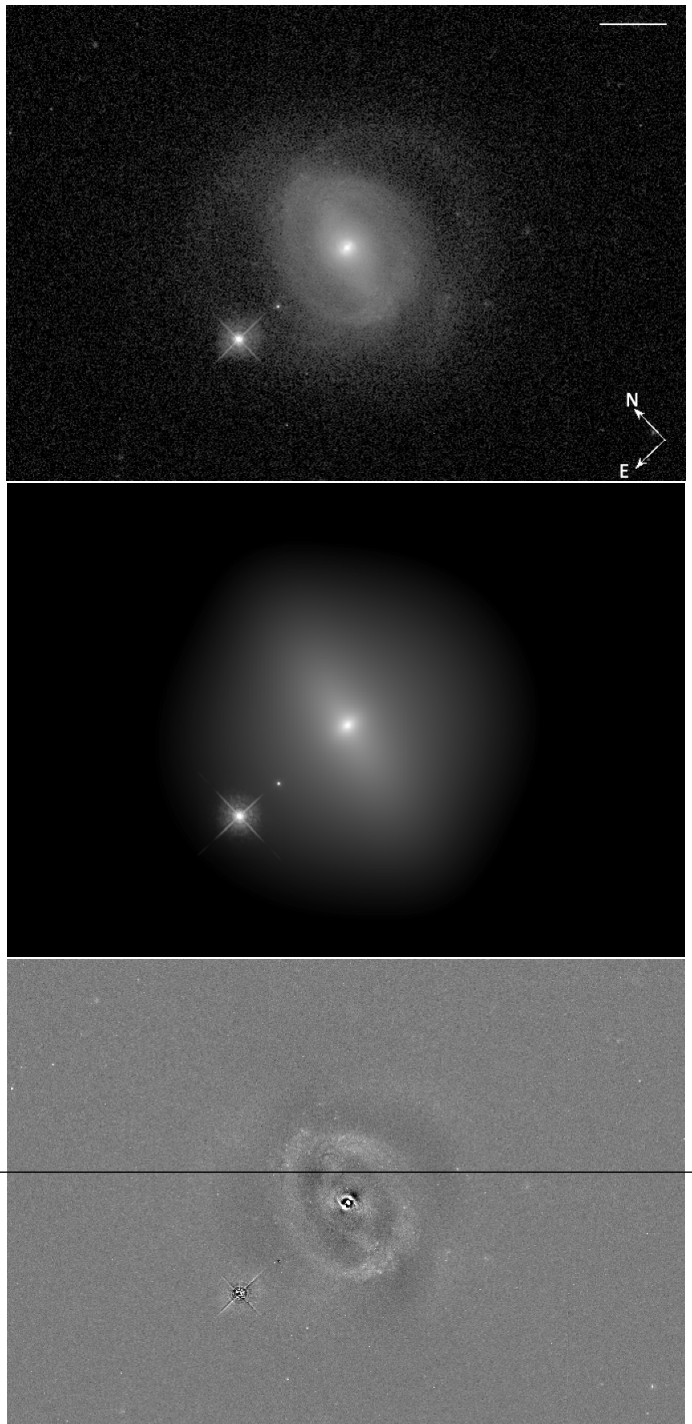

The photometry for the optical light curves was performed by B. Vazquez and presented in Vazquez (2015). The optical light curve is a combination of data from LT (B band, measured with 1.2" aperture), PTF (r band, measured with 5.1" aperture), and CSS (clear, measured with 6.3" aperture). Using the process described in Chapter 3, the galaxy contribution was subtracted as shown in the right subplot of Figure 5.2. However, as was the case in Chapter 3 for the AGN with a faint PSF fraction, negative fluxes were obtained. A different process was used to combine the light curves, described in the next section.

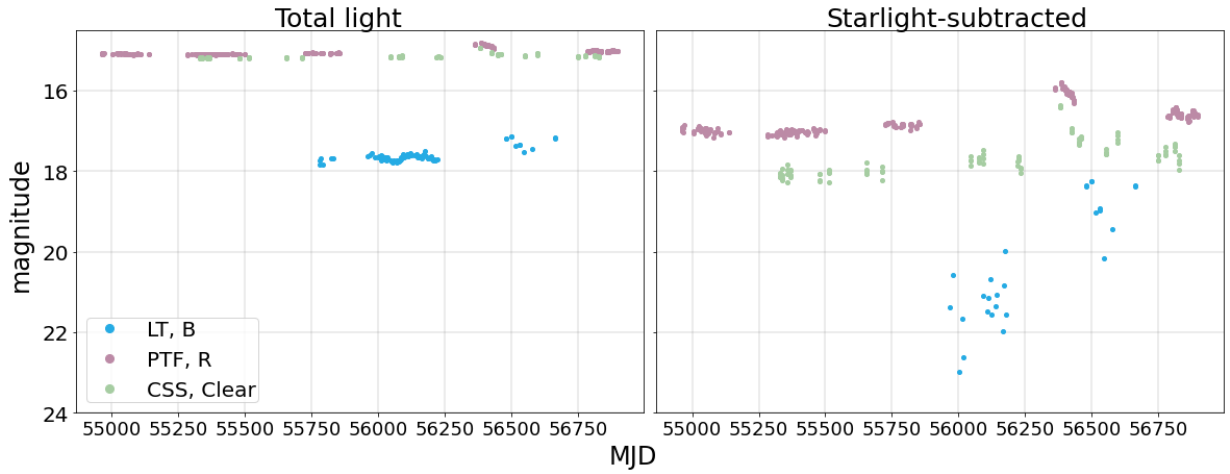

Figure 5.2: NGC 6418 Light Curves: The left subplot shows the light curves before subtracting the starlight contribution, while the right subplot has been starlight-subtracted.

5.3 IR and Optical Light Curves

The optical light curve was provided by Dr. Michael Richmond. For completeness, the method he used is described here. The goal is to combine the light curves of LT, PTF, and CSS. First, we can define a few regions in the photometric images (see Figure 5.3). The first region we define is N, the nuclear region, which is composed of variable nuclear light. The next two regions we define are composed of starlight from the host galaxy: S_i which is starlight from the inner region, unable to be spatially separated from the nucleus, and S, an annulus of starlight from a larger region.

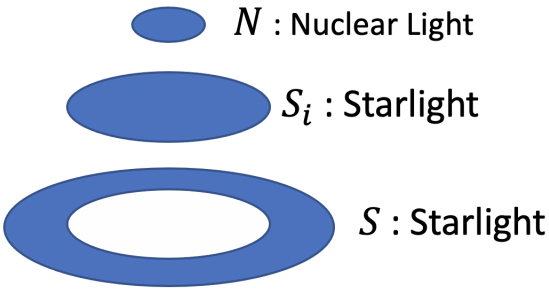

Figure 5.3: Defining the regions contained in the photometric measurements, which include the nuclear light, an inner region of starlight, and an annulus of starlight in a larger region.

With good seeing, the total light within a small aperture should be able to be measured

$$A(t) = N(t) + S_i. \tag{5.1}$$

Typically, due to poor seeing, photometric measurements use a larger aperture size

$$I(t) = A(t) + S. \tag{5.2}$$

Choosing a time when the nucleus is quiescent (t_0), the measurements through the large aperture are

$$I(t_0) = A(t_0) + S, \tag{5.3}$$

which is the lowest possible intensity. During quiescence, we can define the fraction of total light due to the smaller region

$$f = \frac{A(t_0)}{A(t_0) + S}. \tag{5.4}$$

and using Equation 5.3, the starlight in the outer region during quiescence can be represented as

$$S = I(t_0)(1 - f). \tag{5.5}$$

Now, at a time outside of quiescence, the amount of light measured in the large aperture that is due to the central region is

$$\begin{aligned} A(t) &= I(t) - S \\ &= I(t) - (I(t_0)(1 - f)) \end{aligned} \tag{5.6}$$

The fraction of total light in the small region can be calculated using Equation 5.4. The LT data shows a quiescent period during MJD 56087 and the LT photometry used a 1.2" aperture size. For PTF, in which a 5.1" radius aperture was used, f is measured:

$$f = \frac{\text{Light in 1.2"}}{\text{Light in 5.1"}} = 0.28 \tag{5.7}$$

and for CSS, in which the photometry was performed with a 6.3" aperture radius:

$$f = \frac{\text{Light in 1.2"}}{\text{Light in 6.3"}} = 0.23 \tag{5.8}$$

Once for each telescope, the intensity of starlight in the outer region (S) is calculated, using the values of f. For each light curve, we subtract this starlight in the outer region, leaving us with $A(t)$.

These $A(t)$ values still have an offset in flux, mainly due to each light curve being in a different waveband. Each data set was scaled to "match" by multiplying by a factor to match the PTF data. The LT data was multiplied by 3, and CSS was multiplied by 1.3. We now have the intensity of light in the inner regions and are able to combine the three light curves, although there is still some starlight contribution in the inner region (S_i).

The IR light curves were also made by B. Vazquez and presented in Vazquez (2015). Figure 5.4

shows the combined optical and IR light curves.

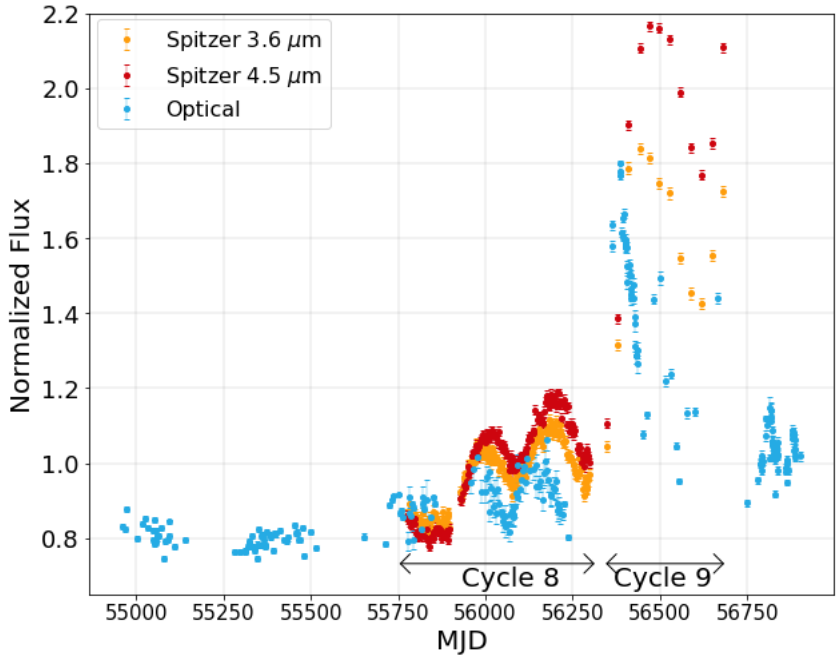

Figure 5.4: NGC 6418 Light Curves: The orange and red points represent the IR Spitzer data, while the blue points represent the optical data. Cycles 8 and 9 are labeled.

Spitzer Channel 1 (3.6 μm) and Channel 2 (4.5 μm) observations were obtained at a 3-day cadence during Cycle 8 (MJD 55774-56297). From the beginning of the optical light curve until the onset of the Spitzer campaign, only small optical variations occur. From MJD 55960 to 56235, the optical light curve shows two distinct peaks on the order of 20%, with the maximum values separated by 150 days. Both IR channels clearly respond with similar variability amplitudes, but with a clear delay.

The cycle 9 (MJD 56348-56679) IR observations have a longer cadence of once every 30 days. The main feature of the light curves occur after a gap of 128 days in the optical, where an optical flare occurs and peaks at MJD 56387, with a flux increase of $\sim 124\%$. Due to the gap in coverage, we only capture the peak of the flare, therefore the timescale to the peak is $\lesssim 120$ days. In the IR, from the end of cycle 8 until the peak in cycle 9 the 3.6 μm light curve increases in flux by 100%,

while the 4.5 μm light curve increases by $\sim 115\%$. The IR light curves are clearly more "smoothed out," compared with the narrow peak seen in the optical light curve.

After the flare, the optical flux sharply decreases by 40% over 64 days. The IR light curves respond, with the 3.6 μm light curve decreasing by $\sim 22\%$ over 175 days, and the 4.5 μm light curve decreasing by $\sim 18\%$ over 150 days. Over the next 300 days (MJD 56450 to 56750), the optical light curve then undergoes two oscillations of $\sim 40\%$. Both IR light curves also begin to rise again by $\sim 20\%$ before the campaign ends.

The light curves clearly display strong optical variability with a strong IR response. The lag corresponding to the sublimation radius estimated from the IR bolometric correction given in Table 2.2 is 143.4 days, which is approximately ~ 0.16 times the length of the Spitzer campaign.

5.4 Cross-Correlation Analysis

The optical-IR lags were measured for the combined Cycles 8 and 9 light curve, and also determined separately for each cycle. I will first discuss the results of cross-correlating the optical with the IR channels, and then discuss cross-correlating the two IR channels with each other.

5.4.1 Optical-IR Analysis

Cycle 8 Initial CCA results for the first half of the observations (cycle 8) were presented in Vazquez et al. (2015), who reported lags of $37.2^{+2.4}_{-2.2}$ for 3.6μm-optical, 47.1 ± 3.1 for 4.5 μm-optical, and $13.9^{+3.7}_{-3.8}$ for 3.6-4.5 μm.

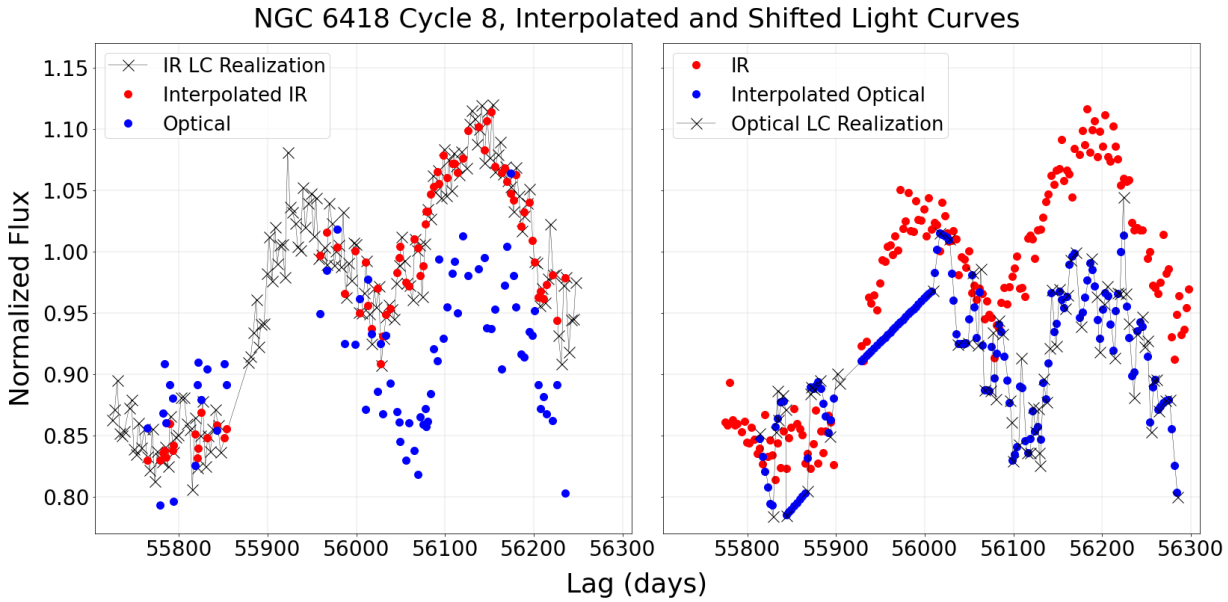

Figure 5.5: Examples of the interpolated optical and 3.6 μm light curves of NGC 6418: The plot on the left includes one IR light curve realization (the black points), the optical light curve is shown as blue points, and the red points represent the IR points linearly interpolated onto the time stamps of the optical data points. Here, the IR light curve has been shifted back by 50 days. The plot on the right is similar, including one of the optical light curve realizations in black, the IR light curve is shown in red, and the blue points represent the optical points linearly interpolated onto the timestamps of the IR data points. Here, the optical light curve has been shifted forward by 50 days

Figure 5.5 shows the optical and 3.6 μm IR channel, with each light curve interpolated onto the other with the interpolated light curve shifted back (IR) or forward (optical) by an arbitrary shift value of 50 days. Using optical interpolation (shown in the right subplot) includes more data points than IR interpolation (shown in the left subplot), and therefore allows coverage of the entire cycle 8 segment. As there are large gaps in the optical light curve, the gaps are filled with linearly interpolated points. While using IR interpolation does not have the issue of large regions of linearly interpolated optical points, these regions are simply left empty. Therefore, there are large gaps in coverage, and a smaller region of cycle 8 is covered for each shifted lag value. Also, fewer data points are included overall. There are positive and negative aspects to each interpolation type. The CCFs and CCCDs are shown in Figures 5.6 and 5.7.

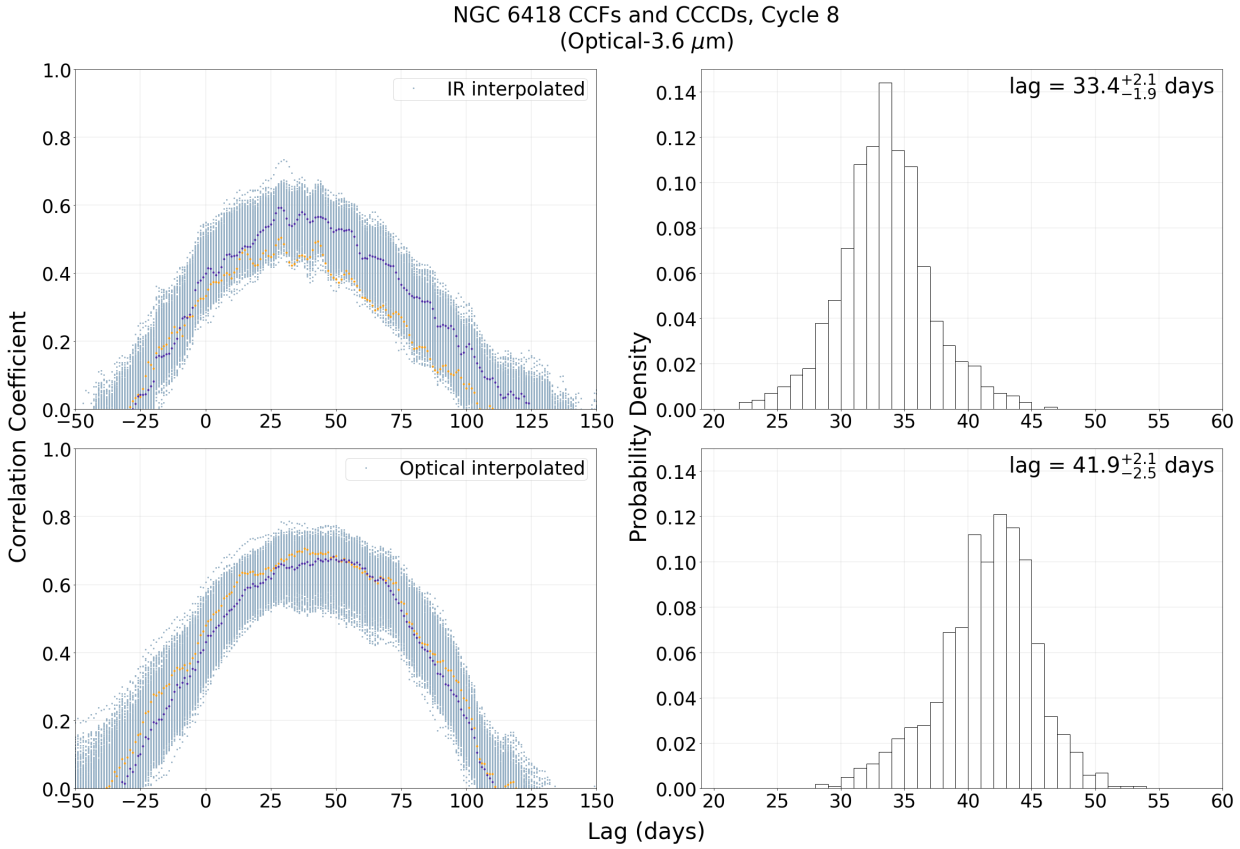

Figure 5.6: NGC 6418 CCFs (left subplots) and CCCDs (right subplots) for the cycle 8 3.6μm-optical analysis. The upper subplots show the results of using IR interpolation, while the lower subplots show the results of using optical interpolation. In the left subplots, 1000 CCFs formed from the Monte Carlo iterations are shown in light blue. As examples, the purple and orange points highlight two individual CCFs. 80% threshold values were used to form the CCCDs and calculate the lag values shown here.

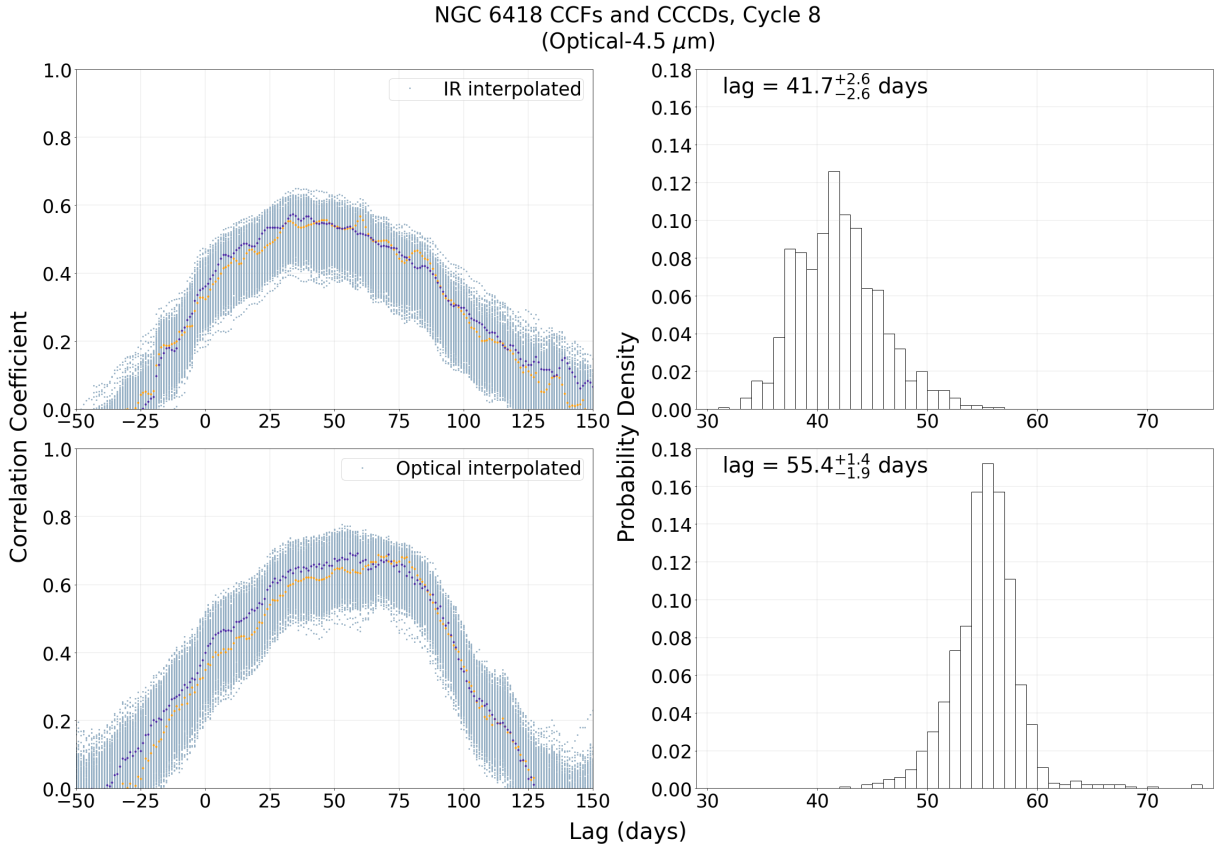

Figure 5.7: NGC 6418 CCFs (left subplots) and CCCDs (right subplots) for the cycle 8 4.5μm-optical analysis. The upper subplots show the results of using IR interpolation, while the lower subplots show the results of using optical interpolation. In the left subplots, 1000 CCFs formed from the Monte Carlo iterations are shown in light blue. As examples, the purple and orange points highlight two individual CCFs. 80% threshold values were used to form the CCCDs and calculate the lag values shown here.

As is often the case, the measured lags differ depending on which interpolation type is used. Looking at Figure 5.8, for both IR channels cross-correlated with the optical it is clear that the lag values converge when using lower percentage threshold values, and diverge as the threshold percentage increases. The cause of this is especially clear when viewing the CCFs in Figure 5.7. Comparing the shape of the CCFs produced with each interpolation type shows that the peaks are slightly skewed in opposite directions, although the overall width of the CCFs are similar. Therefore, as expected, using lower percent threshold values will produce very similar lags for each

interpolation type. Increasing the threshold percentage will produce a lag solely that is increasingly biased towards the peak portion of the CCFs, which are skewed in different directions depending on which interpolation type is used.

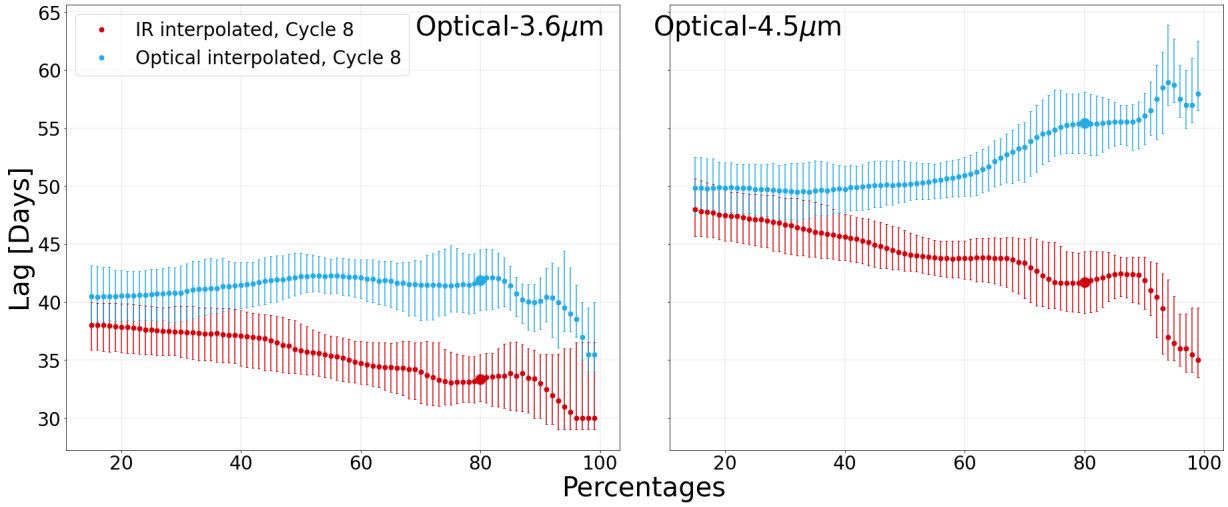

Figure 5.8: NGC 6418 Cycle 8: The dependence of measured lags on CCF percentage threshold values. The plot on the left shows results for 3.6μm-optical, and the plot on the right for 4.5μm-optical. The red points represent IR interpolation, while blue represents optical interpolation. The two larger points in each subplot indicate the 80% threshold values, and the error bars indicate the interquartile range.

Using the 80% threshold percentage value for the 3.6μm-optical analysis, the lag is $33.4^{+2.1}_{-1.9}$ days when using IR interpolation and $41.9^{+2.1}_{-2.5}$ days with optical interpolation. For the 4.5μm-optical analysis, using the 80% threshold percentage value produces a lag of $41.7^{+2.6}_{-2.6}$ days when using IR interpolation and $55.4^{+1.4}_{-1.9}$ days with optical interpolation. We could think of the lag values calculated with each interpolation type as an upper and lower limit for the analysis. If we want a single lag value to report from the Vazquez (2015) code for each IR channel cross-correlated with the optical, we could take the average of the lag values measured using the two interpolation types. This gives a lag value of $37.7^{+2.1}_{-2.25}$ days for the 3.6μm-optical analysis and $48.6^{+2.0}_{-2.25}$ days for the 4.5μm-optical analysis. Since the lag values converge for lower percentage threshold values, it is possible that a lower percentage threshold value could be used as well, although the lags would be

similar to the average lag values.

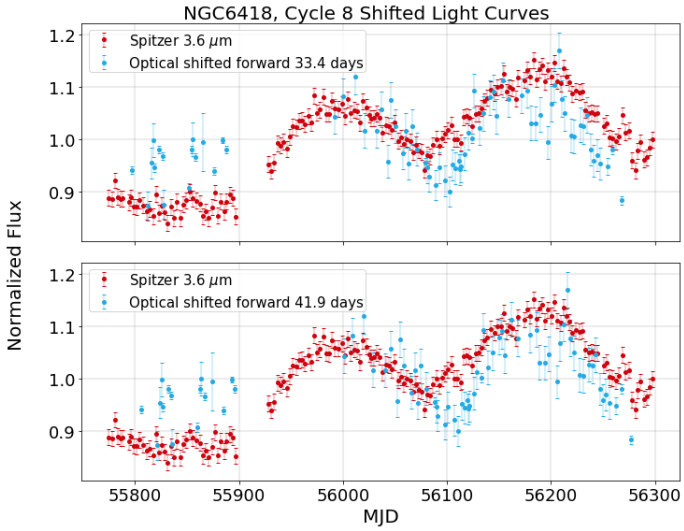

Figure 5.9: NGC 6418 3.6μm and shifted optical light curves: The optical light curve is shifted forward by the measured lag values obtained from IR interpolation (33.4 days) shown in the top plot, and optical interpolation (41.9 days) shown in the bottom plot.

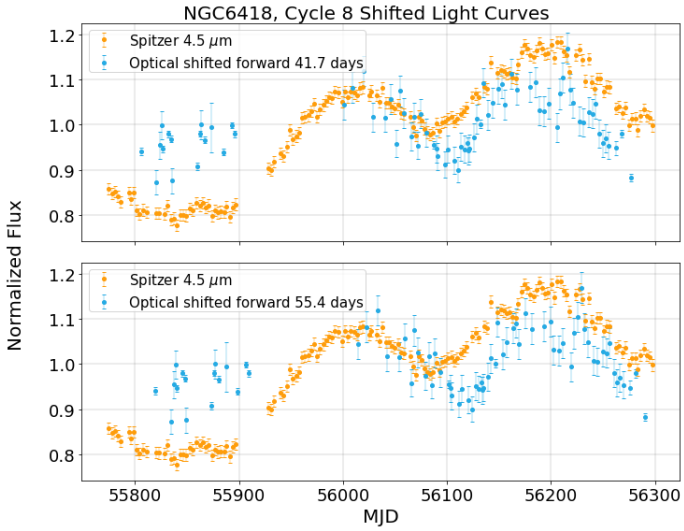

Figure 5.10: NGC 6418 4.5μm and shifted optical light curves: The optical light curve is shifted forward by the measured lag values obtained from IR interpolation (41.7 days) shown in the top plot, and optical interpolation (55.4 days) shown in the bottom plot.

As for the other AGN, analysis was also performed with PYCCF and JAVELIN. The lags are compared in Figures 5.11 and 5.12. The PYCCF results are consistent with the corresponding Vazquez (2015) results. The JAVELIN lag is measured to be $36.7^{+14.8}_{-3.2}$ days for the 3.6μm-optical analysis and $64.4^{+2.6}_{-12.6}$ days for the 4.5μm-optical analysis.

While the JAVELIN result for the 3.6μm-optical analysis is consistent to those of PYCCF and the Vazquez (2015) code, it yields a larger lag value for the 4.5μm-optical analysis. Figure A.1 in Appendix A.1.1 shows the CCCDs formed using JAVELIN. The CCCDs have multiple peaks. For the 4.5μm-optical CCCD, one peak is centered near $\sim$ 66 days, and another near near $\sim$ 48 days. Therefore JAVELIN is also measuring a lag similar to that of PYCCF and the Vazquez (2015) code, although it also measures another higher lag. Looking at the shifted light curves of Figure 5.10, a lag even larger than 55 days seems unreasonably large.

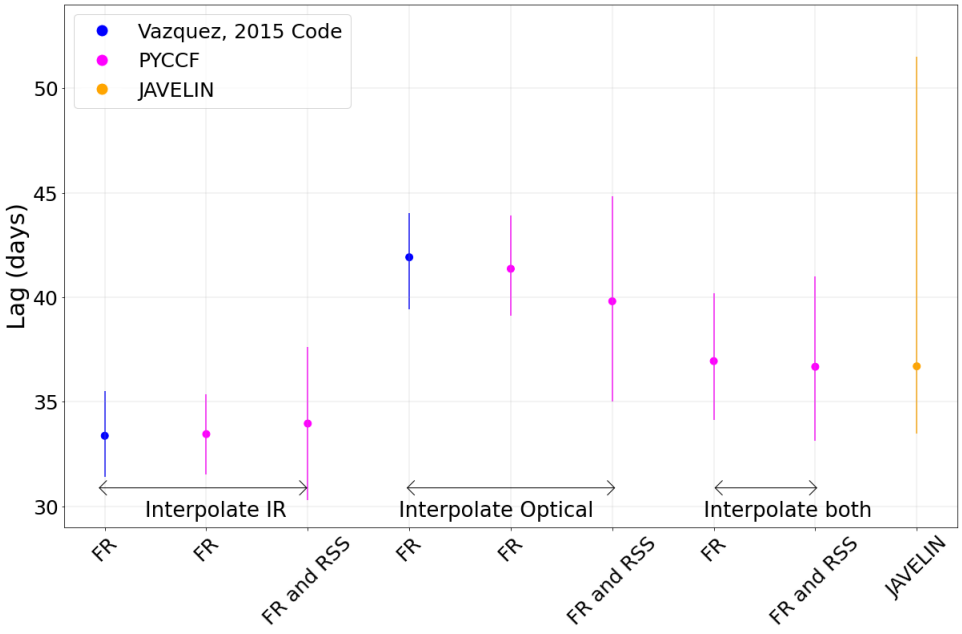

Figure 5.11: NGC 6418 cycle 8 lag comparisons for the 3.6μm-optical analysis. The blue data points represent lag values calculated using the Vazquez (2015) code, the orange point represents the lag calculated using JAVELIN, while the PYCCF results are shown in pink. The labels on the x-axis indicate whether flux randomization (FR) or both flux randomization and random subset selection (FR and RSS) was used. The labels above the x-axis specify whether the corresponding lags were calculated using IR interpolation, optical interpolation, or interpolating both.

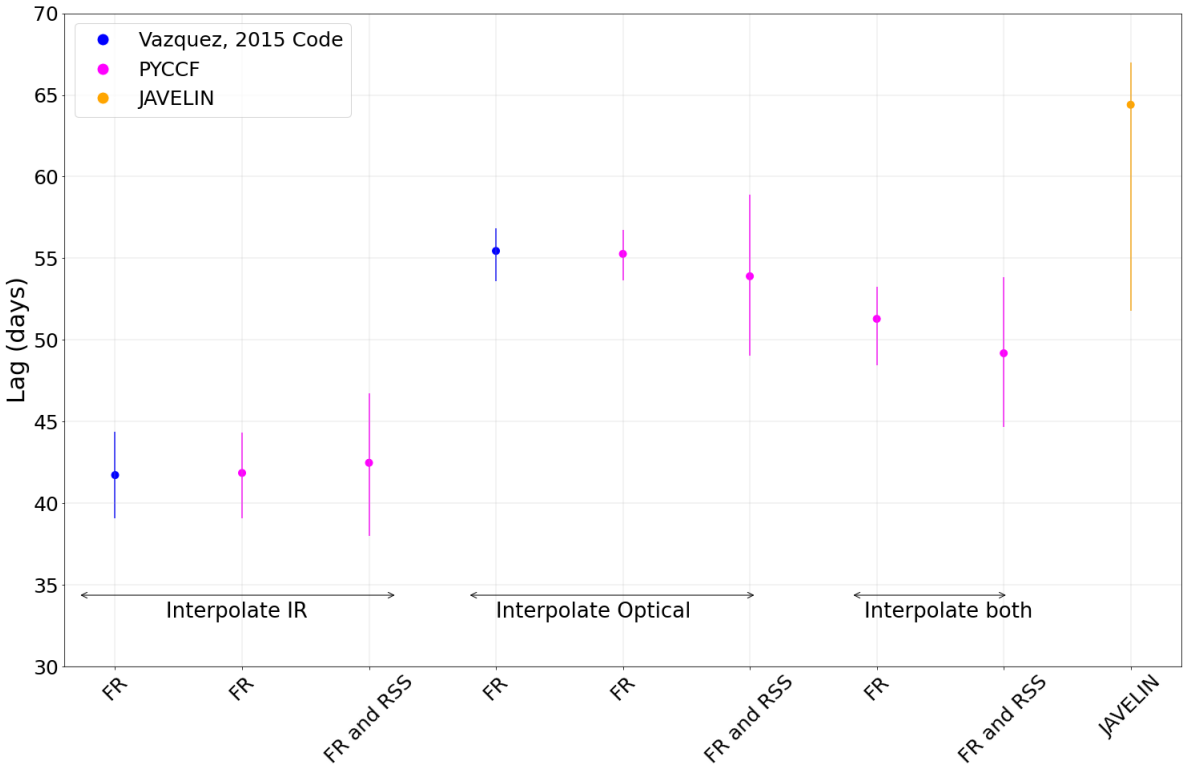

Figure 5.12: NGC 6418 cycle 8 lag comparisons for the 4.5μm-optical analysis. The blue data points represent lag values calculated using the Vazquez (2015) code, the orange point represents the lag calculated using JAVELIN, while the PYCCF results are shown in pink. The labels on the x-axis indicate whether flux randomization (FR) or both flux randomization and random subset selection (FR and RSS) was used. The labels above the x-axis specify whether the corresponding lags were calculated using IR interpolation, optical interpolation, or interpolating both.

Cycle 9 Lags were also measured separately for cycle 9 (see Figure 5.4). The IR observations for cycle 9 have a cadence of once every 30 days, which is significantly longer than the IR cadence of cycle 8. There is also a large gap of 128 days in the optical between the end of cycle 8 and the beginning of the cycle 9 optical data. These issues cause some difficulty in analyzing the cycle 9 data.

As with the CCA of the AGN discussed in the previous chapter, several different methods of analysis were used. First, the two different interpolation types were tested (IR or optical interpolation). Then, the IR and optical data points from the end of cycle 8 were also included in the

light curves (from MJD 56235 to 56297). This was done in order to test the effect of including data defining the beginning of the rise in flux.

Figure 5.13 shows the cycle 9 optical and 3.6 μm IR channel, with each light curve interpolated onto the other for an arbitrary shift value of 50 days. The subplots on the right were formed using optical interpolation, and the subplots on the left were formed using IR interpolation. The two upper subplots include only the cycle 9 data, while the two lower subplots include a few IR and optical data points from the end of cycle 8. Although the extra data points make little difference when using IR interpolation, for optical interpolation this adds many linearly interpolated optical data points that help to define the rise in optical flux.

One negative aspect of using IR interpolation (shown in the left subplots) is that the data covers a smaller range of the cycle 9 data for each shifted value, although the range that is covered is more well-sampled. Using optical interpolation (shown in the right subplots) includes more evenly spaced data points than using IR interpolation and also allows us to sample the full range of cycle 9 for each shifted lag value, although there are fewer data points overall.

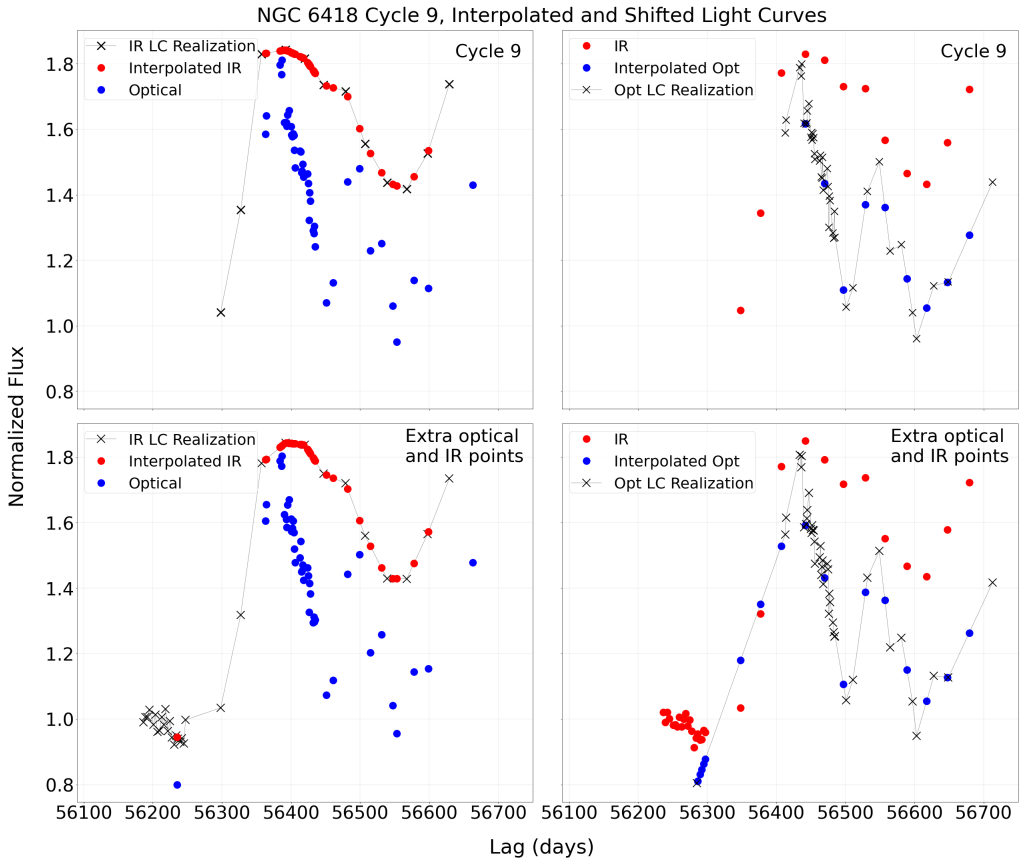

Figure 5.13: Examples of the cycle 9 interpolated optical and 3.6 μm light curves of NGC 6418: The upper subplots cover only the cycle 9 segment, while the lower subplots also include a few data points from the end of cycle 8. The plots on the left use IR interpolation, including one IR light curve realization (the black points), the optical light curve is shown as blue points, and the red points represent the IR points linearly interpolated onto the time stamps of the optical data points. Here, the IR light curve has been shifted back by 50 days. The plots on the right use optical interpolation, including one of the optical light curve realizations in black, the IR light curve is shown in red, and the blue points represent the optical points linearly interpolated onto the timestamps of the IR data points. Here, the optical light curve has been shifted forward by 50 days.

Figures 5.14 and 5.15 show the CCFs for the 3.6μm-optical and 4.5μm-optical analysis. Even within the same subplot, depending on the interpolation type or which version of the light curve is used, there are often multiple peaks within the same CCFs. To explore this further, I tried shifting the optical light curve forward to determine which light curve features correspond to the CCF peak

lag values. For example, in Figure 5.14 each CCF has one peak at ~ 50 days, and all except the CCFs shown in the lower right subplot have another peak at ~ 150 days.

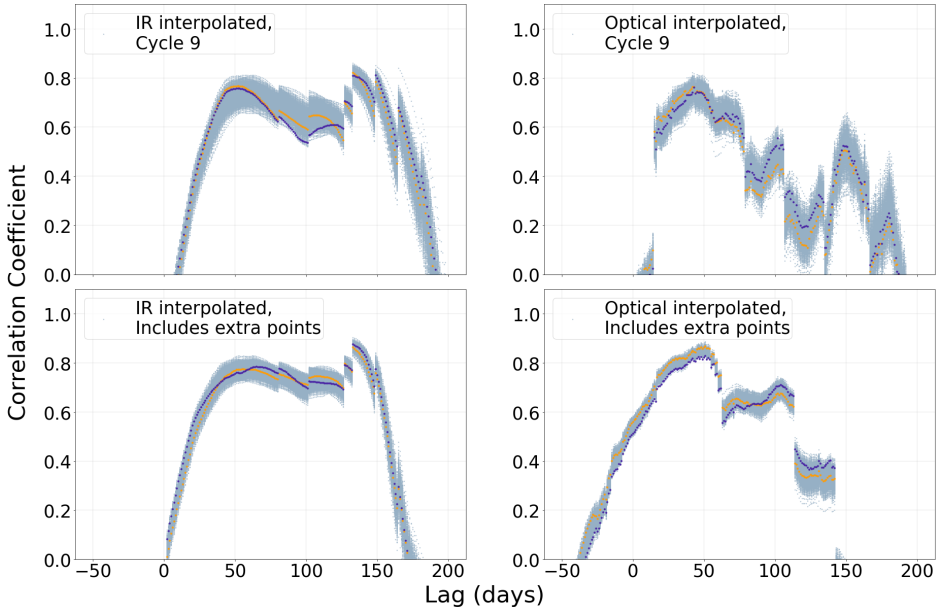

Figure 5.14: NGC 6418 CCFs for the 3.6μm-optical analysis: The top two rows show the results for the cycle 9 light curves and either IR interpolation (upper left), or optical interpolation (upper right). The bottom two rows show the results when a few IR and optical data points from the end of cycle 8 are included, with either IR interpolation (lower left), or optical interpolation (lower right). Each CCF plot includes 1000 CCFs formed from the Monte Carlo iterations, shown in light blue. As examples, the purple and orange points highlight two individual CCFs.

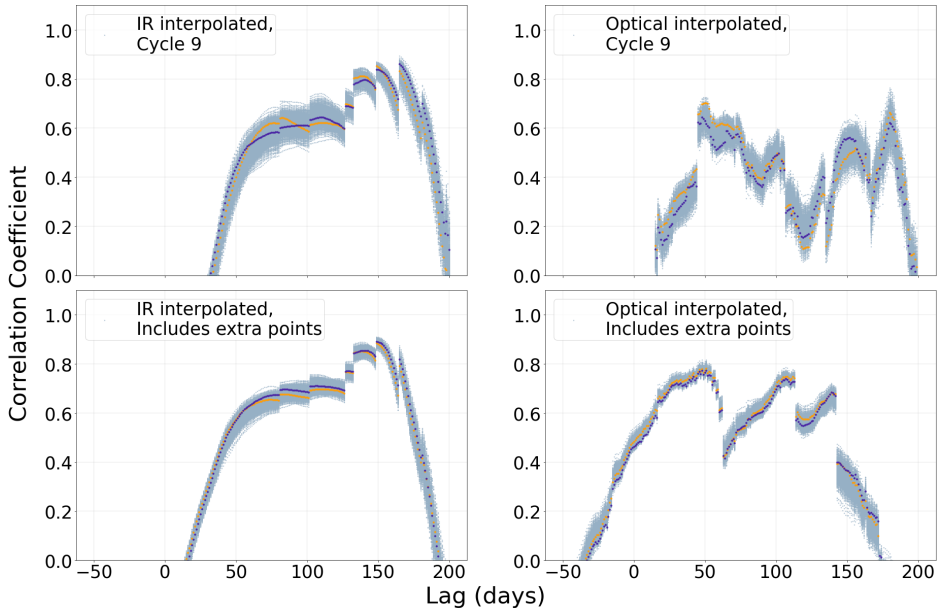

Figure 5.15: NGC 6418 CCFs for the 4.5μm-optical analysis: The top two rows show the results for the cycle 9 light curve and either IR interpolation (upper left), or optical interpolation (upper right). The bottom two rows show the results when a few IR and optical data points from the end of cycle 8 are included, with either IR interpolation (lower left), or optical interpolation (lower right). Each CCF plot includes 1000 CCFs formed from the Monte Carlo iterations, shown in light blue. As examples, the purple and orange points highlight two individual CCFs.

Figure 5.16 shows the cycle 9 3.6μm IR light curve and the optical light curve, shifted forward by 50 days (upper plot) and 150 days (lower plot). The 150 day peak of the CCFs seems to be associated with the dip in flux that occurs directly after the flare. The 50 day CCF peak is associated more with the initial rise in flux of the light curves, as well as the rise in flux much later in the light curves (after ∼MJD 56600). Since the IR light curve response is much more smoothed out than the optical light curve, clearly it is difficult to interpret the lag between them.

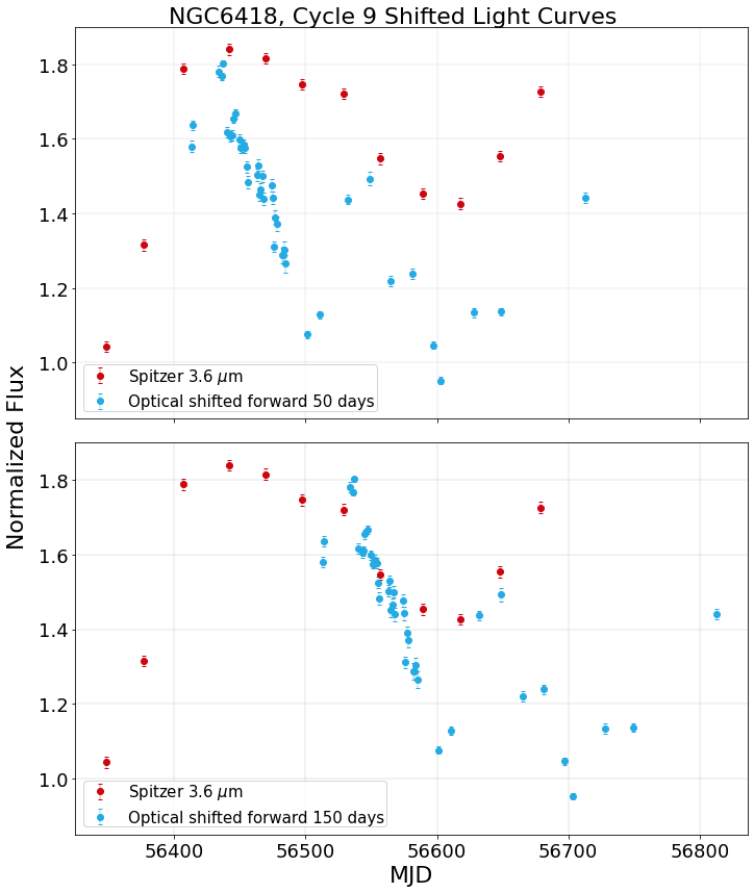

Figure 5.16: NGC 6418 cycle 9 3.6μm and shifted optical light curves: The optical light curve is shifted forward by 50 days in the upper plot, and 150 days in the bottom plot.

To determine which lag to report, we need to decide which features of the light curves are most important. Should we measure the lag between the peaks of the two light curves, or the dip in the flux between the two light curves? The peaks in the CCFs suggest that there is a different lag associated with these two different light curve features.

We also need to determine the appropriate percent threshold value; the variation of the lag with CCF threshold is shown in Figure 5.17. First, we will evaluate the results using IR interpolation. With IR interpolation, a threshold value of 60% or less should be used, as the 80% threshold value is only measuring the peak of the CCF distribution, which is skewed to larger lag values. Using

a 60% threshold percentage value leads to a lag in the middle of this broad distribution. For the 3.6μm-optical analysis, the lag is $96.3^{+3.9}_{-1.6}$ days for the IR interpolated cycle 9 data, and $89.7^{+0.89}_{-0.72}$ days when also including some cycle 8 data. For the 4.5μm-optical analysis, the corresponding lags are $126.4^{+1.6}_{-1.4}$ days and $114.4^{+0.96}_{-0.99}$ days, respectively. The lags derived from the two versions of the IR and optical light curves are statistically inconsistent with each other, although the difference is relatively small. The CCCDs are shown in Figures 5.18 and 5.19.

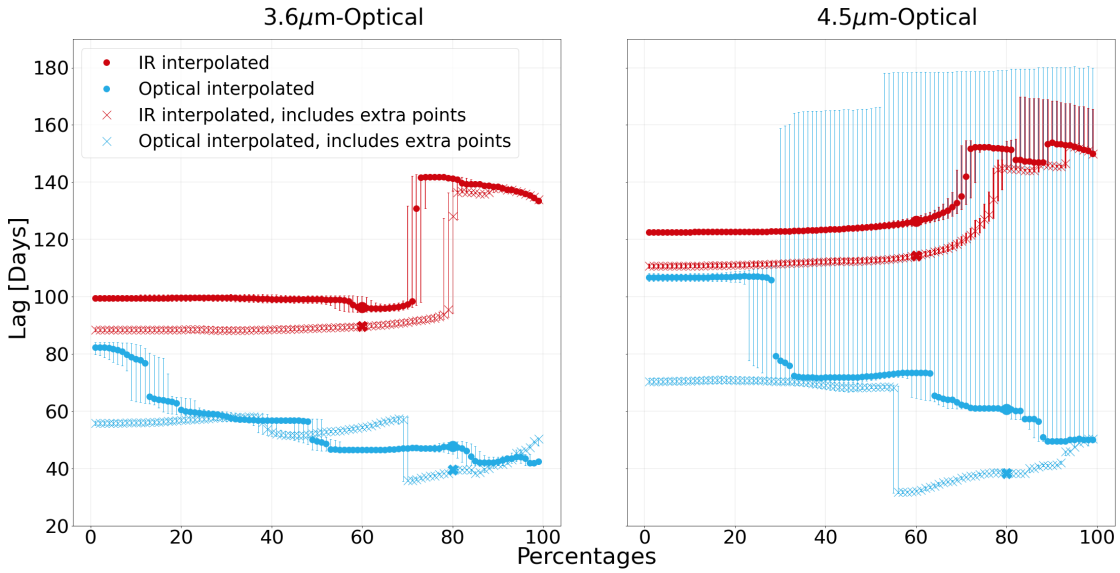

Figure 5.17: NGC 6418 Cycle 9: The dependence of measured lags on CCF percentage threshold values. The plot on the left shows results for 3.6μm-optical, and the plot on the right is 4.5μm-optical. The red points represent IR interpolation, while blue represents optical interpolation. The dots indicate lags calculated using only the cycle 9 portion of the light curves, and crosses represent the lags calculated when also including data points from the end of cycle 8. The larger points indicate the 80% threshold percentage values when using optical interpolation, and 60% threshold percentage values when using IR interpolation. The error bars indicate the interquartile range.

Next, we evaluate the lags calculated with optical interpolation (see the right subplots of Figures 5.14 and 5.15). Clearly, including the extra points at the end of cycle 8 causes some strange features to occur at the peaks of the CCFs (the causes of these effects are discussed in Appendix A.1.3). These features strongly affect the lag results: it is clear visually that the 4.5 μm light curve lags behind the 3.6 μm light curve (This is also shown by cross-correlating the two IR channels at the

end of this chapter). However, when evaluating the lag results calculated with optical interpolation (including the extra points) with an 80% threshold value, the 4.5μm lag is approximately one day shorter than the 3.6μm lag, which is clearly incorrect. Either a different percentage threshold value should be used, or using optical interpolation without the extra points is a better choice.

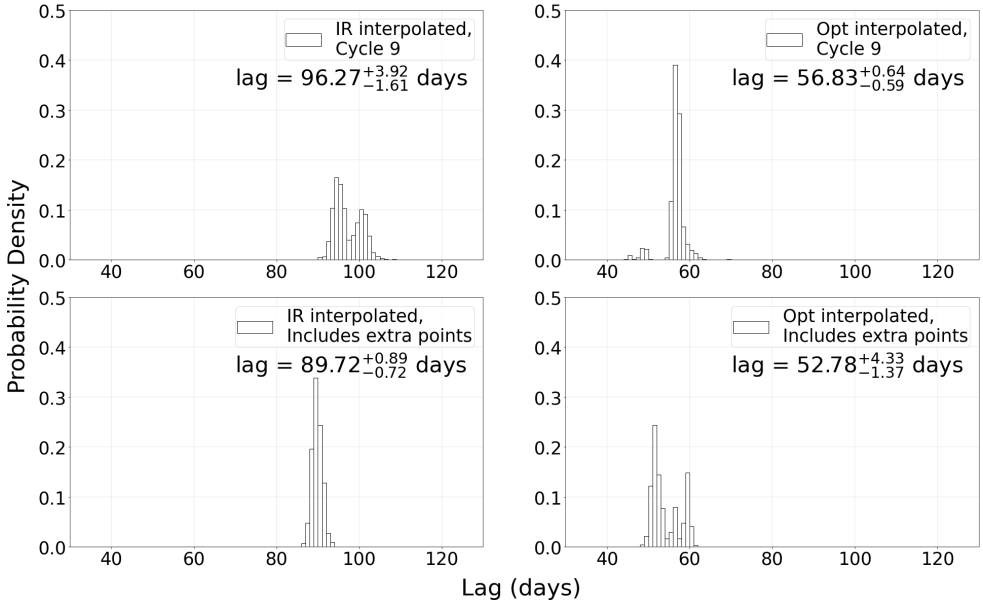

Figure 5.18: NGC 6418 CCCDs 3.6μm-optical analysis: 60% threshold values were used for IR interpolation, and 40% for optical interpolation. The top two rows show the results of using the cycle 9 light curve and either IR interpolation (upper left), or optical interpolation (upper right). The bottom two plots show the results for the case when also including a few IR and optical data points from the end of cycle 8 with either IR interpolation (lower left), or optical interpolation (lower right).

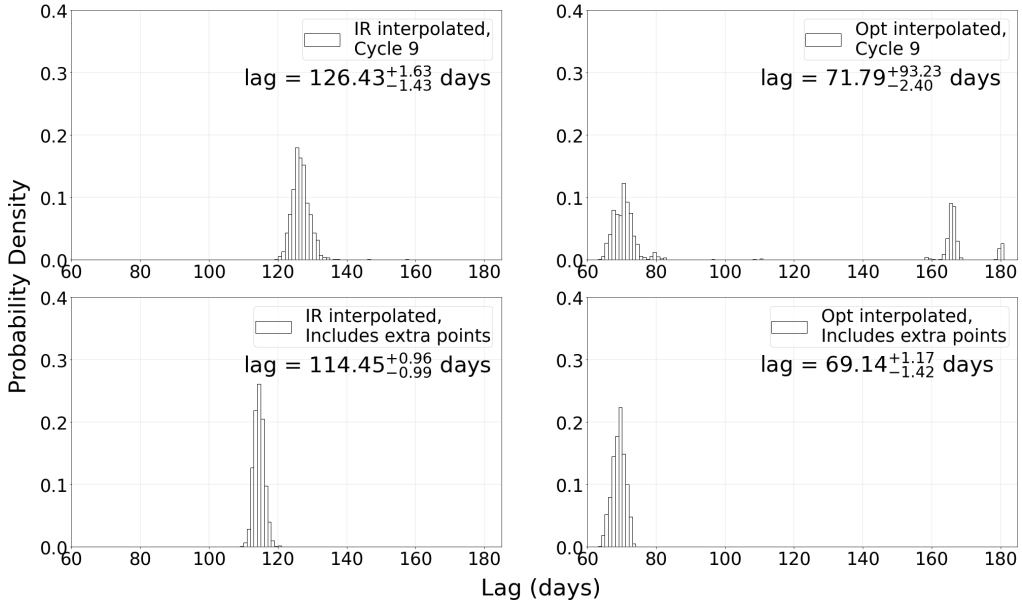

Figure 5.19: NGC 6418 CCCDs 4.5μm-optical analysis: 60% threshold values were used for IR interpolation, and 40% for optical interpolation. The top two rows show the results of using the cycle 9 light curve and either IR interpolation (upper left), or optical interpolation (upper right). The bottom two plots show the results for the case when also including a few IR and optical data points from the end of cycle 8 with either IR interpolation (lower left), or optical interpolation (lower right).

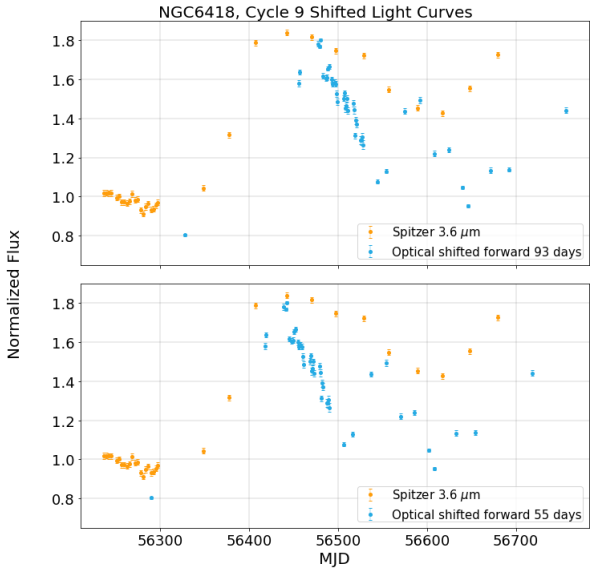

Figure 5.20: NGC 6418 3.6μm and shifted optical light curves: To illustrate the lag values, the optical light curve is shifted forward by the average lag value of the two light curve versions (with or without the extra points) when using IR interpolation (upper plot) or optical interpolation (lower plot).
In the upper plot, the optical light curve is shifted forward by 93 days (calculated with IR interpolation), and the bottom plot has a shift of 55 days (calculated with optical interpolation).

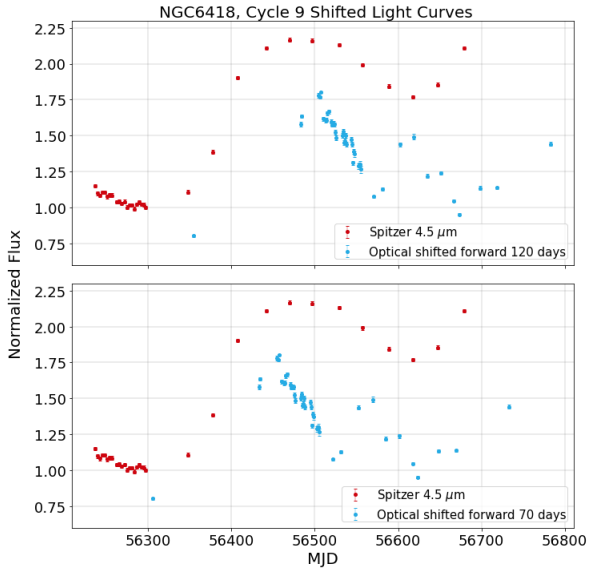

Figure 5.21: NGC 6418 4.5μm and shifted optical light curves: To illustrate the lag values, the optical light curve is shifted forward by the average lag value of the two light curve versions (with or without the extra points) when using IR interpolation (upper plot) or optical interpolation (lower plot). In the upper plot, the optical light curve is shifted forward by 120 days (calculated with IR interpolation), and the bottom plot has a shift of 70 days (calculated with optical interpolation).

Looking at the lag values calculated using higher percentage values, the optically-interpolated lag values in each subplot converge. In other words, the peaks of the optically-interpolated CCFs approximately coincide. However, due to the discontinuitues affecting the peaks of the CCFs, I would not trust this lag value. If we choose a mid-range percentage threshold value the lag values become more stable, and begin to coincide for the two versions of the light curve. Using a percent threshold value of 40% produces a lag of $56.8^{+0.64}_{-0.59}$ days for the optically-interpolated cycle 9 data, and $52.8^{+4.3}_{-1.4}$ days when also including some cycle 8 data for the 3.6μm-optical analysis. For the 4.5μm-optical analysis, the corresponding lags are $71.8^{+93.2}_{-2.4}$ days and $69.1^{+1.2}_{-1.4}$ days, respectively. For both IR channels, these lags (optically interpolated) are consistent with each other for both versions of the light curves.

Due to there being two main features with different lags in the light curves of cycle 9, the upper values for the uncertainties when using optical interpolation are extremely large for the 4.5μm-

optical analysis. In the CCCDs (upper right subplot of Figure 5.19), we see that there are peaks at larger lag values. This occurs because in the CCFs (upper right subplot of Figure 5.15), there is a high correlation between the light curves at ~ 50 days and ~ 180 days. The results of using a smaller range of potential lag values in the CCF calculation are included in Appendix A.5. When using a smaller range, the measured lag values are the same as those reported here, although the uncertainties are smaller.

If we are more interested in the region of the light curve containing the flare that occurs at the beginning of cycle 9, then using optical interpolation is likely a better choice. Using IR interpolation with 60% threshold value gives a lag between the two main features of the light curve shown in Figure 5.16.

The lags measured with the different codes are compared in Figures 5.22 and 5.23. The lags were also measured with JAVELIN, with the CCCDs shown in Appendix A.1.2. The following are the results when using only the cycle 9 data: for the 3.6μm-optical analysis, the measured lag is $50.36^{+0.49}_{-0.57}$ days, which is smaller than the lags calculated with the Vazquez (2015) code and PYCCF. For the 4.5μm-optical analysis, the lag is $61.1^{+54.3}_{-10.5}$ days. As with the analysis of cycle 9 with the other codes, there is a second peak in the CCCDs which causes the upper error to be large. JAVELIN was also used for the light curve version that includes extra data from cycle 8, however the results were inconclusive.

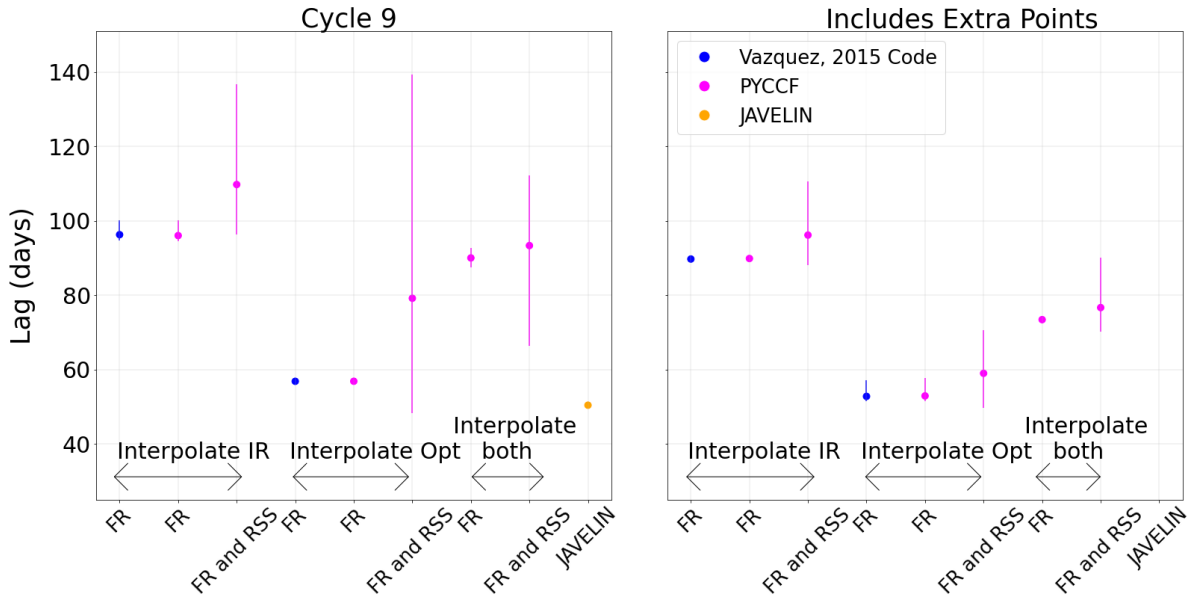

Figure 5.22: NGC 6418 cycle 9 lag comparisons for the 3.6μm-optical analysis. The blue data points represent lag values calculated using the Vazquez (2015) code, the orange point represents the lag calculated using JAVELIN, while the PYCCF results are shown in pink. The labels on the x-axis indicate whether flux randomization (FR) or both flux randomization and random subset selection (FR and RSS) was used. The labels above the x-axis specify whether the corresponding lags were calculated using IR interpolation, optical interpolation, or interpolating both.

For the PYCCF results, using both FR and RSS has a large effect on the uncertainties for the cycle 9 lags, especially when not including the cycle 8 data points. Otherwise, the PYCCF results are consistent with those of the Vazquez (2015) code.

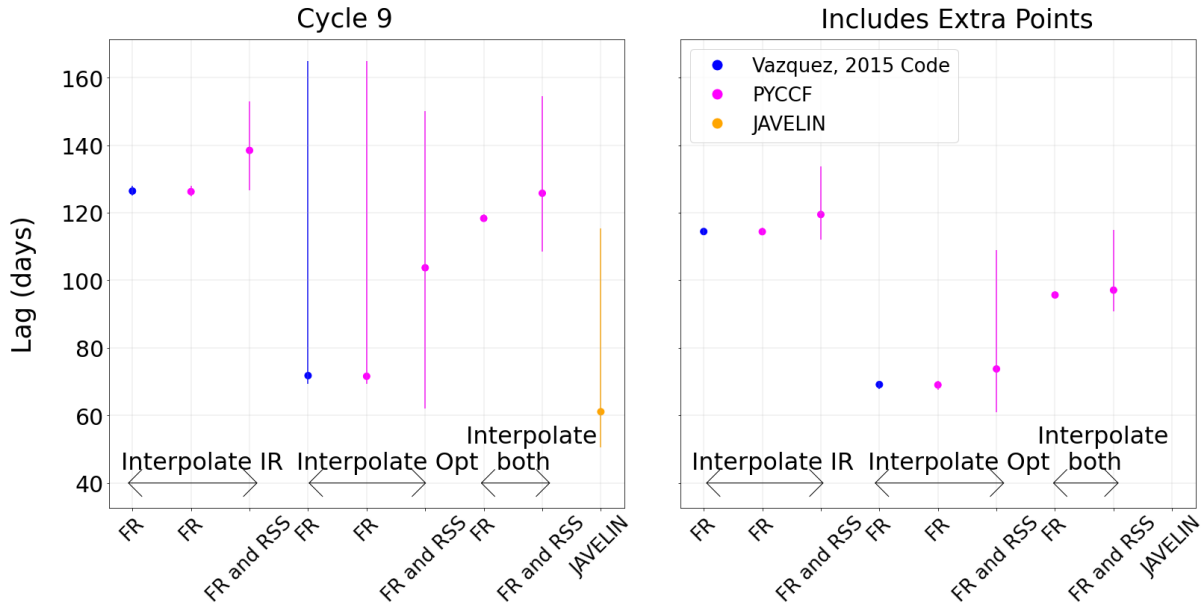

Figure 5.23: NGC 6418 cycle 9 lag comparisons for the 4.5μm-optical analysis. The blue data points represent lag values calculated using the Vazquez (2015) code, the orange point represents the lag calculated using JAVELIN, while the PYCCF results are shown in pink. The labels on the x-axis indicate whether flux randomization (FR) or both flux randomization and random subset selection (FR and RSS) was used. The labels above the x-axis specify whether the corresponding lags were calculated using IR interpolation, optical interpolation, or interpolating both.

Cycles 8 and 9 The combined Cycles 8 and 9 light curves were also cross-correlated, to see if a single lag value can be calculated for the entire campaign. Figure 5.24 shows the interpolated light curves. The CCFs and CCCDs are shown in Figures 5.25 and 5.26. IR interpolation results in CCFs with high correlation coefficients, but have a very broad, flat peak. The CCFs from optical interpolation have a narrower peak, but it is more skewed toward lower lag values, and has a very shallow drop-off.

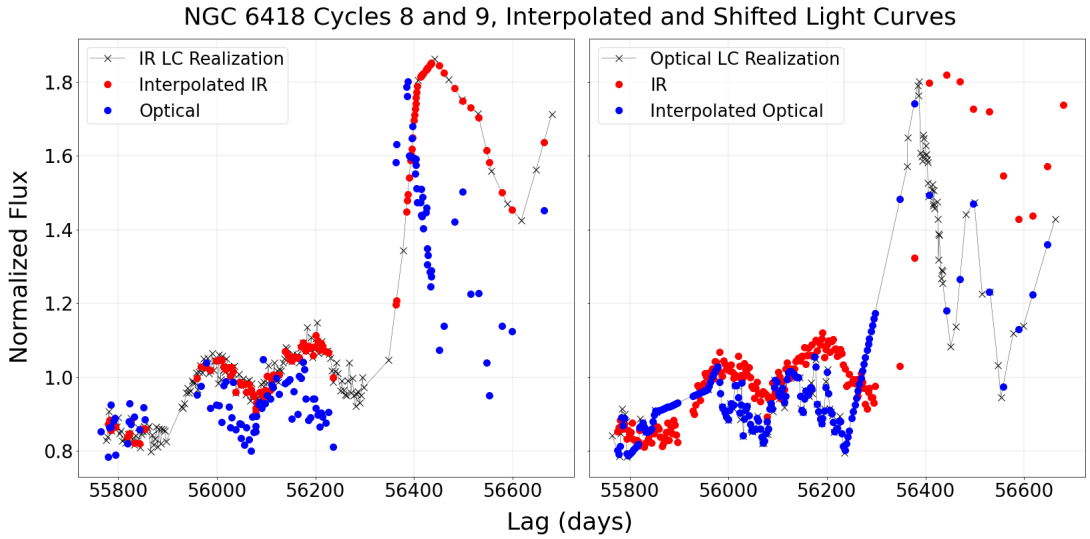

Figure 5.24: Examples of the interpolated optical and 3.6 μm light curves of NGC 6418, combining the Cycles 8 and 9 data: The plot on the left includes one IR light curve realization (the black points), the optical light curve is shown as blue points, and the red points represent the IR points linearly interpolated onto the time stamps of the optical data points. The plot on the right is similar, including one of the optical light curve realizations in black, the IR light curve is shown in red, and the blue points represent the optical points linearly interpolated onto the timestamps of the IR data points. A shift was not applied to either light curve.

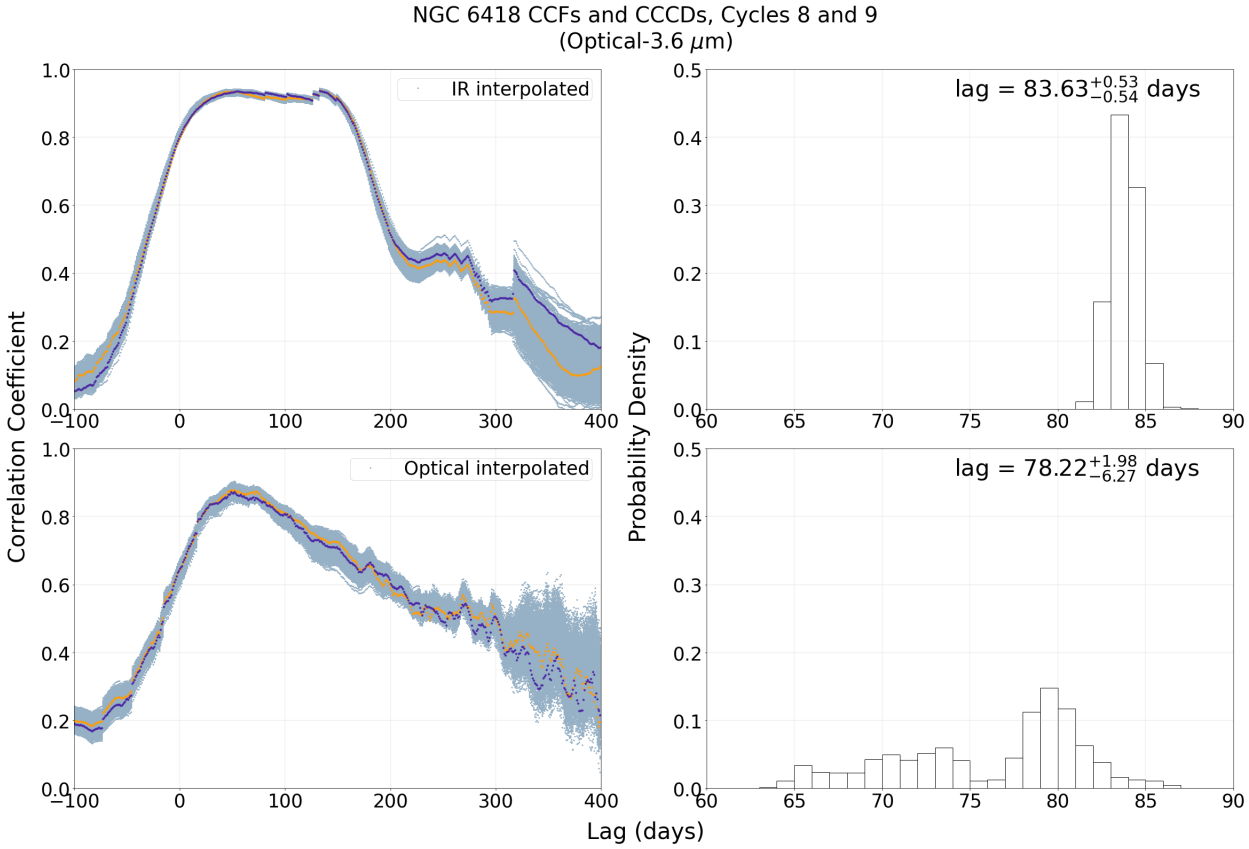

Figure 5.25: NGC 6418 CCFs (left subplots) and CCCDs (right subplots) for the Cycles 8 and 9 3.6 μm-optical analysis. The upper subplots show the results of using IR interpolation, while the lower subplots show the results of using optical interpolation. In the left subplots, 1000 CCFs formed from the Monte Carlo iterations are shown in light blue. As examples, the purple and orange points highlight two individual CCFs. The lag for each iteration was calculated using an 80% threshold value.

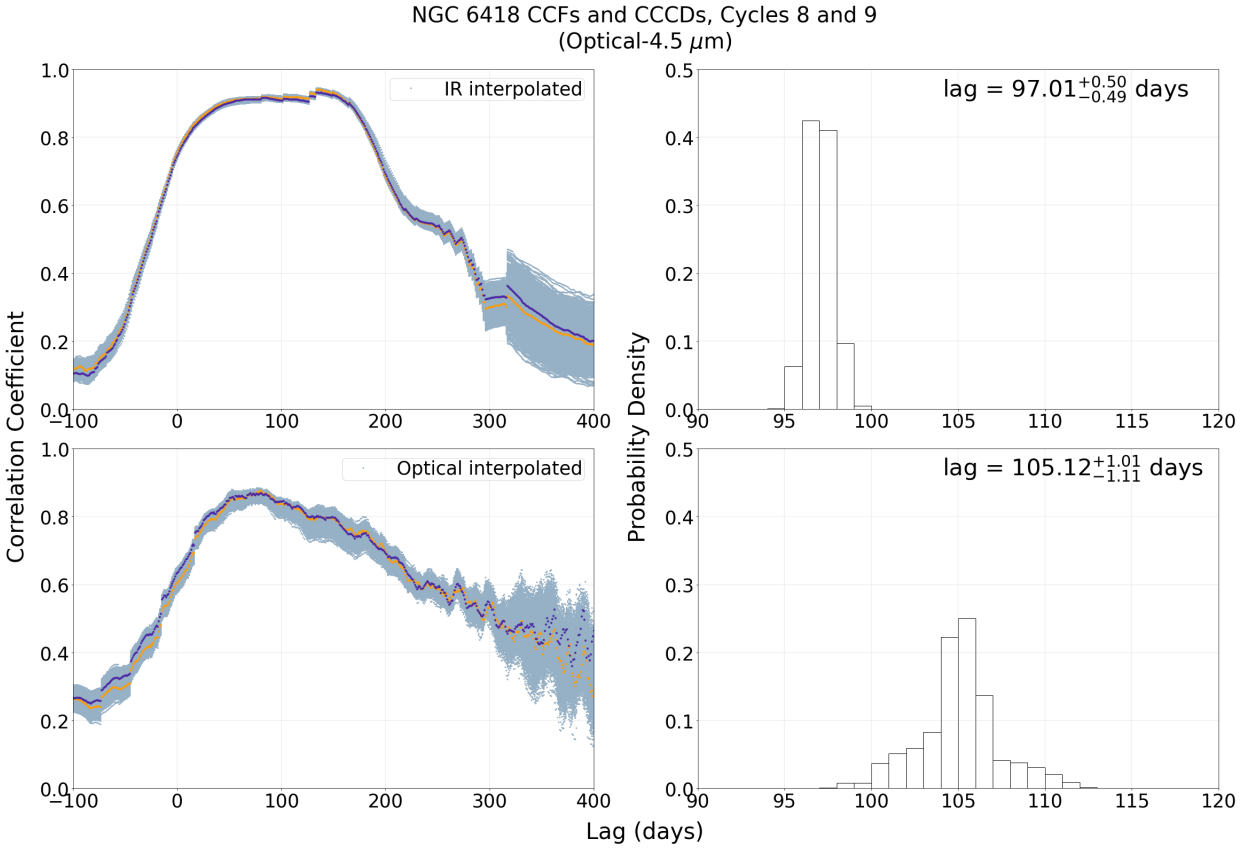

Figure 5.26: NGC 6418 CCFs (left subplots) and CCCDs (right subplots) for the Cycles 8 and 9 4.5 μm-optical analysis. The upper subplots show the results of using IR interpolation, while the lower subplots show the results of using optical interpolation. In the left subplots, 1000 CCFs formed from the Monte Carlo iterations are shown in light blue. As examples, the purple and orange points highlight two individual CCFs. The lag for each iteration was calculated using an 80% threshold value.

Looking at the lag vs percent threshold plots of Figure 5.27, it is clear that using IR interpolation leads to lag values that are much more stable as the threshold percentage varies. Comparing the CCFs for each interpolation type, the CCFs formed using optical interpolation have a peak that is skewed toward lower lag values and drops off more slowly for upper lag values. This makes it more difficult to determine the appropriate threshold lag value to use, as there is not a stable region. Nevertheless, an 80% threshold value was adopted.

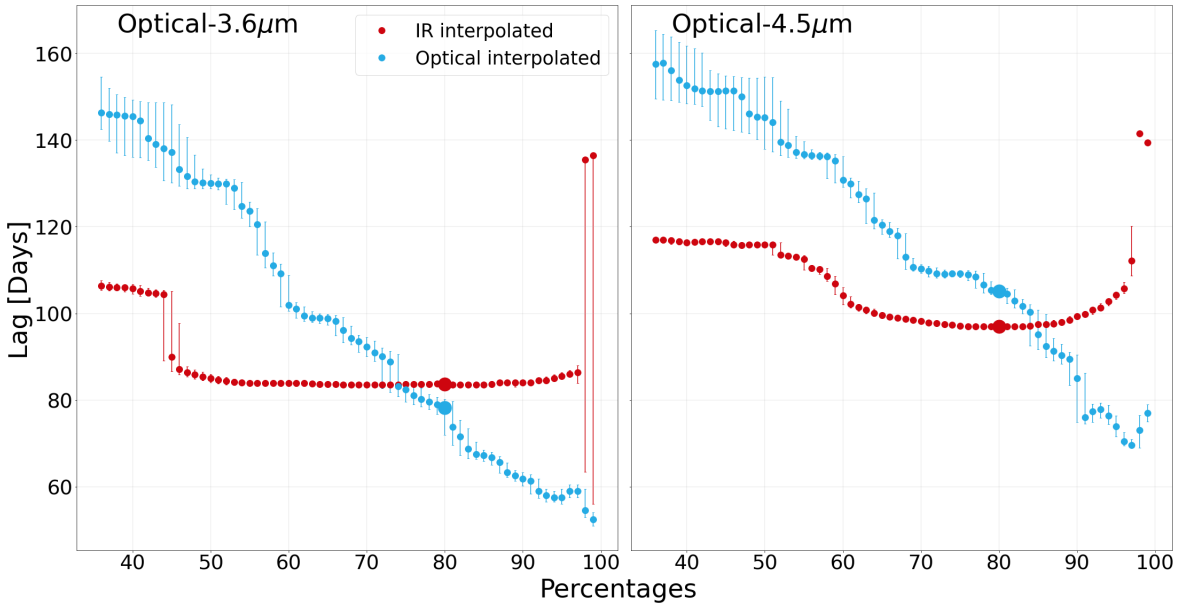

Figure 5.27:
NGC 6418 Cycles 8 and 9: The dependence of measured lags on CCF percentage threshold values for the 3.6μm-optical CCA (left pannel) and the 4.5μm-optical CCA (right pannel). The red points represent the use of IR interpolation, while blue represents optical interpolation. The larger points indicate the 80% threshold percentage values, and the error bars indicate the interquartile range.

Considering both interpolation types, the 3.6μm-optical lag is $\sim$ 80 days and the the 4.5μm-optical lag is $\sim$ 100 days. Figure 5.28 shows the optical light curves shifted forward by these lag values. While the shifted light curves show a reasonable match between the Cycle 9 light curve features (although this lag could possibly be too large), the lags are clearly too large to match the features of the Cycle 8 portion of the light curves. While a lag for the combined Cycle 8 and 9 light curves can be calculated, shifting the optical light curve forward by the derived lag makes it clear that a single value of the lag does not properly capture/describe the response of the IR throughout the entire campaign; the IR lag relative to the two lower amplitude optical peaks in Cycle 8 is evidently shorter than the combined Cycle 8 and 9 lag value suggests.

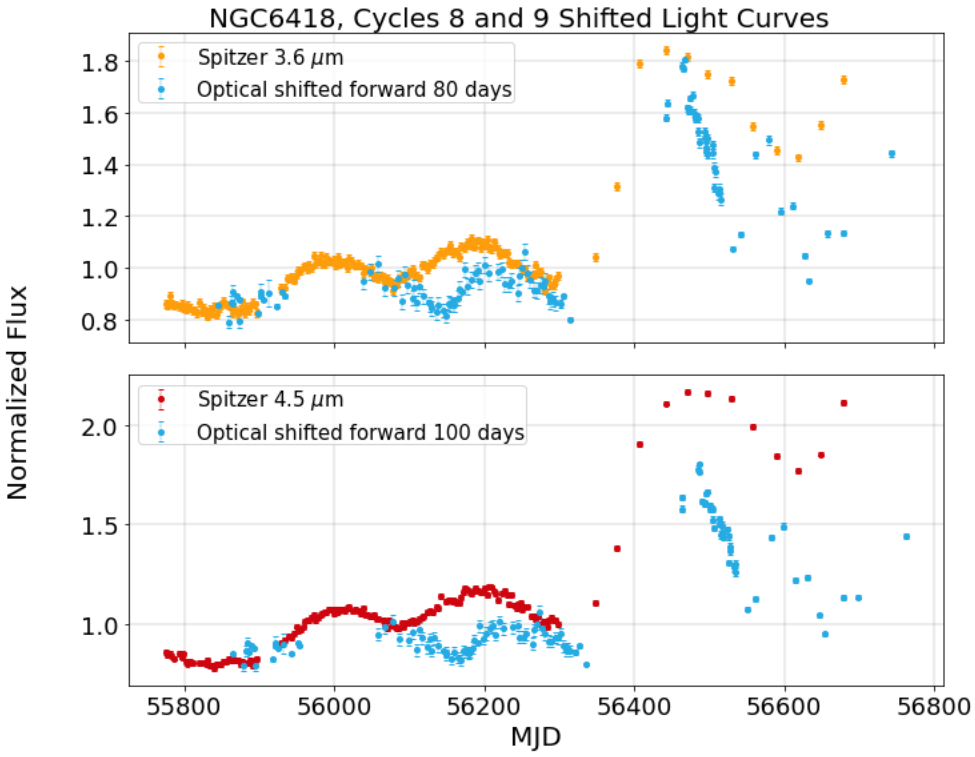

Figure 5.28: NGC 6418 cycles 8 and 9 shifted optical light curves: The optical light curve is shifted forward by the measured lag of 80 days shown in the top plot, 100 days shown in the bottom plot.

The lags measured with the different codes are shown in Figures 5.29 and 5.30. While the PYCCF results are consistent with those of the Vazquez (2015) code, the JAVELIN results are significantly lower. The JAVELIN lags still seem too large for the cycle 8 light curves. Figure 5.31 shows the optical light curves shifted forward by the measured lag values from JAVELIN.

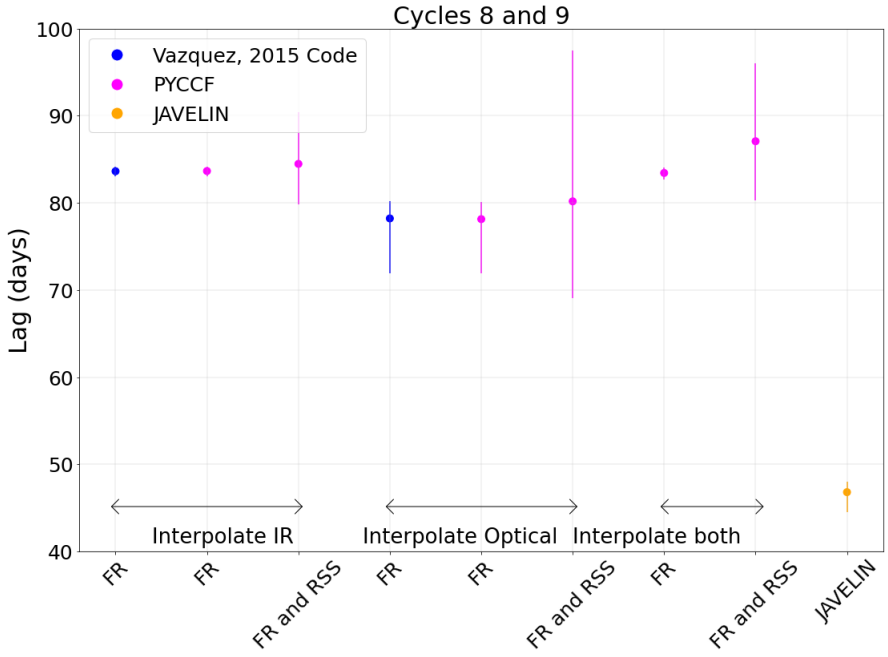

Figure 5.29: NGC 6418 cycles 8 and 9 lag comparisons for the 3.6μm-optical analysis. The blue data points represent lag values calculated using the Vazquez (2015) code, the orange point represents the lag calculated using JAVELIN, while the PYCCF results are shown in pink. The labels on the x-axis indicate whether flux randomization (FR) or both flux randomization and random subset selection (FR and RSS) was used. The labels above the x-axis specify whether the corresponding lags were calculated using IR interpolation, optical interpolation, or interpolating both.

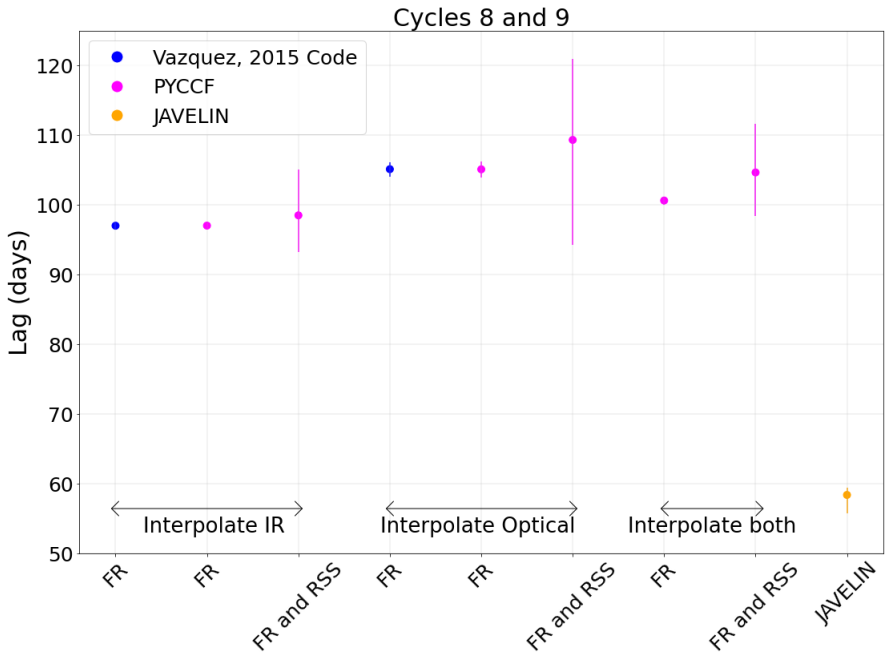

Figure 5.30: NGC 6418 cycles 8 and 9 lag comparisons for the 4.5μm-optical analysis. The blue data points rep- resent lag values calculated using the Vazquez (2015) code, the orange point represents the lag calculated using JAVELIN, while the PYCCF results are shown in pink. The labels on the x-axis indicate whether flux randomization (FR) or both flux randomization and random subset selection (FR and RSS) was used. The labels above the x-axis specify whether the corresponding lags were calculated using IR interpolation, optical interpolation, or interpolating both.

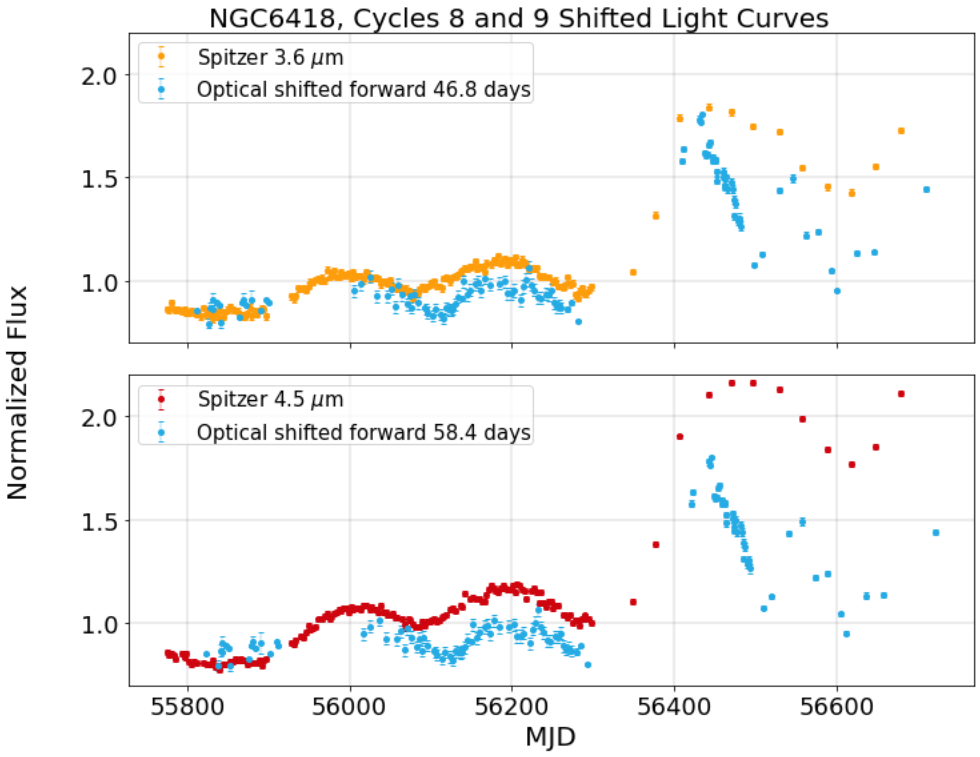

Figure 5.31: NGC 6418 cycles 8 and 9 shifted optical light curves (JAVELIN lag values): The optical light curve is shifted forward by the lags (measured with JAVELIN) of 46.8 days shown in the upper plot, 58.4 days shown in the bottom plot.

5.4.2 3.6-4.5 micron Analysis

Next, the two IR channels are cross-correlated with each other. Looking at the IR light curves in Figure 5.32, it is clear that the 4.5μm light curve lags the 3.6μm light curve. To test the possibility of a different lag being calculated for each cycle, the light curves were cross-correlated separately for cycle 8 and cycle 9, and also for both cycles 8 and 9 together.

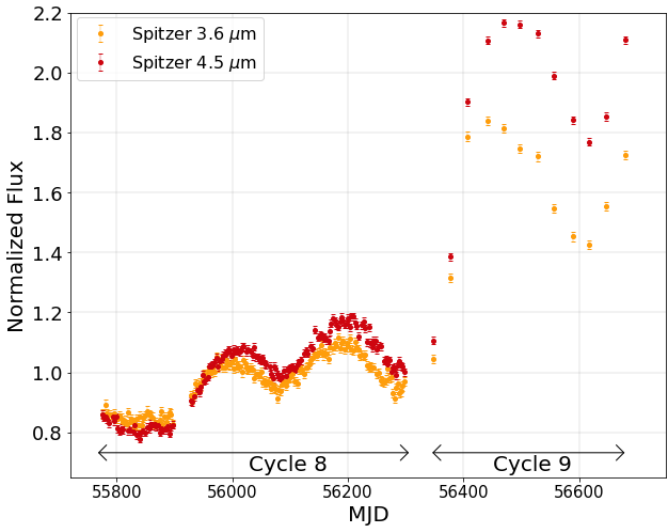

Figure 5.32: NGC 6418 IR light curves: the yellow points represent the 3.6 μm data and the red points represent the 4.5 μm data. Cycles 8 and cycle 9 are labeled.

Cycle 8 First, the cycle 8 sections of the IR light curves were cross-correlated with each other. Both 3.6μm and 4.5μm interpolation was tested. Examples of these interpolation types are shown in Figure 5.33. Since both IR light curves include small gaps in coverage, both interpolation types include a linear sequence of points. There does not appear to be an advantage to either interpolation type.

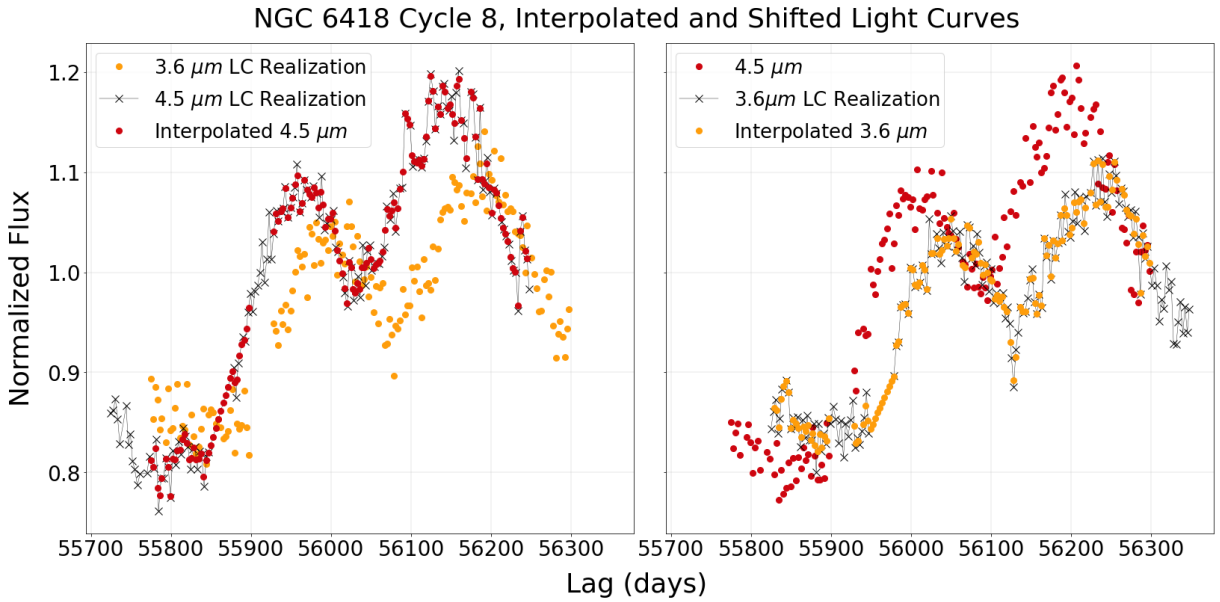

Figure 5.33: Examples of the interpolated 3.6 and 4.5 μm light curves of NGC 6418: The plot on the left includes one 4.5μm light curve realization (the black points), the 3.6μm light curve realization is shown as orange points, and the red points represent the 4.5 μm data linearly interpolated onto the time stamps of the 3.6 μm data points. Here, the 4.5μm light curve has been shifted back by 50 days.
The plot on the right is similar, including one 3.6μm light curve realization (the black points), the 4.5μm light curve realization is shown as red points, and the orange points represent the 3.6 μm data linearly interpolated onto the time stamps of the 4.5 μm data points. Here, the 3.6μm light curve has been shifted forward 50 days.

CCFs and CCCDs are shown in Figure 5.34 for each interpolation type, using an 80% threshold value. With 4.5μm interpolation, the lag is ~twice as large as the lag calculated with 3.6μm interpolation ($12.87^{+0.94}_{-0.58}$ compared to $6.69^{+0.99}_{-0.91}$, respectively). Looking at Figure 5.35, the lag values clearly converge as the percent threshold value is increased. Therefore, it seems appropriate to measure the lag value using a larger percentage value, or simply take the average lag value of the two interpolation types, yielding a lag of $9.72^{+0.96}_{-0.75}$ days.

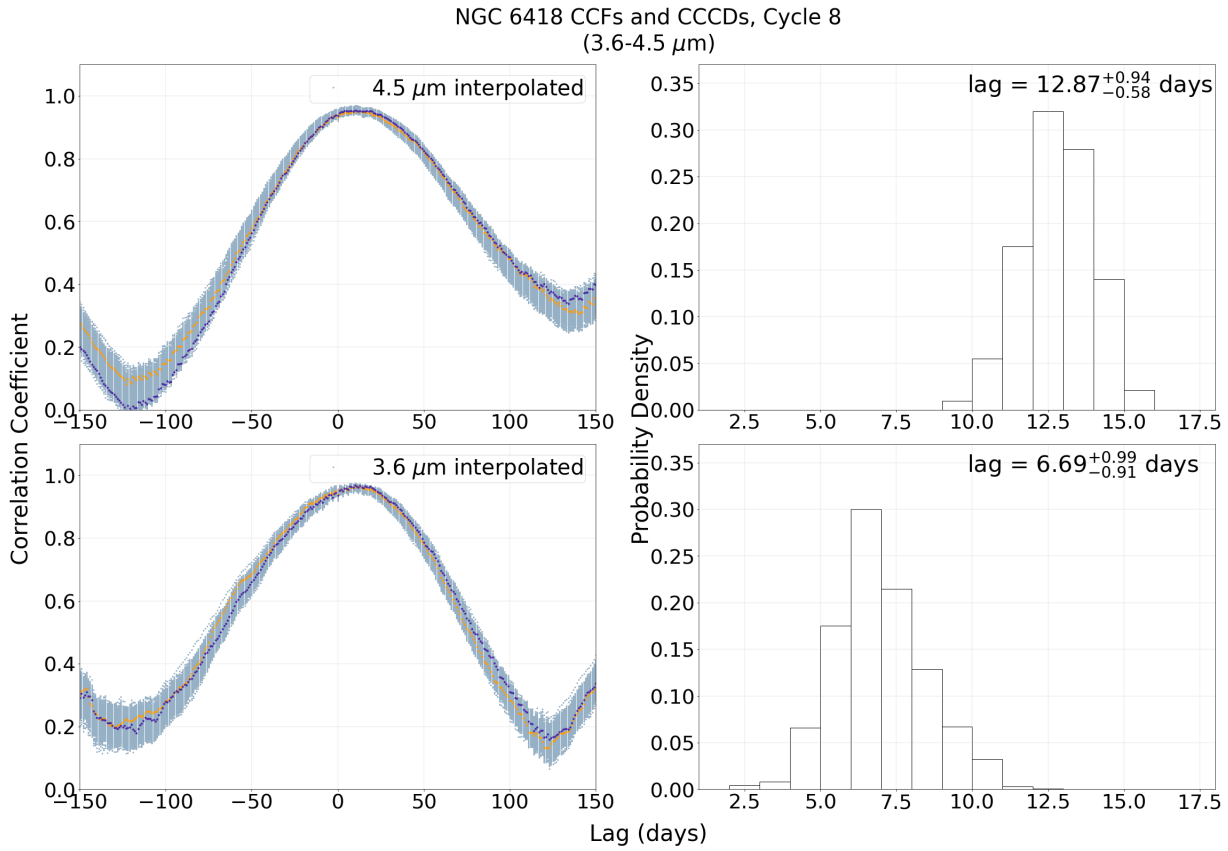

Figure 5.34: NGC 6418 CCFs (left subplots) and CCCDs (right subplots) for the 3.6-4.5 μm analysis. The subplots on the top show the results of using 4.5 μm interpolation, while the lower subplots show the results of using 3.6 μm interpolation. 80% threshold values were used to form the CCCDs. In the left subplots, 1000 CCFs formed from the Monte Carlo iterations are shown in light blue. As examples, the purple and orange points highlight two individual CCFs.

The PYCCF and JAVELIN lag values are shown in Figure 5.36. The lag values obtained with PYCCF and the Vazquez (2015) code were calculated using an 80% threshold value. Using the average lag of the two interpolation types discussed above ($9.72^{+0.96}_{-0.75}$ calculated with the Vazquez code), we can see that this lag is consistent with the PYCCF results when interpolating both light curves, and also is consistent with the JAVELIN lag value. Specifically, the JAVELIN lag is measured to be $9.38^{+0.81}_{-0.80}$ days.

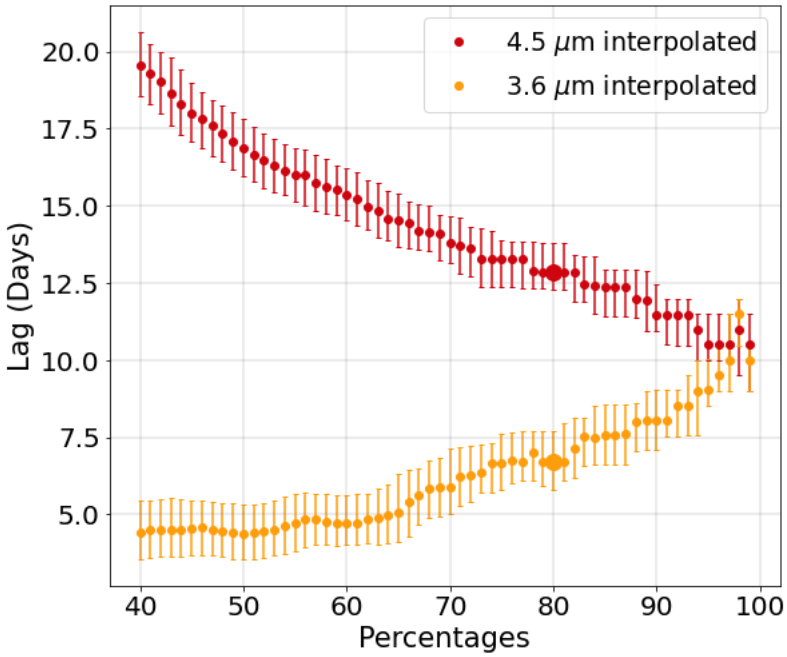

Figure 5.35: NGC 6418 Cycle 8, 3.6-4.5μm: The dependence of measured lags on CCF percentage threshold values. The red points represent the use of 4.5 μm interpolation, while orange represents 3.6 μm interpolation. The larger points indicate the 80% threshold percentage values, and the error bars show the interquartile range.

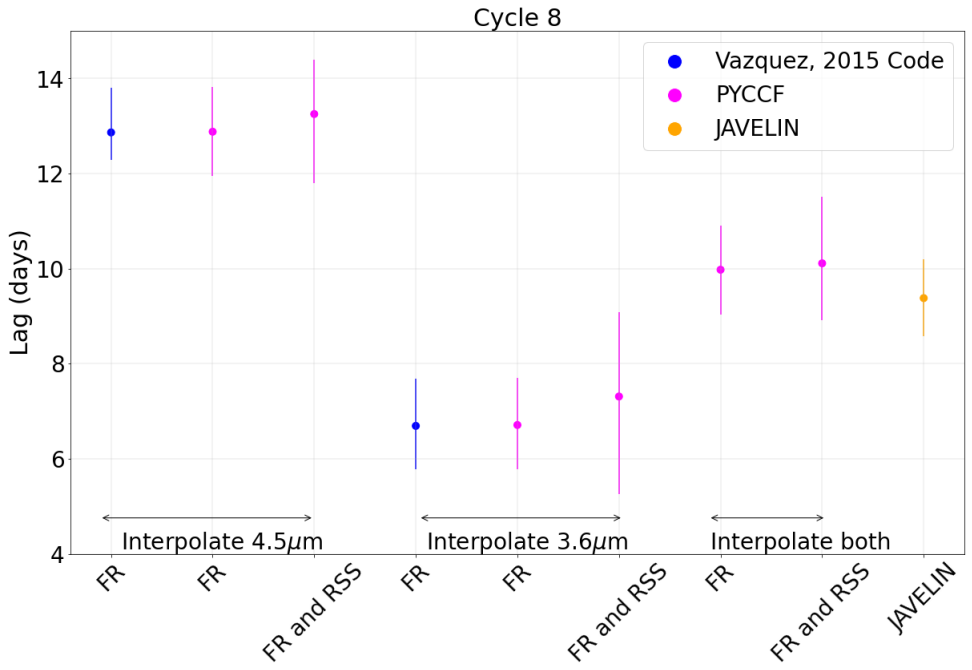

Figure 5.36: NGC 6418 cycle 8 lag comparisons for the 3.6-4.5μm analysis. The lag results from PYCCF and the Vazquez (2015) code were calculated using an 80% threshold value. The blue data points represent lag results calculated from the Vazquez (2015) code, while the PYCCF results are shown in pink. The 'FR' and 'FR and RSS' labels on the x-axis indicate whether the lag was measured with the code using only flux randomization (FR) or both flux randomization and random subset selection (FR and RSS). Above the x-axis, it is specified whether the corresponding lags were calculated using IR interpolation, optical interpolation, or interpolating both.

Cycle 9 The cycle 9 region of the 3.6 and 4.5 μm light curves is shown in Figure 5.32. Interestingly, the 4.5 μm light curve has a much higher flux variation amplitude than the 3.6 μm light curve in this region. Interpolated light curves are shown in Figure 5.37. There is no clear advantage to either interpolation type.

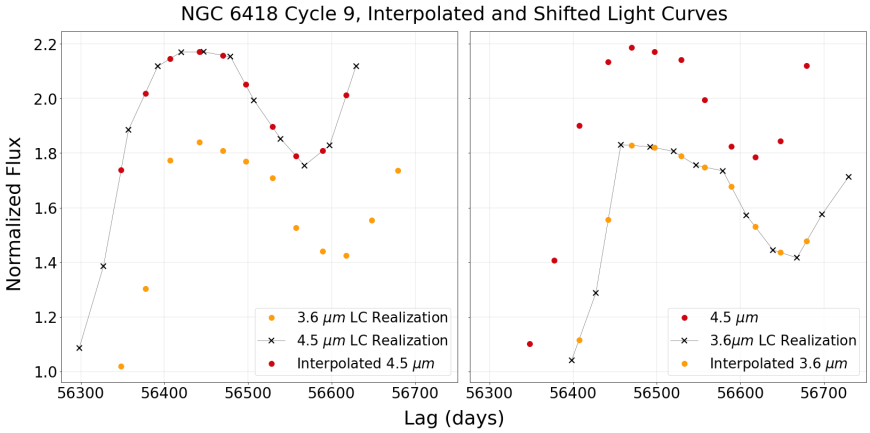

Figure 5.37: Examples of the interpolated 3.6 and 4.5 μm light curves of NGC 6418: The plot on the left includes one 4.5μm light curve realization (the black points), the 3.6μm light curve realization is shown as orange points, and the red points represent the 4.5 μm data linearly interpolated onto the time stamps of the 3.6 μm data points. Here, the 4.5μm light curve has been shifted back by 50 days.
The plot on the right is similar, including one 3.6μm light curve realization (the black points), the 4.5μm light curve realization is shown as red points, and the orange points represent the 3.6 μm data linearly interpolated onto the time stamps of the 4.5 μm data points. Here, the 3.6μm light curve has been shifted forward 50 days.

The CCFs and CCCDs are presented in Figure 5.38. The sharp discontinuities seen in the CCFs are due to the small number of data points in Cycle 9. This effect is explained in Appendix A.1.3 for the Cycle 9 optical-IR analysis, although the reason is the same here.

Similar to the cycle 8 analysis, the lag values calculated with the two different interpolation types differ by ∼10 days ($20.32^{+0.55}_{-0.54}$ days for 3.6μm-optical and $9.25^{+0.94}_{-0.93}$ days 4.5μm-optical) when using an 80% threshold value. Looking at Figure 5.39, the lag values coincide for larger percent threshold values. Again, taking an average of the two values will also give a similar result to using a larger percentage threshold, with a lag of $14.74^{+0.75}_{-0.74}$ days.

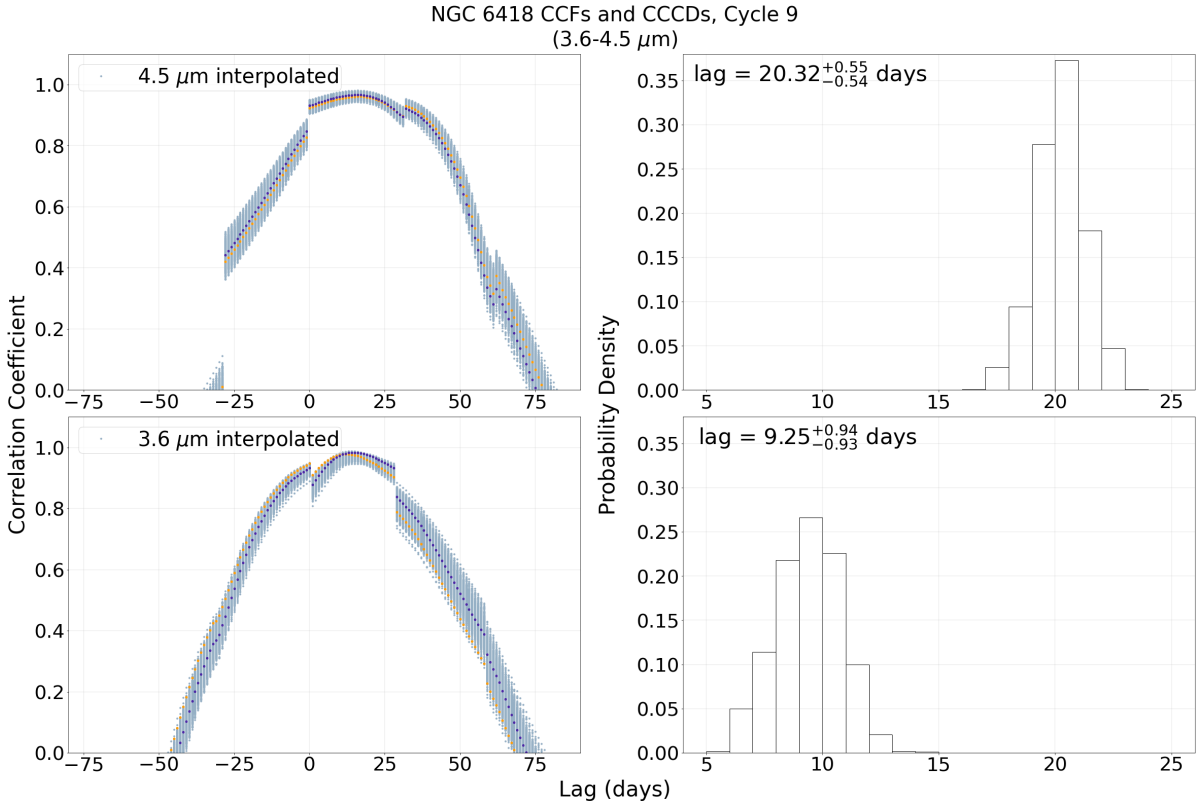

Figure 5.38: NGC 6418 CCFs (left subplots) and CCCDs (right subplots) for the 3.6-4.5 μm analysis of cycle 9. The upper subplots show the results of using 4.5 μm interpolation, while the lower subplots show the results of using 3.6 μm interpolation. 80% threshold values were used to form the CCCDs. In the left subplots, 1000 CCFs formed from the Monte Carlo iterations are shown in light blue. As examples, the purple and orange points highlight two individual CCFs.

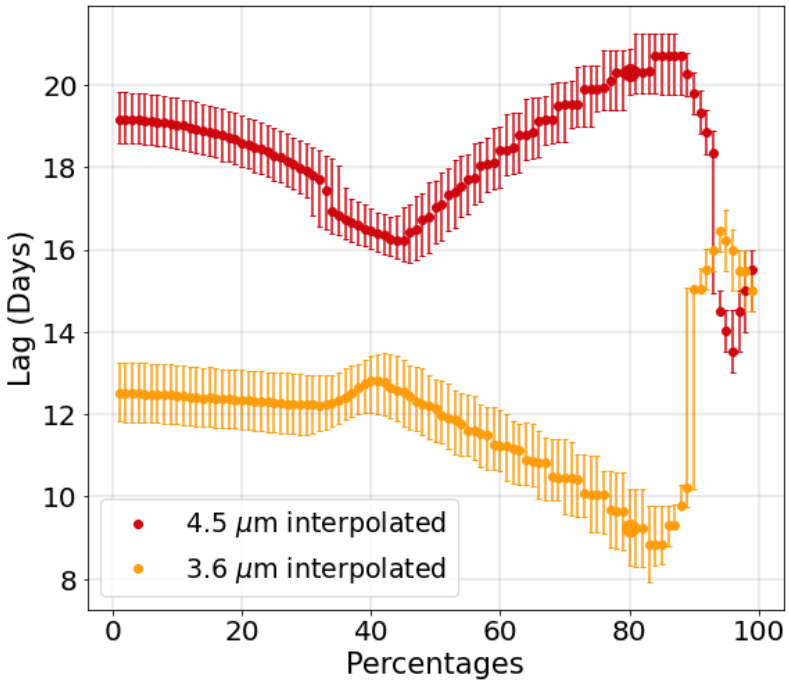

Figure 5.39: NGC 6418 Cycle 9, 3.6-4.5μm: The dependence of measured lags on CCF percentage threshold values. The red points represent the use of 4.5 μm interpolation, while orange represents 3.6 μm interpolation. The two larger points indicate the 80% threshold percentage values, and the error bars show the interquartile range.

PYCCF and JAVELIN results are shown in Figure 5.40. The lag value measured using the Vazquez code and taking the average lag of the two interpolation types ($14.74^{+0.75}_{-0.74}$) days is consistent with the PYCCF results when interpolating both light curves. The JAVELIN lag is measured to be $10.79^{+2.78}_{-2.83}$ days which is not quite consistent with that of the Vazquez code.

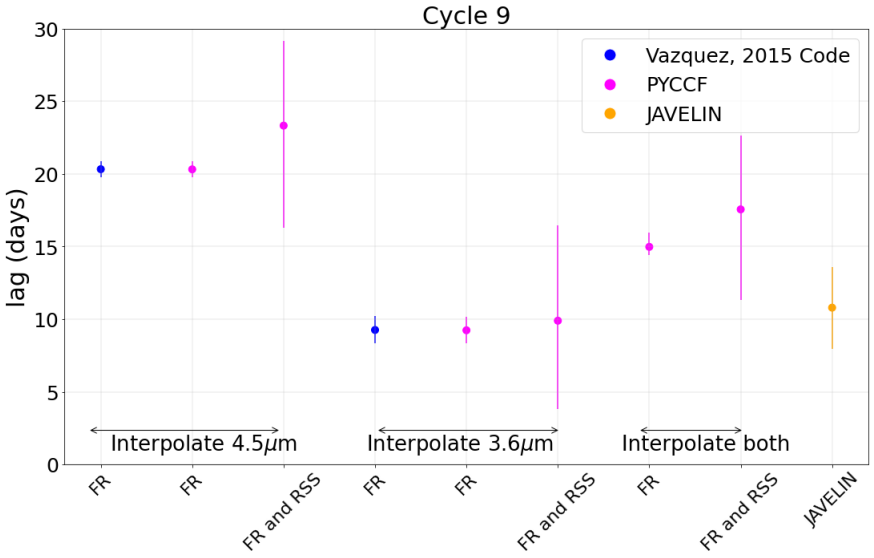

Figure 5.40: NGC 6418 Cycle 9 lag comparisons for the 3.6-4.5μm analysis. The lag results obtained with PYCCF and the Vazquez (2015) code were calculated using an 80% threshold value. The blue data points represent lags calculated from the Vazquez (2015) code, while the PYCCF results are shown in pink. The 'FR' and 'FR and RSS' labels on the x-axis indicate whether the lag was measured with the code using only flux randomization (FR) or both flux randomization and random subset selection (FR and RSS). Above the x-axis, it is specified whether the corresponding lags were calculated using IR interpolation, optical interpolation, or interpolating both.

Cycles 8 and 9 Finally, the combined Cycles 8 and 9 light curves were cross-correlated. Interpolated light curves are presented in Figure 5.41. Clearly the main difference between the interpolation types here is due to the number of data points used in Cycle 9.

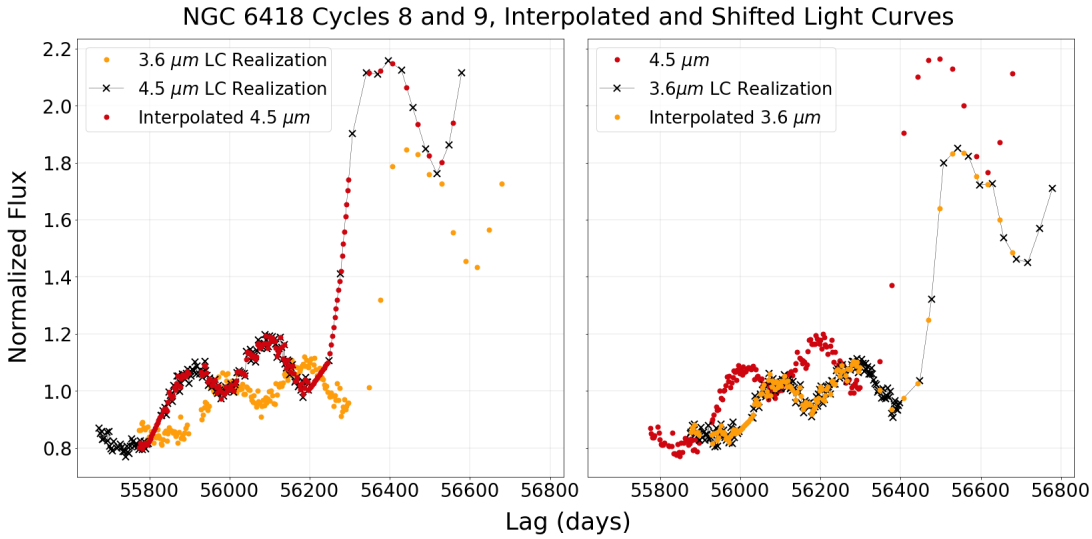

Figure 5.41: Examples of the interpolated 3.6 and 4.5 μm light curves of NGC 6418: The plot on the left includes one 4.5 μm light curve realization (the black points), one 3.6 μm light curve realization shown as orange points, and the red points represent the 4.5 μm data linearly interpolated onto the time stamps of the 3.6 μm data points. Here, the 4.5 μm light curve has been shifted back by 100 days. The plot on the right is similar, including one 3.6 μm light curve realization (the black points), the 4.5 μm light curve realization is shown as red points, and the orange points represent the 3.6 μm data linearly interpolated onto the time stamps of the 4.5 μm data points. Here, the 3.6 μm light curve has been shifted forward 100 days

CCCDs and CCFs are presented in Figure 5.42, with the CCCDs calculated using 80% threshold values. The 80% threshold appears to be a very reasonable value to use, with the measured lag values only differing by $\sim$1 day. Figure 5.43 confirms this, as the lag values coincide for percentage values from 80-100%. The Cycle 8, Cycle 9, and combined Cycle 8 and 9 IR light curves are shown in Figure 5.44, with the 3.6 μm light curve shifted forward by the lag values measured with the Vazquez (2015) code.

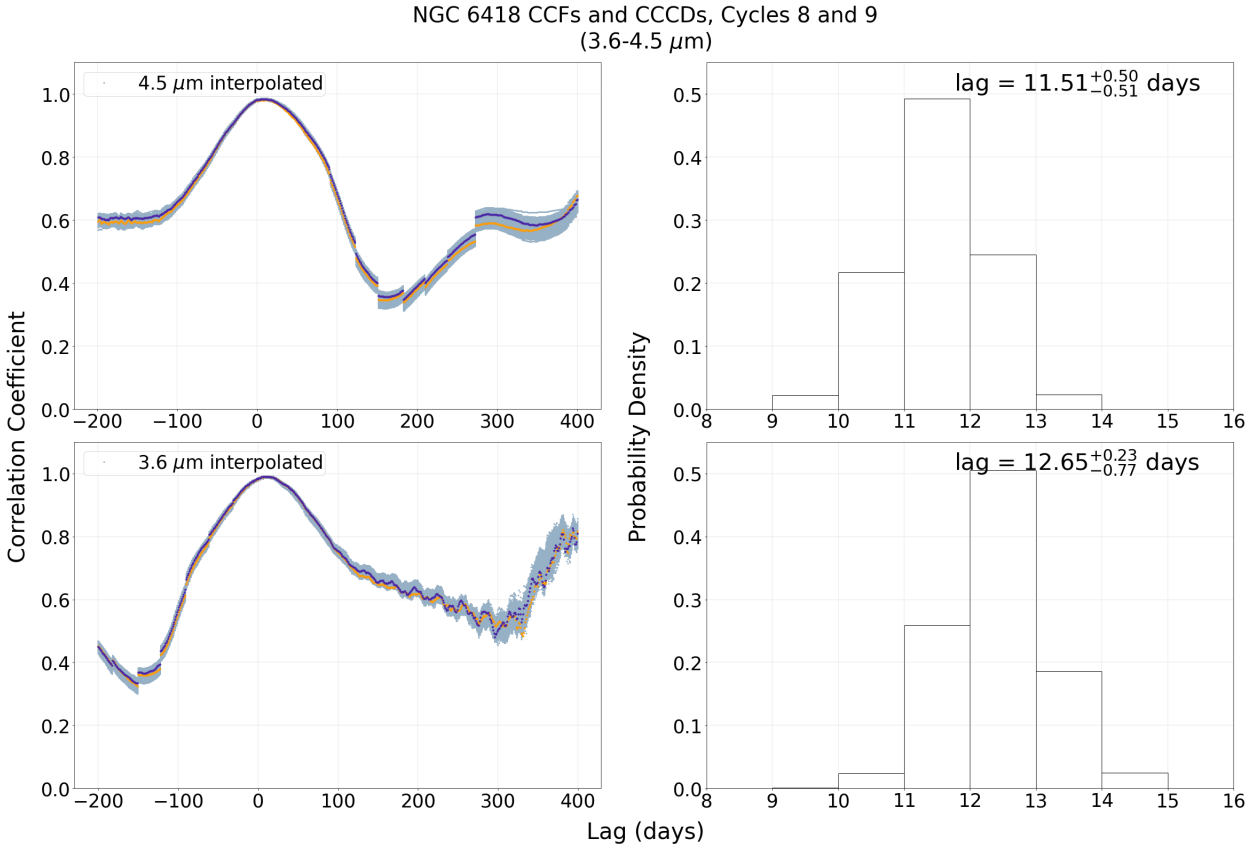

Figure 5.42: NGC 6418 CCFs (left subplots) and CCCDs (right subplots) for the 3.6-4.5 μm analysis of cycles 8 and 9. The upper subplots show the results of using 4.5 μm interpolation, while the lower subplots show the results of using 3.6 μm interpolation. 80% threshold values were used to form the CCCDs. In the left subplots, 1000 CCFs formed from the Monte Carlo iterations are shown in light blue. As examples, the purple and orange points highlight two individual CCFs.

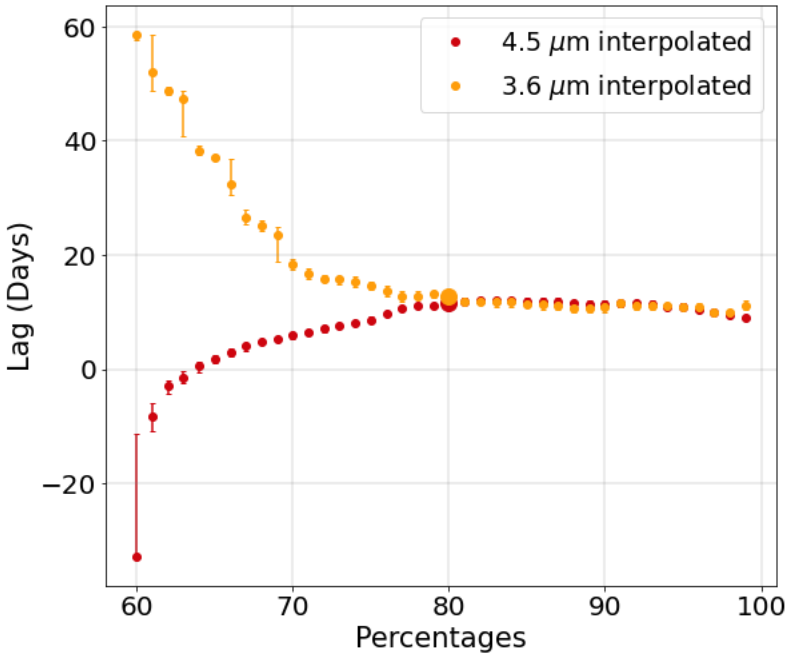

Figure 5.43: NGC 6418 Cycles 8 and 9, 3.6-4.5μm: The dependence of measured lags on CCF percentage threshold values. The red points represent the use of 4.5 μm interpolation, while orange represents 3.6 μm interpolation. The larger points indicate the 80% threshold percentage values, and the error bars show the interquartile range.

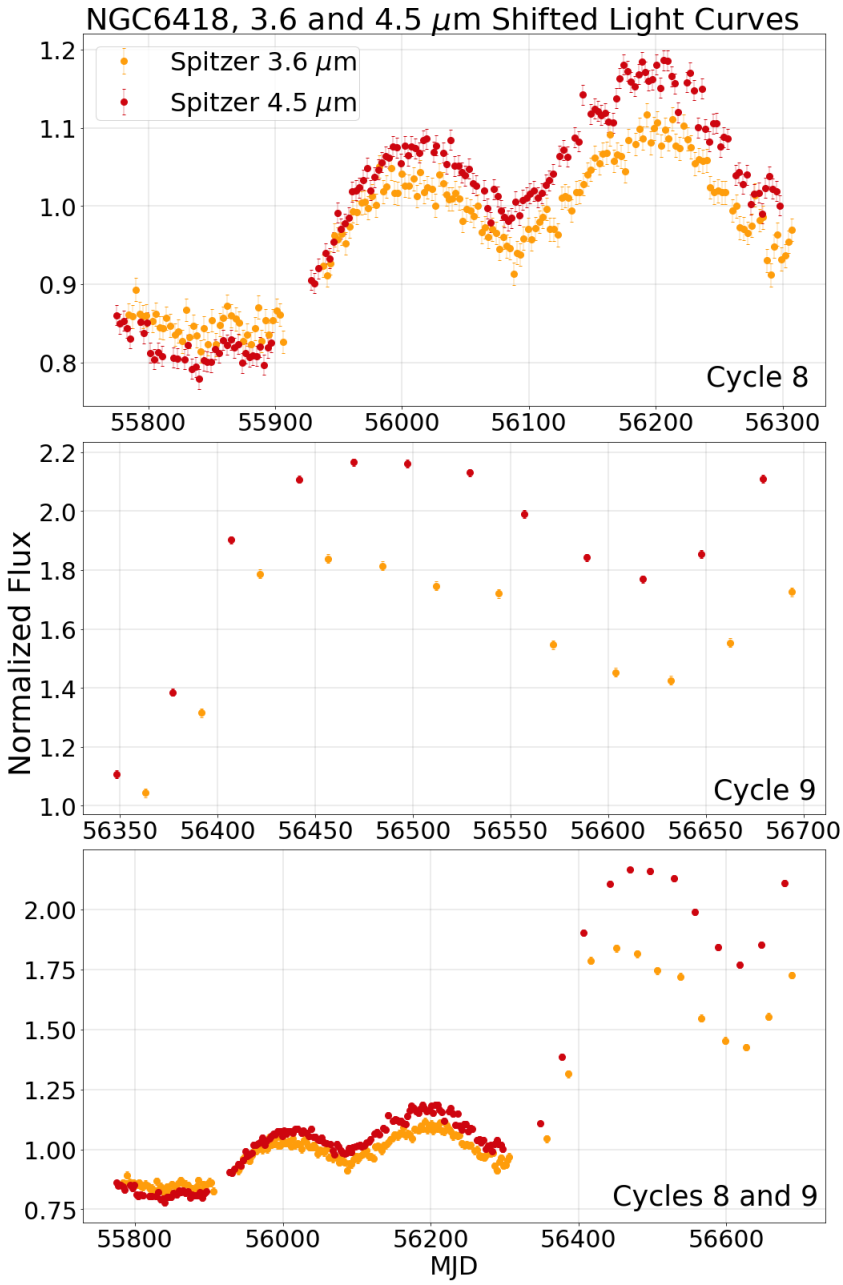

Figure 5.44: NGC 6418 shifted IR light curves. In each subplot, the 3.6μm light curve is shifted forward by the lag value measured using the Vazquez code. The upper plot includes the Cycle 8 section, with a 9.7 day shift, the middle plot includes the Cycle 9 section with a 14.7 day shift, and the lower plot includes both Cycles 8 and 9 with a 9.1 day shift.

A comparison of the lags calculated with the three codes is shown in Figure 5.45. The JAVELIN lag is measured to be $9.69^{+0.68}_{-0.68}$ days, consistent with the PYCCF values using both FR and RSS, although differs by a few days from the Vazquez code.

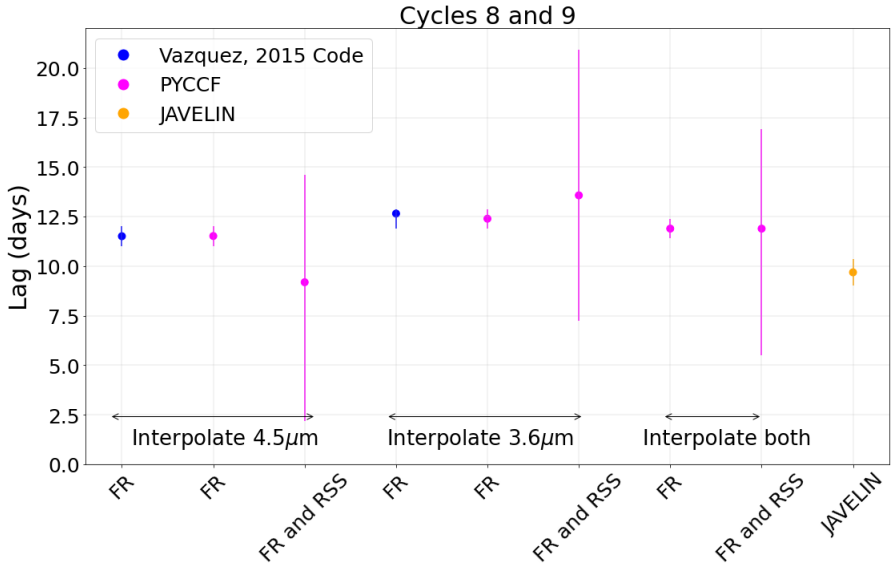

Figure 5.45: NGC 6418 cycles 8 and 9 lag comparisons for the 3.6-4.5μm analysis. The lag results calculated with PYCCF and the Vazquez (2015) code were calculated using an 80% threshold value. The blue data points represent lag results calculated from the Vazquez (2015) code, while the PYCCF results are shown in pink. The 'FR' and 'FR and RSS' labels on the x-axis indicate whether the lag was measured with the code using only flux randomization (FR) or both flux randomization and random subset selection (FR and RSS). Above the x-axis, it is specified whether the corresponding lags were calculated using IR interpolation, optical interpolation, or interpolating both.

5.5 NGC 6418 Spectra

An optical spectrum of NGC 6418 obtained in April 2001 was retrieved from the SDSS archive (see left subplot of Figure 5.46). This shows a weak H-α line as the only visible broad line, which is typical of a Sy 1.9 AGN. A new optical spectrum was obtained at the Apache Point Observatory (APO) 3.5m telescope in January 2014, a few months after the cycle 9 flare (see right subplot of Figure 5.46). Comparing the pre-flare and post-flare spectra, it is clear that the features of each

spectrum are very different. The post-flare spectrum has strong H-alpha, H-beta, H-gamma, He I, and Fe II broad lines, which is typical of a Sy 1 AGN.

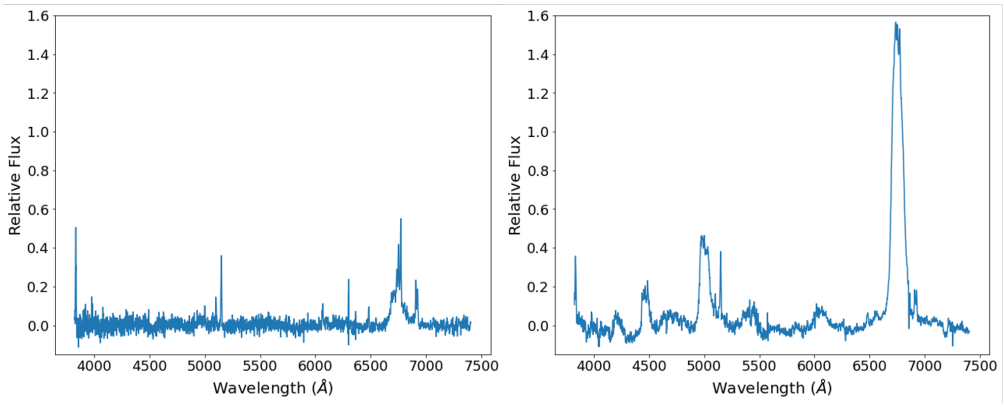

Figure 5.46: The 2001 SDSS spectrum is shown in the left subplot, and the 2014 APO spectrum is shown on the right.

We have also continued to obtain spectra for several years after the flare (Jan 2014-Sep 2018) shown in Fig 5.47, the broad lines have continued to fade since 2014, although not quite to the low level of the 2001 spectrum.

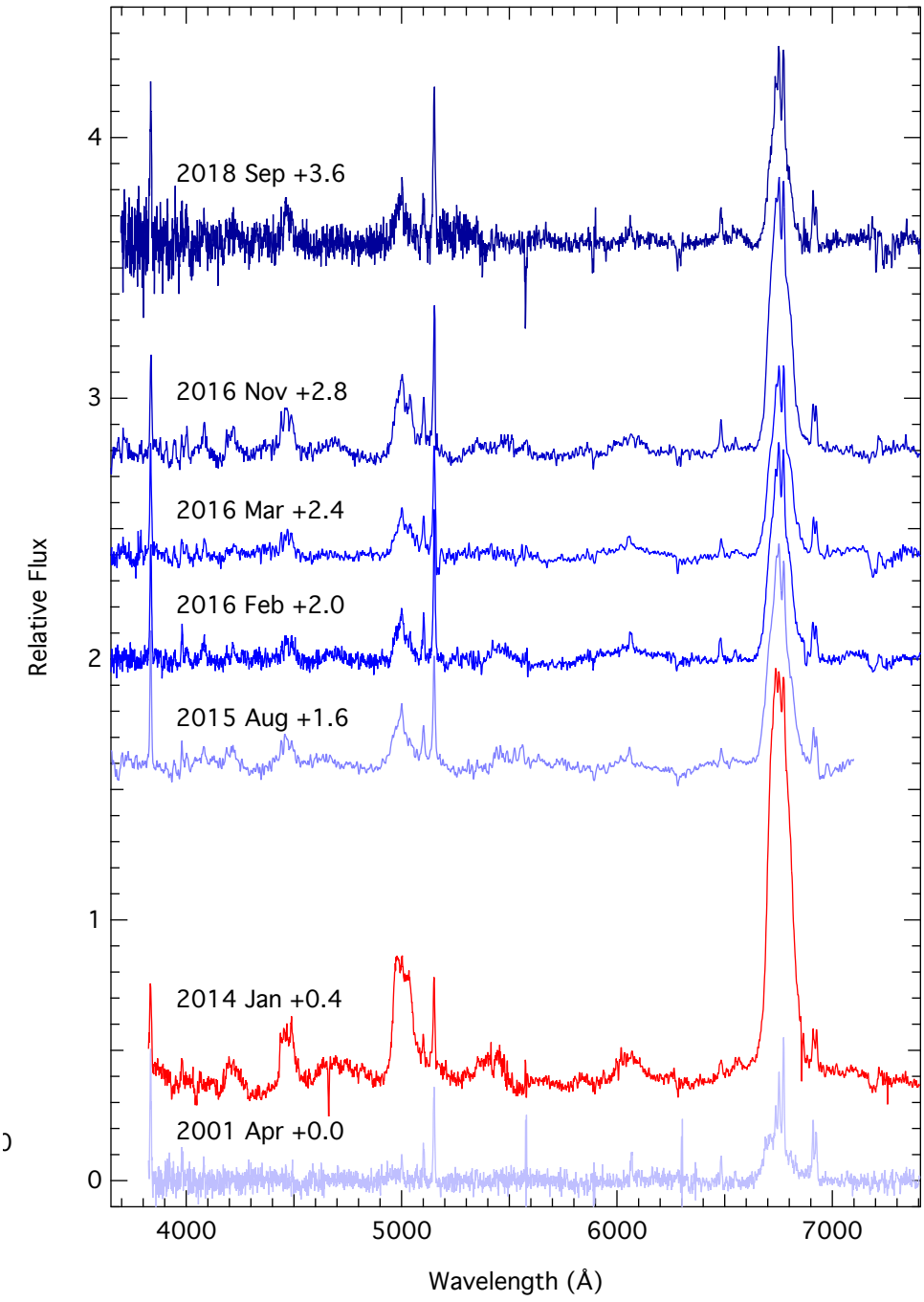

Figure 5.47: Emission line spectra of NGC 6418. The continuum has been fitted and subtracted. The spectra are arranged in a time sequence and offset in relative flux for clarity.

5.6 Summary

Light Curves The light curves clearly display strong optical variability with a strong IR response. During cycle 8, there were optical variations (two peaks) on the order of 20%, with the IR clearly responding with a similar amplitude. An optical flare occured at the beginning of cycle 9, where the brightness increased by 124%. In the IR, from the end of cycle 8 until the peak in cycle 9 the 3.6 μm light curve increases in flux by 100%, while the 4.5 μm light curve increases by $\sim$ 115%, evidently in response to the optical flare.

CCA: Cycle 8 The lags from cycle 8 are compared in Table 5.2. The Vazquez code produces CCFs and CCCDs with clear peaks (see Figures 5.6 and 5.7). Taking an average of the lags measured using IR and optical interpolation (with 80% threshold values) gives a reasonable lag value when comparing the lag vs. percentage threshold value plots (see Figure 5.8). The lag values calculated with JAVELIN are consistent with those of the Vazquez code and PYCCF for the 3.6μm-optical analysis, although the lag computed with JAVELIN is larger for the 4.5μm-optical analysis (see Figures 5.11 and 5.12 for comparisons of the lag values). This is due to the multiple peaks in the CCCDs from JAVELIN (see Figure A.1), where one peak is located at a larger lag value, and another peak occurs at $\sim$48 days, consistent with the lags of PYCCF and the Vazquez code.

There is also a lag between the 3.6 and 4.5 μm channels for the cycle 8 region. The reported lag value from the Vazquez code and PYCCF were measured by calculating the average lag value of the two interpolation types (3.6 or 4.5 μm interpolation), with 80% threshold values. Looking at Figure 5.35, the lag values also coincide when using a larger percent threshold value. We can compare the 3.6-4.5 μm lag with the difference between the 3.6 μm-optical and the 4.5 μm-optical lags, as reported in the last two columns of Table 5.2. Excluding the JAVELIN results, these values are consistent.

CCA: Cycle 9 During cycle 9, the IR observational cadence is longer than that of cycle 8 (once every 30 days, compared to once every 3 days). There is also a large optical gap of 128 days that

	3.6μm-optical	4.5μm-optical	Δt	3.6-4.5μm
Vazquez (2015)	$37.7^{+2.1}_{-2.3}$	$48.6^{+2.0}_{-2.3}$	10.9	$9.72^{+0.96}_{-0.75}$
PYCCF (FR and RSS)	$36.9^{+4.3}_{-4.2}$	$48.2^{+4.6}_{-4.7}$	11.3	$10.28^{+1.46}_{-1.76}$
JAVELIN	$36.7^{+14.8}_{-3.2}$	$64.4^{+2.6}_{-12.6}$	27.7	$9.38^{+0.81}_{-0.82}$

Table 5.2: NGC 6418 Cycle 8 Summary of Lag Results: The '3.6μm-optical' and '4.5μm-optical' columns show the lag results of each IR light curve cross-correlated with the optical. The lags reported here were calculated by taking an average of the lags measured using IR and optical interpolation (with 80% threshold values). Each row gives the lag results with the Vazquez (2015) code using FR only, PYCCF using both FR and RSS, and JAVELIN. The column 'Δt' shows the difference between the '3.6μm-optical' and '4.5μm-optical' lag values. The '3.6-4.5μm' column shows the lag result of the two IR channels cross-correlated with each other.

occurs during the rise in flux. The IR light curve response is significantly more smoothed out than the optical light curve, making it difficult to determine the lag. The lags from cycle 9 are compared in Table 5.3.

Including the end portion of cycle 8 with the cycle 9 data does not have much influence on the lag that is measured, differing by only 3-12 days with the Vazquez code. The differences are larger with PYCCF when using both FR and RSS, although the lags are consistent within the uncertainties. As for which threshold percentage value is best to use, a 60% value for IR interpolation and a 40% value for optical interpolation both occur in stable regions of Figure 5.17.

	3.6μm-opt		4.5μm-opt		Δt		3.6-4.5 μm
	IR interp	Opt interp	IR interp	Opt interp	IR interp	Opt Interp	
Vazquez (2015)	$89.7^{+.89}_{-0.72}$	$52.8^{+4.3}_{-1.4}$	$114.4^{+0.96}_{-0.99}$	$69.1^{+1.2}_{-1.4}$	24.7	16.3	$14.74^{+0.75}_{-0.74}$
PYCCF (FR and RSS)	$96.2^{+14.5}_{-8.1}$	$59.0^{+11.6}_{-9.3}$	$119.5^{+14.2}_{-7.4}$	$73.8^{+35.1}_{-12.8}$	23.3	14.0	$16.60^{+6.19}_{-6.55}$
JAVELIN	$50.36^{+0.49}_{-0.57}$		$61.1^{+54.3}_{-10.5}$		10.74		$10.79^{+2.78}_{-2.83}$

Table 5.3: NGC 6418 Cycle 9 Summary of Lag Results: The lag results were calculating using the cycle 9 light curve that includes the data points from the end of cycle 8 (except for the JAVELIN results, in which the light curves only contained cycle 9 data). The '3.6μm-optical' and '4.5μm-optical' columns show the results for each IR light curve cross-correlated with the optical light curve, for each type of interpolation. Each row gives the lag results using the Vazquez (2015) code using FR only, PYCCF using both FR and RSS, and JAVELIN. A 60% percentage threshold value was used for IR interpolation and a 40% value for optical interpolation. The column 'Δt' shows the difference between the '3.6μm-optical' and '4.5μm-optical' lag values for each interpolation type. The '3.6-4.5μm' column shows the lag result of the two IR channels cross-correlated with each other.

There are different lag values associated with different regions of the cycle 9 light curves: one is associated with the rise of the light curve, another associated with the decrease in flux. The CCFs make this clear to see, as the various peaks appear to correspond with these light curve features (see Figures 5.14, 5.15, and 5.16). If we are more interested in the region of the light curve containing the flare that occurs at the beginning of cycle 9, then using optical interpolation is likely a better choice. Using IR interpolation with 60% threshold value gives a lag intermediate between the two main features of the light curve shown in Figure 5.16. The JAVELIN results give lags smaller than those calculated with either of the other codes, although the lags are most similar to those calculated using optical interpolation.

The lag between the two IR channels for cycle 9 was also calculated. An average value was calculated between the lag measured using 3.6μm interpolation and 4.5μm interpolation. Again, as shown in Figure 5.39, the lag values coincide for larger percent threshold values. We can compare the lag between the two IR channels with the difference between the 3.6μm-optical and 4.5μm-optical lag values, which is shown in the last 3 columns of Table 5.3. Since different lag values are calculated depending on which interpolation type is used, this was done separately for the lags calculated using IR interpolation and optical interpolation. Excluding JAVELIN, these values are consistent with the lag values calculated using optical interpolation.

Comparing Tables 5.2 and 5.3, we can see that there is a different lag measured for cycle 8 compared to cycle 9. Except for the 4.5μm-optical JAVELIN lag values, for each IR channel cross-correlated with the optical there is an increase in the lag from cycle 8 to cycle 9.

CCA: Cycles 8 and 9 Based on the results summarized so far, there is a lag increase from cycle 8 to cycle 9, although we attempted to find a single lag value for the combined cycle 8 and cycle 9 data. When interpolating the IR with the optical, using IR interpolation measures lag values with stable lag results when plotting the lag vs percentage threshold values, although the CCFs have a very broad peak.

The optical light curve was shifted forward by the measured lag values and is shown in Figures

5.28 and 5.31. The shorter lags (measured with JAVELIN) appear to be a more accurate lag value, although the lags still seem too large for the cycle 8 region.

For the cycles 8 and 9 3.6-4.5μm lags, Figure 5.27 shows that the lag values calculated with each interpolation type coincide for threshold values of 80-99 percent. An average of the 80% lags was calculated for the Vazquez code and PYCCF lags reported here. Figure 5.44 includes the shifted IR light curves for each cycle. These lag values give a reasonable match between the light curve features.

	3.6μm-optical	4.5μm-optical	Δt	3.6-4.5μm
Vazquez (2015)	$83.63^{+0.53}_{-0.54}$	$97.01^{+0.50}_{-0.49}$	13.4	$9.10^{+0.74}_{-0.71}$
PYCCF (FR and RSS)	$84.48^{+5.97}_{-4.66}$	$98.50^{+6.60}_{-5.22}$	14.02	$10.28^{+1.46}_{-1.76}$
JAVELIN	$46.8^{+1.21}_{-2.28}$	$58.39^{+1.08}_{-2.64}$	11.59	$9.69^{+0.68}_{-0.68}$

Table 5.4: NGC 6418 Cycles 8 and 9 Summary of Lag Results: The '3.6μm-optical' and '4.5μm-optical' columns show the lag results of each IR light curve cross-correlated with the optical. The lags reported here were calculated using IR interpolation. Each row gives the lag results with the Vazquez (2015) code using FR only, PYCCF using both FR and RSS, and JAVELIN. The column 'Δt' shows the difference between the '3.6μm-optical' and '4.5μm-optical' lag values. The '3.6-4.5μm' column shows the lag result of the two IR channels cross-correlated with each other.

NGC 6418 Spectra We can compare the features in the spectra from before and after the flare, shown in Figure 5.46. In the 2001 spectrum (obtained prior to the flare), a weak Hα component is the only visible broad line, which is typical of a Seyfert 1.9 AGN. In the 2014 APO spectrum taken by Dr. Jack Gallimore (obtained after the flare), the spectrum changed significantly in that the broad lines are clearly visible. This is typical of a Seyfert 1 AGN. It should be noted that the pre-flare spectrum was taken $\sim$ a decade before the flare, and the post-flare spectrum was obtained $\sim$ a year after the flare, so we do not have measurements of the spectrum directly before and after the flare. In the spectra we have continued to obtain several years after the flare (Jan 2014-Sep 2018) shown in Fig 5.47, the broad lines have continued to fade, likely due to a change in the AGN luminosity.

5.7 Discussion

Several conclusions can be drawn from this analysis. By looking at the features of the light curves (optical variations followed by IR response) and comparing the pre-flare and post-flare spectra, we conclude that NGC 6418 has undergone a changing-look event. There are several possibilities as to the cause of this phenomenon, one of which is a change in obscuration. Within a clumpy torus model, the movement of clouds of dust could temporarily obscure our view of the central region, causing the classification of the AGN to change from Type I to Type II AGN (or vice versa, depending on the movement of the dust clouds). Another possibility for this phenomenon is due to an increase in the accretion rate, and hence the luminosity of the AGN. An increase or decrease of the accretion rate affects the AGN luminosity, which will affect the strength of the broad lines.

We conclude that NGC 6418 has undergone a changing-look event, occuring due to both a change in obscuration and also a change in the intrinsic luminosity of the AGN. The visual extinction has been measured using the broad line balmer decrements from each spectra, and are shown in Figure 5.48. We see that the balmer decrement changes from $\sim$12 (in the pre-flare 2001 SDSS spectrum) to a value of $\sim$ 3.7 (in the post-flare 2014 spectrum). This suggests a decrease of $\sim$ 4 magnitudes in extinction after the flare. This could possibly be caused by a dust cloud being destroyed or moving out of our line of sight. The change in extinction would not cause a change in the profile shapes however, which could be due to dynamical changes or reverberation.

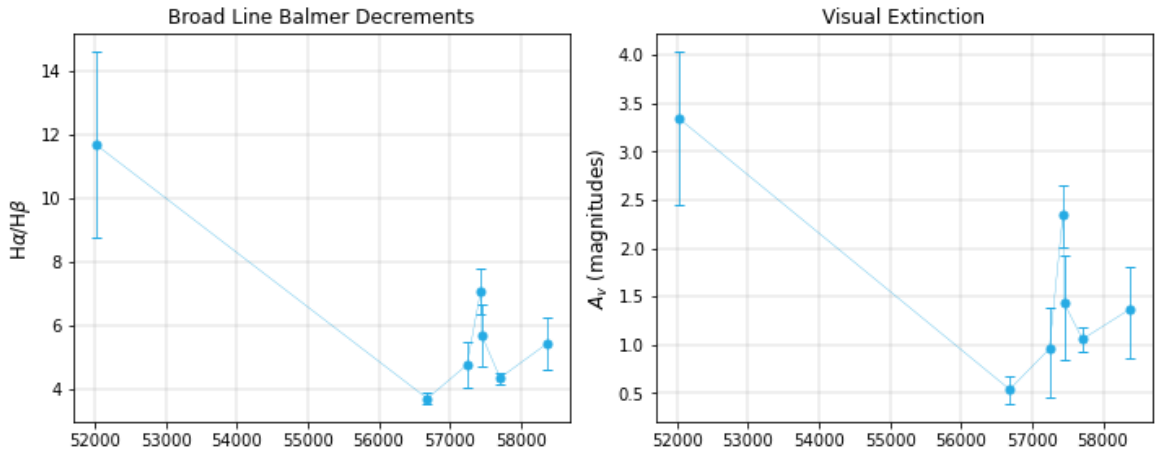

Figure 5.48: NGC 6418 Broad Line Balmer Decrements (left subplot) and Extinction values (right subplot)

However, the observations demonstrate that the change in type of NGC 6418 is not solely due to a change in extinction, but is also due to an intrinsic increase in the luminosity of the AGN (possibly caused by a change in accretion rate). One would expect a change in extinction to have a large effect on the optical emission, but little effect on the IR emission. The changes seen in the optical spectrum could be attributed to a decrease in extinction. However, we clearly see in the light curves that the IR responds to the optical flare with a similar amplitude. By looking at both the light curves and the spectra for NGC 6418, we interpret this changing-look event as occurring due to both a change in extinction, and an intrinsic change in the luminosity of the AGN.

There is also strong evidence for an increase in the lag between cycles 8 and 9. Other than the 4.5μm-optical lag value measured with JAVELIN, the results of all the CCA codes indicate a lag increase corresponding to the optical flare. Using a single lag for the entire campaign does not adequately represent the observed behavior.

Although we see an increase in the lag, it is important to note that the optical coverage is sparse, especially near the flare. There is a gap in the optical coverage just before the peak of the flare (from MJD 56235 to MJD 56363). Also the flare is only seen in the PTF data, since the other two light curves that form the entire optical light curve (LT and CSS) do not have data covering

the time period of the flare. Despite these caveats, there is strong evidence for a significant increase in the lag. The difference between the IR-optical lags is also consistent with the 3.6-4.5μm lags.

We interpret the increase in the lag as an increase in the size of the 3.6 and 4.5 μm emitting regions, which implies that there is an increase in the sublimation radius. We conclude that this lag increase is due to the flare destroying dust grains at the inner radius of the torus, through sublimation.

CHAPTER 6

TORMAC MODELING

Our goal in using TORMAC for this project is to produce model IR responses for a few selected AGN in our sample (KAZ 163, MRK 876, and MRK 507). These three AGN were selected because their light curves show two different types of behavior which were outlined in Chapter 2, which is "comparable optical and IR variability" for KAZ 163 and MRK 507, and "significant optical variability with a slow secular IR response" for MRK 876. These three AGN also span a wide range of estimated sublimation radii.

TORMAC can produce simulated IR light curves at several selected wavelengths, given any input AGN (optical, starlight-subtracted) light curve. Given specific torus parameters as input, the emission from each dust cloud is computed by interpolating in a pre-computed grid of radiative transfer models. The IR emission is computed as a function of time taking light travel delays into account, by integrating over the cloud ensemble at each time step. We can compare the TORMAC model IR responses to our observed IR light curves, in order to constrain other torus parameters.

6.1 TORMAC Description

TORMAC considers the torus to be composed of optically thick clouds of dust, based on the clumpy torus model described in Nenkova et al. (2008a,b), and is also based on the response mapping code of Robinson & Perez (1990) and Perez et al. (1992). The 3D ensemble of dust clouds within the torus is modeled as a flared disk in spherical polar coordinates (r, β, ϕ). The clouds are distributed using a power-law in the radial direction, with an index of p ($\propto r^p$). In the azimuthal angle ϕ, they are distributed uniformly. Within the complement of the polar angle, β, they can be distributed either uniformly or as a Gaussian distribution.

Several global and local effects are included in TORMAC, which are cloud orientation, cloud shadowing, cloud occultation, and anisotropic illumination of the torus. With anisotropic illumination, the incident flux from the accretion disk onto each torus cloud depends on the clouds polar angle, as well as its radial distance from the central source. This effect is due to edge darkening of the accretion disk. Less radiation will be emitted along the equatorial plane than at the poles, causing the dust sublimation radius to depend on the polar angle. The incident flux onto a cloud is given by $F(\theta, r) = \frac{L(\theta)}{4\pi r^2}$, and the emission from the accretion disk is

$$L(\theta) = \big(s + (1-s)(1/3)\cos\theta(1+2\cos\theta)\big)L_{AGN}, \tag{6.1}$$

with θ as the polar angle, and s specifying the degree of anisotropy.

For the case of isotropic illumination, a value of $s = 1$ is used in Equation 6.1 and the incident flux is given by $F(r) = \frac{L}{4\pi r^2}$ which only depends on r, the cloud's radius from the disk. Anisotropic illumination has the effect of allowing dust to exist at radii closer to the central source than in the case of isotropic illumination. Including anisotropic illumination of the torus in TORMAC has the effect of producing IR response with shorter lags and sharper features at both short and long wavelengths.

The effect of cloud orientation is necessary in order to accurately calculate the time-dependent emission of the torus. With this effect, the spectrum of each cloud depends on which surface of the

cloud is seen by the observer. The illuminated side of the cloud (the side directly facing the central engine) will have a higher temperature than the non-illuminated side (the side facing away from the central engine), which leads to each cloud emitting anisotropically. An observer could detect emission from the illuminated side or the non-illuminated side, depending on where the cloud is located.

Another global effect is cloud shadowing: because the torus is composed of clumps of dust, then some clouds will be "shadowed" from view of the accretion disk by the inner clouds of the torus (Nenkova et al., 2008b). These outer clouds are heated indirectly due to the radiation from nearby directly heated clouds.

The final global effect is cloud occultation, which involves the attenuation of emission from one cloud, due to intervening clouds along the observer's line of sight. This effect highly depends on the cloud optical depth, wavelength, and volume filling factor.

When forming TORMAC models, several parameters can be specified. First of all, the AGN bolometric luminosity, L_{AGN}, is the parameter that sets the sublimation radius. TORMAC considers the sublimation radius to be the inner torus radius.

As discussed above, the parameter p describes the radial dust cloud distribution. The values for p that were tested in the models include $p = 0, 1, 2$, corresponding to a cloud number density of $n(r) \propto r^{p-2}$.

The parameter σ, the angular width of the torus, defines the height of the torus above the midplane. The value of σ can range from that of a thin disk, to a sphere ($\sigma = 90°$). This parameter corresponds to the value of β that defines the edge of the torus. The edge can be either a "sharp edge" or "fuzzy edge", shown in Fig. 6.1. For the sharp edge, clouds are distributed uniformly within $\cos\beta$. The fuzzy edge is most likely a more realistic way to model the torus, with the clouds having a gaussian distribution in β, with width σ. For most of the models here, a value of $\sigma = 45$ was used, which corresponds to a thick disk, although some models with other σ values were formed.

While the individual clouds are optically thick (with τ_V=40, where τ_V is the V band optical

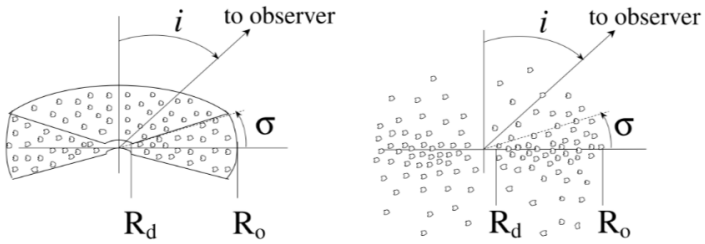

Figure 6.1: Figure from Nenkova et al. (2008b), with the left side showing the torus defined as having a "sharp" edge, and the right side showing the "fuzzy" edge of the torus. i represents the inclination angle to the observer, σ is the angular width of the torus, R_d is the dust sublimation radius and R_o is the outer radius.

depth), the volume filling factor (VFF) determines whether the torus is globally optically thick or thin. This parameter is defined as $\left(\Phi = \frac{NV_{cloud}}{V_{torus}}\right)$, where N is the total number of clouds in the torus, V_{cloud} refers to the volume of an individual cloud ($\frac{4}{3}\pi {R_{cloud}}^3$), and V_{torus} refers to the volume of the torus. The volume filling factor sets the size of each cloud, with the number of clouds and radial extent held fixed. The torus should be globally optically thick, which causes cloud shadowing and cloud occultation effects to be important. Typical values of the volume filling factor used here are $\Phi = 0.001, 0.01$.

The inclination angle can range from face-on ($i = 0°$) to edge-on ($i = 90°$), or any intermediate angle. Since these three AGN are Type I, when considering the inclination angle and the σ value, the observer should still be able to see the accretion disk emission. Typically $\sigma = 45°$ was used for the angular thickness of the torus above the midplane, therefore the inclination values that were tested were the two extreme cases, 0° and 45°.

Other torus parameters that can be specified include the total number of clouds (N), and the radial extent of the torus (Y, defined as the ratio between the outer and inner edge of the torus). These two parameters, along with the volume filling factor and p, give us constraints on which models are valid to create. The first constraint is for the torus to be globally optically thick. Typically, there should not be a clear path through the torus without a single cloud interfering.

Therefore, the number of clouds along each equatorial ray should not be less than 1. The number of clouds between r and $r + dr$ is

$$\begin{aligned} d(N(r)) &= N(r)dr \\ &= A_0(r/R_0)^p dr, \end{aligned}$$

where A_0 is a normalization constant that satisfies $\int_{R_d}^{R_0} A_0(r/R_0)^p dr = N$, where N is the total number of clouds in the torus and R_0 is the outer radius of the torus. Another similar constraint is that the number of clouds along a single equatorial ray should not be greater than 15, as suggested in Nenkova et al. (2008b) using IR SED fitting.

The last constraint to our models is the cloud volume. For each model, the volume of each cloud is set by the volume filling factor, the number of clouds, and the radial extent of the torus, so the cloud sizes vary from model to model. We do not want each individual cloud to be too large. When individual clouds are too big, the torus response will be dominated by only a few large clouds closest to the accretion disk that are directly heated, while most other clouds will be "shadowed" from view (and thus indirectly heated). We have set an arbitrary limit for each cloud's cross-section to not be greater than 1% of the torus inner surface area.

Depending on the model parameters, each model can take a significant amount of time to run. Due to time constraints, some of the AGN have more detailed model grids formed than others. For MRK 876 and KAZ 163, we do not have the parameter space fully sampled. To form models for these two AGN, trial and error was relied on to determine which models to form, as well as our knowledge on how varying different parameters will affect the IR response.

To determine the best-fitting models, a χ^2 value was calculated. To do this, the observed light curve was averaged in 10 day increments for KAZ 163 and MRK 507. 30 day increments were used for MRK 876 as there was significant scatter in the light curves, and using larger increments captured the overall trend more accurately.

The error of the averaged light curve is calculated using the windowed standard deviation values shown in Table 3.1 of Vazquez (2015). These values were calculated using ten window sizes ranging from 3 to 30 days. In this process, the standard deviation was calculated for the data points within the first window size, starting from the beginning of the light curve. This standard deviation is calculated and the window is then shifted one day forward. The process is repeated throughout the whole light curve, and the median standard deviation is recorded. This process is repeated for each window size. Ultimately, the average value of the list of median standard deviations is calculated, and Table 3.1 of Vazquez (2015) presents these values as a percentage. For KAZ 163, the values are $\sigma_{36} = 0.9\%$ and $\sigma_{45} = 0.36\%$. For MRK 507, the values are $\sigma_{36} = 0.95\%$ and $\sigma_{45} = 0.87\%$. For MRK 876, the values are $\sigma_{36} = 1.09\%$ and $\sigma_{45} = 0.45\%$, where σ_{36} and σ_{45} represent the standard deviations of the 3.6 and 4.5 μm light curves, respectively.

The model light curve was linearly interpolated onto the timestamps of the averaged light curve, and a χ^2 value was calculated, as shown below

$$\frac{1}{N}\sum \frac{(F_{Spitzer} - F_{Model})^2}{\sigma^2}, \tag{6.2}$$

where $F_{Spitzer}$ is the flux of a point in the Spitzter light curve, F_{Model} is the flux of a point in the model light curve, N is the number of Spitzer data points, and σ^2 is the standard deviation calculated from Vazquez (2015). The version of the model light curves used for the χ^2 values were truncated so that they only cover the region of time of the Spitzer campaign, and were normalized to their own mean value. Then, the light curve was multiplied by a factor to match with either the peak or low point in flux of the observed light curve, depending on the AGN.

For the AGN which we did not form models for the full parameter space (KAZ 163 and MRK 876), the models shown are those for the 4.5 μm light curve. It should be noted that the typical number of clouds used for each model is $\sim$ 50000. Also the models shown are an average of the emission from several iterations of the code, typically 3-5.

6.2 KAZ 163

Using the x-ray bolometric correction factor discussed in Chapter 2, the bolometric luminosity that was input into TORMAC is $L_{AGN} = 3.78 \times 10^{45}$ erg/s with an estimated light crossing time of 926.8 days. Figure 6.2 shows the starlight-subtracted optical light curve that was presented in Chapter 3, along with the IR light curves.

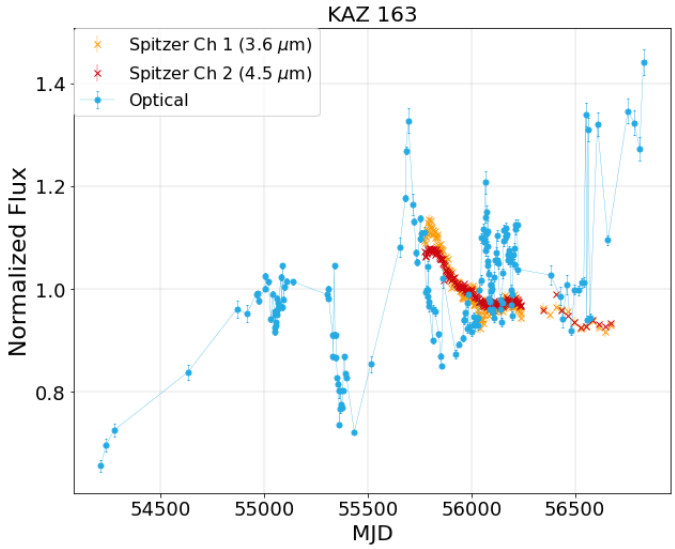

Figure 6.2: KAZ 163 light curves: IR and starlight-subtracted optical light curve, with each light curve normalized to its own mean.

We will start with the more "simple" TORMAC models (isotropically illuminated, sharp edge torus). Figure 6.3 shows a small grid of models of the 4.5 μm light curve, all of which were formed with the following parameters: Φ=0.01, isotropic illumination, $\sigma = 45$, and a sharp torus edge. This figure shows how the TORMAC models change as you adjust the p and Y values. Clearly none of these models provide a good match to our observed light curves.

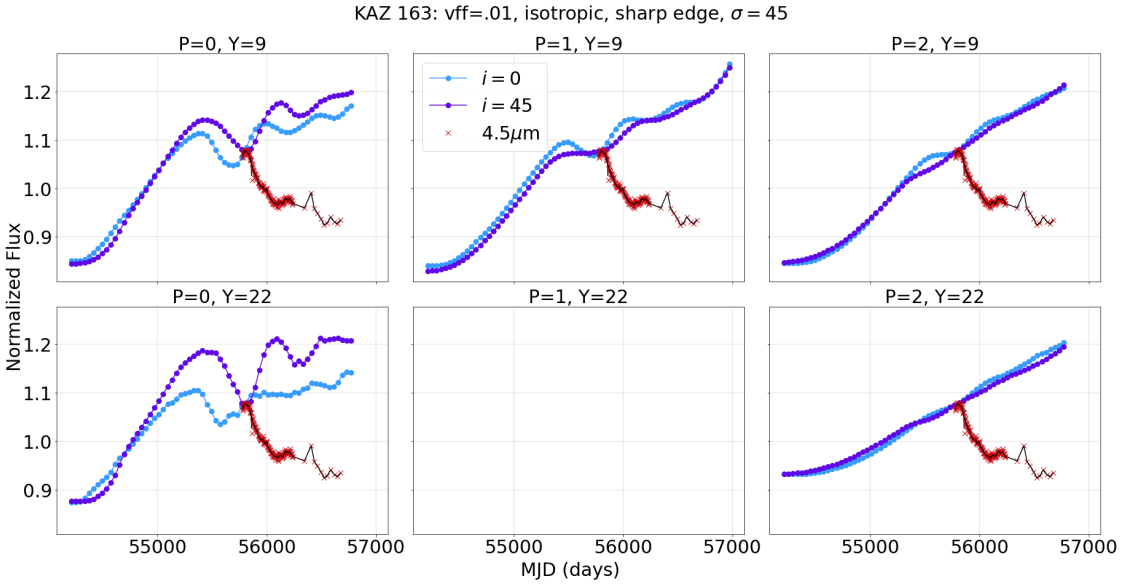

Figure 6.3: KAZ 163 TORMAC Models: Each plot includes two TORMAC models ($i = 0°$ and $i = 45°$), and the 4.5μm light curve. Models were formed with a volume filling factor of 0.01, isotropic illumination, $\sigma = 45°$, and a sharp torus edge. The upper row shows the $Y = 9$ models, and the lower row shows the $Y = 22$ models. Each column uses a different value of p ($p = 0, 1, 2$). The model light curves have been multiplied by a factor to match the peak of the observed IR light curve. Due to time constraints, the $p = 1$, $Y = 22$ model was not formed.

Next, we can see how including anisotropic illumination will affect these models. Figures 6.4 and 6.5 show the models formed with the following parameters: $\Phi = 0.01$, anisotropic illumination, $\sigma = 45$, and a sharp torus edge. Comparing Figure 6.3 to Figure 6.4, we see that using anisotropic illumination tends to create more sharp peaks and dips in the model light curves, as well as decreasing the lag slightly. We see that using anisotropic illumination begins to create models that provide a better match to the oberved Spitzer light curve. The $p = 0$ models with $Y = 9$ or $Y = 22$ and $i = 0°$ of Figures 6.4 and 6.5 provide a better match to the observed light curves, although the match is still not ideal.

It is easier to see in the anisotropic models exactly which optical light curve features the IR models are responding to. Comparing the models to Figure 6.2, the main optical light curve features that are apparent in the IR response include the dip in flux just prior to ∼MJD 55500, as well as

the peak around ∼MJD 55700, just prior to the start of the Spitzer campaign. The increase in optical emission beginning around ∼MJD 55900 until ∼56200 also has a clear effect on the models.

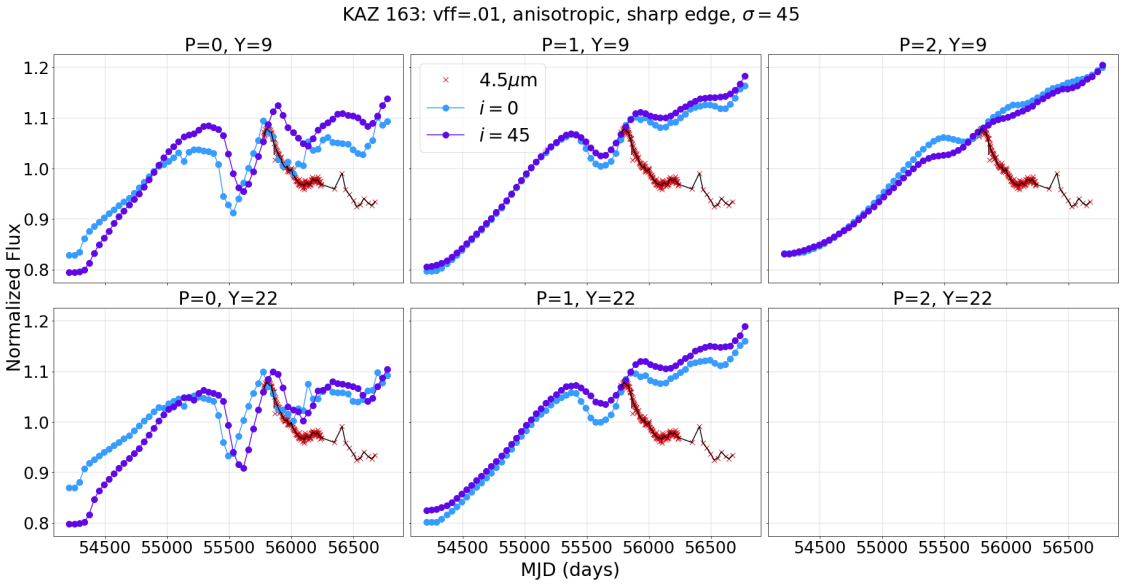

Figure 6.4: KAZ 163 TORMAC Models: Each plot includes two TORMAC models ($i = 0°$ and $i = 45°$), and the 4.5μm light curve. Models were formed with $\Phi = 0.01$, anisotropic illumination, $\sigma = 45°$, and a sharp torus edge. The upper row shows the $Y = 9$ models, and the lower row shows the $Y = 22$ models. Each column uses a different value of p ($p = 0, 1, 2$). The model light curves have been multiplied by a factor to match the peak of the observed IR light curve. Due to time constraints, the $p = 2$, $Y = 22$ model was not formed.

The anisotropically illuminated light curves still have a major issue: The model light curves show a secondary peak (around the region ∼ MJD 56100 to 56600) that the observed light curves do not show. In the observed IR light curve, the emission is quite flat in this region. We will attempt to find what parameters will suppress this peak in flux of the model light curves.

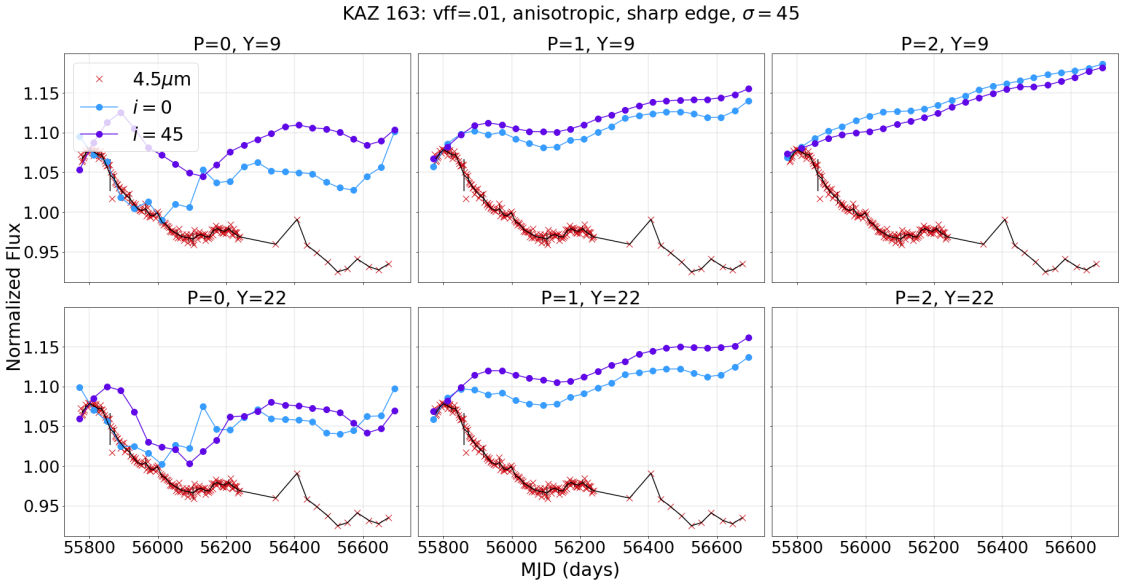

Figure 6.5: The same TORMAC models as Figure 6.4: To form these plots, the model light curves were truncated to cover only the region of time of the Spitzer campaign, and then normalized to their own mean value. The model light curves have been multiplied by a factor to match the peak of the observed IR light curve.

We will explore how using a fuzzy edge will affect the models in Figures 6.4 and 6.5. We expect that using a fuzzy edge will slightly smooth out the response, which might produce models that better match the lower secondary peak of our observed light curves. Figures 6.6 and 6.7 show the models produced with the parameters $\Phi = 0.01$, anisotropic illumination, $\sigma = 45°$, with a fuzzy edge. When comparing Figures 6.6 and 6.7 to Figures 6.4 and 6.5, we see that the fuzzy edge has the effect of smoothing the response of the $i = 45°$ light curves, with little effect on the $i = 0°$ light curves. Even the best-fitting models here (the $i = 0°$ models of the left two plots) still have too high of a peak from ∼MJD 56000 to 56600.

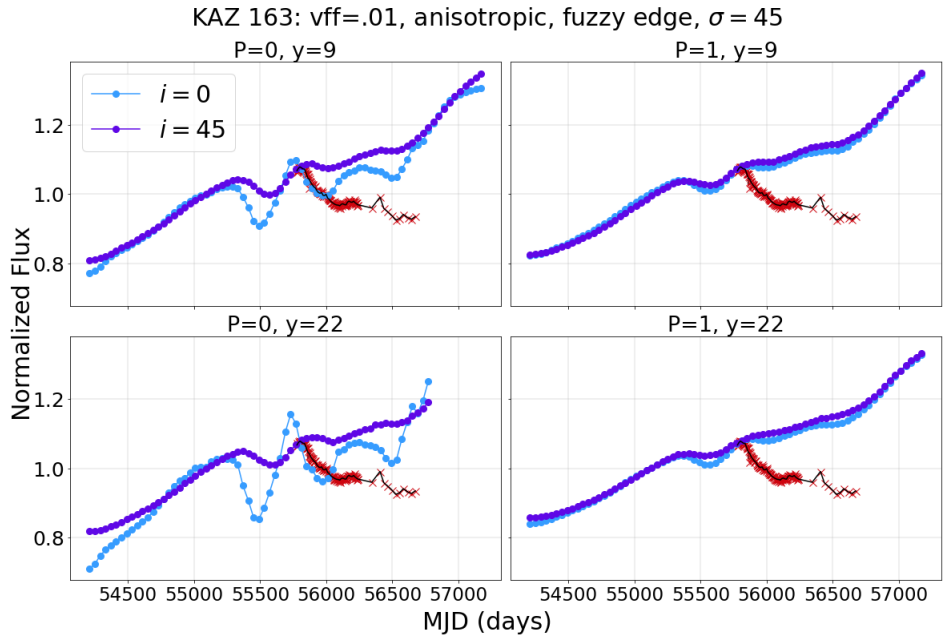

Figure 6.6: KAZ 163 TORMAC Models: Each plot includes two TORMAC models ($i = 0°$ and $i = 45°$), and the 4.5μm light curve. Models were formed with $\Phi = 0.01$, anisotropic illumination, $\sigma = 45°$, and a fuzzy torus edge. The upper row shows the $Y = 9$ models, and the lower row shows the $Y = 22$ models. Each column uses a different value of p ($p = 0, 1$). The model light curves have been multiplied by a factor to match the peak of the observed IR light curve.

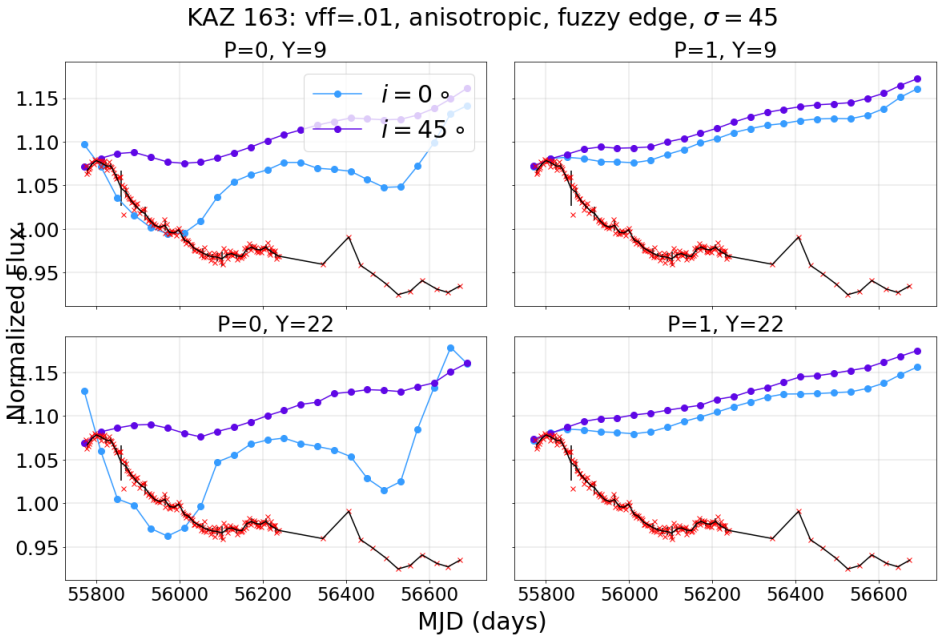

Figure 6.7: The same as Figure 6.6: To form these plots, the model light curves were truncated to cover only the region of time of the Spitzer campaign, and then normalized to their own mean value. The model light curves have been multiplied by a factor to match the peak of the observed IR light curve.

Next we will form models using a smaller volume filling factor. The models using $\Phi = 0.001$ with isotropic illumination are not a good match, and will not be presented here. Instead, we will begin by looking at $\Phi = 0.001$ with anisotropic illumination, comparing the sharp to fuzzy edge models. Figures 6.8 and 6.9 show the models formed using $\Phi = 0.001$, anisotropic illumination, and $\sigma = 45°$, for $p = 0$. Different values of Y are shown in each row, with sharp edge models on the left and fuzzy edge on the right. We see that using a fuzzy edge smooths out the response again of the $i = 45°$ models.

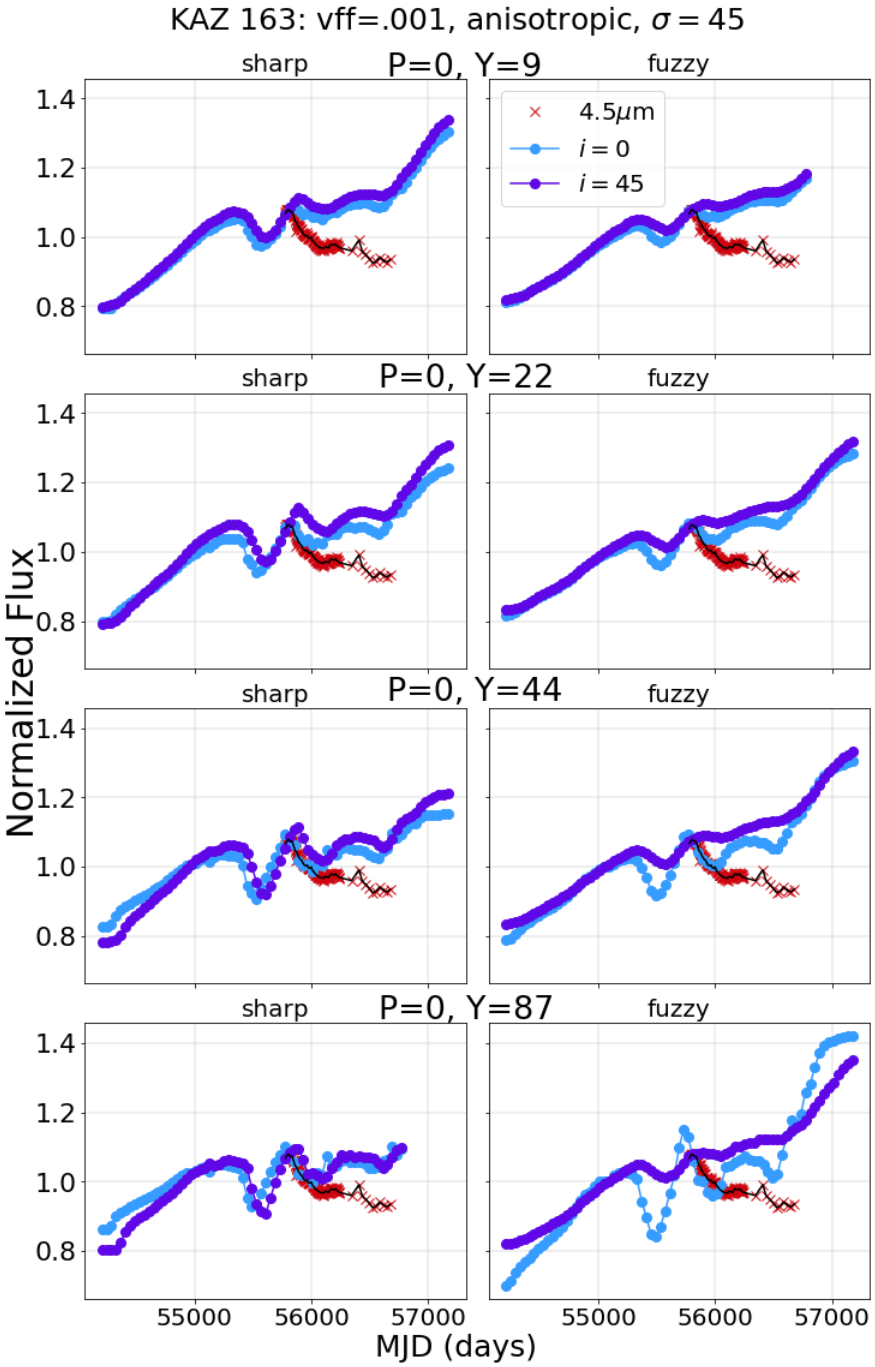

Figure 6.8: KAZ 163 TORMAC Models: Each plot includes two TORMAC models ($i = 0°$ and $i = 45°$), and the 4.5μm light curve. Models were formed with $\Phi = 0.001$, anisotropic illumination, $p = 0$, and $\sigma = 45°$, with the models on the left using a sharp edge and the right using a fuzzy edge. Each row shows models using a different Y value. The model light curves have been multiplied by a factor to match the peak of the observed IR light curve.

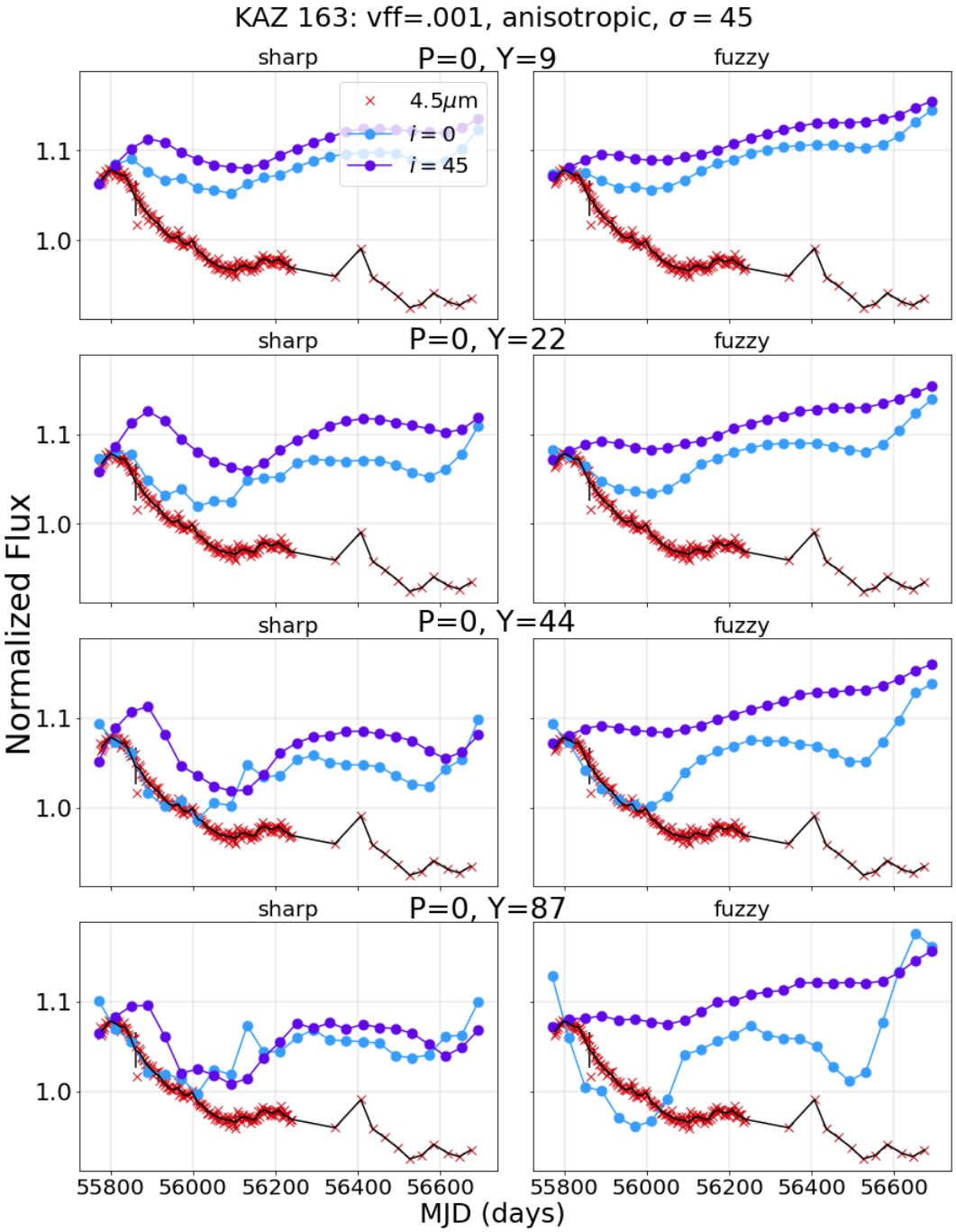

Figure 6.9: The same as Figure 6.8, but only showing the region of the Spitzer campaign To form these plots, the model light curves were truncated to cover only the region of time of the Spitzer campaign, and then normalized to their own mean value. The model light curves have been multiplied by a factor to match the peak of the observed IR light curve.

Looking at Figure 6.9, we see that the $i = 0$ models are once again a better match to our observed light curve than the $i = 45$ models. Also, $p = 0$ with this combination of parameters creates models with a lag value similar to our observed light curves (the main peak of the light curves match in time), although the model light curves still have a second peak that does not match the observations.

We need to explore why our observed light curves display a more suppressed secondary peak, compared to the model light curves. This is likely due to how TORMAC treats dust sublimation in the models presented thus far. In the torus, there is a temperature gradient within each dust cloud. When a cloud reaches the sublimation temperature, the grains near the hot, illuminated surface will sublimate. This means that the dust clouds "wither away," rather than the cloud being instantaneously destroyed. However, dust sublimation is handled differently in TORMAC. Here, when dust clouds reach the sublimation temperature, they continue to produce a constant flux that corresponds to the dust sublimation temperature ($T = 1500$ K), and are not actually destroyed. Dust destruction and reformation is not modeled in TORMAC. This means that the models are likely overestimating the IR emission, if in fact some of clouds were destroyed after the optical peak that occurs at ∼MJD 55700.

TORMAC does include another option to handle dust sublimation: Here, when the surface of the dust cloud reaches the sublimation temperature, then the emission from that cloud is "turned off," which represents a dust cloud being destroyed. These clouds are not reformed. To test whether the treatment of dust sublimation is causing the discrepancy between the models and the observed light curves, we created a few models where the dust clouds are destroyed once the sublimation temperature is reached. This is seen in Figures 6.10 and 6.11. The plots labeled "original" indicate the models in which the clouds continue to emit flux when they reach the sublimation temperature, while the plots labeled "clouds destroyed" indicate models in which the cloud emission is 'turned off' once reaching the sublimation temperature.

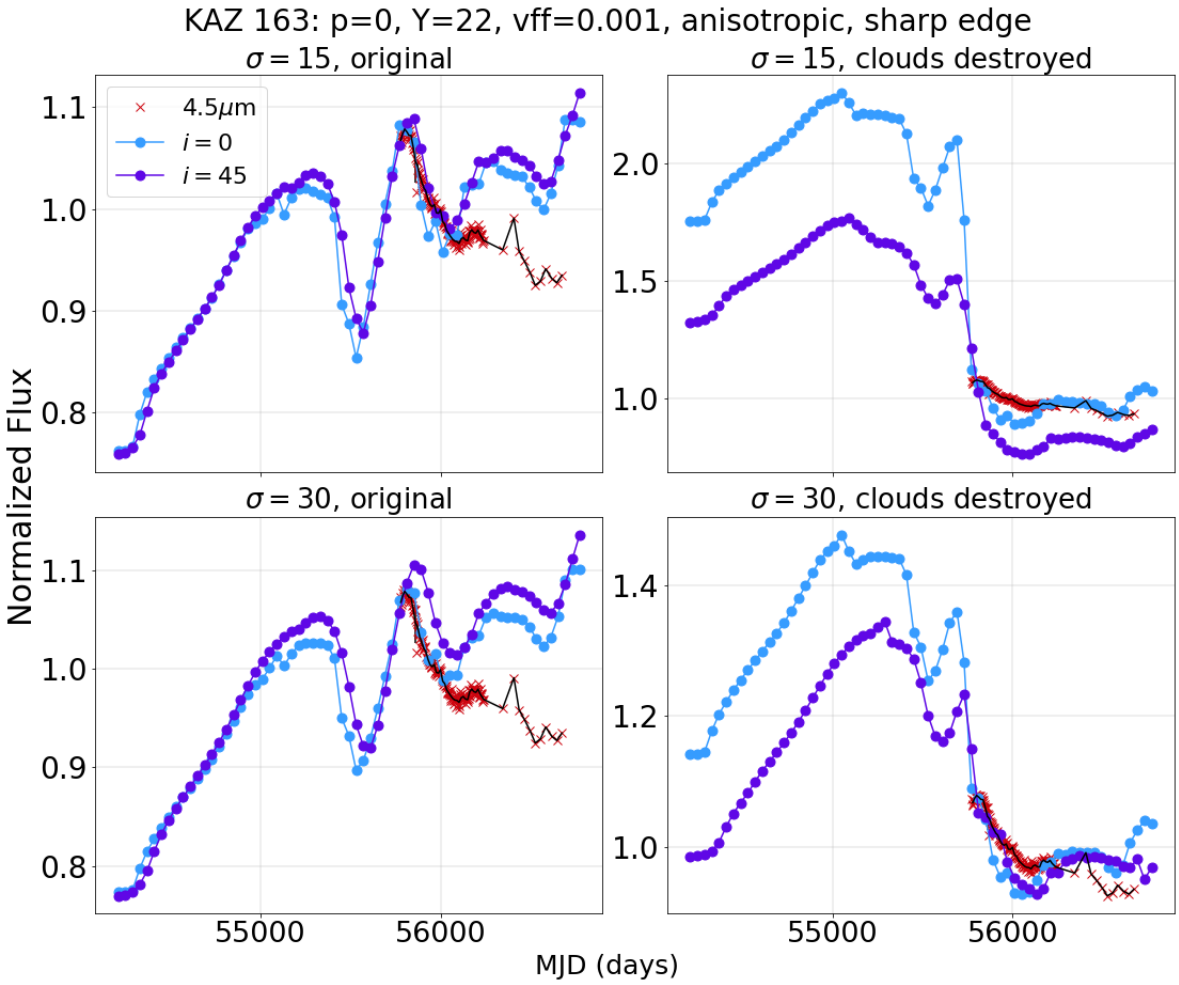

Figure 6.10: KAZ 163 TORMAC Models: Each plot includes two TORMAC models ($i = 0°$ and $i = 45°$), and the 4.5μm light curve. Models were formed with $p = 0$, $Y = 22$, $\Phi = 0.001$, anisotropic illumination, and a torus edge. The upper row shows the $\sigma = 15°$ models, and the lower row shows the $\sigma = 30°$ models. The left column uses the original version of the code, while the right column destroys dust clouds once it reaches the sublimation temperature. The model light curves have been multiplied by a factor to match the peak of the observed IR light curve.

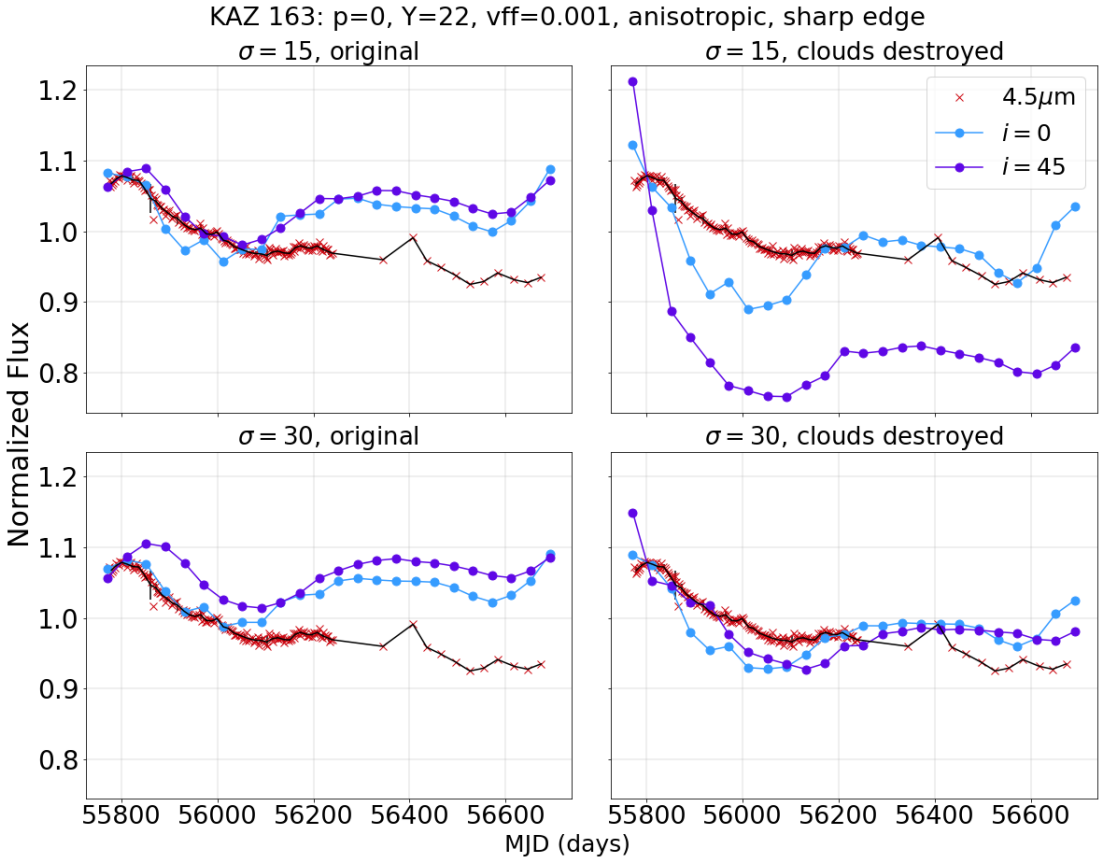

Figure 6.11: The same as Figure 6.10: To form these plots, the model light curves were truncated to cover only the region of time of the Spitzer campaign, and then normalized to their own mean value. The model light curves have been multiplied by a factor to match the peak of the observed IR light curve.

As you can see in Figure 6.10, the overall shape of the models are very different when turning off the emission of clouds that reach the sublimation temperature. The steep drop in flux (around MJD 55900) exhibited by the models corresponds to the dust cloud emission being turned off once reaching the sublimation temperature. It is especially clear in Figure 6.11 that the second peak of the TORMAC models is at a more similar amplitude to that of the observed light curve. It is likely that dust sublimation is causing the discrepancy between our TORMAC models and observed IR light curves.

Although we did not fully sample the parameter space, χ^2 values were calculated for the models

we created. The five models with the lowest χ^2 values for the 3.6 and 4.5 μm light curves are shown in Figures 6.12 and 6.13. The plots with "clouds destroyed" indicate that the dust cloud emission was "turned off" in the code once they reach the sublimation temperature. Several of these models fit our light curves best, as they tend to allow a better match between our observations and the models for the second half of the light curves.

It should be noted that both options of handling dust sublimation are extreme cases. For the first option, when the surface of a dust cloud reaches the sublimation temperature, it continues to emit a constant flux corresponding to T_{sub}, without any dust cloud or grain destruction. This causes an overestimate of the IR response, if in reality some of the dust clouds have been destroyed. The other option is to instantaneously turn off the emission of a dust cloud once it reaches the sublimation temperature, without any dust reformation being modeled. This is also unrealistic in that typically a cloud may not be fully destroyed once the sublimation temperature is reached, and instead only the hottest surface of the cloud would sublimate.

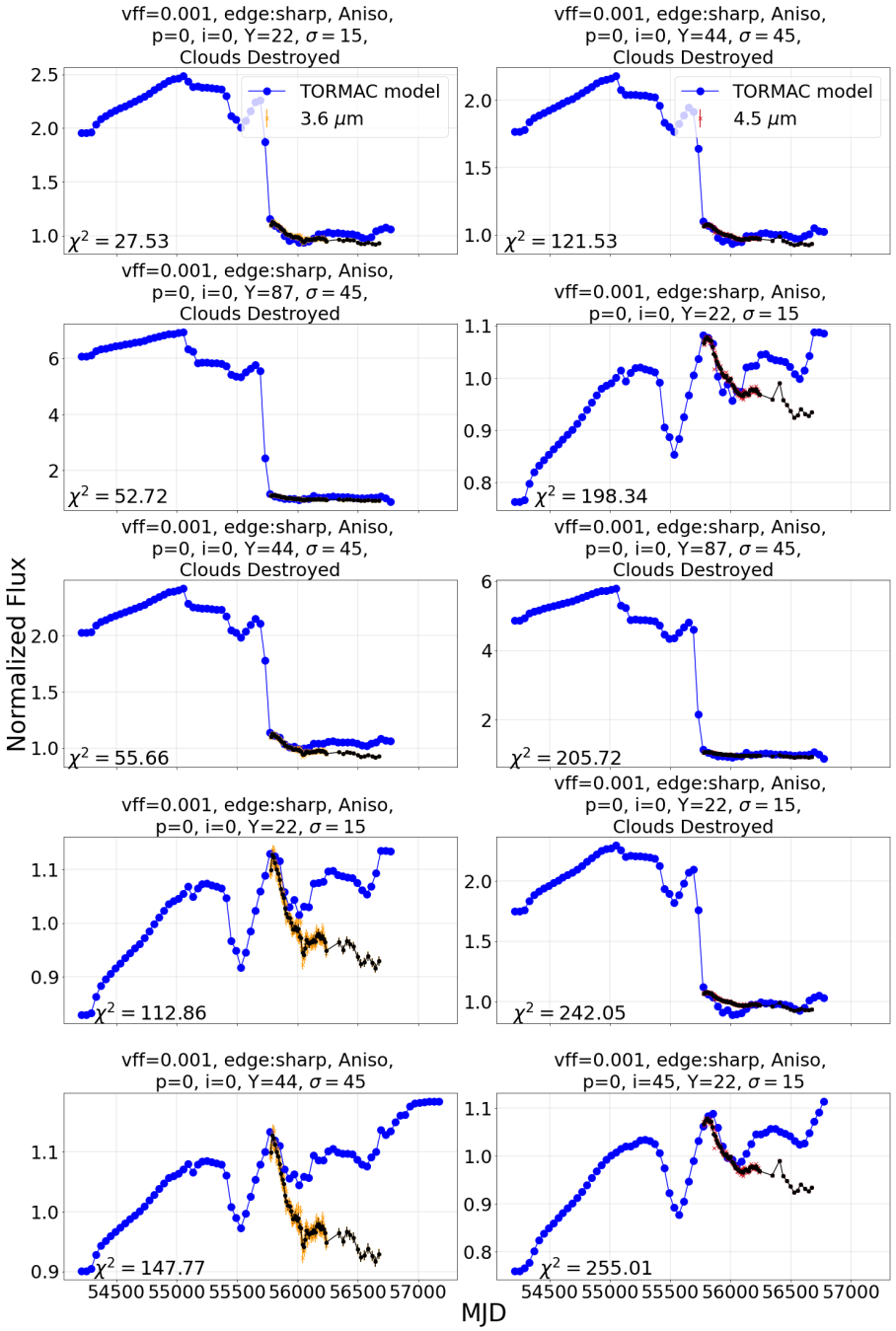

Figure 6.12: The best-fitting TORMAC models for KAZ 163: The left panels show 3.6 μm results, and the right panels show 4.5 μm results. The titles of the plots indicate the parameters used. Plots labeled 'Clouds Destroyed' uses the version of the code in which dust clouds are destroyed once reaching the sublimation temperature. The model light curves have been multiplied by a factor to match the peak of the observed IR light curve.

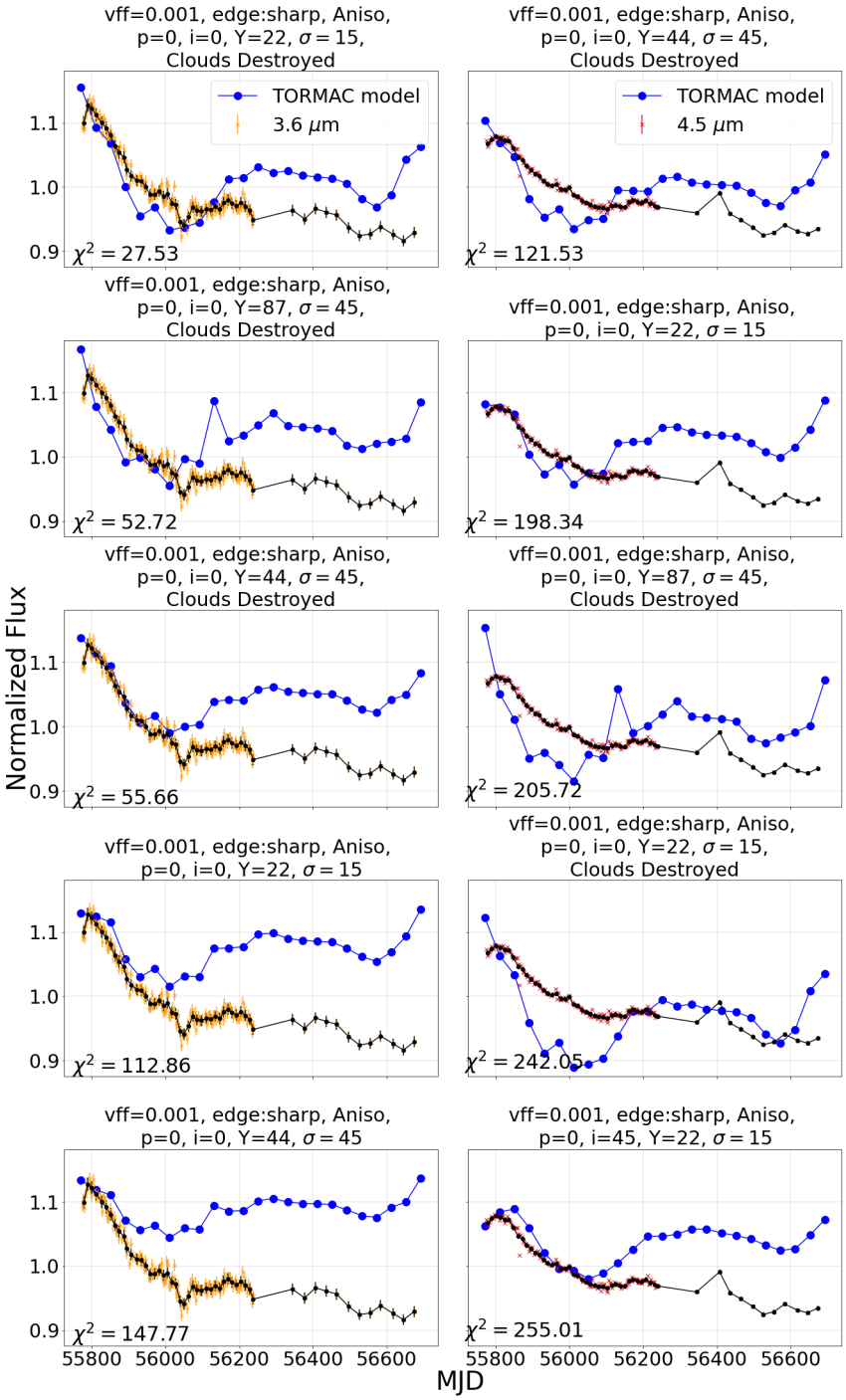

Figure 6.13: The same as Figure 6.12, but only showing the region of the Spitzer campaign: To form these plots, the model light curves were truncated to cover only the region of time of the Spitzer campaign, and then normalized to their own mean value. The model light curves have been multiplied by a factor to match the peak of the observed IR light curve.

Although we do not have models for the entire parameter space, we can draw some conclusions about KAZ 163. In general, the $i = 0°$ models provide a better result than the $i = 45°$ models, although few models were made at intermediate angles. It is likely that this AGN is at a lower inclination towards the observer. Including anisotropic illumination also provides significantly better fits to the light curves. The $p = 0$ models also tend to create models with a better match to the observed IR, so it seems that the cloud distribution is also more centrally concentrated. Finally, there is strong evidence for dust sublimation, as including the destruction of clouds that reach the sublimation temperature tends to give a more accurate match between the model and observed light curve in the range of ∼MJD 56000 to 56600.

While several of our top models include a lower σ value, it is difficult to make a definite conclusion about the best value of σ, as very few models were made with a value other than $\sigma = 45°$. Also, although all of the best models have a value of $\Phi = 0.001$, it is difficult to make a definite conclusion about whether this is the best value of the volume filling factor. Many of the more complicated models (e.g. different σ values, testing including destroying clouds that reach the dust sublimation temperature) were only formed using $\Phi = 0.001$.

6.3 MRK 876

For MRK 876, the x-ray and IR bolometric corrections both give very similar values, ($L_{AGN} = 7.36 \times 10^{45}$ erg/s and $L_{AGN} = 7.23 \times 10^{45}$ erg/s, respectively), with a corresponding light crossing time of $\sim$ 1280 days. As input into TORMAC, $L_{AGN} = 7.23 \times 10^{45}$ erg/s was used. Figure 6.14 shows the starlight-subtracted optical light curve that was presented in Chapter 3, along with the IR light curves.

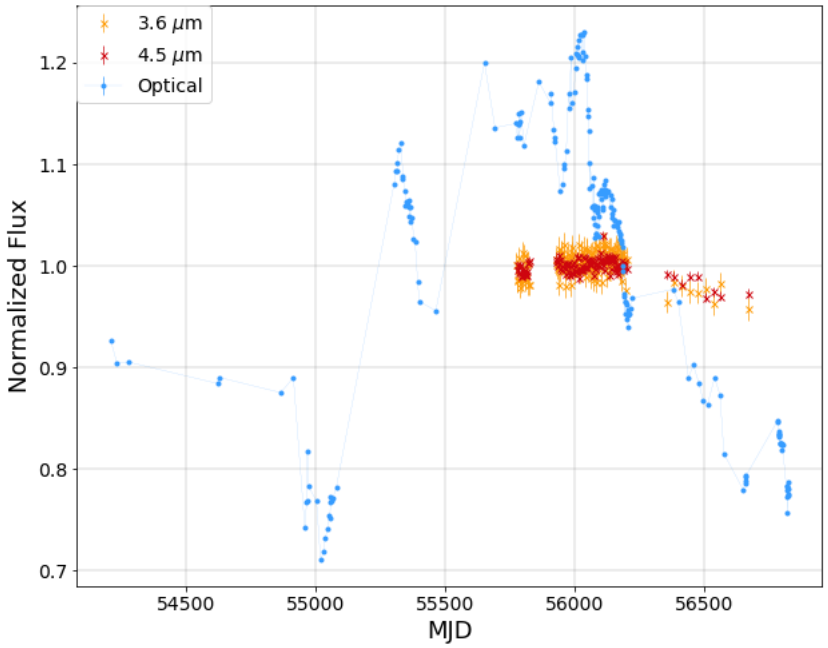

Figure 6.14: MRK 876 light curves: IR and starlight-subtracted optical light curve, with each light curve normalized to its own mean.

Figure 6.15 displays a few of the more "simple" TORMAC models (isotropically illuminated, sharp edge torus), using $\Phi = 0.001$ and $\sigma = 45°$. None of these models are a good match to the observed light curve, as you can see a lag between the observed light curve and the TORMAC models.

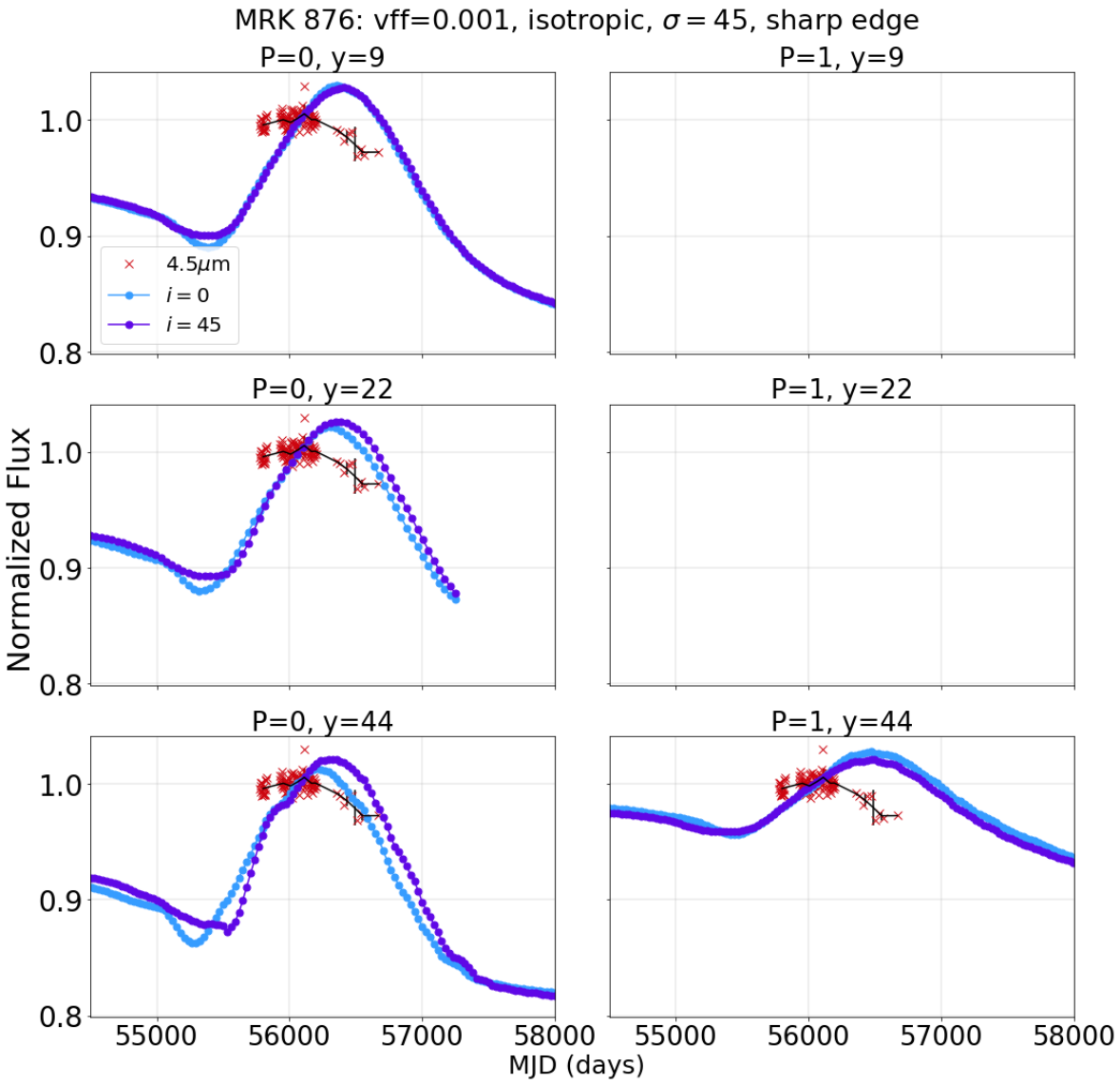

Figure 6.15: MRK 876 TORMAC Models: Each plot includes two TORMAC models ($i = 0°$ and $i = 45°$), and the 4.5μm light curve. Models were formed with $\Phi = 0.001$, isotropic illumination, $\sigma = 45°$, and a sharp torus edge. The upper row shows the $Y = 9$ models, and the middle row shows the $Y = 22$ models, and the lower row shows the $Y = 44$ models. Each column uses a different value of p (P=0,1). The model light curves have been multiplied by a factor to match the peak of the observed IR light curve. Due to time constraints, the $p = 1$, $Y = 9$ and $p = 1$, $Y = 22$ models were not formed.

Next, we form more "simple" models, with a larger volume filling factor, $\Phi = 0.01$, shown in

Figure 6.16. When comparing this to Figure 6.15, we see that the IR response falls off more steeply when using models with a larger volume filling factor. There is still a significant lag between the observed and model light curves when using larger values of p. However, the $p = 0, i = 0$ models begin to provide a better match to the observed light curve.

Thus far, the IR models seem to be responding to the larger features displayed in the optical light curve shown in Figure 6.14. This includes the increase in optical emission that occurs beginning at ∼MJD 55000 and reaches a peak at ∼56000, and falls again until ∼56700. Next, we can try using anisotropic illumination to see how this changes the models.

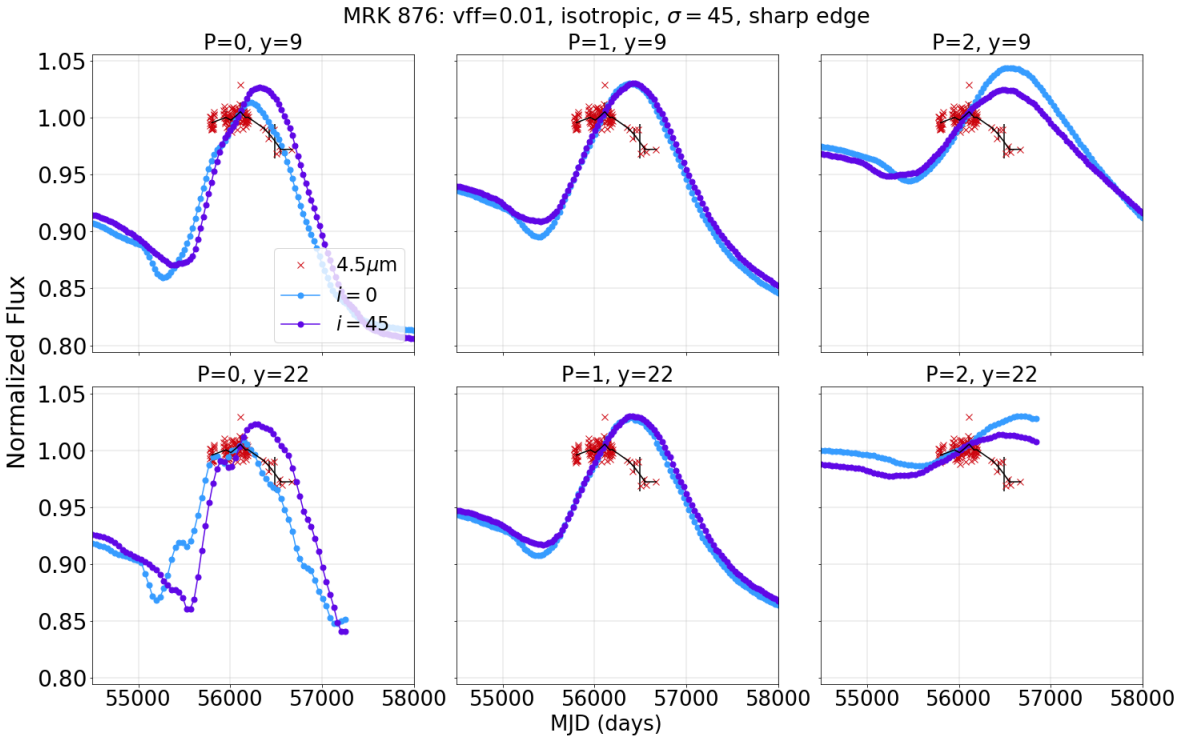

Figure 6.16: MRK 876 TORMAC Models: Each plot includes two TORMAC models ($i = 0°$ and $i = 45°$), and the 4.5μm light curve. Models were formed with $\Phi = 0.01$, isotropic illumination, $\sigma = 45°$, and a sharp torus edge. The upper row shows the $Y = 9$ models, and the lower row shows the $Y = 22$ models. Each column uses a different value of p ($p = 0, 1, 2$). The model light curves have been multiplied by a factor to match the peak of the observed IR light curve.

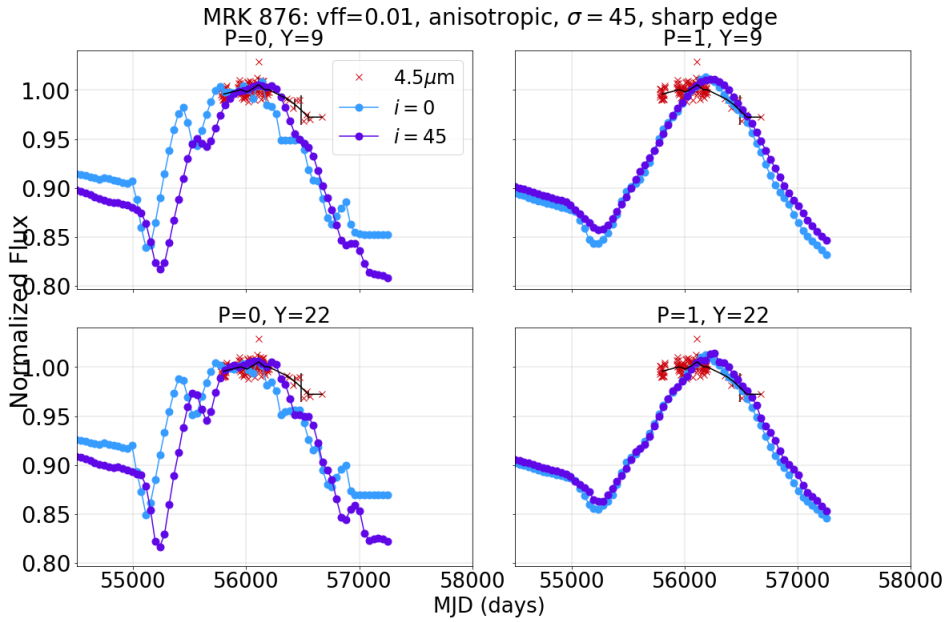

Figure 6.17: MRK 876 TORMAC Models: Each plot includes two TORMAC models ($i = 0°$ and $i = 45°$), and the 4.5μm light curve. Models were formed with $\Phi = 0.01$, anisotropic illumination, $\sigma = 45°$, and a sharp torus edge. The upper row shows the $Y = 9$ models, and the lower row shows the $Y = 22$ models. Each column uses a different value of p ($p = 0, 1, 2$). The model light curves have been multiplied by a factor to match the peak of the observed IR light curve.

Figure 6.17 includes anisotropic illumination with $\Phi = 0.01$, $\sigma = 45°$, and a sharp edge. For the $p = 0$ models, we see that including anisotropic emission broadens the peak of the model response, corresponding to the broad peak of the optical light curve from ∼MJD 55600 to 56000.

The $p = 0$ models provide a better match between the observed and model light curves, although the decrease of flux in the observed light curve (from ∼MJD 56100 to 56600) has a more shallow flux decrease than the models. Including a fuzzy edge could potentially solve this issue. Figure 6.18 shows the anisotropic fuzzy edge models with $\Phi = 0.01$, $\sigma = 45°$. This does provide a better match to the end portion of the light curve for the $i = 45$ models, although including a fuzzy edge also smooths the beginning portion of (from ∼MJD 55750 to 56100). Using a smaller volume filling factor of $\Phi = 0.001$ was also attempted, and shown in Figure 6.19. Again, it is difficult to simultaneously fit both the rise in flux of the IR as well as the fall in flux.

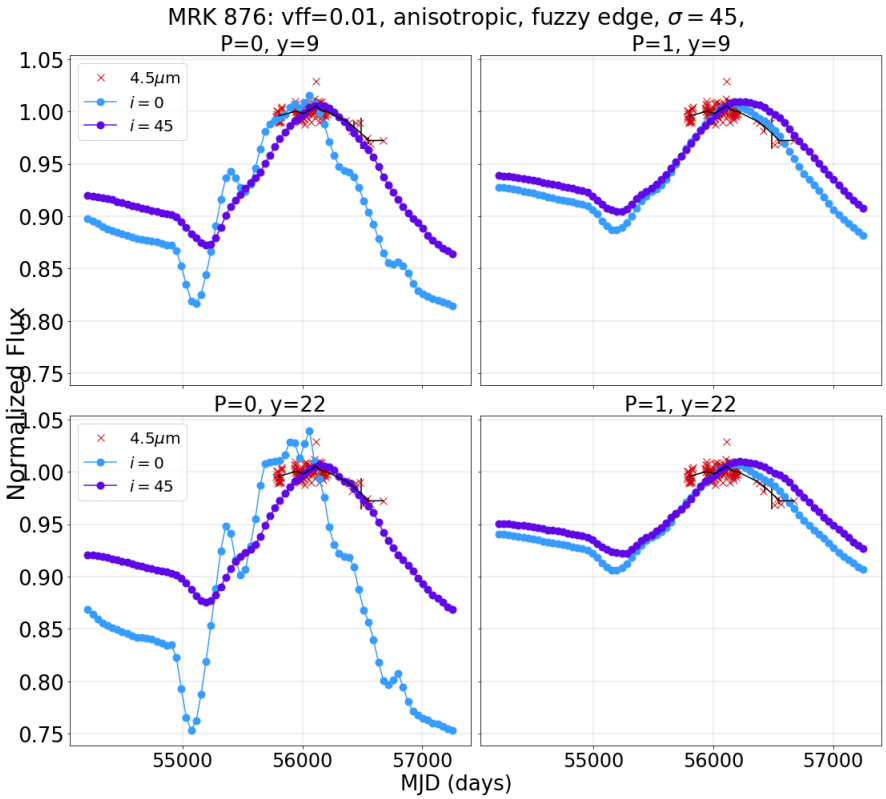

Figure 6.18: MRK 876 TORMAC Models: Each plot includes two TORMAC models ($i = 0°$ and $i = 45°$), and the 4.5μm light curve. Models were formed with $\Phi = 0.01$, anisotropic illumination, $\sigma = 45°$, and a fuzzy torus edge. The upper row shows the $Y = 9$ models, and the lower row shows the $Y = 22$ models. Each column uses a different value of p ($p = 0, 1$). The model light curves have been multiplied by a factor to match the peak of the observed IR light curve.

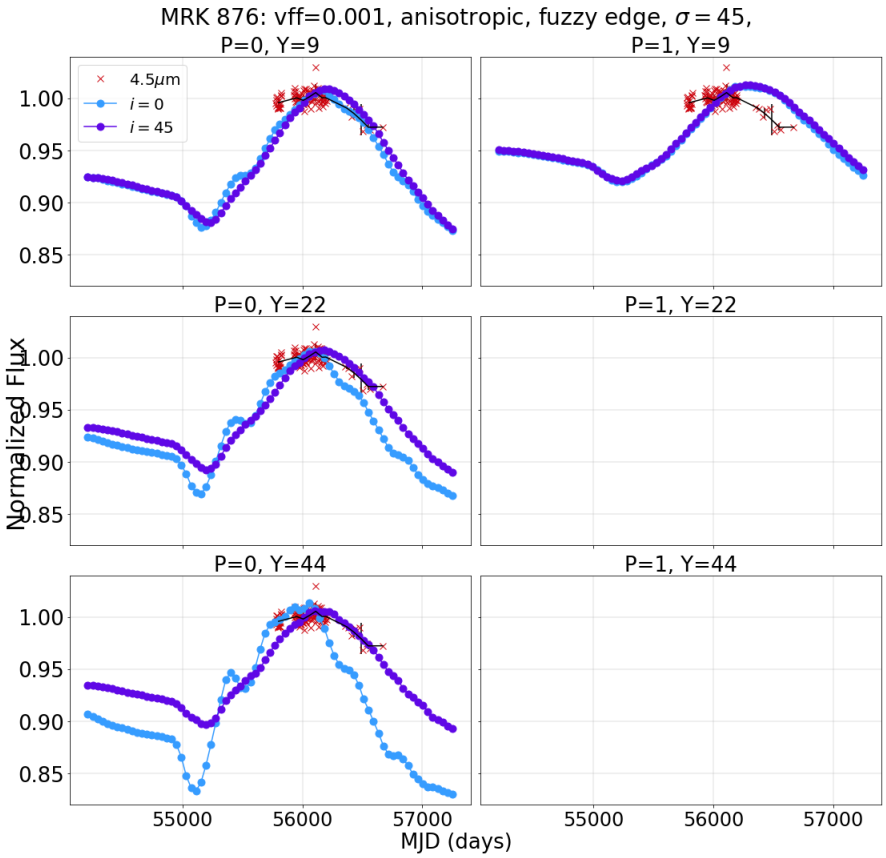

Figure 6.19: MRK 876 TORMAC Models: Each plot includes two TORMAC models ($i = 0°$ and $i = 45°$), and the 4.5μm light curve. Models were formed with $\Phi = 0.01$, anisotropic illumination, $\sigma = 45°$, and a fuzzy torus edge. The upper row shows the $Y = 9$ models, and the middle row shows the $Y = 22$ models, and the lower row shows the $Y = 44$ models. Each column uses a different value of p ($p = 0, 1$). The model light curves have been multiplied by a factor to match the peak of the observed IR light curve.

The models with the lowest χ^2 values for both the 3.6 and 4.5 μm light curves are shown in Figures 6.20 and 6.21. Few of these models are able to match both the rise and fall of the flux in the observed light curves, although there are a few trends to note. Anisotropic illumination gives better results in most cases, although the best-fit model for the 3.6μm light curve includes isotropic illumination. A value of $p = 0$ also seems to work best regardless of the value of Y, although $p = 1$ also gives a good result in one case. It is difficult to make concrete conclusions about which parameters are best for this AGN without better sampling the parameter space. Interestingly,

one of the models with $\sigma = 60$ works best for both the 3.6 and 4.5 μm light curves, so forming models with different σ values might be helpful for this AGN. Also forming more models at other inclinations would be useful.

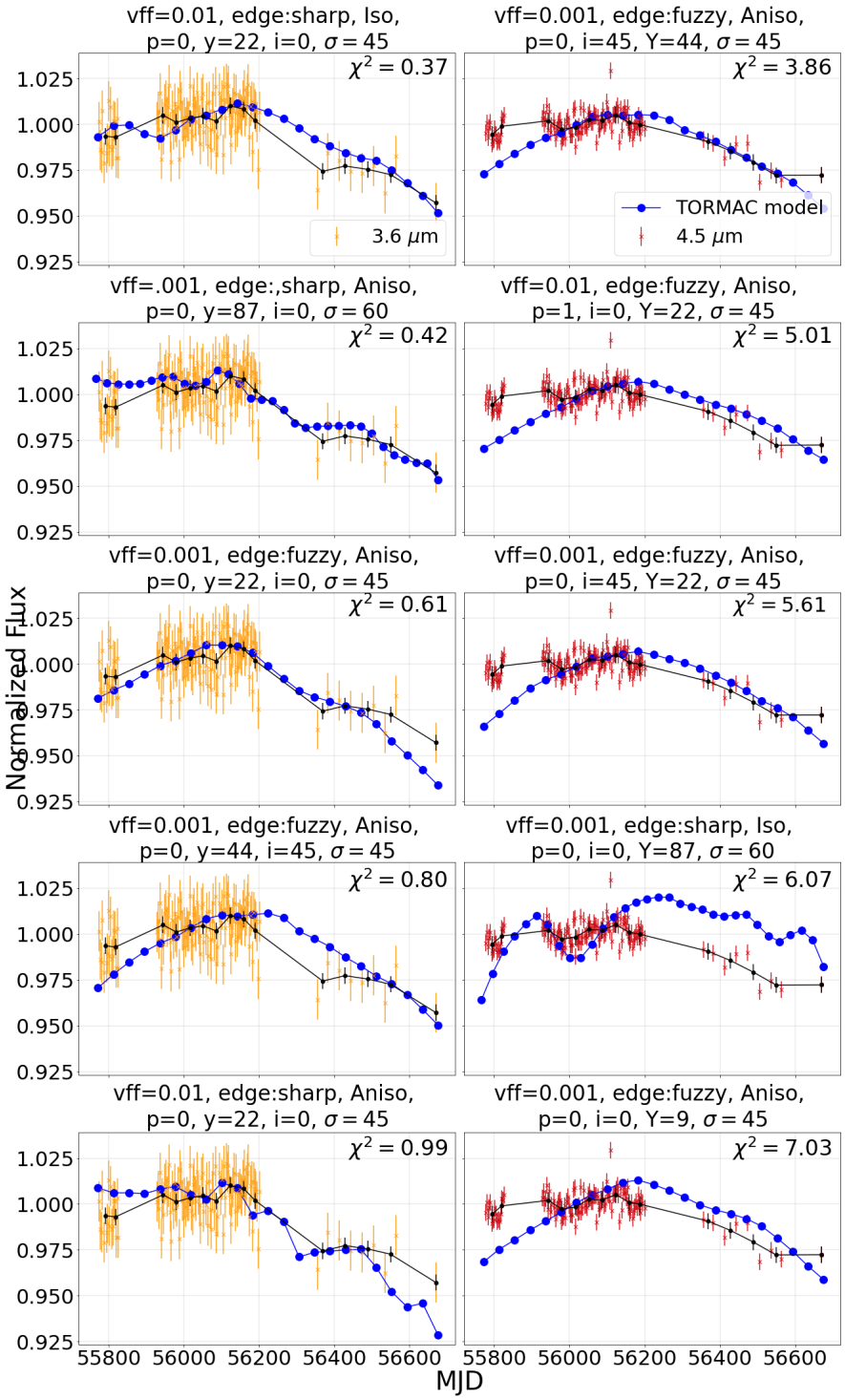

Figure 6.20: The top five best models for 3.6 and 4.5 μm light curves of MRK 876, ordered by χ^2 value, showing only the region covered by the Spitzer campaign.

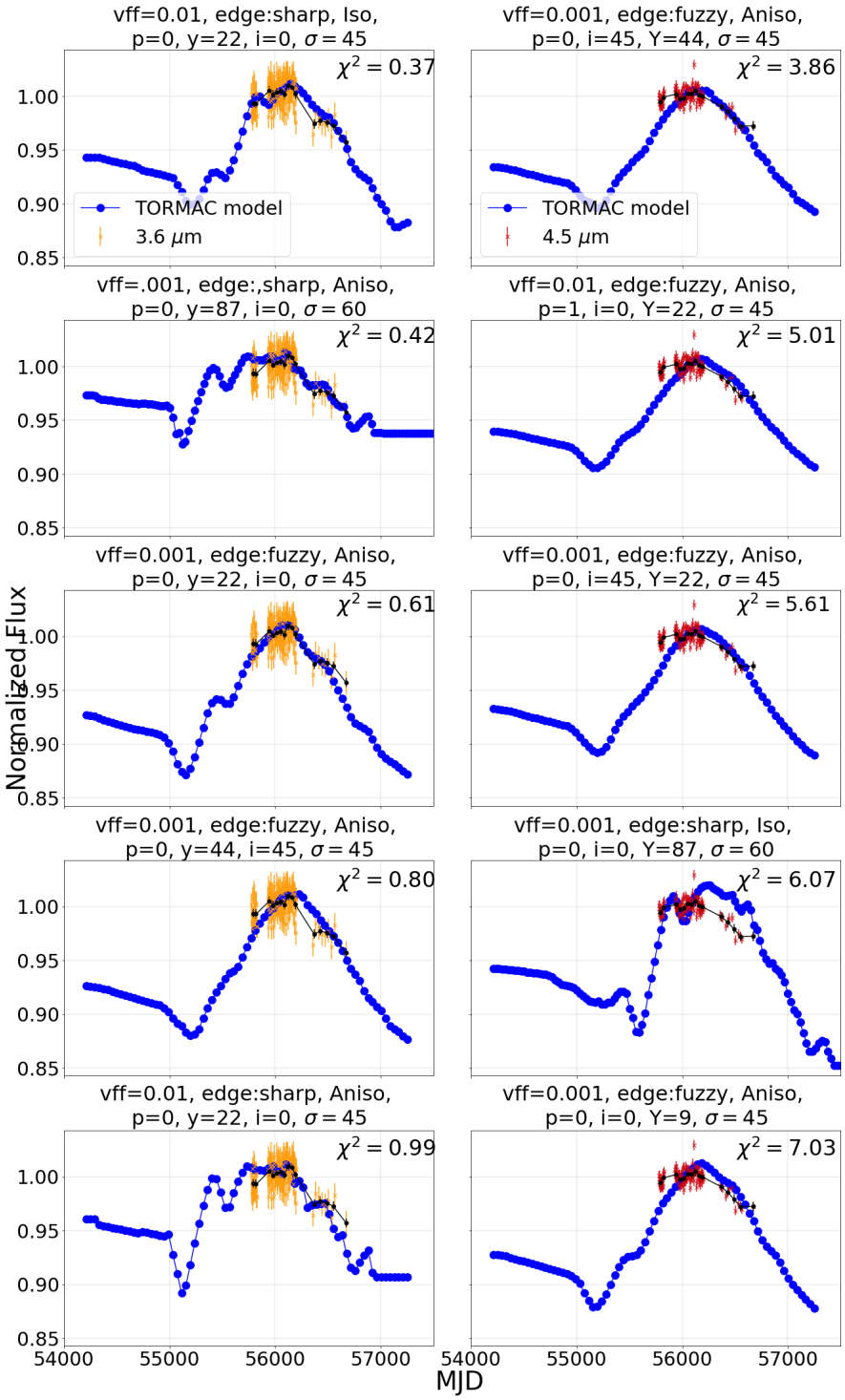

Figure 6.21: The top five best models for 3.6 and 4.5 μm light curves of MRK 876, ordered by χ^2 value.

6.4 MRK 507

For MRK 507, a different bolometric luminosity was calculated depending on whether the x-ray or IR data was used. With the x-ray correction, $L_{AGN} = 2.63 \times 10^{45}$ erg/s was calculated and using the IR correction $L_{AGN} = 1.26 \times 10^{45}$ erg/s was calculated (corresponding to light crossing times of 772.3 days and 534.6 days, respectively). As input into TORMAC, an average of the two values was used, $L_{AGN} = 1.945 \times 10^{45}$ erg/s. Figure 6.22 shows the starlight-subtracted optical light curve that was presented in Chapter 3, along with the IR light curves. MRK 507 is the AGN for which we have the most detailed model grids. We have modeled the full parameter space which includes the following parameters:

- inclinations of 0°, 22°, and 45°
- $p = 0, 1, 2$
- $Y = 9, 22, 44$
- isotropic or anisotropic illumination
- $\Phi = 0.01$ and 0.001
- sharp or fuzzy edge

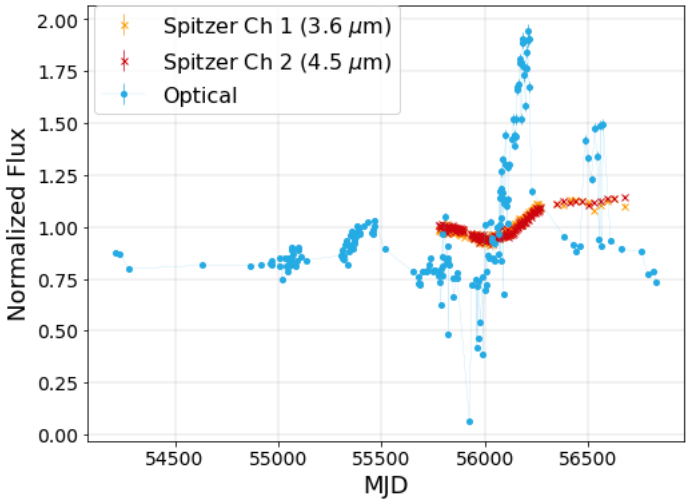

Figure 6.22: MRK 507 light curves: IR and starlight-subtracted optical light curve, with each light curve normalized to its own mean.

Figures 6.23 and 6.24 show an example of a grid of models for an anisotropically illuminated torus with $\Phi = 0.01$, a sharp torus edge, and $\sigma = 45°$. Each model has been multiplied by a factor to match the low point of the observed light curve. We can see that the models are clearly responding to a few features in the optical light curve of Figure 6.22. These optical features include the slight increase in flux prior to the Spitzer campaign (∼MJD 55500), the dip in flux just prior to MJD 56000, and the sharp increase in flux until ∼56200.

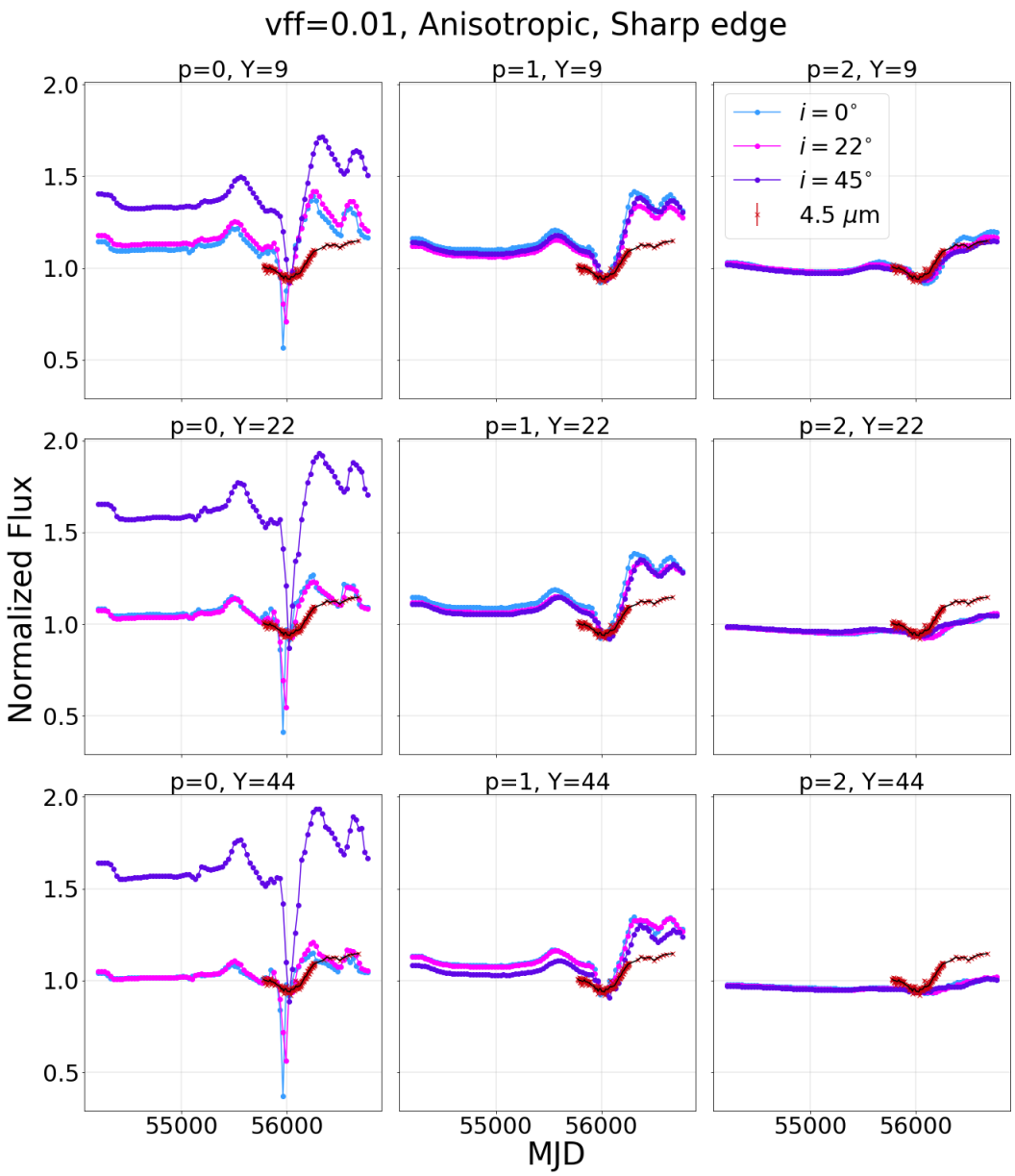

Figure 6.23: MRK 507 TORMAC Models: Each plot includes three TORMAC models ($i = 0°$, $i = 22°$, $i = 45°$), and the 4.5μm light curve. Models were formed with $\Phi = 0.01$, anisotropic illumination, $\sigma = 45°$, and a sharp torus edge. The upper row shows the $Y = 9$ models, and the middle row shows the $Y = 22$ models, and the lower row shows the $Y = 44$ models. Each column uses a different value of p ($p = 0, 1, 2$). The model light curves have been multiplied by a factor to match the low point in flux of the observed IR light curve.

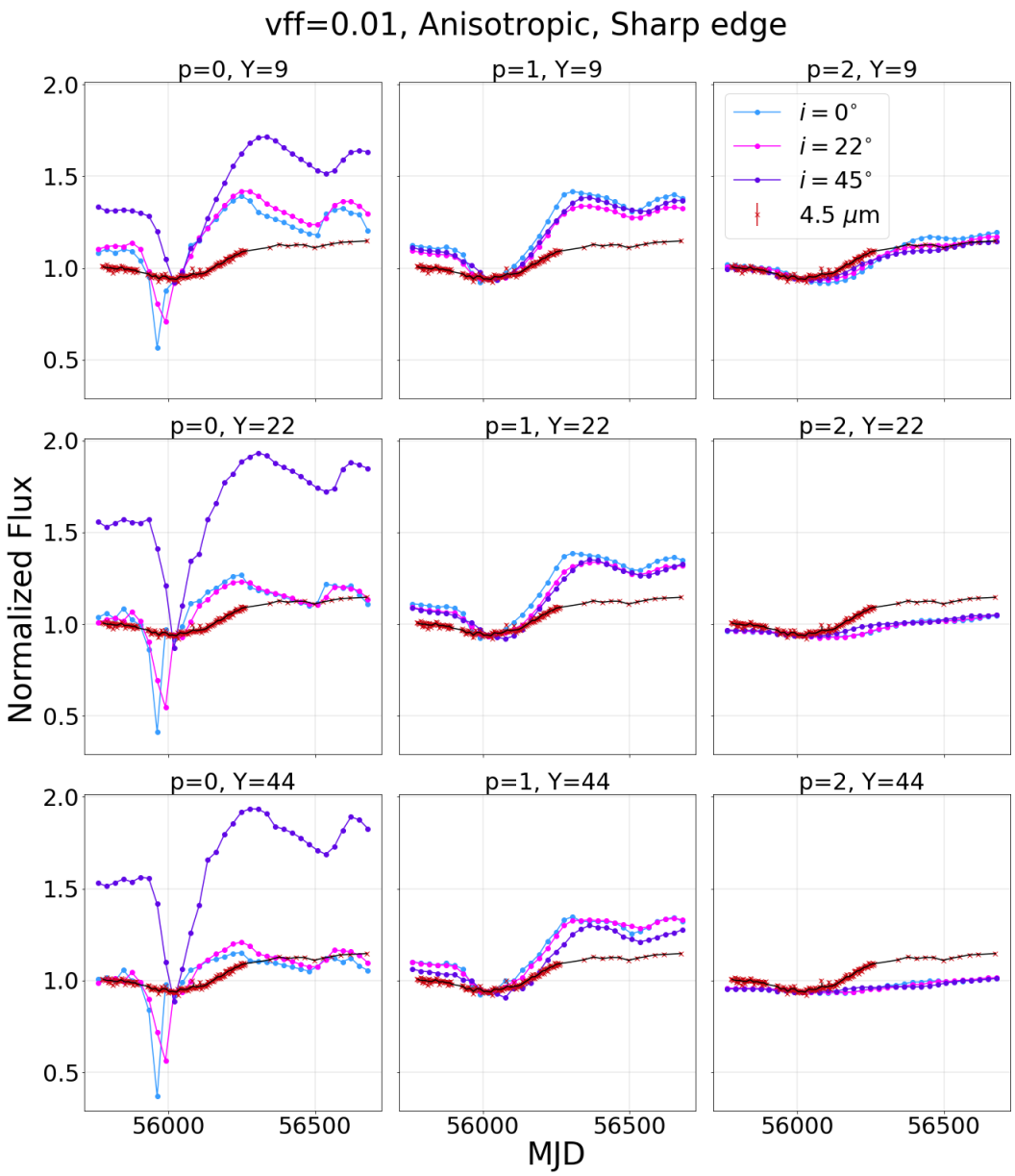

Figure 6.24: The same as Figure 6.23, but only showing the region of the Spitzer campaign To form these plots, the model light curves were truncated to cover only the region of time of the Spitzer campaign, and then normalized to their own mean value. The model light curves have been multiplied by a factor to match the low point of the observed IR light curve.

The χ^2 values were used to determine which models most closely matched our observed light curves. Figures 6.25 and 6.26 show the five models with the lowest chi-squared values for the

3.6μm (left panels) and 4.5μm (right panels) light curves. Especially for the 4.5 μm light curve, these models provide a very close match to the observed light curves.

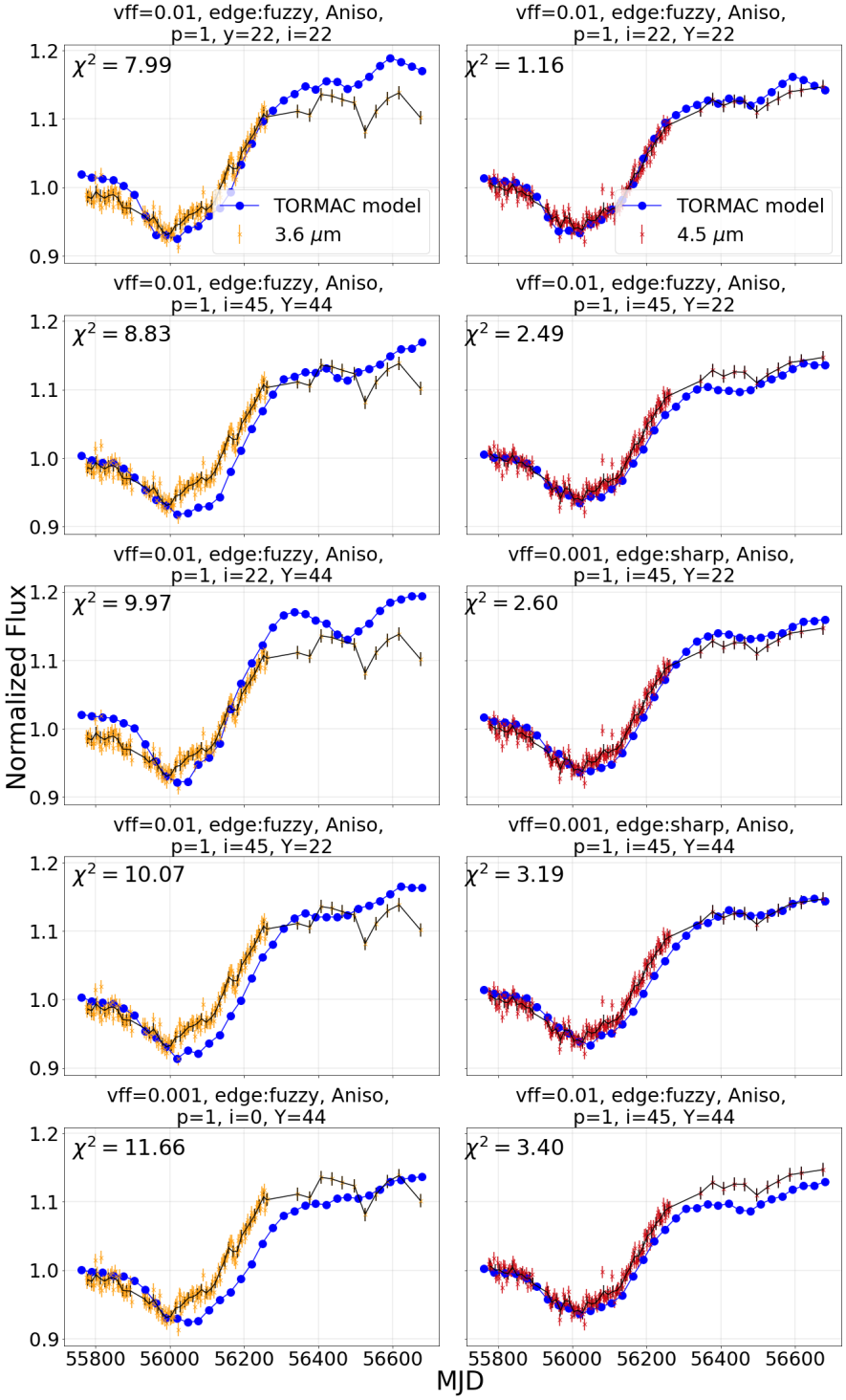

Figure 6.25: The top five best models for 3.6 and 4.5 μm light curves of MRK 507, ordered by χ^2 value, showing only the region covered by the Spitzer campaign.

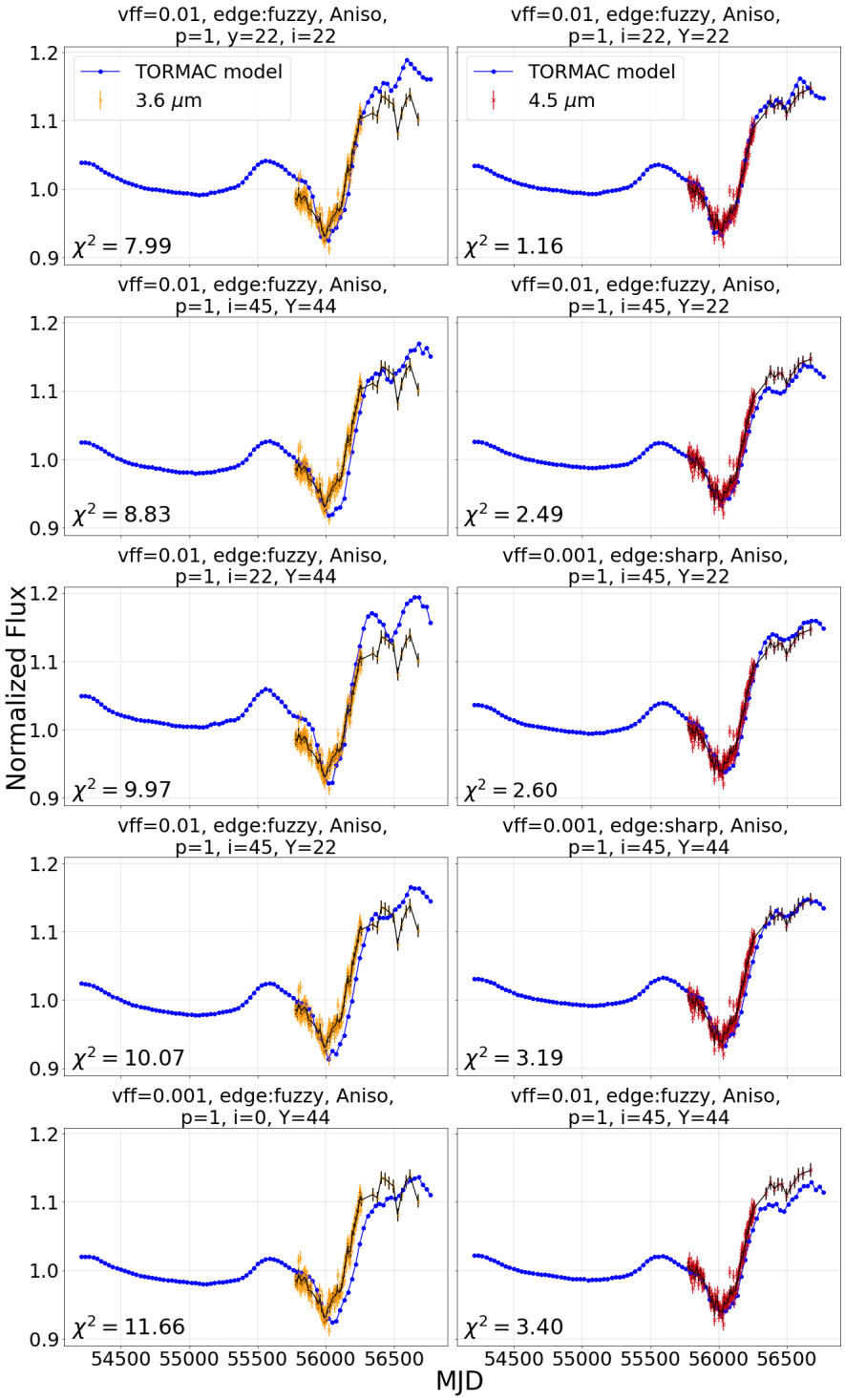

Figure 6.26: The top five best models for 3.6 and 4.5 μm light curves of MRK 507, ordered by χ^2 value.

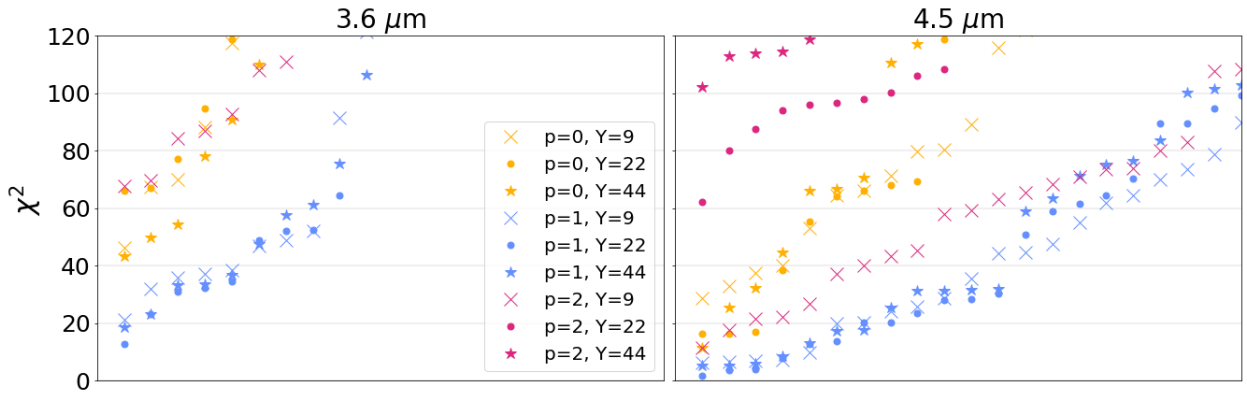

Figure 6.27: The MRK 507 χ^2 values corresponding to values of p and Y: Only the models with the lowest χ^2 values are plotted here. The left panel shows the 3.6μm χ^2 values, and the right panel displays the 4.5μm values. The models for each parameter are ordered from left to right in order of increasing χ^2, with each symbol representing one TORMAC model. The colors of the symbols represent the value of p ($p = 0$ is yellow, $p = 1$ is blue and $p = 2$ is pink) while the symbol marker represents the value of Y (the crosses are $Y = 9$, the circles are $Y = 22$, and the stars are $Y = 44$).

Figure 6.27 shows how the values of p and Y correspond to the measured χ^2 values. For both the 3.6 and 4.5 μm light curves, the $p = 1$ models give the best results, regardless of the value of Y. Although, the $p = 2, Y = 9$ models as well as several $p = 0$ models also give good results.

Other parameters are plotted along with their χ^2 values in Figure 6.28. The upper row plots the χ^2 values as they correspond to the inclination. The very best-fit models are those at higher values of inclination ($i = 45°$ and $i = 22°$), although there are good models for any of the three inclinations. The second row shows the volume filling factor. While the best 3.6 μm models show a slight preference for a higher volume filling factor ($\Phi = 0.01$), in general there is not a preference for either value, especially for the 4.5 μm light curve. The third row shows the results of using isotropic or anisotropic illumination of the torus. Using anisotropic illumination provides significantly better models for both wavelengths. The lower row shows the sharp or fuzzy edge results. For the 3.6 μm light curve, fuzzy models are significantly better. For the 4.5 μm light curve, there is not much of a difference in the fitting for the very best models, although in general the fuzzy models provide a better match.

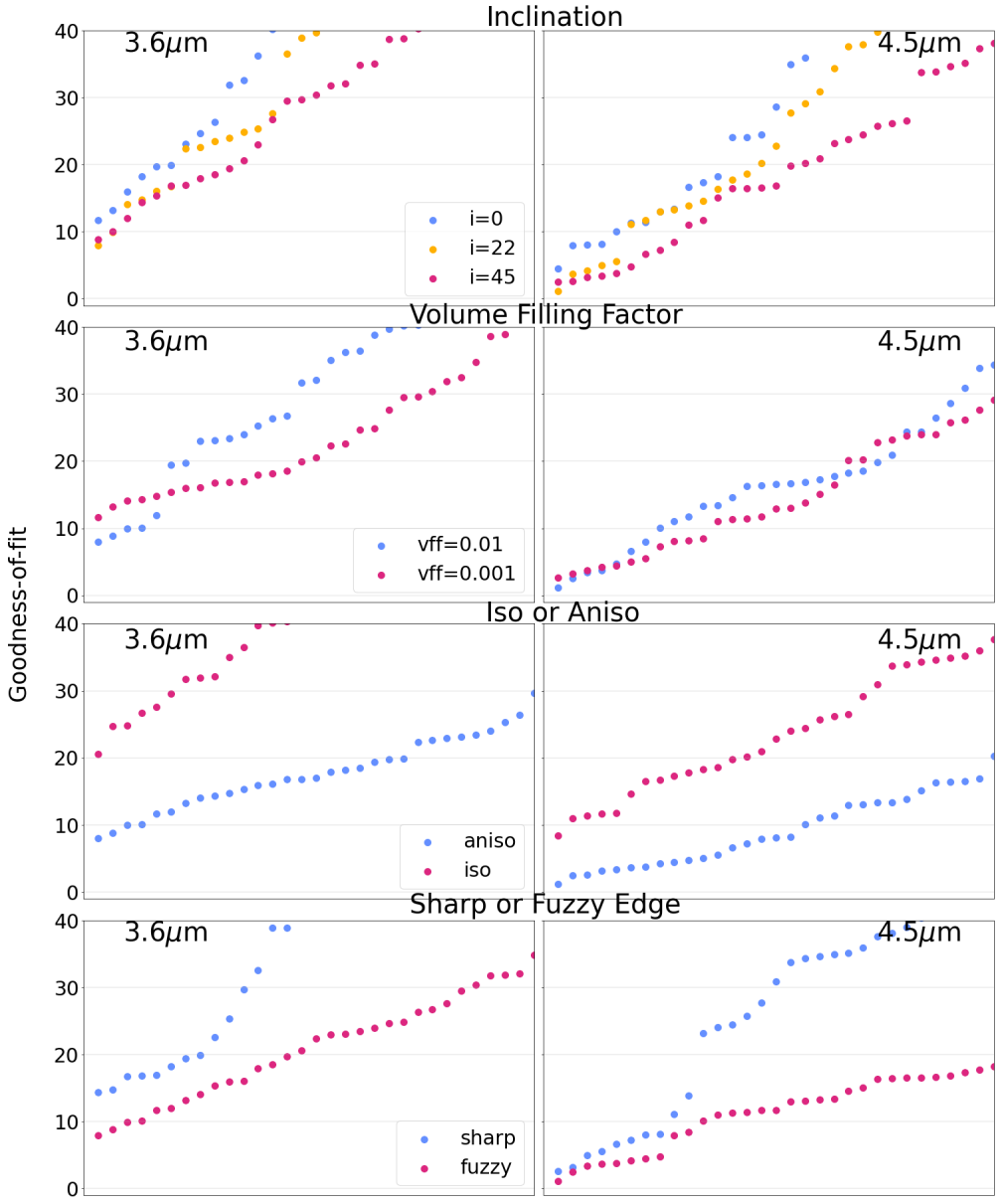

Figure 6.28: The MRK 507 χ^2 values corresponding to values inclination: Only the models with the lowest χ^2 values are plotted here. The models for each parameter are ordered from left to right in order of increasing χ^2. Each symbol represents one TORMAC model. The left side shows the 3.6μm χ^2 values, and the right side displays the 4.5μm values. The colors of the symbols represent the value of inclination (top row), volume filling factor (second row), isotropic or anisotropic (third row), and sharp or fuzzy edge (fourth row).

To summarize, the best-fitting models of MRK 507 include a dust cloud distribution of $p = 1$, which means that the clouds are not centrally-concentrated, however they are not uniformly distributed throughout the torus. It is unclear as to the radial extent of the torus, as each value of Y can provide a model that fits well to the data, depending on the other parameters. Higher values of inclination tend to provide a better fit. The best-fitting models are those with $i = 45°$, with the second-best inclination value being $i = 22°$. Therefore, MRK 507 likely is located at a higher inclination with respect to the observer.

6.5 Summary

We were able to form models and constrain parameters for three of the AGN in our sample. For all three AGN, using anisotropic illumination provides models that match better with the observed light curves. It is expected that a geometrically thin optically thick accretion disk will emit anisotropically, and these models seem to confirm this, as they better match our observed IR light curves.

Fewer models were formed for KAZ 163 and MRK 876, therefore our results for these two AGN are not quite as robust. KAZ 163 is likely at a low inclination with respect to the observer, with a centrally-concentrated distribution of dust clouds ($p = 0$). There is also evidence of dust sublimation. For MRK 876, it seems that a centrally-concentrated distribution of dust clouds ($p = 0$) is preferred, although it would be helpful to form more models with other inclinations and σ values.

Our most in-depth results are for MRK 507, for which we were able to more fully explore our chosen parameter space. MRK 507 seems to be located at a high inclination with respect to the observer, and a cloud distribution of $p = 1$ is likely. There seems to be no preference for either volume filling factor, as accurate models are able to be formed regardless of the value of this parameter.

CHAPTER 7

CONCLUSIONS

7.1 Conclusions

This dissertation has produced mid-IR reverberation mapping results for four AGN (KAZ 163, MRK 507, NGC 6418, and UGC 10697). While the mid-IR region is relatively unexplored with respect to reverberation mapping, there have been a few mid-IR reverberation mapping studies recently (Lyu et al., 2019; Yang et al., 2020). These studies provide mid-IR reverberation mapping results for large samples of AGN using the *Wide-field Infrared Survey Explorer* (WISE) with IR data covering approximately a decade, however the sampling is sparse (∼once every 6 months). While our IR measurements cover a shorter period of time (∼2.5 years), the observational cadence is much shorter, varying from once every 3 days to once every 30 days. Our light curves are very well-sampled, allowing us to conduct an in-depth analysis of the lags for this sample. However, the duration of the campaign is insufficient for the most luminous objects, specifically those exhibiting a slow IR response to strong optical variability.

There are several general conclusions we can draw from the cross-correlation analysis. For all of the AGN we analyzed, the 4.5μm-optical lags are larger than those of the 3.6μm-optical. This is what we expect within the structure of the torus: the grains closest to the center will be hotter

(and thus emit at shorter wavelengths) than those farther from the center. We also find that the differences between the 3.6μm-optical and 4.5μm-optical lags tend to correspond well to the lag value calculated for the 3.6-4.5μm analysis.

For two of the AGN (MRK 507 and KAZ 163), we were able to conduct cross-correlation analysis with the optical light curves both before and after starlight subtraction. When comparing the optical-IR lags calculated using the two different versions of the light curves, we find there to be little difference in the measured lags. This is expected, given that the fully-combined starlight-subtracted optical light curve include the same features as the pre-starlight subtracted light curves, albeit with larger amplitudes.

The cross-correlation analysis was conducted with different interpolation orders (optical, IR interpolation, or both). The choice of interpolation order has a significant impact on the measured lags. Interpolation order makes less of a difference when there are more data points (better sampling). However even the lags between the IR light curves, which have the same sampling rate, are different depending on the which light curve is interpolated.

One interesting result regarding the analysis involves the recommended use of an 80% threshold value when determining lag values using CCFs (Peterson, 2001). In many cases, there are significant lag differences depending on the percent threshold value that is used. While 80% works well for CCFs with a more symmetric shape, for those with significant discontinuities or those skewed in one direction, the resulting lag depends strongly on the threshold percentage.

NGC 6418 was analyzed in detail, with the lags measured separately both before and after a strong optical flare (to which the IR also displays a response of a similar amplitude). There is a significant increase in the lag for both IR channels following the flare. Through the analysis of the light curves and the spectra, NGC 6418 appears to have undergone a changing-look event. The cause of this is likely due to both a change in obscuration (from the change in the broad line balmer decrement and the corresponding values of the extinction), as well as a change in the accretion rate (which leads to a change in the intrinsic luminosity) of the AGN. As we see the flare in both optical and the IR, this also indicates that the change in luminosity is intrinsic, not solely due to reddening.

Given that changing-look AGN are relatively rare, the cross-correlation analysis for this AGN adds very unique results: the increase in lag suggests that the sublimation radius increased as a result of the flare.

As discussed in Chapter 1, there is a relation between the radius and luminosity ($R \propto L^{1/2}$) implied through theory (see Equation 1.1), and also established through BLR reverberation mapping, dust reverberation mapping, and IR interferometry. The optical-IR lags obtained in this work are plotted vs. bolometric luminosity (presented in Table 2.2), in Figure 7.1. A calculation of the slope between our data points yields $\sim 0.2 - 0.3$, depending on whether the slope is calculated using the points of 3.6μm-optical or 4.5μm-optical lag results, and also depending on whether one uses the Cycle 8 or Cycle 9 lags of NGC 6418. While our measurements do not follow the slope of 1/2 as expected through theory, this is a very small sample of AGN, and it is reasonable to expect significant scatter within the $R - L$ relation.

The final step of this project included using TORMAC to model light curves of three AGN (KAZ 163, MRK 507, MRK 876), with the goal of constraining other torus properties. The models include stratification in dust grain composition and size, to account for selective sublimation in which large graphite grains can survive at hotter temps (and therefore closer to the source). This is one of the first studies in which TORMAC has been used to model light curves in a sample of AGN. For all three AGN, using anisotropic illumination of the torus by the UV/Optical continuum provides models that match much better with the observed light curves, which is expected from a geometrically thin accretion disk. Other parameters we were able to constrain include the radial distribution of dust clouds (p, indicating whether the clouds are radially concentrated or uniformly distributed), and the torus inclination angle (i, indicating whether the torus is face-on or edge-on with respect to the observer). The use of TORMAC has also revealed another AGN in our sample for which there is strong evidence of sublimation (KAZ 163), given that turning off the dust cloud emission is the only way to produce models that match the observed light curves after the optical flare. The models for MRK 507 are especially well-matching to our observed light curves, especially for the 4.5 μm light curve.

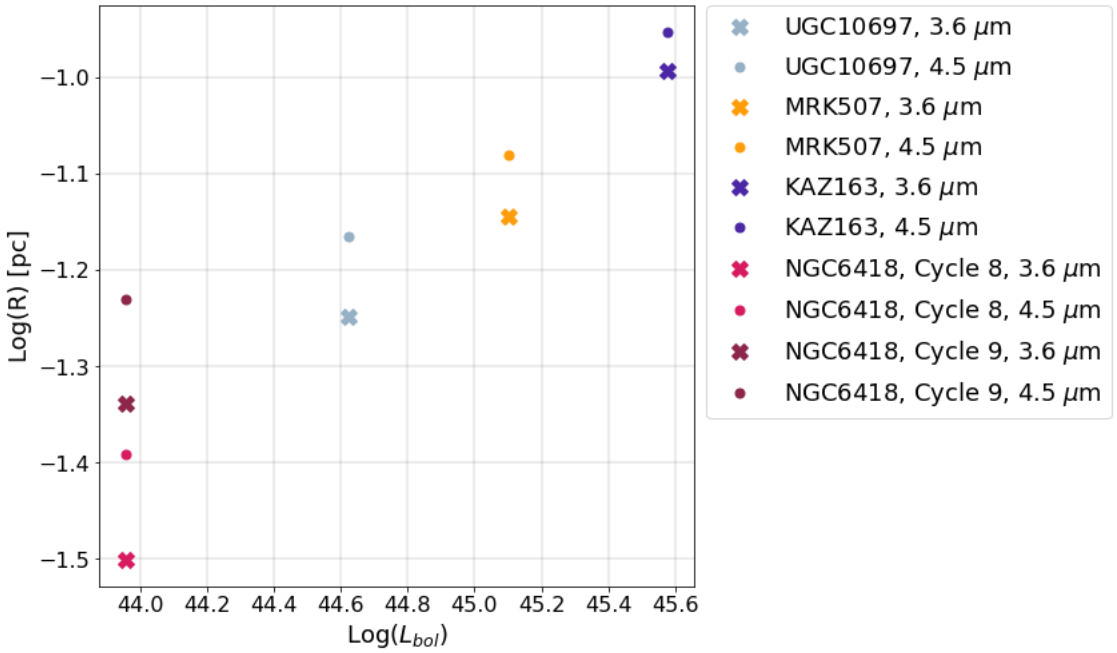

Figure 7.1: Radius-Luminosity relation for our sample of AGN: Each data point indicates one lag value. Lag values from MRK 507 and KAZ 163 are those calculated using the fully-combined, starlight-subtracted optical light curves. The lags from UGC 10697 were calculated using the PTF optical light curve. The symbols indicate the 3.6μm-optical or 4.5μm-optical lag results.

7.2 Future Work

More in-depth TORMAC modeling of KAZ 163 and MRK 876 can be performed. It is easier to determine which parameters best describe the torus in each AGN when creating grids of models that fully explore a chosen parameter space. For these two AGN, we did not run many models exploring the thickness of the torus (σ), and inclination angles other than $i = 0°$ and $i = 45°$. We can constrain more torus parameters in these AGN by expanding the model grid. We can also create TORMAC models for KAZ 102, which is the other AGN for which we were able to construct a starlight-subtracted light curve, without negative fluxes. TORMAC was recently optimized to run much faster, so it will be easier to explore the model parameter space.

We can also use these grids of models with a new version of the Markov Chain Monte Carlo (MCMC) fitting code clumpyDREAM (Sales et al., 2015) developed by collaborator Jack Gallimore,

to fit the observed IR light curves. This code performs an MCMC search within the model grid to produce a posterior probability distribution for each of the torus parameters. This will allow us to more accurately constrain parameters for these AGN.

APPENDIX A

SUPPLEMENTARY FIGURES

A.1 NGC 6418

A.1.1 Cycle 8 Optical-IR Analysis

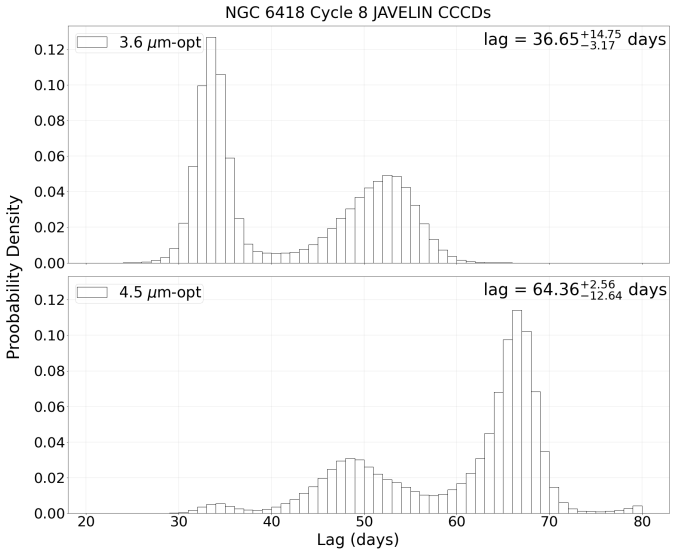

Figure A.1: NGC 6418 CCCDs formed using JAVELIN for the cycle 8 optical-3.6 μm (upper subplot) and optical-4.5 μm (lower subplot) analysis.

A.1.2 Cycle 9 Optical-IR Analysis

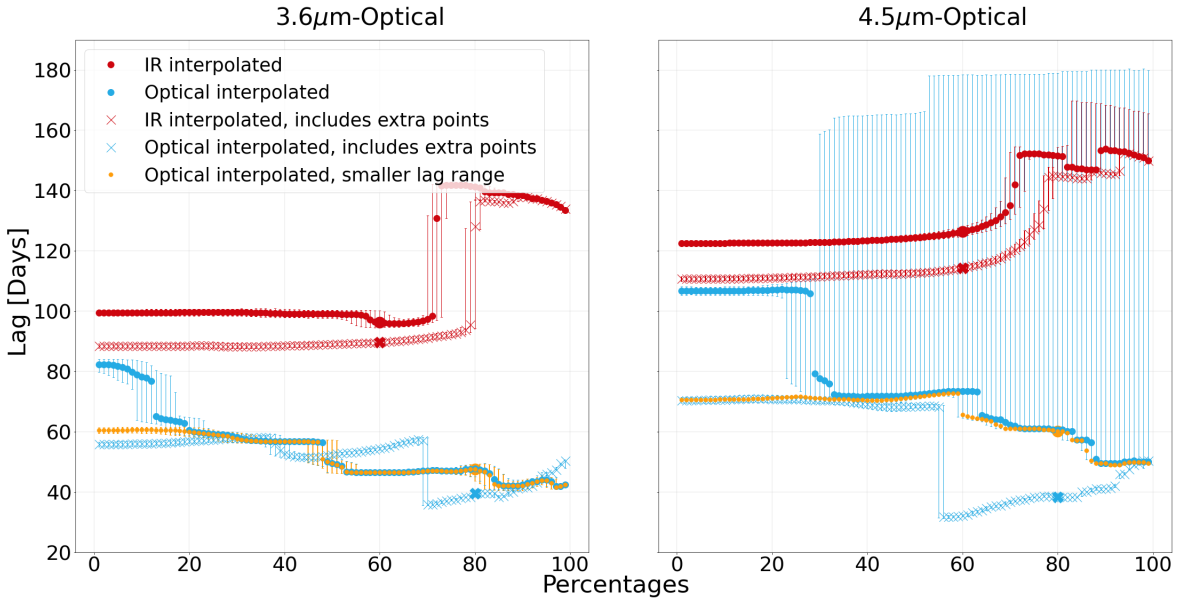

Figure A.2:
NGC 6418 measured lag vs CCF threshold percentage values for the 3.6 μm-optical analysis (left plot) and the 4.5 μm-optical analysis (right plot): The red points represent IR interpolation, while blue represents optical interpolation. The dots indicate lags calculated using the cycle 9 portion of the light curve, and crosses represent the lags calculated also including data points from the end of cycle 8. The larger symbols indicate the 80% threshold percentage values when using optical interpolation, and 60% threshold percentage values when using IR interpolation. The results of using optical interpolation with a smaller lag range is overplotted in yellow.

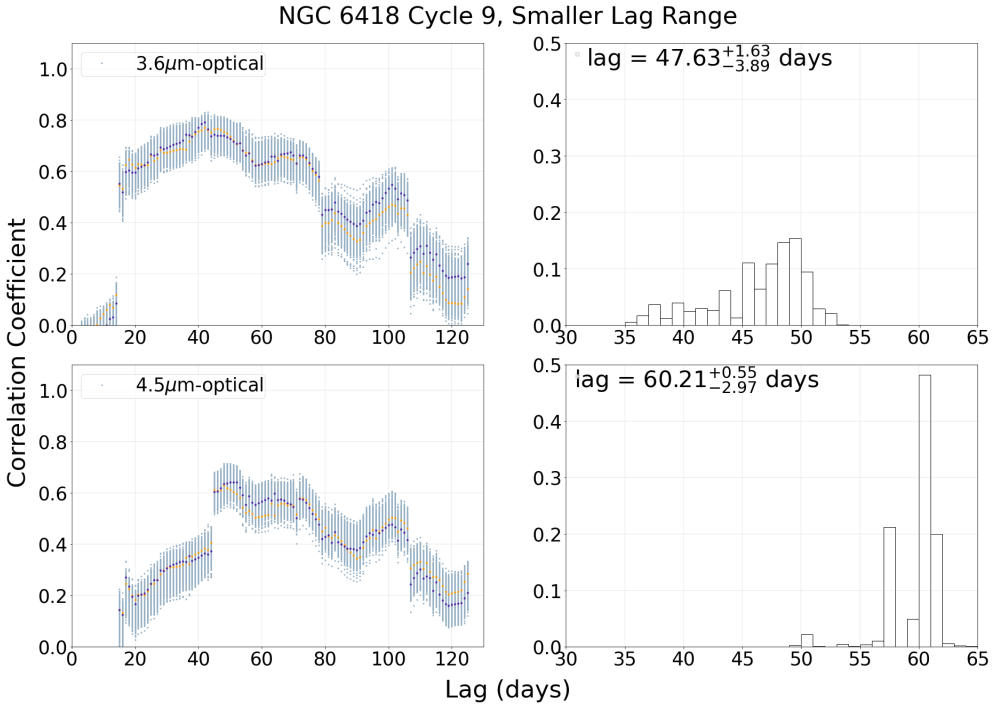

Figure A.3:
NGC 6418 CCFs and CCCDs for the 3.6μm-optical analysis (upper subplots) and 4.5μm-optical analysis (lower subplots), using a smaller lag range. Each CCF plot includes 1000 CCFs formed from the Monte Carlo iterations, shown in light blue. As examples, the purple and orange points highlight two individual CCFs.

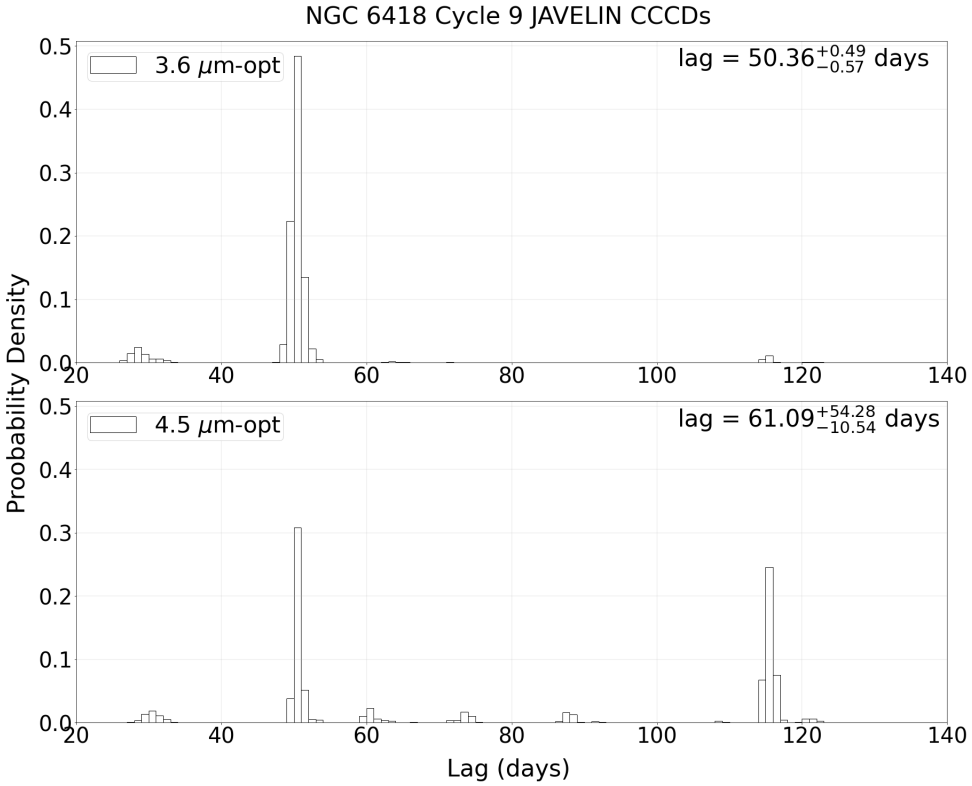

Figure A.4: NGC 6418 CCCDs formed using JAVELIN for the cycle 9 optical-3.6 μm (upper subplot) and optical-4.5 μm (lower subplot) analysis.

A.1.3 Cycle 9 CCF Features: Optical-IR Analysis

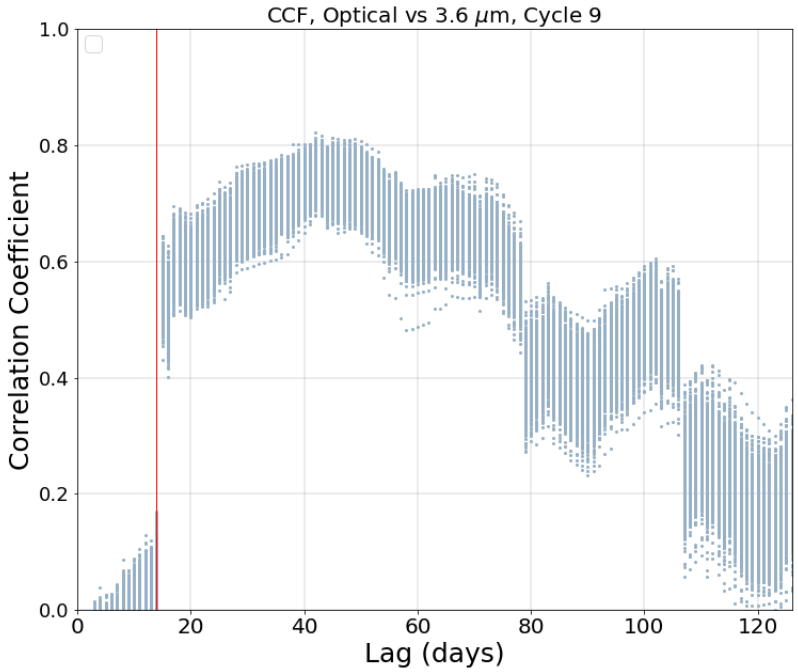

Figure A.5: NGC 6418 CCFs for the 3.6μm-optical analysis, showing a smaller lag range. This plot includes 1000 CCFs formed from the Monte Carlo iterations, shown in light blue. The vertical red line is located at a lag of 14 days.

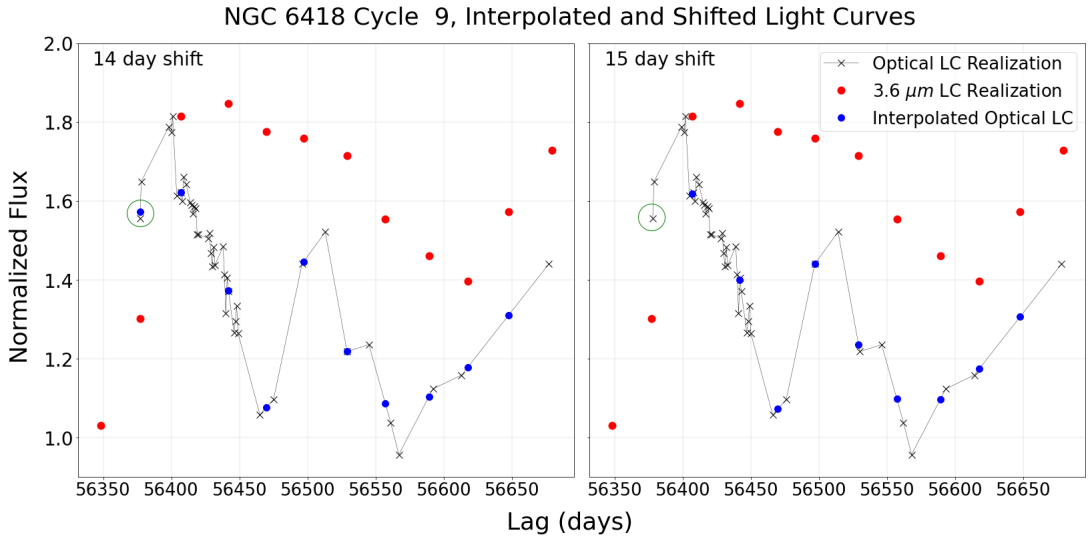

Figure A.6: Examples of the interpolated optical and 3.6 μm light curves of NGC 6418: The plot on the left shows the interpolated optical light curve shifted forward by 14 days, while the right plot has a 15 day shift. Each plot includes one 3.6μm light curve realization (the red points), the optical light curve realization is shown as black points, and the red points represent the optical data linearly interpolated onto the time stamps of the 3.6 μm data points. A green circle surrounds the data point of interest.

As seen in Figure A.6, there are several discontinuities in the CCFs. This is an edge effect that occurs due to there being so few data points for the cycle 9 section. For example, a prominent discontinuity (indicated in Figure A.5) occurs between a lag of 14 and 15 days in the 3.6μm-optical CCFs. Figure A.6 shows an example of an IR light curve realization, and the corresponding interpolated optical light curve realization shifted forward by lag values of 14 and 15 days. Note that in this figure, the only data points used in the CCA are the pairs of red and blue points which correspond to the same day. A green circle surrounds the optical data point of interest. For a 14 day lag (see left subplot), the circled optical point still overlaps in time with an IR data point, and therefore is able to be interpolated onto the IR timestamp. However, when shifting the optical light curve forward one more day (corresponding to a lag of 15 days), the optical data point can no longer be interpolated onto the IR timestamp, as the 15 day shift has moved the optical light curve past the IR data point. If there were more data points in the IR light curve, then the discontinuities

seen in the CCFs would not occur

BIBLIOGRAPHY

Almeyda, T., Robinson, A., Richmond, M., Nikutta, R., & McDonough, B. 2020, ApJ, 891, 26

Almeyda, T., Robinson, A., Richmond, M., Vazquez, B., & Nikutta, R. 2017, ApJ, 843, 3

Almeyda, T. R. 2017, PhD thesis, Rochester Institute of Technology

Alonso-Herrero, A., Quillen, A. C., Rieke, G. H., Ivanov, V. D., & Efstathiou, A. 2003, AJ, 126, 81

Antonucci, R. 1993, ARAA, 31, 473

Asmus, D., Hönig, S. F., & Gandhi, P. 2016, ApJ, 822, 109

Barvainis, R. 1987, ApJ, 320, 537

—. 1992, ApJ, 400, 502

Baskin, A., & Laor, A. 2018, MNRAS, 474, 1970

Bentz, M. C., Peterson, B. M., Netzer, H., Pogge, R. W., & Vestergaard, M. 2009, ApJ, 697, 160

Bentz, M. C., et al. 2013, ApJ, 767, 149

Blandford, R. D., & McKee, C. F. 1982, ApJ, 255, 419

Boller, T., Brandt, W. N., & Fink, H. 1996, A&A, 305, 53

Burtscher, L., et al. 2013, A&A, 558, A149

Cappellari, M. 2017, MNRAS, 466, 798

Clavel, J., Wamsteker, W., & Glass, I. S. 1989, ApJ, 337, 236

Collins, K. A., Kielkopf, J. F., Stassun, K. G., & Hessman, F. V. 2017, AJ, 153, 77

Denney, K. D., et al. 2014, The Astrophysical Journal, 796, 134

Drake, A. J., et al. 2009, ApJ, 696, 870

Gravity Collaboration et al. 2020, A&A, 635, A92

Green, P. J., et al. 2022, ApJ, 933, 180

Grier, C. J., et al. 2019, ApJ, 887, 38

Healey, S. E., Romani, R. W., Taylor, G. B., Sadler, E. M., Ricci, R., Murphy, T., Ulvestad, J. S., & Winn, J. N. 2007, ApJS, 171, 61

Heckman, T. M., & Best, P. N. 2014, ARAA, 52, 589

Hickox, R. C., & Alexander, D. M. 2018, ARAA, 56, 625

Honeycutt, R. K. 1992, PASP, 104, 435

Hönig, S. F. 2019, ApJ, 884, 171

Hönig, S. F., Kishimoto, M., Antonucci, R., Marconi, A., Prieto, M. A., Tristram, K., & Weigelt, G. 2012a, ApJ, 755, 149

—. 2012b, ApJ, 755, 149

Hönig, S. F., et al. 2013, ApJ, 771, 87

Jaffe, W., et al. 2004, Nature, 429, 47

Kaspi, S., Smith, P. S., Netzer, H., Maoz, D., Jannuzi, B. T., & Giveon, U. 2000, ApJ, 533, 631

Kawaguchi, T., & Mori, M. 2010, ApJL, 724, L183

—. 2011, ApJ, 737, 105

Khachikian, E. Y., & Weedman, D. W. 1974, ApJ, 192, 581

Kim, M., Ho, L. C., Peng, C. Y., Barth, A. J., & Im, M. 2008, ApJS, 179, 283

—. 2017, ApJS, 232, 21

Kishimoto, M., Hönig, S. F., Antonucci, R., Barvainis, R., Kotani, T., Tristram, K. R. W., Weigelt, G., & Levin, K. 2011, A&A, 527, A121

Kishimoto, M., Hönig, S. F., Antonucci, R., Kotani, T., Barvainis, R., Tristram, K. R. W., & Weigelt, G. 2009, A&A, 507, L57

Kishimoto, M., Hönig, S. F., Beckert, T., & Weigelt, G. 2007, A&A, 476, 713

Kishimoto, M., et al. 2022, ApJ, 940, 28

Kokubo, M., & Minezaki, T. 2020, MNRAS, 491, 4615

Koshida, S., et al. 2014, ApJ, 788, 159

Krist, J. E., Hook, R. N., & Stoehr, F. 2011, in Society of Photo-Optical Instrumentation Engineers (SPIE) Conference Series, Vol. 8127, Optical Modeling and Performance Predictions V, ed. M. A. Kahan, 81270J

Krolik, J. H., & Begelman, M. C. 1988, ApJ, 329, 702

LaMassa, S. M., et al. 2015, ApJ, 800, 144

Law, N. M., et al. 2009, PASP, 121, 1395

Leftley, J. H., Tristram, K. R. W., Hönig, S. F., Asmus, D., Kishimoto, M., & Gandhi, P. 2021, ApJ, 912, 96

López-Gonzaga, N., Burtscher, L., Tristram, K. R. W., Meisenheimer, K., & Schartmann, M. 2016, A&A, 591, A47

Lynden-Bell, D. 1969, Nature, 223, 690

Lyu, J., Rieke, G. H., & Smith, P. S. 2019, ApJ, 886, 33

MacLeod, C. L., et al. 2019, ApJ, 874, 8

Maoz, D., et al. 1991, ApJ, 367, 493

Minezaki, T., et al. 2019, ApJ, 886, 150

Nenkova, M., Sirocky, M. M., Ivezić, Ž., & Elitzur, M. 2008a, ApJ, 685, 147

Nenkova, M., Sirocky, M. M., Nikutta, R., Ivezić, Ž., & Elitzur, M. 2008b, ApJ, 685, 160

Netzer, H. 2015, ARAA, 53, 365

Osterbrock, D. E. 1977, ApJ, 215, 733

—. 1981, ApJ, 249, 462

Peng, C. Y., Ho, L. C., Impey, C. D., & Rix, H.-W. 2002, AJ, 124, 266

—. 2010, AJ, 139, 2097

Perez, E., Robinson, A., & de La Fuente, L. 1992, MNRAS, 255, 502

Peterson, B. M. 1993, PASP, 105, 247

Peterson, B. M. 2001, in Advanced Lectures on the Starburst-AGN, ed. I. Aretxaga, D. Kunth, & R. Mújica, 3

Peterson, B. M., Wanders, I., Horne, K., Collier, S., Alexander, T., Kaspi, S., & Maoz, D. 1998, PASP, 110, 660

Remillard, R. A., Bradt, H. V. D., Brissenden, R. J. V., Buckley, D. A. H., Roberts, W., Schwartz, D. A., Stroozas, B. A., & Tuohy, I. R. 1993, AJ, 105, 2079

Robinson, A., & Perez, E. 1990, MNRAS, 244, 138

Rodríguez-Pascual, P. M., et al. 1997, ApJS, 110, 9

Roth, N., Kasen, D., Hopkins, P. F., & Quataert, E. 2012, ApJ, 759, 36

Runnoe, J. C., Brotherton, M. S., & Shang, Z. 2012a, MNRAS, 427, 1800

—. 2012b, MNRAS, 422, 478

—. 2012c, MNRAS, 426, 2677

Runnoe, J. C., et al. 2016, MNRAS, 455, 1691

Sales, D. A., et al. 2015, ApJ, 799, 25

Salpeter, E. E. 1964, ApJ, 140, 796

Shappee, B. J., et al. 2014, ApJ, 788, 48

Steele, I. A., et al. 2004, in Society of Photo-Optical Instrumentation Engineers (SPIE) Conference Series, Vol. 5489, Ground-based Telescopes, ed. J. Oschmann, Jacobus M., 679–692

Suganuma, M., et al. 2006, ApJ, 639, 46

Sun, M., Grier, C. J., & Peterson, B. M. 2018, PyCCF: Python Cross Correlation Function for reverberation mapping studies

Swain, M., et al. 2003, ApJL, 596, L163

Tristram, K. R. W., et al. 2007, A&A, 474, 837

—. 2009, A&A, 502, 67

Urry, C. M., & Padovani, P. 1995, PASP, 107, 803

Vazquez, B. 2015, PhD thesis, Rochester Institute of Technology

Vazquez, B., et al. 2015, ApJ, 801, 127

Véron-Cetty, M. P., & Véron, P. 2006, A&A, 455, 773

Wang, S., Liu, J., Qiu, Y., Bai, Y., Yang, H., Guo, J., & Zhang, P. 2016, ApJS, 224, 40

Weedman, D. W. 1978, MNRAS, 184, 11P

Weigelt, G., et al. 2012, A&A, 541, L9

Yang, Q., et al. 2020, ApJ, 900, 58

Zu, Y., Kochanek, C. S., Kozłowski, S., & Peterson, B. M. 2016, ApJ, 819, 122